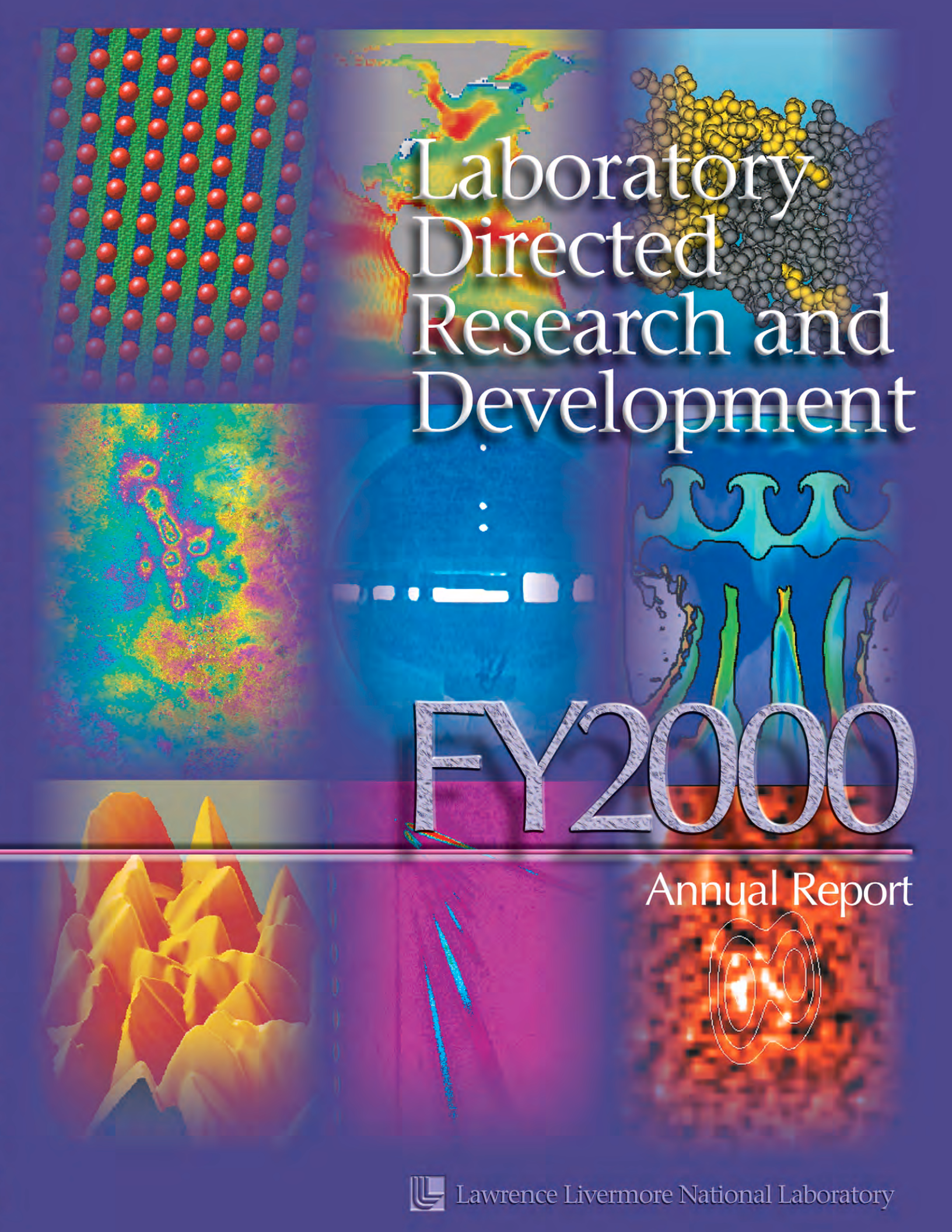

Laboratory Directed Research and Development

FY2000

Annual Report

Lawrence Livermore National Laboratory

This work was performed under the auspices of the U.S. Department of Energy by University of California Lawrence Livermore National Laboratory under contract No. W-7405-Eng-48.

Laboratory Directed Research and Development

FY2000

Annual Report

UCRL-LR-113717-00

Lawrence Livermore National Laboratory

Acknowledgments

This Annual Report provides an overview of the FY2000 Laboratory Directed Research and Development (LDRD) Program at Lawrence Livermore National Laboratory (LLNL) and presents a summary of the results achieved by each project during the year. We extend our sincere appreciation to the principal investigators of these LDRD projects for providing the technical content of this report, and to the publications team, whose names are listed below. A special thanks goes to Gordon Struble and Louis Terminello for their assistance in the technical review. We also thank the dedicated LDRD staff: Cathleen Sayre, Resource Manager; Nancy Campos, Database Administrator; and Tracey Barnes, Office Administrator.

At LLNL, Laboratory Director C. Bruce Tarter and Deputy Director for Science and Technology Jeffrey Wadsworth are responsible for the LDRD Program, which is in compliance with Department of Energy (DOE) Order 413.2 and other relevant DOE orders and guidelines. The Laboratory Director delegates responsibility for the operation of the LDRD Program to the Director of the Laboratory Science and Technology Office, Rokaya Al-Ayat.

Scientific Editor
Rokaya A. Al-Ayat

Publication Editor
Karen Kline

Publication Designer
Daniel Moore

Publications Staff
Coralyn McGregor (editorial)
Irene Hedman (editorial)
Sylvia McDaniel (editorial)
Linda Moore (illustration)
Nancy Campos (database administration)

Contents

The FY2000 LDRD Program at LLNL

Overview of the LDRD Program at LLNL

As a Department of Energy (DOE) National Nuclear Security Administration (NNSA) laboratory, Lawrence Livermore National Laboratory (LLNL or the Laboratory) has an essential and compelling primary mission to ensure that the nation's nuclear weapons remain safe, secure, and reliable and to prevent the spread and use of nuclear weapons worldwide. A multidisciplinary laboratory with over 7,000 employees, LLNL has been managed since its inception in 1952 by the University of California (UC). This long association with UC, one of the premier university systems in the nation, has enabled LLNL to establish an atmosphere of intellectual freedom and innovation that attracts a world-class workforce to tackle important national challenges.

Developing new scientific and technological innovations forms the very core of LLNL's unique capabilities and is the foundation of its intellectual vitality. Research and development (R&D) projects that foster new scientific and technical expertise enable LLNL to stay at the forefront in its mission areas. Through its emphasis on multidisciplinary R&D, LLNL has continually renewed and advanced its wide range of skills—including those in high-performance computing, advanced engineering, and the management of large R&D projects—to become a science and technology leader for an impressive range of national needs.

Over the years, LDRD has become the Laboratory's primary means for conducting innovative, long-term, high-risk, and potentially high-payoff research at the forefront of science and technology.

The Laboratory Directed Research and Development (LDRD) Program was authorized by the United States Congress to fund creative and innovative R&D activities that ensure the scientific and technical vitality of the NNSA laboratories in their mission areas. The LDRD Program has enabled some of the most renowned achievements of the national laboratories and has contributed the science and technology essential to making the Stockpile Stewardship Program possible. As part of the NNSA 's commitment to scientific excellence, the LDRD Program enables the Laboratory Director to encourage development of new scientific and technical capabilities that respond to LLNL's continually evolving missions.

Over the years, LDRD has become the Laboratory's primary means for conducting innovative, long-term, high-risk, and potentially high-payoff research at the forefront of science and technology. The Program plays a vital role in engaging our best researchers, in recruiting our future scientists and engineers, and in promoting numerous collaborations with the scientific community in academia, national and international laboratories, and industry.

Structure of the LDRD Program at LLNL

In FY2000, the Laboratory continued to invest in important areas supporting national security efforts within the LDRD Program's three major categories: Strategic Initiatives (SI), Exploratory Research (ER) projects, and the Laboratory-Wide (LW) Competition. The LDRD Program also funds a few projects in a fourth category, Feasibility Studies/Project Definition (FS/PD). Figures 1 and 2 show the distribution of funding dollars and the number of projects in each category.

Strategic Initiatives. The Strategic Initiative (SI) component focuses on innovative research and development activities that are likely to set new directions for existing programs, may help develop new programmatic areas within LLNL mission responsibilities, and/or enhance the Laboratory's science and technology base. Projects in this category are usually larger and more technically challenging than projects funded in the other categories. An SI project must be aligned with the strategic R&D priorities of at least one of the four Laboratory strategic councils: (1) the Council on Bioscience and Biotechnology, (2) the Council on Energy and Environmental Systems, (3) the Council on National Security, and (4) the Council on Strategic Science and Technology. Although many deserving proposals are considered, less than one-third of the proposals are funded.

In FY2000, the LDRD Program funded 13 SI projects that ranged from computational biology research to the application of global and regional climate simulations. Several of these diverse research projects take advantage of the Accelerated Strategic Computing Initiative's (ASCI's) high-performance computing capability at LLNL.

Exploratory Research. The Exploratory Research (ER) component of LDRD is aligned with a Laboratory directorate's (ERD) or institute's (ERI) strategic R&D needs. Examples include global and climate simulations, research on remote detection of bioaerosols, and ultrafast production of highly stable nanostructures on semiconductors. Typically, fewer than half of the proposals submitted to the directorates and institutes are forwarded to an ER oversight committee for

further review and selection. Over 66% of LDRD funds are allocated to the ER category. In FY2000, 113 of the 145 projects funded (78%) were ER proposals.

Laboratory-Wide Competition. Projects in the third LDRD component—the Laboratory Wide (LW) competition—emphasize innovative research concepts and ideas with limited management filtering to encourage the creativity of individual researchers. The competition is open to all LLNL staff in programmatic, scientific, engineering, technical support, or administrative areas. In FY2000, we funded 16 LW projects of the 99 proposals submitted.

Feasibility Studies/Project Definition. The LDRD Program also funds a few projects in a fourth category called Feasibility Studies/Project Definition (FS/PD). This special category of LDRD projects provides the flexibility to define and develop potential projects in other categories. In FY2000, we funded three projects in the FS/PD category, which represented less than 0.3% of the LDRD budget. For *Annual Report* purposes the FS/PD category is included with the ER category.

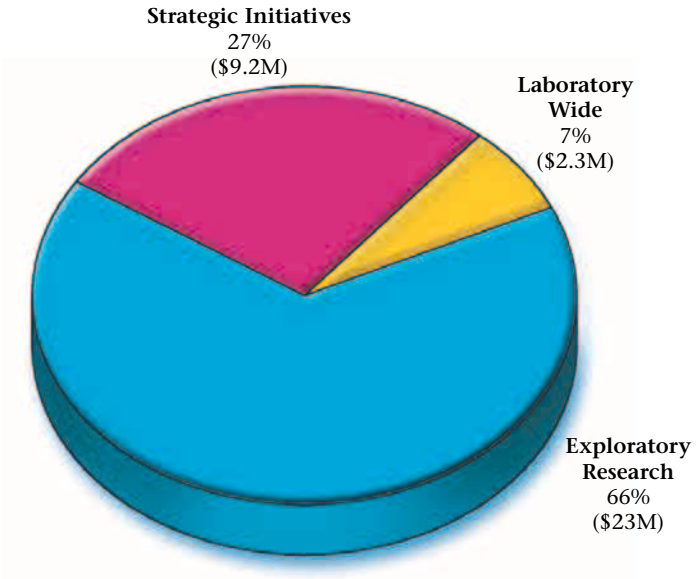

Figure 1. Distribution of FY2000 funding ($34.5 M) among the three main categories of the Laboratory's LDRD Program. Due to the small dollar amount it received ($112 K, about 0.3% of total funding), the Feasibility Studies category is included with the Exploratory Research category.

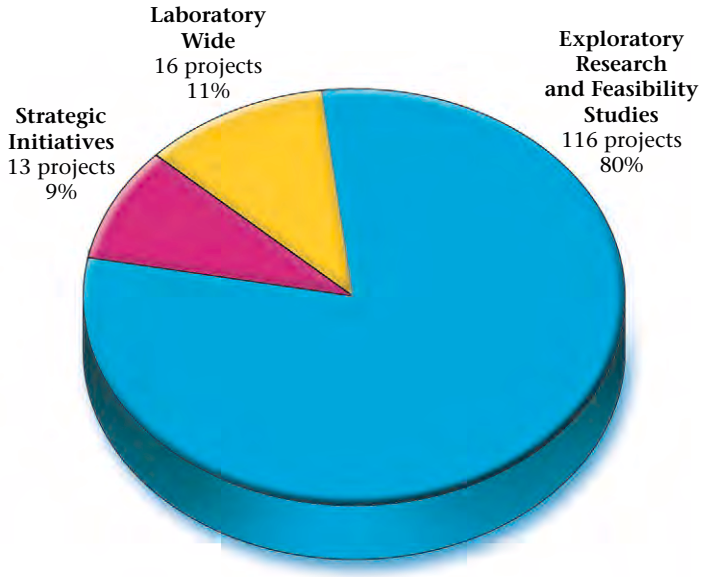

Figure 2. Number and percentage of the 145 FY2000 LDRD projects in each category.

The FY2000 LDRD Portfolio

The FY2000 LDRD portfolio described in this *Annual Report* was carefully structured to continue the vigorous support for the strategic vision and long-term goals of NNSA and the Laboratory. The projects chosen for LDRD funding undergo a stringent selection process, which emphasizes strategic relevance and requires technical peer reviews of proposals by external and internal experts. The FY2000 projects focus on the Laboratory's national security missions: stewardship of the U.S. nuclear weapons stockpile, responsibility for the counter- and nonproliferation of weapons of mass destruction, development of high-performance computing, and support of DOE environmental research and waste-management programs. Analysis shows that our FY2000 LDRD portfolio is highly supportive of the Laboratory's national security mission. About 95% of the LDRD funds supported LLNL's national security activities in FY2000, which far exceeds the National Security Program percentage of LLNL's overall budget, estimated to be 66% for FY2000.

For FY2000, Section 308 of the Energy and Water Development Appropriations Bill (HR 2605) directed a reduction in the allowable funding level for DOE LDRD Programs from 6% of the Laboratory's total budget to 4%. The Bill stated: "Of the funds in this Act provided to government-owned contractor-operated laboratories, not to exceed 4 percent shall be available to be used for Laboratory Directed Research and Development: Provided: That none of the funds in the Environmental Management programs are available for Laboratory Directed Research and Development."

For LLNL, the cut resulted in a nearly 40% reduction in the FY2000 LDRD budget from the FY1999 level (from $57.8M in FY1999 to $34.5M for FY2000), which had a negative impact on the scope of the LDRD portfolio. The reduced funding for LDRD in FY2000 resulted in many cancelled projects as well as reduced resources for many others. The LDRD Program at LLNL responded to this cut by designing the FY2000 portfolio to place major emphasis on protecting the Laboratory's strategic investments and long-term strategic goals, with particular attention to the Laboratory's need for attracting and retaining essential personnel. Despite our best efforts, the reduction had a detrimental impact on our research staff. We are still feeling the effects of the FY2000 cut.

Highlights of FY2000 LDRD Projects

We highlight six LDRD projects funded in FY2000—two projects each from the SI, ER, and LW categories—that illustrate the diverse scope of LDRD research. The list demonstrates the LDRD Program's emphasis on the science and technology needs of the NNSA's national security mission.

Strategic Initiatives (SI)

- *Large Aperture, Lightweight Space Optics* (00-SI-003), R. Hyde, Principal Investigator

National security- and science-related space programs require large, low-mass optics for their Earth-observation and astronomy missions. Important characteristics for deploying space-based optics include space-proof materials, low weight, and foldability. In this project, the LDRD research team, led by R. Hyde, has proposed a new concept for using diffractive optics that offers a radically different approach from mirrors or conventional lenses. The team has developed chromatic correction techniques to overcome the limitations of diffractive lenses, while retaining their advantages of low mass. Building on LLNL's expertise in fabricating meter-size diffractive optics in fused silica, the project team has demonstrated that large, low-mass, foldable, optical-quality lenses can be successfully fabricated from materials that withstand the radiation environment of space.

In FY2000, the first year of the project, the team built and tested a 75-cm foldable lens comprised of six panels of commercially available microsheet glass that is smooth to an accuracy of 0.1-µm. Panels are attached with precise, foldable joints to create a multipanel, foldable lens that can be focused as accurately as a monolithic lens (see Fig.). In the next phase, the project will scale up to a lens size of 5 m and 81 segments. The ultimate goal of this technology is the eventual deployment in space of 20 to 50-m-diameter optics with a mass of less than 500 kg. For more information about this project, see p. 6–22.

- *High-Power Inertial Fusion Energy Driver Component Development* (00-SI-009), C. Bibeau, Principal Investigator

The Mercury laser system, the next-generation high-power, diode-pumped, solid-state laser driver system for inertial fusion energy (IFE), integrates three technologies: crystals, diodes, and gas cooling. Mercury is scalable to kilojoule and megajoule energy levels for fusion energy applications and high-energy-density plasma physics. LDRD researchers in this two-year project focused on developing one of the crucial technologies needed for the Mercury laser system: large, high-quality ytterbium-doped, fluorapatite (YB:S-FAP) crystals. During laser amplification, the beam passes four times through two gas-cooled amplifier-head assemblies, each of which contains seven crystalline slabs. The design calls for 4 × 6 × 0.75-cm crystalline slabs of YB:S-FAP, which offer 1-ms storage and can be pumped with 900-nm laser diodes.

Growing such large, high-optical-quality crystals depends on understanding and eliminating the defects that can be present in the crystals—cloudiness, anomalous absorption, grain boundaries, bubble-core, cracking and small inclusions. In FY2000, C. Bibeau and her team concentrated on the growth characteristics and defect chemistry of Yb:S-FAP crystals. In collaboration with experts in the high-temperature crystal-growth community, LDRD researchers have developed a reproducible process to nearly eliminate each of the defects in the crystals. Future work will focus on growing subscale, lower-defect crystals (see Fig.) and on an innovative technology to seamlessly bond together two subscale slabs from these crystals to form a full-size (4 × 6 cm) slab. For more information about this project, see p. 6–23.

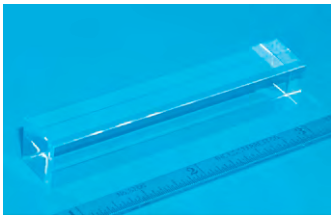

Exploratory Research (ER)

- *Remotely Interrogated Gigabit-per-Second Free-Space-Laser Communications* (99-ERD-011), A. Ruggiero, Principal Investigator

The evolving sophistication of remote-sensing systems for military and intelligence applications has led to an increasing demand for high-data-rate (gigabit per second) communications links that can relay encoded information over a turbulent atmospheric path from the sensor to a command center. The communications link that is traditionally proposed for this type of operation, a retromodulator phase-conjugate mirror (RM-PCM), has several advantages. Phase conjugation removes deleterious amplitude-modulated noise due to atmospherics, permits a high signal-to-noise communications link to be established, and provides an automatic pointing and tracking function by precisely returning the probe or beacon beam to its origin. However, until this LDRD project, actual implementation of this type of passive RM-PCM link has proved to be both difficult and limited.

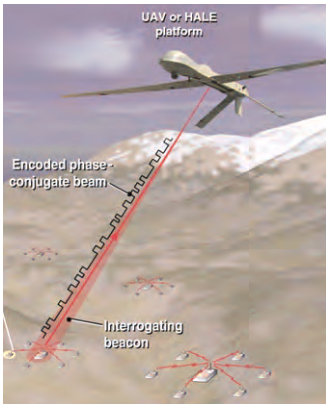

Ruggiero's team focused on developing a novel, laser-based communications system that provides an innovative solution to the limitations of phase-conjugation technology (see Fig.). The system uses an active RM-PCM link that is based on nondegenerate four-wave mixing in a broad-area laser diode. In FY2000, A. Ruggiero and his team of researchers completed laboratory

feasibility experiments and constructed and successfully demonstrated a surrogate two-dimensional microphase conjugator structure. Now that the LDRD project is complete, the technology has moved into the patent process and the Laboratory has partnered with a major diode laser manufacturer for further development. For more information about this project, see page 1–5.

- *Hydrogen Bonding and Molecular Dissociation at High Pressure: Low-Z Liquids and Liquid Mixtures* (00-ERD-031), G. Galli, Principal Investigator

This project uses first-principles molecular dynamics codes to simulate the structural and dynamical properties of hydrogen bonds in liquids and liquid mixtures under pressure. Although hydrogen bonds are the most prominent low-*Z*, or "weak," interactions in solids, liquids, and gases, their nature is poorly understood. At high pressure, the nature and behavior of hydrogen bonds is virtually unknown. First-principles simulations performed in this LDRD project provide information about hydrogen bonding and molecular dissociation, such as a detailed description of the liquid structure, that is not directly accessible by experiment. Results of these computer simulations can complement those of real experiments and help interpret experimental data.

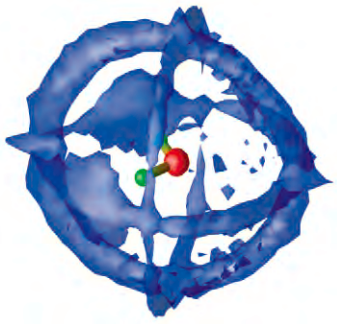

In FY2000, G. Galli and her team had four major scientific achievements. They (1) predicted the microscopic structure of water (see Fig.)—the most important liquid in the physical sciences and biology—and hydrogen fluoride (HF) under pressure; (2) obtained data on the equations of state (EOS) of water and HF that are useful for simulating energetic materials; (3) interpreted experiments on hydrogen-bonded liquid and liquid mixtures; and (4) predicted structural and thermodynamic properties of several low-*Z* molecular systems that are not hydrogen bonded. This last result played an essential role in identifying a newly discovered compressed phase of solid CO_2, for which the team received a Laboratory award. For more information about this project, see page 4–23.

Laboratory Wide(LW)

- *Dynamic Focusing of Acoustic Energy for Nondestructive Evaluation* (99-LW-045), J.V. Candy, Principal Investigator

Components parts of highly sophisticated experimental systems must undergo periodic inspection as part of a scheduled maintenance and monitoring program. Most materials, especially in optical components, have many small defects that are distributed throughout the material. Inspections are critical because even minute defects can grow into larger flaws that could lead to malfunction or even catastrophic failure of the entire system.

In FY2000, this team of LDRD researchers worked to develop a new nondestructive evaluation technique that focuses acoustical energy to detect and characterize flaws in parts undergoing ultrasonic testing. The technique uses a combination of detailed simulations, algorithm development, and hardware to focus acoustic energy successively on the strongest scatterer in the material (see Fig.). Once the focus has been detected, the individual scatterer is extracted from the measured data. The focusing, selection, and extraction process is repeated for the next strongest scatterer until a flaw map develops that pinpoints the exact location of each flaw. For more information about this project, see p. 1–11.

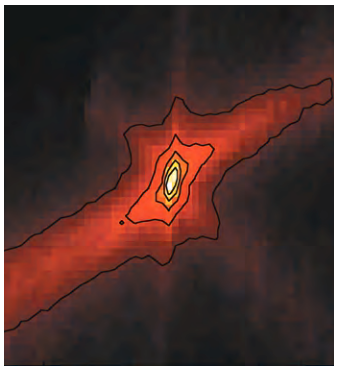

- *Polarized Light Imaging through Scattering Media* (99-LW-011), D. J. Maitland, Principal Investigator

Experimental results from this project suggest that polarized light can be used to image and diagnose objects that are embedded in optically turbid media. These results have a variety of applications in medical diagnostics, underwater imaging, and atmospheric optics. For example, initial research points to the possibility of using polarized light to discriminate cancerous tumors from the healthy tissue in which they are embedded—a breakthrough for cancer research.

The photons of polarized light passing through an optically turbid medium, like human tissue, are differentially scattered by the various densities of material they encounter in the medium. By discriminating the weakly scattered photons, which have traveled nearly a linear path through a medium, from highly scattered photons, which have traveled a more circular path, the LDRD team experimentally demonstrated that polarized light can be used to detect and characterize objects within a turbid medium (See Fig.). This result is a novel first step towards explaning why polarized light propagates as it does in tissue. For more information about this project, see page 3–5.

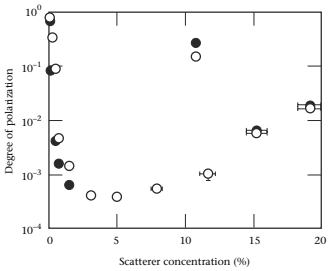

LDRD Funding for FY2000

In FY2000, the DOE authorized the LDRD Program to fund $34.5 M for projects in three categories: approximately 66% for ER, 27% for SI, and 7% for LW (see Fig. 1 on p. 2).

The LDRD projects vary in size: 29 projects were funded at less than $100K, while one was funded at more than $1M; the average funding for an LDRD project in FY2000 was $238K. Figure 3 shows the distribution of funds for the FY2000 portfolio of projects.

Projects are categorized into nine competency areas. Although projects often address more than one competency area, this report classifies each project in the most appropriate category. Figure 4 shows the FY2000 funding distribution among these competency areas.

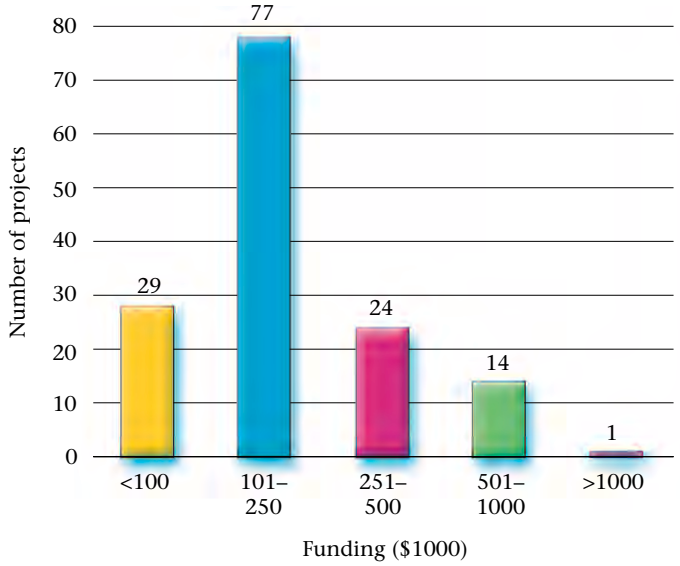

Figure 3. Distribution of FY2000 funding dollars among the Laboratory's 145 LDRD projects.

Recent LDRD Program Accomplishments

Over the years, LDRD-sponsored projects have realized major scientific and technical breakthroughs and have been widely reported in the technical community. Statistics on publications, patents, staff-member hires, and national awards, confirm that the LDRD Program is extremely productive.

Here, we highlight a few of the achievements of recent, successful LLNL projects, which also illustrate the diversity of LDRD-funded research.

- **Gordon Bell Prize.** An LLNL team won the Gordon Bell prize, one of the most prestigious awards in the field of supercomputing. The prize was awarded for Richtmeyer-Meshkov simulations on the ASCI Blue Pacific machine at the Supercomputing '99 Conference. An LDRD-funded project that focuses on visualization of terascale scientific datasets was an integral part of the work being honored.

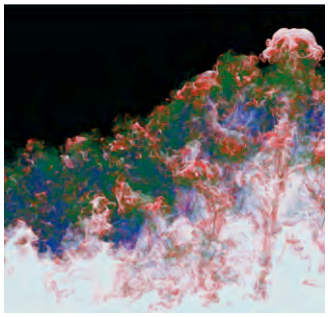

- **Technology Transfer Award.** PEREGRINE—a three-dimensional Monte Carlo radiation dose calculation system that

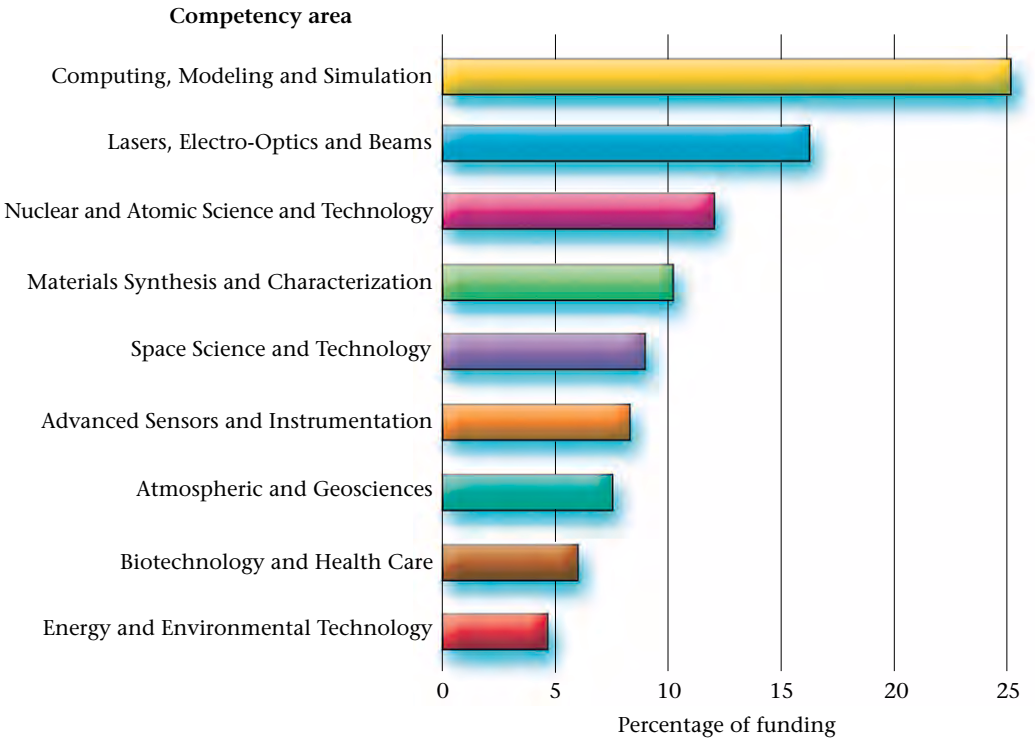

Figure 4. Distribution of FY2000 funding among the Laboratory's nine competency areas.

includes both hardware and software for calculating accurate radiation therapy dosage using fundamental physics—has garnered yet another award. The project was initiated as an SI several years ago, and was transferred to NOMOS Corporation for commercialization. This year, PEREGRINE received one of two LLNL Federal Laboratory Consortium awards for Excellence in Technology Transfer.

- **Patents Based on LDRD-Funded Projects.** In FY1996, 35 of 83 patents issued for LLNL research were based on LDRD-funded research; in FY1997, 29 of LLNL's 64 patents were LDRD-based; and in FY1998, LDRD-based research accounted for 39 of 78 patents issued to LLNL. LLNL scientists received a total of 84 patents in FY1999. Of these, 45 patents, or 54%, were LDRD based.

- **Element 114 Team Honored.** In collaboration with scientists from Dubna, Russia, LLNL LDRD researchers have discovered Element 114, which lasted for 30 seconds before decaying, a longevity that could verify predictions of "an island of stability" beyond the lighter, less stable nuclei already observed. The team was honored this year by both *Chemical Engineering News* and *Popular Science* for this discovery.

- **Counterproliferation Analysis and Planning System (CAPS).** Begun several years ago as an LDRD project and later funded as a Work for Others (WFO) project, CAPS is an extensive computer database/planning tool for analysis of worldwide weapons of mass destruction (WMD) capabilities and response options. This analysis tool has emerged as a major asset for STRATCOM and other senior members of the Department of Defense. This year, the Secretary of Defense named CAPS as the preferred counterproliferation tool for use by the nation's armed services.

- **Global Climate Research.** LLNL leadership and global climate research, built largely through LDRD-funded research, was rewarded with major roles on several carbon sequestration projects, including the DOE Ocean Sequestration Center.

- **R&D 100 Award.** An LLNL technology, Waste Inspection Tomography for Non-Destructive Assay (WIT-NDA) won an R&D 100 Award in 2000 for its LLNL researchers and their industrial partner Bio-Imaging Research, Inc. (BIR). Each year, R&D Magazine presents this award to "the 100 most technologically significant new products and processes of the year." The WIT-NDA system, an outgrowth of an FY1992 LDRD project, combines active and passive computed tomography and nuclear spectroscopy to accurately quantify all detectable gamma rays emitted from waste containers (see Fig.).

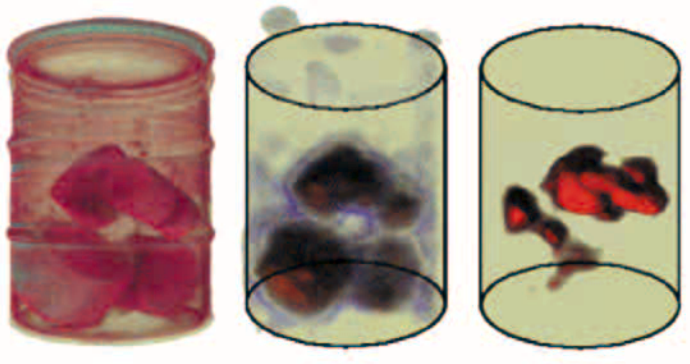

The DOE has more than 600,000 drums of radioactive waste stored at 30 sites across the nation, with possibly thousands more containers to come as more weapons are dismantled. As recently as ten years ago, researchers could accurately assay the contents of waste drums only by sampling an open drum, which posed a risk to the workers and the public. Now, WIT-NDA assays containers safely, accurately, and without having to open them. The LLNL-developed technology forms part of BIR's mobile Waste Inspection Tomography system, which provides waste assays for the DOE and corporate customers.

The FY2000 LDRD Annual Report

This LLNL *FY2000 LDRD Annual Report* provides a summary of LDRD-funded projects in the past fiscal year. Each article, submitted by the principal investigators, summarizes the project scope and discusses its motivation, goals, and progress for FY2000. Articles are arranged in sections by competency areas and assigned a unique tracking code (e.g., 98-SI-010), which consists of three elements. The first element is the year the project began (1998); the second is the LDRD category in which the project is funded (Strategic Initiative), and the third identifies the order in which the proposal was received.

The *Annual Report* also includes several appendices: compilations of LDRD publications, an author index, a title index, and a project index arranged by LDRD tracking Code.

Advanced Sensors and Instrumentation

1

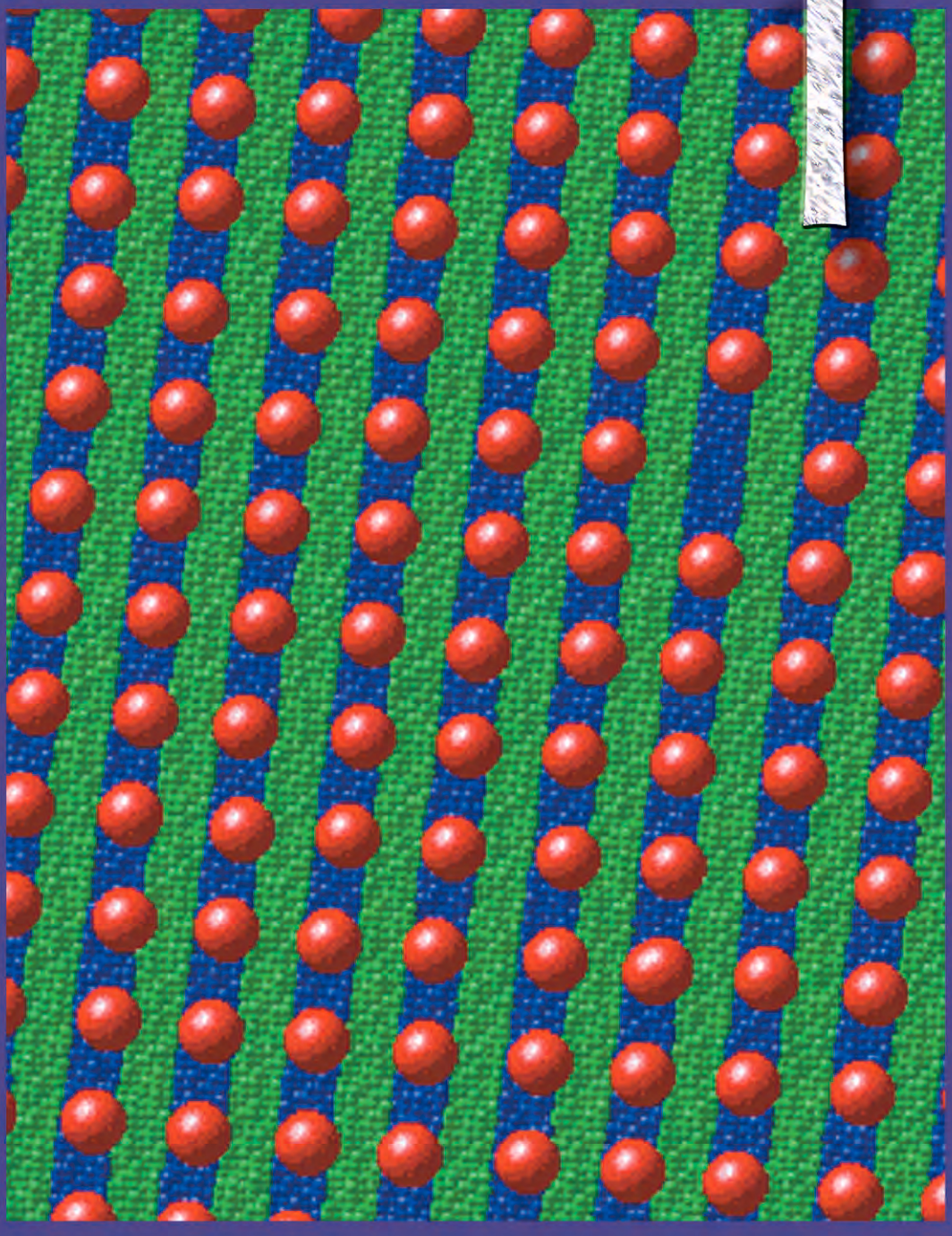

Section 1—Advanced Sensors and Instrumentation

Back to main TOC

A Full-Volume-Imaging Gamma-Ray Detector for Enhanced Sensitivity

K. P. Ziock, D. Archer, A. Dougan, J. Luke, S. Prussin

98-ERD-025

To address the problem of smuggled nuclear materials, we are developing a new class of gamma-ray detector that will significantly enhance the detectability of such materials. The detector works on the principle of Compton scattering. In this process, gamma-rays (~0.2 to 2.0 MeV) from the nuclear materials "bounce-off" the electrons in the detector, depositing energy at the scatter location. The recoiling gamma-ray is also stopped and its energy and location of capture measured. With the information from the two deposition sites, we can recreate the kinematics of the Compton scatter, and determine the direction of incidence of the gamma-ray within a narrow ring of directions. During operation, the source will appear as a region of overlapping rings in the image. Our simulations show that the ratio of ring solid angle to the solid angle of all directions reduces background radiation by a factor of 200, a tenfold increase in the detectability of smuggled sources compared to a classic omnidirectional detector.

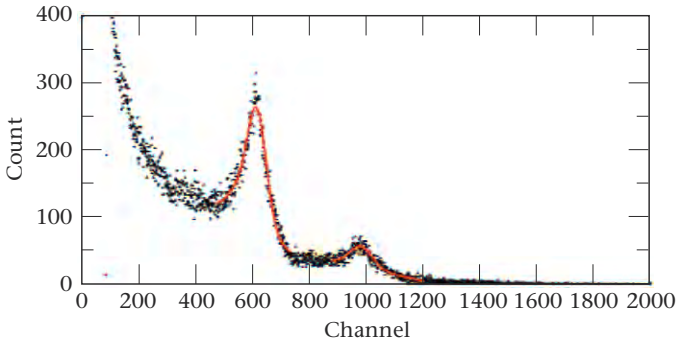

A spectrum of a ^{133}Ba source measured with the system using a microwell readout plane. The high-energy peak (~channel 1000) is identified as the 81 keV radiation from the source, the lower energy peak (~ channel 600) is identified as the K-fluorescence escape peak from this line. Due to the small volume of the active area of the detector (~ 2 × 2 cm) the escape peak is much larger than the primary peak.

During FY2000, our goal was to bring the apparatus constructed in FY1999 on line and test the system performance for use as a full-volume gamma-ray detector. The instrument comprises a volume filled with high-pressure noble gas (xenon) in which the gamma-ray interactions create electron–ion pairs. Using an applied electric field, electrons are made to drift toward a readout plane, where the number of electrons and their location is read out.

The detector uses both high pressures (up to 50 atm) and cryogenic gas handling techniques. We first demonstrated that the system could operate safely, and obtained the necessary approvals to begin experiments. Next, we focused on developing the readout plane used to amplify the number of electrons detected and to determine the location of each event. A planer charge collector was used to bring the system on line and verify our ability to detect charged particles from the ambient cosmic-ray flux traversing the unit. A subsequent collector, a wire-plane readout, provided some charge amplification and demonstrated the ability to detect gamma-rays. We concluded with a microstructure readout plane, manufactured using microlithography techniques. This plane is required for obtaining the three-dimensional position resolution and simultaneous charge amplification needed for full Compton event reconstruction. The Fig. shows a sample spectrum obtained with the microstructured readout.

Our results from the system, particularly when used with the microstructure readout plane, confirm that the detector operates as expected, correctly amplifying and detecting the gamma-ray-induced electrons generated in the xenon gas. We found no technical obstacles to successful construction of a fully functional full-volume detector. Clearly, further work remains on the design and construction of cost-effective readout planes that are suitable for operation at high pressures. The system constructed under this project provides an excellent testbed for such future efforts. This project is complete.

Back to main TOC

Femtoscope: A Time Microscope Using Parametric Temporal Imaging

B. Kolner, C. Bennett

98-ERD-027

An interesting duality exists between the equations that describe the natural spreading of optical beams in space and the spreading of short pulses in space–time. The former is known as diffraction, and the latter as dispersion. Building on these analogies forms the basis of a technique that we call "temporal imaging," the time domain analog of a conventional spatial imaging system. With it, we recently demonstrated a hundredfold temporal magnification of subpicosecond optical waveforms.

The capability of generating optical pulses of less than 100 fs has become almost routine. The principles of generating, detecting, and characterizing these pulses underlie much of modern optical telecommunications and ultrafast science in general. For several years, we have been investigating the possibility of stretching out short optical waveforms to a time scale that is accessible to conventional instrumentation, such as digitizing or sampling oscilloscopes. The key feature of our approach is that the expanded waveform maintains the integrity of the original envelope profile. Just as conventional imaging devices, such as cameras and microscopes, maintain the relative brightness levels between specific regions of the object plane, the temporal image maintains the relative amplitude levels between different portions of the expanded waveform—hence the term "temporal image."

The principal components and operation of a time microscope are relatively straightforward. Dispersive networks, such as diffraction grating pairs or optical fibers, play the role of the free-space diffraction, like the object-to-lens or lens-to-image-plane distance in a camera. A quadratic time-phase modulator that we call the “time lens”plays the role of a conventional space lens. A time lens can be realized with an electro-optic phase modulator, but these only produce a weak phase modulation. What is needed is hundreds or thousands of radians of modulation. We have taken the approach of mixing the dispersed waveform with a linearly chirped pump in an up-conversion nonlinear mixing crystal. By combining the input and output dispersions with the proper amount of chirped pump, we satisfy the time-domain equivalent of the imaging condition, and waveforms can be magnified or demagnified according to the output-to-input dispersion ratio.

In our LDRD-funded proof-of-principle experiment, we set a goal of 100× magnification and 100-fs resolution. The experiment consisted of a mode-locked Ti:sapphire laser producing 100-fs pulses, adjustable diffraction-grating dispersive delay lines, and an interferometer for creating a two-pulse test pattern. We achieved 103× magnification, as verified on a high-speed sampling oscilloscope, and less than 200-fs resolution, which is consistent with theory. The temporal field of view was about 10 ps, yielding more than 50 resolvable points.

As is the case with its spatial counterpart, temporal imaging is subject to aberrations, which arise from the nonideality of the dispersive delay lines and the time-lens phase function. We have made a detailed theoretical study of these effects and have measured them in our experimental setup. Although they impact the quality of the expanded waveform, we have found that the aberrations are almost insignificant on the time scales we are currently using. This is equivalent to using relatively high *f*-number optical systems where systematic aberrations are usually negligible.

Temporal imaging is very appealing because it is fundamentally a single-shot process, as we recently demonstrated with the aid of a streak camera. This feature, combined with subpicosecond resolution, makes the technique attractive as a high-power laser diagnostic. We expect that further development using compact-fiber Bragg gratings and integrated optical sum-frequency converters will produce a compact, high-performance optical waveform recording instrument with diverse applications in science and technology.

Back to main TOC

Real-Time Detection and Identification of Biological Aerosols with Mass Spectrometry

K. Langry, M. Frank, E. Gard, J. Horn, S. Labov, F. Magnotta, J. Ullom, W. Benner

98-ERD-097

Techniques for rapidly and accurately identifying microorganisms are important for a range of environmental, medical, and national security applications. Mass spectrometry has been used to identify microorganisms for over 25 years; lately, matrix-assisted laser desorption and ionization time-of-flight mass spectrometry (MALDI-TOF-MS) has emerged as a particularly promising technique for this purpose. The MALDI-TOF-MS technique enables the identification to be performed with intact cells and is sensitive enough to distinguish between strains of the same bacterial species. However, MALDI-TOF-MS requires some preparation of the analyte material: the addition of a chemical matrix to enhance desorption and ionization of the biomarkers. This sample preparation is a major impediment to real-time and in situ analysis.

As a step towards real-time identification of microorganisms, during FY2000 we used both a 337-nm nitrogen laser and an infrared (IR) laser tunable between 2.9 and 3.8 µm to desorb ions for TOF-MS from whole bacterial spores with no matrix or preprocessing. The use of lasers with mid-IR emission frequencies for matrix-free desorption of signature molecules from micro-organisms is novel. We selected the nitrogen laser because it is commonly used in MALDI-MS and because the output frequency matches the absorbance of the amino acid tryptophan. The IR laser was chosen because its frequency overlaps the 3-µm absorption caused by the bond vibrational stretching modes of O-H, N-H, and C-H. This absorbance is common to organic molecules, proteins, and water. We found that the IR laser desorbs both more types of ions and heavier ions than the nitrogen laser.

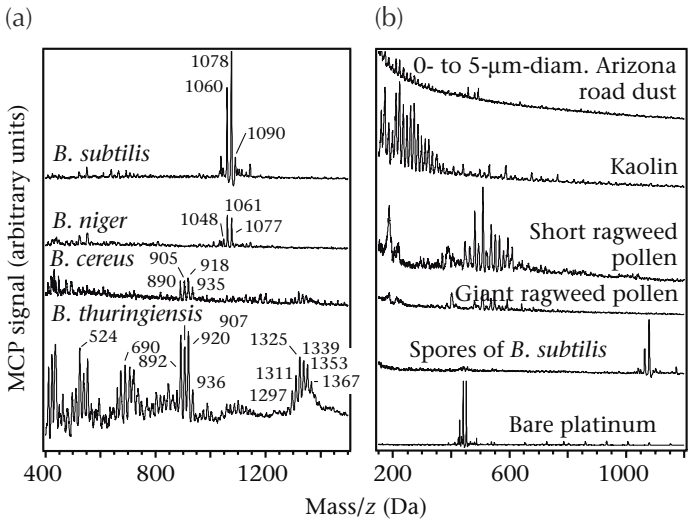

Time-of-flight mass spectrometry (TOF-MS) spectra of (a) matrix-free spores desorbed with a pulsed, mid-infrared laser, and (b) very different spectra of common aerosol particles, where MCP refers to a microchannel plate and z is the electric charge.

We studied desorption from whole spores of *Bacillus cereus, B. thuringiensis, B. subtilis*, and *B. niger* [see Fig. (a)]. The biomarkers desorbed from *B. subtilis* and *B. niger* were entirely distinct from those desorbed from the distantly related *B. cereus* and *B. thuringiensis*. However, the markers desorbed from the closely related *B. subtilis* and *B. niger* differed only slightly. Likewise, substantial similarities occurred between the markers desorbed from the closely related *B. cereus* and *B. thuringiensis*. In general, the number of biomarkers produced by matrix-free ultraviolet or mid-IR laser desorption was less than was typically observed with MALDI.

Our results are significant in light of recently developed techniques for characterizing individual aerosol particles in real time with TOF-MS. Generating ions by laser irradiation of aerosol particles drawn through a pumped inlet is ideal for real-time analysis, but it is not presently amenable to the addition of a matrix or to preprocessing of the aerosol. However, because we have shown that biomarkers can be generated from microbes without a matrix, a real-time monitor of microbial aerosols merits consideration. Such an instrument must be able to distinguish between background aerosols and pathogenic microbes. Therefore, we also measured mass spectra from materials that might be present in common background aerosols [see Fig. (b)] and found them to be significantly different from the spectra derived from spores. These positive results suggest that a mid-IR laser can produce molecular signatures from bioaerosols in real time.

During FY2001, we will use the pulsed output from the mid-IR laser to irradiate aerosol particles flowing through an aerosol mass spectrometer. We hope to demonstrate that molecular signatures can be generated from biological particles in real time using lasers that deposit energy directly into specific-bond vibrational frequencies of the particles' molecular components.

Remotely Interrogated Gigabit-per-Second Free-Space-Laser Communications Link

A. Ruggiero, J. D. Cooke, R. P. Ratowsky

99-ERD-011

Moving data from terrestrial distributed microsensor networks and airborne sensor suites is an essential capability for special operations missions during peacetime, and during war against defended/denied areas. As reliance on these sensors increases, communication bottlenecks between the sensors and their respective base stations will limit their effectiveness, particularly for near-real-time multisensor data fusion. We are developing a novel communications system based on remotely interrogated laser communications links to address this issue. Our solution is based on a novel, nonlinear, optical semiconductor laser, microphase-conjugator technology, we call an active, retromodulated microphase conjugator (ARMPC). Compact, solid-state microphase conjugators function as actively modulated retroreflectors, which amplify and encode the interrogating laser beacon and return it precisely to the beacon source. Applications include data uplinks from covert emplaced sensors to unmanned aerial vehicles (UAVs), data downlinks from UAVs to ground-based special operation units, and air-to-air data transfer between aircraft performing wide-area, near-real-time reconnaissance, surveillance, and target acquisition missions.

Our efforts in FY2000 focused on completing our initial laboratory feasibility experiments and on modeling the ARMPC concept. These experiments involved intracavity, four-wave mixing studies in surrogate, commercially available, broad-area diode laser structures. We characterized both noncavity-resonant and doubly resonant operation with respect to both input and output laser beams. Efficient nonresonant four-wave mixing was possible for cavity detunings between about 2 GHz to about 4 GHz, and then decreased rapidly until the next cavity resonance was approached. Detunings of less than 2 GHz resulted in injection locking of the laser. Gains greater than 30 dB were observed for cavity resonant, conjugate four-wave mixing signals, with greater than 100 nW of injected probe power in these laser structures. Efficient frequency conversion of the input signal beams was demonstrated for resonant detunings up to the fourth cavity resonance at about 100 GHz. These results were obtained with intracavity pump beams on the order of about 20 mW. Detuning bandwidths for the resonance-enhanced four-wave mixing experiments were determined to be on the order of 1.5 GHz. Experimental detuning results were in good agreement with theory based on a coupled-mode formalism, including cavity-resonance effects,

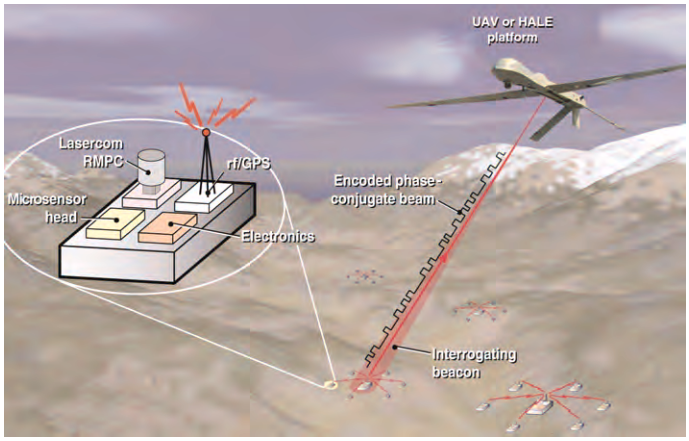

High-data-rate, interrogated communications links based on semiconductor-laser, retromodulator, microphase-conjugator technology can be used for data uplinks and downlinks between air and ground assets. Illustrated as a data uplink from an unattended ground sensor to an unmanned aerial vehicle (UAV) or high altitude long endurance (HALE) platform, the link is initiated by irradiation of the sensor system with a laser beacon. The sensor system responds by returning an encoded phase conjugate beam. The ground system consists of the microsensor head, interface electronics, retromodulator phase conjugator (RMPC), and a low-power radio-frequency global-positioning system (rf/GPS) for initial sensor location.

carrier-density modulation, carrier heating, and spatial hole burning. Calculating the reflected and transmitted probe and conjugate signal fields required calculating the intracavity laser pump beam and then solving a two-point boundary value problem. The theory was refined to include the variation of intensity gain and saturation across the beam aperture, along with the angular dependence of the four-wave mixing signals. Once again theory and experiment were in good agreement. We also demonstrated frequency conversion of gigahertz-amplitude-modulated optical signals and conversion of multiple wavelength, division-multiplexed signals in parallel.

Using the knowledge gained in this project, we developed a conceptual design for an optimal 2-D microphase conjugator. An initial surrogate device was constructed in-house from available semiconductor laser die to establish first-order viability of the design geometry. We are currently pursuing patent positions on this technology, and have partnered with a major diode laser manufacturer for its further development. This project was completed in FY2000.

Stand-Off Detection and Tracking of Bioaerosol Clouds: Scattering Simulations

F. M. Magnotta, W. M. Pfenninger, D. C. Johnson

99-ERD-013

The use of biological weapons (BWs) is considered a very real threat on today's battlefield. Military planners in the U.S. are under pressure to provide tools to troops in the field that would diminish the impact and limit the casualties from such an attack through early detection. Stand-off sensing using mid-wave infrared (MWIR) light intensity detection and ranging (LIDAR) could be used to provide significant warning of an attack by detecting a bioaerosol cloud well in advance of its reaching a protected area.

Light scattering by aerosols results in two readily observable effects that can be sampled in the forward and reverse directions to the laser beam by differential absorption LIDAR (DIAL) and differential scattering (DISC). Initial Mie scattering calculations done at LLNL (based on the absorption feature of a simulated bioagent in a water aerosol) suggested that a spectral signature indicative of the materials properties should be present in the DISC return pulse. Previous laboratory measurements employing infrared absorption analysis of bacterial thin-films showed that the vibrational band fingerprints of vegetative cells are unique and that they can be used to differentiate among strains of bacteria. Together, these two studies suggested that scattering might contain sufficient spectral information to (1) differentiate bioaerosols from nonbioaerosols, and (2) uniquely identify the bioaerosol.

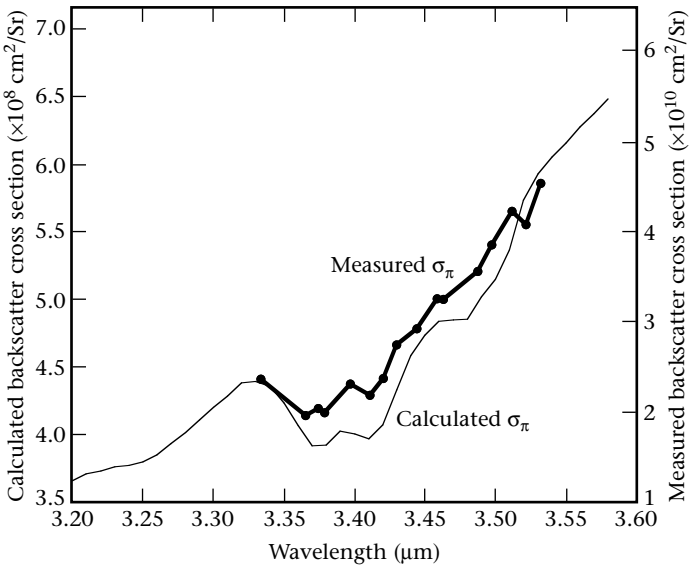

The calculated cross sections (σ_π Mie scattering signatures) reproduce much of the spectral structure measured during our experiment at the Aberdeen Proving Ground (APG). Note that the individually measured samples are connected with straight lines to display the trend.

To explore these possibilities, we conducted a field test at Aberdeen Proving Grounds (APG) during FY1999 in which three bioaerosols and three bioaerosol-free dusts were dispersed as clouds and subsequently detected using LLNL's frequency-agile MWIR LIDAR system. Test results showed that the spectra of the backscatter closely mirrored the absorption features of the individual samples and that the optical extinction was nearly completely devoid of spectral structure.

At about the same time, a commercial research group measured the extinction caused by single spores of one of the materials released during our APG tests [*Bacillus subtilis var. niger* (BG)]. Although their apparatus could not measure backscattered light, their results, which displayed significant spectral structure in the extinction, are apparently at odds with our measurements.

In FY2000, we performed a comprehensive computational study of the expected Mie scattering signatures of BG bioaerosols in an attempt to reproduce our APG measurements and to resolve the apparent discrepancy between these two sets of results. Our simulations, which spanned a large variety of particle sizes and realistic size distributions, provide significant insights into the scattering characteristics of BG bioaerosols and reproduce both sets of results. That is, for very small particles such as the individual spores measured by the commercial firm, our calculated extinction spectrum very closely matches the spectral structure of their measured extinction. When we examine the scattering of realistic particle distributions (which are dominated by larger agglomerations of spores), the spectral structure in the extinction washes out and is replaced by increased spectral structure in the backscatter. This agrees with our measurements at APG (see Fig.).

Having resolved the apparent discrepancy between the two sets of measured results, we now have a useful tool for predicting the scattering characteristics of aerosol clouds. Future work would apply these techniques to other materials of interest and would refine our simulations to include more accurate agglomerated-spore models.

Scalable Wireless-Sensor Networks with Distributed Data Interpretation

R. M. Bryant, C. T. Cunningham, F. U. Dowla, R. R. Leach, J. Baker

99-ERD-014

Intelligent and easily deployable wireless-sensor systems are important for many national security applications, particularly those relating to nonproliferation and tactical systems. To develop sensor networks that are small, low power, and capable of scaling to hundreds or thousands of sensor nodes, it is important to minimize the amount of information communicated and the power of the transmitter and receiver. In fact, many applications do not require the collection of raw transducer data, thereby allowing data processing to be performed at the sensor and requiring only target-recognition information to be communicated. In addition, the energy consumption of recently developed processor chips has dropped low enough that processing data at the sensor can be more efficient than sending it elsewhere for processing. By reducing energy consumption and associated battery size, the overall size and weight of sensor nodes can be significantly reduced.

In this project, we investigated signal-processing and data-fusion algorithms and developed prototype sensor nodes capable of recognizing and tracking vehicles driving along a roadway. Sensor nodes that are capable of acting independently are placed along a roadway, where they sense the passage of vehicles and communicate detections of interest to neighboring sensors and to a user-interface node.

During FY2000, we focused on developing efficient signal-processing and data-fusion algorithms that can be implemented in a low-power digital signal processor (DSP), as illustrated in the Figure.

We collected signal waveforms for three types of vehicles—a light car, a pickup truck, and a large, three-axle truck—being driven in different directions and at different speeds. We tested the performance of various seismic, magnetic, and acoustic sensors by placing them next to the gravel road used for this testing. We found that the smallest seismic sensors did not have sufficient sensitivity and determined that the magnetic sensors provided signals that could enhance the discrimination ability of the seismic sensor. However, 3/4-in.-diam geophones provided adequate signatures and were used for subsequent work.

Using the geophone data, we defined templates for the vehicular signals and a comparison algorithm that provides a numerical value for the likelihood that a seismic signal denotes a particular vehicle. We then defined a data-fusion algorithm that fuses the likelihood values from adjacent nodes with its own sensor likelihood calculation.

We integrated hardware platforms using a commercial, low-power DSP; a radio-frequency (rf) communication unit developed by LLNL; and seismic and magnetic sensor modules that we designed. Using a commercial DSP development environment, we developed the software modules, including software for vehicular detection, template matching and discrimination, communication between sensor nodes and the user node, data-fusion algorithms, and the user node. The software was downloaded and debugged through an emulator port on the DSP module. By successfully implementing the software in the DSP's 128-kB internal memory, we demonstrated that our algorithms could operate in a small, low-power platform.

We tested the vehicle-detection and discrimination software installed in the DSP by running previously collected raw data through it. We also (1) performed two sets of road tests in which the sensor node correctly identified the vehicle more than 95% of the time, and (2) verified that the sensors could communicate with each other and with the user interface node.

Follow-on research and development areas include (1) investigating system performance with different road conditions, higher vehicular speeds, and situations where multiple vehicles pass the sensor at the same time; (2) implementing a smaller hardware platform; and (3) integrating our software magnetic sensors into the sensor nodes.

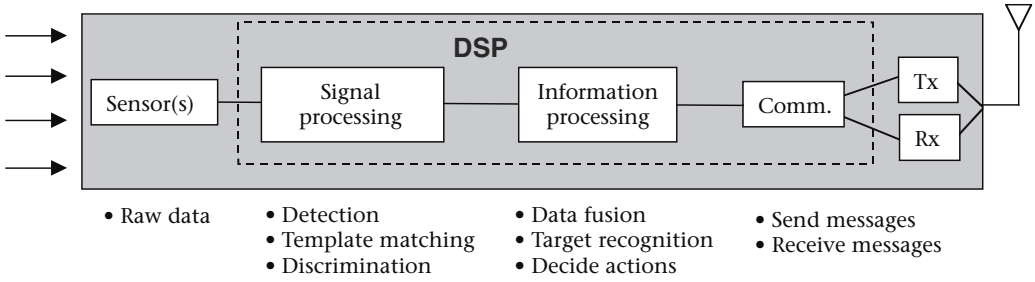

Sensor node containing a low-power digital signal processor (DSP) runs vehicular detection and discrimination algorithms on raw sensor data, then fuses and communicates likelihood information with neighboring sensor nodes. (Tx and Rx indicate the transmitter and receiver, respectively.)

Back to main TOC

Speckle Reduction for LIDAR Using Optical Phase Conjugation

M. W. Bowers, C. Kecy

99-ERD-024

Remote detection systems can be used to monitor the production and use of chemical, biological, and nuclear weapons as well as environmental conditions around the world. Light-intensity detection and ranging (LIDAR) is well suited for these applications. In a LIDAR system, a laser beam is transmitted toward an area to be probed. The return scatter from an aerosol or from the topographical background is detected and measured. LIDAR systems are complicated by noise sources. For example, speckle results when light scatters off a diffuse surface and interferes with itself to create light and dark spots at the detector plane. Optical phase conjugation is a nonlinear optical method of removing speckle by exactly reversing the light so that it returns to its point of origin and appears similar to the way it did before it left. The result is uniform illumination of the detector and reduction in the associated noise. Our goal in this project has been to show that it is possible, under most normal LIDAR operating conditions, to use optical phase conjugation to mitigate the effects of speckle.

During FY1999, we focused on studying phase-conjugation properties in the laboratory and evaluating how phase conjugation would perform under conditions similar to those found on LIDAR systems. During that year, we found that it is possible to correct for speckle under most normal operating conditions. However, our work revealed that bulk, nonlinear optical approaches to the phase-conjugation problems could not handle the extended sources that would be present in a fully speckled field. After studying liquid-filled and solid optical waveguides to determine their usefulness for such an application, we found that the power levels necessary to achieve adequate phase-conjugation reflectivities in the liquid-filled waveguide caused localized heating. This heat, trapped inside the waveguide, could not be conducted away as it is in a bulk or flowing system, and quickly formed bubbles that prevented phase conjugation from occurring.

Our dual objectives for FY2000 were to (1) modify the LIDAR system for pulse width and energy so that it could accommodate the optical phase-conjugation system, and (2) find an appropriate solid-state waveguide phase conjugator that would allow for high-fidelity phase conjugation at the 1.5-µm wavelengths we were using.

Our first choice for a solid-state waveguide phase conjugator consisted of single-crystal, tapered sapphire fibers, a theoretically "perfect" material for our phase conjugator. However, we were not able to reach the stimulated-Brillouin-scattering (SBS) threshold, even at power levels far higher than theory would predict. Researchers at the University of Rochester, collaborators during the first portion of the project, are looking into this attribute of SBS suppression to see if it can be exploited as a method of suppressing SBS in high-power fiber-optic systems such as long-haul telecommunications systems.

Our second choice, composed of tapered silica fibers, showed good phase-conjugate qualities in our experiments. However, tapered silica fibers do not have the input acceptance angle that is necessary to completely capture the entire speckle field and allow for high-fidelity phase conjugation. At year's end, we were pursuing the possibility of expanding this input numerical aperture and decreasing the acceptance angle of the receiving telescope in the LIDAR system to improve the conjugate fidelity of the system.

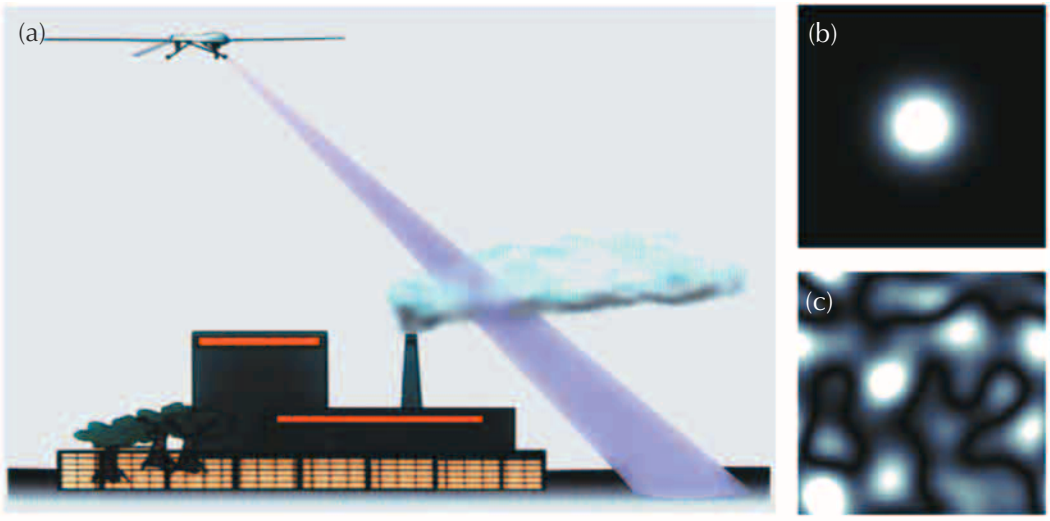

Speckle reduction as used in (a) one possible application of a light-intensity detection and ranging (LIDAR) system. The speckle was reduced by optical phase conjugation in (b); optical phase conjugation was not used in (c).

Nanolaminate Structures for Bioelectrorecognition

W. D. Wilson, T. Barbee Jr., A. Shestakov, M. Surh, C. Orme, B. Sadigh

99-ERD-066

Though nanolaminate structures are well understood, our goal in this project is to make them small enough—significantly smaller than microlithographic scales—to be used as probes to manipulate biomolecules.

During FY00, we used our nanolaminate structures to accelerate the nucleation and growth of ordered protein assemblages, with the ultimate goal of driving protein crystal growth. Preliminary results are extremely encouraging and suggest that this technology can contribute to protein crystallography.

To date, we have developed a variety of fabrication, characterization, and simulation techniques needed to achieve our goal. We have successfully synthesized nanolaminate structures that are the same size as typical proteins, with control over feature size and surface composition; the patterned substrate dictates the epitaxial deposition of an adlayer of protein. Using atomic-force microscopy (AFM), which also helps characterize the bare nanolaminate and assess the protein-substrate interactions, we analyze the resulting growth of this adlayer. Simultaneously, we have developed simulation tools to understand the driving forces and kinetics of deposition and to predict the optimal template design. The Fig. shows a sample AFM image of rapidly deposited proteins, called ATCase, with a simulated image of idealized colloidal particles on a substrate. Calculations suggest that long-range, crystalline order on nanolaminates is achievable even under conditions of rapid growth.

Heterogeneous template surfaces are made from magnetron-sputter-deposited nanolaminates that are cut across the layers and polished. The layers acquire different surface charges in water, giving a striped charge distribution. Selecting the proper materials (e.g., alumina and silica) and pH, produces alternating positive and negative charges. The resulting pH-dependent electrostatic fields are imaged by AFM, and potential new structures are predicted using Poisson–Boltzmann calculations.

The periodic surface potential directs adsorbates such as proteins into ordered rows, which we demonstrated by dipping a nanolaminate into a supersaturated solution of the protein ATCase. The substrate is removed, rinsed, air-dried, and imaged with AFM using a carbon nanotube. The resulting extremely high resolution makes nonspherical proteins individually distinguishable atop silica stripes (right-hand panels on Fig.). Images of the same deposition onto a homogeneous silica surface (left-hand panels) are very different, lacking any long-range linear order.

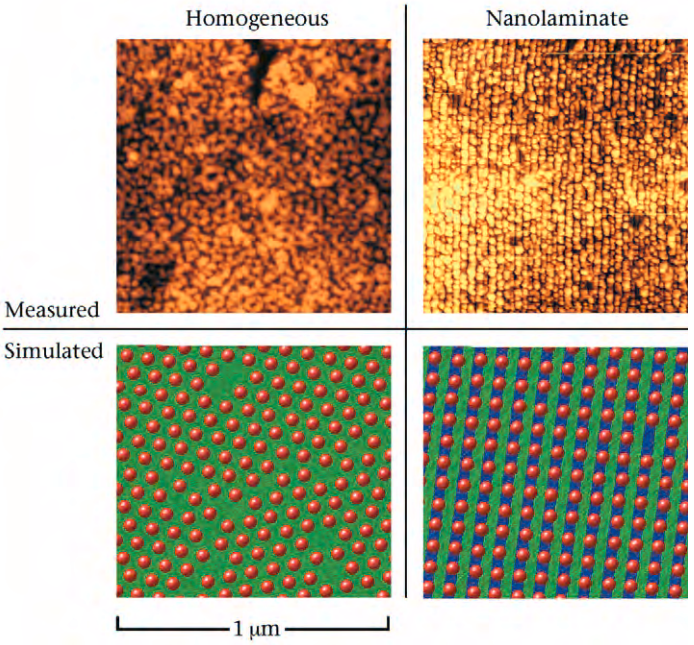

Measured (top) and simulated (bottom) protein adlayers on homogeneous (left) and nanolaminate (right) substrates. Experiment (top right) shows linear arrangements, while simulation (bottom right) gives 2-D order.

These results are consistent with our simulations. Our simplified model treats proteins as spherical colloidal particles with short-range forces. We then deposit particles using Langevin dynamics to account for diffusive mobility. As the Fig. shows, our simulations on a homogeneous substrate yield only short-range order. In contrast, imposing charged stripes breaks the substrate symmetry, and yields linear order among the adsorbed particles. When the stripes are lattice-matched to the protein, a highly ordered 2-D crystalline adlayer results. This outcome is very robust—it occurs even at high supersaturation and rapid growth rates. Our simulations further suggest that the template can be adjusted to select for different protein crystal faces. In FY2001, we will continue to evaluate these nanolaminate templates with the objective of growing ordered crystals suitable for diffraction.

Single-Fluorescent-Molecule Confocal Microscopy: A New Tool for Molecular Biology and Biosensor Research

C. Darrow, C. Hollars, T. Huser, R. Balhorn, S. Lane

99-ERD-067

Fluorescent molecules, like rhodamine, when chemically attached to antibodies, can be used to tag or label a target species (e.g., a toxin) in an assay sample. By then detecting and identifying single rhodamine labels one can achieve theoretically unprecedented sensitivities for such an assay. Our goal is to demonstrate the sensitivity of a specific single-molecule detection (SMD) assay for *botulinum* neurotoxin. This particular toxin is an ideal candidate because of its extreme toxicity to humans, the low contamination levels at which it is harmful, and the possibilities of exposure through contaminated food products or terrorist activities.

During FY2000, we modified our SMD system to accommodate the simultaneous detection of two distinct (i.e., different wavelength) fluorescent tags. Theoretically we planned to use a single excitation source (a 514-nm argon-ion laser) in conjunction with fluorescein and rhodamine. On paper, it appeared that both materials could be excited by 488-nm light while using high-quality filters to maintain wavelength separation of the emitted light. However, in practice, we were not satisfied with the minimum achievable crosstalk between the two emission channels. Therefore, we added a red 632.8-nm HeNe excitation source to the argon-ion excitation source. The light-collection beam path was divided into two subpaths using a dichroic splitter that separated the emission light generated by the two fluorophores and prevented the passage of the excitation light into the collection system. By adding a 0.25-m spectrometer and a thermo-electric-cooled, charged-coupled-device (CCD) camera, we gave the system the capability to perform spectral analysis of single molecular entities. Figure (a) shows our system.

Our experimental work during FY2000 concentrated on various SMD aspects of an assay based on colocalization of two fluorescently labeled antibodies on a single hCG target. We selected hCG as the test target because it and several antibodies are readily available and are well characterized. We labeled two antibodies with 565-nm em tetramethyl rhodamine (TMR) and 665-nm em Cy5. To prepare samples, we incubated the antibodies with known concentrations of the target hCG for a specified time, and then captured them onto a clean, glass surface that had been treated with 3-glycidoxyproplytrimethoxy silane (GPTMS). Figure (b) shows a false-color SMD image of such a sample in which labeled antibodies have nonspecifically bonded to the treated glass surface. Green dots correspond to lone TMR-labeled antibodies, and red dots to Cy5-labeled antibodies. Yellow dots correspond to colocalized antibodies, presumably on a single antibody.

Our work during FY2001 will concentrate on (1) reducing the occurrence of nonspecific binding of antibodies to the glass, using one of several possible surface chemistries, and (2) using spectral means to ascertain colocalization on a 100-nm scale. We will then continue optimizing and quantifying the sensitivity of the technique.

(a)

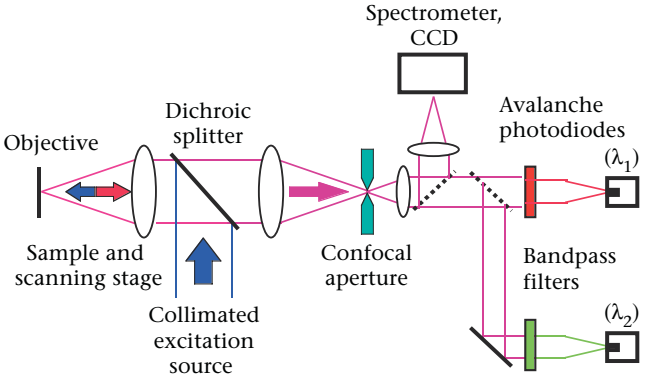

(b)

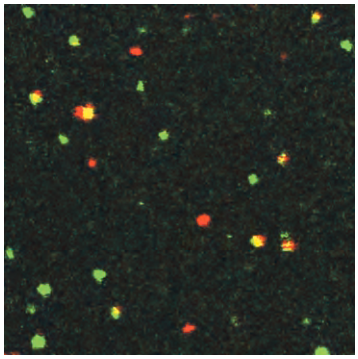

Progress towards labeling toxins in an assay, showing (a) our two-channel, single-molecule detection (SMD) system; and (b) an SMD image of antibodies labeled with TMR (green) and Cy5 (red), including those colocalized on hCG (yellow).

A New, Ultraspecific Optical Method for Sensing Biological Agents: Direct Detection of Biological Activity

J. H. Satcher, Jr., R. L. Balhorn, C. B. Darrow, D. R. Cary, J. P. Bearinger

99-LW-021

Both the public health and defense sectors have an important need for ultrasensitive biosensors and assays that are capable of rapidly detecting dangerous biological agents—viruses, bacteria, parasites, and toxins. The bioagent-detection technologies available today are limited by time-consuming or multistep sample processing and the inability to identify specific bioagents. We are investigating a detection method that (1) requires little or no processing, (2) significantly increases sensitivity, and (3) quickly reports the presence of infectious airborne, waterborne, or blood-borne organisms or toxin-producing micro-organisms.

Our detection scheme is based on the ability of two dye-labeled molecules to transfer energy when, and only when, they are in close proximity, which then can be detected by fluorescence spectroscopy. By eliminating nonspecific binding, our detection scheme would distinguish between live and inactive viral particles—something no current detection method is capable of doing—and would greatly improve the performance of existing sensors.

In work begun in FY1999 and completed in FY2000, we investigated a protein-coat portion of the HIV virus to demonstrate the effectiveness of our method. We chose the HIV virus because it has two protein receptors that bind specific sites on the virus's surface protein coat. Once these sites on the viral surface are occupied, the HIV virus changes its protein structure to physically collocate the two protein receptors.

First, we established energy transfer with two dyes (Coumarin and Nile Blue) in solution. To demonstrate that energy transfer can indicate specific interactions between proteins, we labeled hairpin DNA on opposite ends with two dyes (Cy5 and TMR). When the ends of the DNA strand interacted (through hydrogen-bonding forces), we observed energy transfer.

Next, to demonstrate that energy transfer can indicate interaction between a protein and a small molecule, we labeled two different molecules with different dyes (biotin with Cy5 and avidin with PE). When the two molecules were mixed, energy transfer took place. By labeling the same donor with different dyes (biotin with Cy5, biotin with PE, and avidin unlabeled), we also demonstrated that energy transfer could indicate that a large receptor molecule was bringing two small donor molecules into close proximity. Energy transfer occurred when the dyes were mixed (see Fig.). These experiments established that our technique for using energy transfer to detect donor–acceptor interactions could distinguish between live and inactive viral particles, as we propose to do for HIV detection.

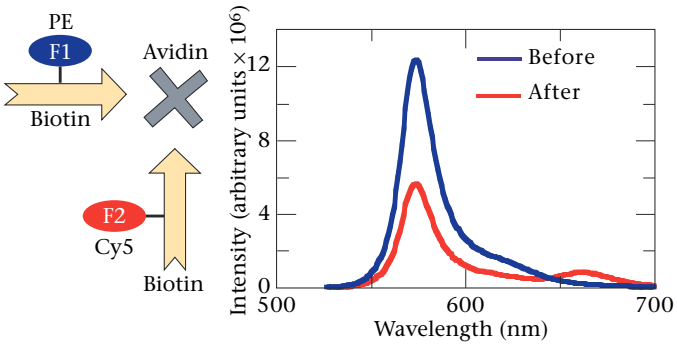

The emission spectrum of the two labeled biotins using the excitation band (494 nm) of the PE label. In the* before *spectrum, only the PE emission band is seen because the Cy5 label is not excited and no energy transfer occurs. In the* after *spectrum, with avidin added, the two biotins are collocated, energy transfer occurs, and the emission band of the Cy5 label is detected.

Our work on larger molecules with complementary binding sites met with some success. We first demonstrated the ability of the technique when applied to larger molecules by using a large (~100+ Å, >50,000 g/mole) protein (Cd8) with two different complementary labels (Cy5 and PE). We observed energy transfer. To demonstrate that the interaction of two complementary large proteins could be indicated by energy transfer, two large proteins were labeled with different dyes (Cd4 with Cy5 and anti-Cd4 with PE).

Initial results showed large baseline and background corrections prevented easy detection of energy transfer for the larger molecules. Although manipulation of the excitation energy eliminated some of the interferences, energy transfer was detected for only one label (PE) and not the other (Cy5). Results of our attempts to resolve this discrepancy indicated that nonspecific interactions can influence intensity changes. Along with the baseline and background problems, this suggests that different dyes probably are necessary for clearer detection of energy transfer for the Cd4 and anti-Cd4 pair.

Back to main TOC

Dynamic Focusing of Acoustic Energy for Nondestructive Evaluation

J. V. Candy, J. G. Berryman, D. H. Chambers, R. D. Huber, G. H. Thomas

99-LW-045

Component parts, whether they be lenses for optical systems or components of sensitive weapon systems, must be inspected regularly as part of scheduled maintenance and monitoring program, especially during the assembly process. These inspections are critical—even minute defects can propagate into still larger flaws that lead to a malfunction or possible catastrophic destruction of the system. Most materials, especially in optical components, have many small defects that are distributed throughout. For example, even a small flaw in a lens can propagate and cause the lens to shatter, leading to malfunction of the entire system. A nondestructive-evaluation (NDE) technique that could detect and characterize the largest defects first would have considerable value for inspecting optics in advanced laser systems and component parts for stockpile stewardship, for noninvasive medical treatments, and for locating underground targets.

In this project, we are developing an NDE technique for dynamically focusing acoustical energy for both detecting and characterizing flaws in parts undergoing ultrasonic testing. Our systematic approach incorporates detailed simulations, algorithm development, hardware, proof-of-principle NDE experiments, and the design of a prototype flaw-detection/localization/imaging system.

Dynamic focusing techniques are based on the concept of time reversal (T/R). Time-reversal processing of noisy measurements by an ultrasonic sensor array is a technique for focusing energy in various media. The T/R processor can detect flaws (or scatterers) by using its primary attribute—the ability to iteratively focus on the strongest flaw. A T/R processor receives the multichannel time series radiated from the region under investigation, collects the array data, digitizes, time-reverses the signals from the sensor array, and retransmits the signals back through the medium to a focus.

During FY1999, we developed algorithms to iteratively decompose the received field into its constituent scatterers, even when they overlap temporally, using the T/R focusing property as the core of the algorithm. During FY2000, we developed temporal techniques that exploit the T/R focusing property and constructed new processing algorithms for detection and localization so that once the focus has been detected, that particular scatterer is removed from the measured data. We can then recursively detect the next scatterer and the next, until all have been detected and removed.

Next, we attacked the localization problem by exploiting the dominant scatterer-focusing property of the T/R processor. Here, a nonparametric model of the received wavefront is matched with the measured data by varying the assumed flaw (scatterer) location until the best match occurs. A global search obtains starting values for the local focusing algorithm. Once focused, each individual scatterer is recursively extracted from the measurement data, and a flaw map is developed that localizes the position of each flaw. The Fig. shows typical results of the global and local iterations for a homogeneous aluminum part with flaws. The procedure culminates in a wavefront match and a final map of the flaw(s).

In FY2001, we plan to continue the theoretical investigation of the T/R operator and time-domain decomposition algorithms, investigate imaging techniques using the estimated number and location of the flaws, complete the development of a prototype system, and perform proof-of-principle NDE experiments on materials and parts of high interest to LLNL.

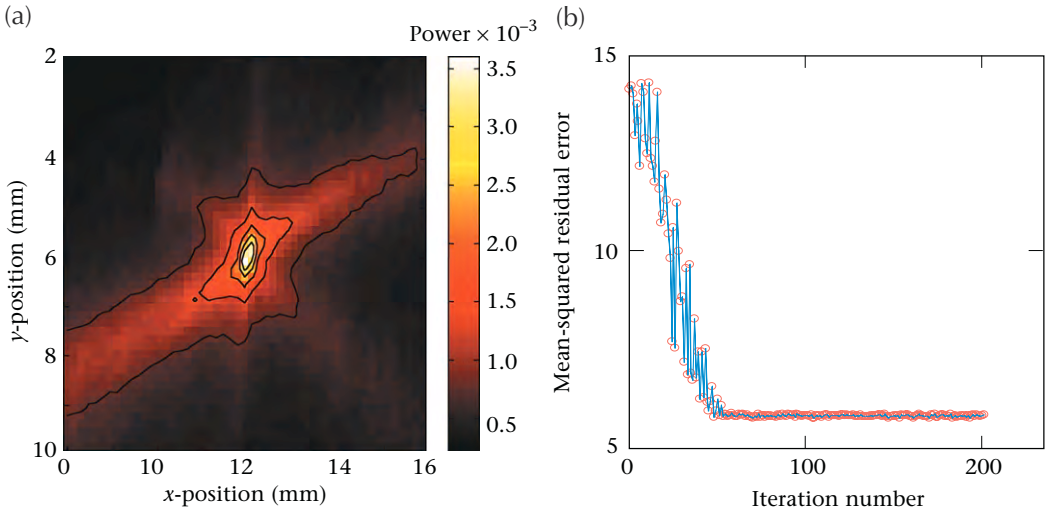

Application of flaw localization and mapping algorithms using time-reversal (T/R) processing. Shown are (a) global (ultrasonic source localization), and (b) local (weighting-function estimation) search results for a synthesized aluminum slab. The actual flaw is located at x = 12.0, y = 6.0, with the global results of x = 11.92, y = 6.08 in (a), and refined using the local search at x = 12.01, y = 6.00 in (b).

A Cooperative Control Architecture for Mobile Robotic Agents

R. Hills, R. S. Roberts, C. T. Cunningham

00-ERD-023

Large networks of land-based sensors are becoming increasingly important for sensing natural and man-made phenomena. The deployment and operation of large, land-based sensor networks can pose difficult problems, particularly in time-critical situations or rugged terrain. An example would be monitoring ground conditions in a forest to model and predict the advance of a forest fire. Autonomous deployment and operation of land-based sensor networks in such a scenario is highly desirable for maximizing sensing efficiency while minimizing human risk. Other national security applications involve remote monitoring of sites and facilities (e.g., chemical and biological manufacturing facilities).

Our approach to the deployment and operation of a land-based sensor network is to use cooperating, unmanned air vehicles (UAVs) that deploy the sensors and then serve as communication hubs for the sensors. In this approach, a group of cooperating UAVs deploys sensors over a region of interest. After the sensors have been deployed, the sensor network is logically partitioned into subnetworks (subnets), with one UAV assigned per subnet (see Fig.). Partitioning the network into subnets allows the UAVs to service sensors in parallel while minimizing interference or duplication of effort. A UAV services the sensors in its subnet by flying a path through the subnet, uplinking data collected by the sensors, and forwarding the data to a central point. Cooperation among UAVs is maintained through the exchange of status information among UAVs; information includes the status of the UAVs and the status of sensors in the network. Through this cooperative control architecture, exceptional events (such as a UAV leaving the network for refueling or the failure of a group of sensors) can be detected and properly managed by the UAVs.

During FY2000, we focused on a key component of the architecture—the adaptive path-planning algorithm. This algorithm initializes the paths and then adapts the subnets (and paths through the subnets) in response to one of four basic exceptions: (1) one UAV leaves the network, (2) one UAV enters the network, (3) several sensors leave the network, and (4) several sensors enter the network. More complex situations can be derived as combinations of these basic exceptions.

The algorithm models the sensor network as a set of directed graphs. In this model, the sensors in a subnet are nodes of a graph, and the UAV path through the subnet is a set of directed links between the nodes. Over the years, several approaches have been proposed to find paths through a graph, but these algorithms find the shortest path between two nodes, not a closed path. For the case of one UAV, the problem reduces to the "traveling salesman problem." However, we are interested in applications where multiple UAVs are required to properly service the network.

In the algorithm developed this year, subnet and path adaptation is driven by a global cost function that shifts sensors into and out of subnets to reach a minimum cost. Our heuristic approach, which uses good approximate solutions and makes only minor alterations to them, is quite different from conventional techniques, which consider much more general distortions of existing paths. For example, we found that our method performs significantly better than synthetic-annealing methods used in the past.

In FY2001, we will focus on several aspects of the cooperative control architecture, including exception detection, exception handling, and communication networking.

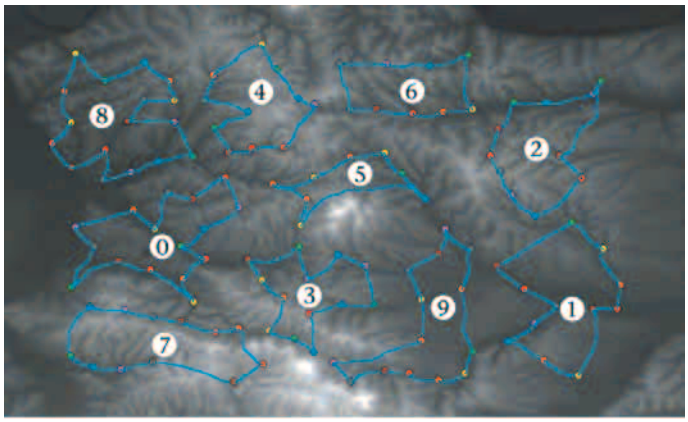

Paths and subnets for the case of 124 sensors and ten unmanned air vehicles (UAVs). The locations for the sensors were determined using a digital terrain map.

Back to main TOC

Early-Time Optical Counterparts of Gamma-Ray Bursts

H.-S. Park, R. A. Porrata, G. G. Williams

00-ERD-027

Gamma-ray bursts (GRBs) are brief, randomly located releases of gamma-ray energy from unknown celestial sources that occur almost daily. The study of GRBs has undergone a revolution in the past three years because of an international effort to make follow-up observations. These follow-up observations have shown that GRBs are at cosmological distances and interact with surrounding material—as described by a fireball model. However, because prompt optical counterparts have only been seen in one case, we know that such GRBs are either very rare or much too dim for the sensitivity of current instruments.

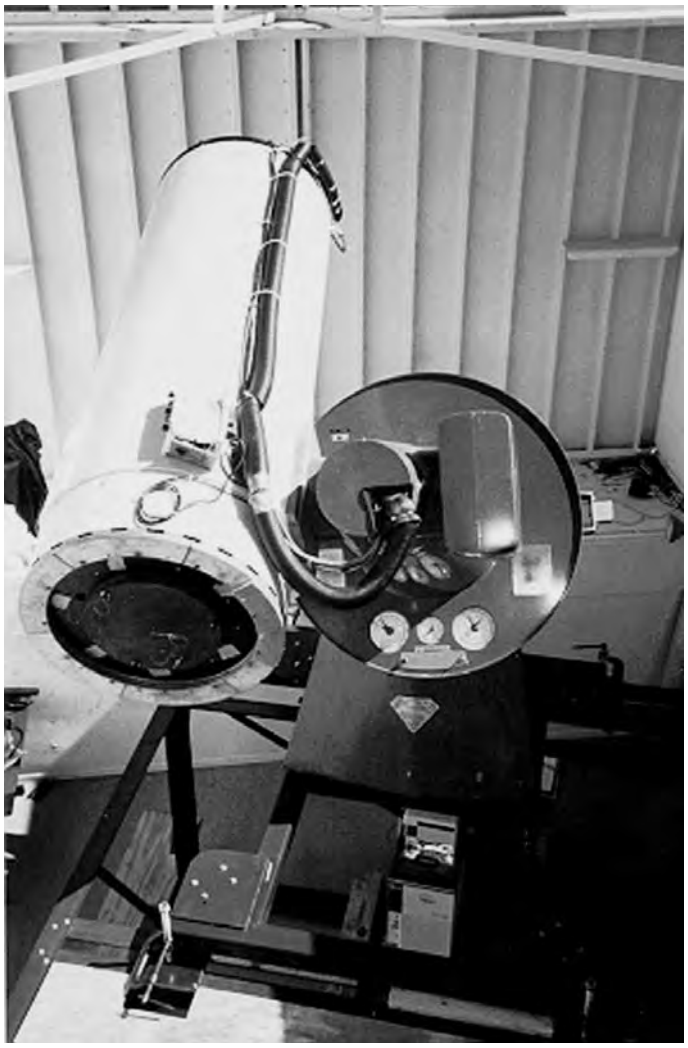

Super-LOTIS telescope at Kitt Peak National Observatory.

Unlike the observed later-time afterglows, prompt optical measurements would provide information about the GRB progenitor. Prompt measurements are only made possible by the instantaneous distribution of reliable GRB coordinate information over the Internet—as provided by the National Aeronautics and Space Administration's (NASA's) GRB Coordinates Network (GCN).

The objective of this project was to measure the intensity of any prompt, visible radiation accompanying the GRB by using a small but sensitive robotic telescope that rapidly takes images of the GRB coordinates given by the GCN.

The instrument developed for this project, the Livermore Optical Transient Imaging System (LOTIS), was the first of its kind and also the longest running—collecting data on over 75 GRBs during its three-year running period. LOTIS consists of four charge-coupled device (CCD) cameras covering a 17.6- by 17.6-deg field of view.

In FY2000, we continued to operate the LOTIS telescope at LLNL's Site 300 by responding to any GCN triggers and collecting all-sky archival-image data. The study of 75 GRBs covered by LOTIS provided published numerical limits for the density of the matter surrounding GRBs and also for other environmental parameters associated with GRB progenitors. Analysis of LOTIS data shows that the GRBs are created at low surrounding matter density, high initial Lorentz factors, low surrounding magnetic-field energy, and in a high-electron-energy environment. These results provide constraints on the external-reverse-shock GRB model that predicts prompt optical counterparts.

In addition to running LOTIS and analyzing LOTIS data, a major accomplishment during FY2000 was the commissioning of the next-generation system, Super-LOTIS, a 0.6-m, *f*/3.5 reflective telescope, at its permanent site at the Kitt Peak National Observatory (see Fig.). [The commissioning was supported both by this project and by the National Aeronautics and Space Administration (NASA).] We modified Super-LOTIS—by adding computer-controllable drives, a coma corrector for better optical quality over the large desired field of view, an electronic-imaging CCD camera, and sophisticated on-line software—so that it automatically responds to GRB triggers. Our first results show that Super-LOTIS is 40 times more sensitive than LOTIS.

The Super-LOTIS instrument is now ready to receive real-time GRB coordinates from the High Energy Transient Explorer (HETE) satellite that was launched successfully in October 2000.

Back to main TOC

Investigation of Capillary Optics with Magneto-Electrostatic Control

A. Toor, D. Ryutov

00-FS-003

The DOE Office of Basic Energy Science has entered its third year of funding research and development for a fourth-generation light source based on a linac-driven x-ray free-electron laser (XFEL). A collaboration of national laboratories and universities conducting this research has proposed to construct the Linac Coherent Light Source (LCLS) to produce an XFEL with unprecedented brilliance. The wavelength of the XFEL will be continuously variable between 1.5 and 15 Å. The LCLS will generate x-ray pulses with ~10 mJ per pulse, having a beam diameter of ~100 µm, a pulse length of ~200 fs, and a rep-rate of 120 Hz. At the longer wavelengths, a single pulse from the LCLS will transform any solid material placed in the beam into plasma. This new environment presents many new challenges for x-ray optics.

The objective of this project is to investigate the possibility of developing a totally new class of x-ray optics based on liquid films. Such optics could address a much broader range of applications than those associated with LCLS. Developing the ability to create optical components at 100-Hz rep-rate would provide a striking extension of capability for all future light sources.

In FY2000, we examined the feasibility of constructing thin-film liquid mirrors that can be used at high fluence, with no damage to the permanent elements of the structure; these films can be formed over flat or figured substrates. We examined the feasibility of orienting the optics arbitrarily with respect to gravity and operating in a rep-rate mode with the optical surface renewed after each shot. We investigated (1) controlling the film surface by capillary and electrostatic forces, taking into consideration the role of surface tension, viscosity, conductivity, and wettable vs. non-wettable surfaces on the formation and damping of capillary waves; and (2) both shaping the surface of a fluid by pulsed electrostatic forces and exciting capillary waves by a periodic wire array embedded in the substrate. From these experiments, we derived an analytic theory for the general performance of thin-film liquid optics and reduced it to a complete set of engineering equations that can be used to design a broad range of capillary- and electrostatic-controlled optical components. A paper describing the theory, design equations, and examples of thin-film optics has been prepared for publication and we have submitted three patent applications describing various elements of our concept.

After assembling a tabletop test facility, we evaluated the performance of liquid films formed over porous substrates with pore dimensions ranging from 6 to 50 µm. Our initial results, using water as the working fluid, demonstrated that, at a rep-rate of up to a few hertz, optical surfaces formed that reflect a laser line-source onto a screen, where we are able to measure the optical properties of the surface.

Follow-on work to this project includes (1) using an interferometer to measure the optical properties of the films with several different working fluids, (2) investigating the use of electrostatic and magnetic forces to create appropriately figured surfaces on tilted or inclined mirrors and to ensure steady-state equilibrium, and (3) performing a theoretical analysis of optical characteristics of diffraction gratings and zone plates created by pulsed electrostatic actuators.

High-Sensitivity, Optically Polarized NMR of Surfaces in Materials Science and Biology

S. E. Hayes, M. Balooch, L. N. Dinh, J. A. Reimer, A. K. Paravastu

00-LW-040

Detection of nuclear magnetic resonance (NMR) signals from rare spins (e.g., nuclei with low isotopic abundance, species at surfaces or interfaces, or small sample quantities) is a significant challenge. Although NMR is a powerful tool for determining structures, local bonding geometries, and molecular dynamics, conventional NMR is a bulk-averaged technique that lacks spatial selectivity and suffers from low sensitivity (~10^{20} NMR-active nuclei are needed for detection). Recent developments have combined NMR with direct, optically polarized NMR (OPNMR). In OPNMR, laser light is used to excite spin-polarized electron-hole pairs, which in turn polarize nuclear spins to which they are coupled. Because NMR amplitudes are directly proportional to the nuclear-spin polarizations, signal enhancement factors of about 10^5 are possible.

The aim of this project is to provide a new NMR capability for LLNL that has both high sensitivity and spatial selectivity and that can be used to analyze systems with dilute nuclear spins. Examples are surfaces or interfaces (i.e., semiconductor/insulator barriers and nanoclusters) or very small quantities of samples (e.g., biological samples and trace analyses). A number of potential applications can be realized, such as the investigation of metal hydriding, membrane protein structures, cell receptor sites, and semiconductor heterostructures.

During FY2000, we designed and constructed an OPNMR apparatus that consists of homebuilt, radio-frequency (RF) transmission-line NMR probes; a low-temperature cryostat; and a vacuum system outfitted for optical access. The hardware is configured to permit optical excitation at the sample space using a tunable laser. We observed OPNMR signals from single-crystal wafers of GaAs. These signals exhibit a dependence on the polarization of the laser, which creates positive and negative circularly polarized light. The NMR signals become absorptive or emissive depending on the degree and sign of circular polarization [see Fig. 1(a)], which indicates that the angular momenta of the nuclear spins and the photon spins are coupling. This OPNMR signal develops with increasing irradiation time as more nuclear spins become polarized over time. By comparison, an equivalent experiment done in the "dark" (without laser illumination) resulted in an attenuated signal.

We also synthesized GaAs nanoclusters through laser-ablation methods using ultrashort, pulsed-laser deposition. Films deposited onto various substrates were characterized by x-ray diffraction, atomic force microscopy (AFM), and transmission electron microscopy (TEM). Their structure [see Fig. 1(b)] consists of a crystalline core surrounded by an amorphous, mixed-oxide outer shell. The crystalline nature of the GaAs clusters was confirmed, and we examined the distributions of cluster sizes for various preparation conditions. When we evaluated chemical etching and passivation of these clusters and the concomitant photoluminescence (PL), we found that passivation increases the strength of the PL signal for both single-crystal wafers and cluster samples. We are probing this connection between photoluminescence and OPNMR because optical absorption is a prerequisite for optical polarization, and the electronic structure inherent in the material will be reflected in the PL spectra.

In FY2001, we will continue our research in OPNMR methods, applying the technique to (1) other Group III-V materials (e.g., InP), and (2) possibly also Group II-VI (i.e., CdSe) and Group IV (e.g., silicon) materials. We will also continue our nanocluster-synthesis activities and apply our OPNMR techniques to these materials to understand their structure, electronic states, and surface chemistry.

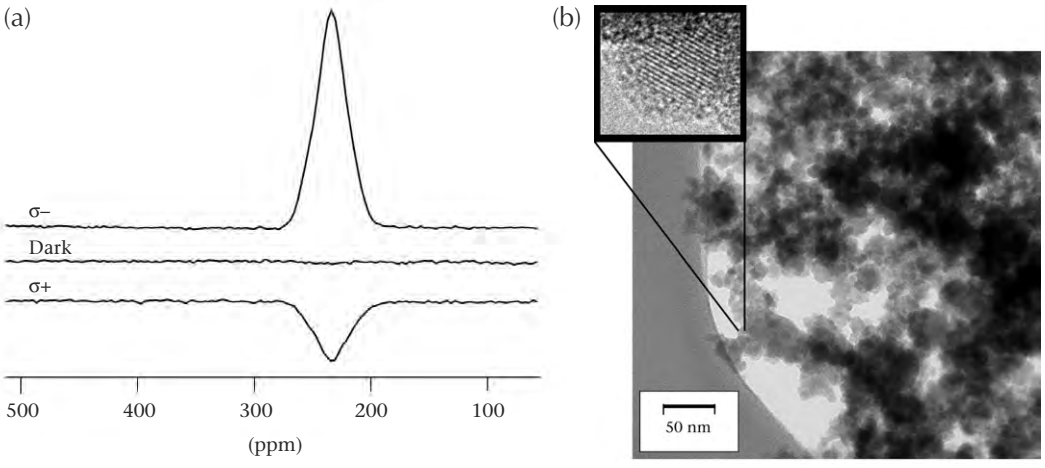

Results of work with optically polarized nuclear magnetic resonance (OPNMR) and the connection between photoluminescence and OPNMR, showing (a) OPNMR spectra for a circularly polarized light (σ– and σ+) and an equivalent dark experiment, and (b) a transmission electron microscopy (TEM) image of GaAs nanoclusters. The inset image in (b) shows lattice fringes from one cluster. The presence of both absorptive (pointing upward) and emissive (pointing downward) peaks in (a) indicates that the polarized light is having an effect on the NMR signals.

Atmospheric and Geosciences 2

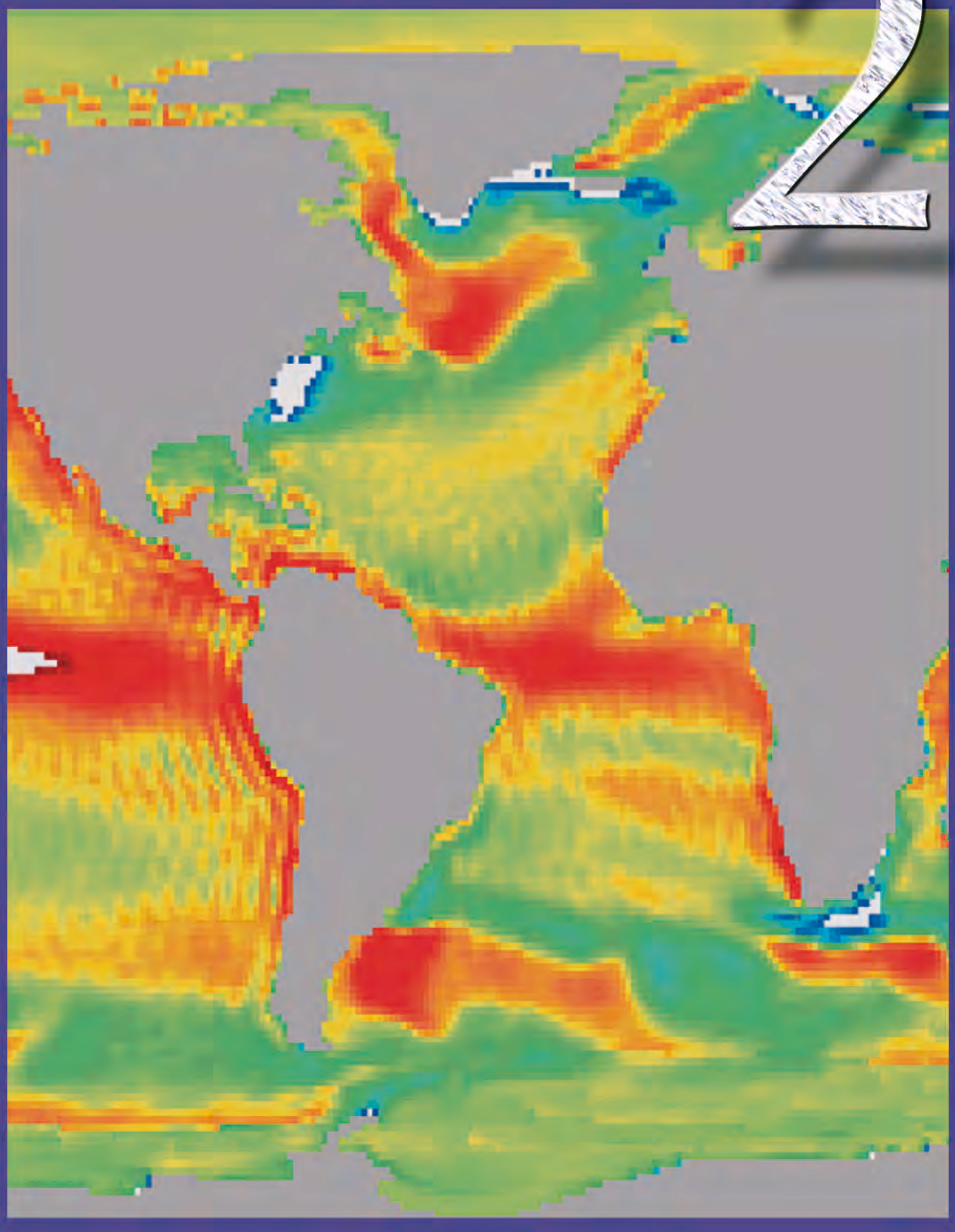

Section 2—Atmospheric and Geosciences

Back to main TOC

Martian Carbonates: Hot or Cold?

I. D. Hutcheon, A. J. R. Kent, F. J. Ryerson

98-ERD-042

In 1996, scientists working for the National Aeronautics and Space Administration (NASA) announced the discovery of fossil life in Martian meteorite ALH 84001 and unleashed a firestorm of scientific controversy. Scientists around the world scrambled to test and assess these startling conclusions. Numerous studies examined the composition and formation of ALH 84001, the meteorite containing the putative fossil remnants. In particular, the carbonate minerals containing the microscopic, fossil-like structures have been subject to intense scrutiny. Much of this work has centered on the formation temperature of these minerals. Because terrestrial life is only viable over a relatively narrow and well-defined range of temperatures (~0 to 150˚C), knowledge of the formation temperature and thermal history of the carbonate minerals in ALH 84001 would provide a direct constraint on the possibility that this meteorite hosts the fossil remains of ancient Martian biota. The primary focus of these experiments is to enhance our understanding of reactive chemical transport relevant to CO_2 sequestration in the terrestial environment.

Previous studies by researchers at the University of Tennessee and NASA Johnson Space Center showed abrupt changes in the abundances of iron (Fe), magnesium (Mg), and calcium (Ca) within the ALH 84001 carbonates over distance scales as short as 1 µm. Over time, diffusion will act to homogenize such chemical zoning; therefore, because diffusion is a temperature-driven process, we can use cation diffusivities to constrain the temperature history of the carbonate minerals.

During FY2000, we applied techniques developed during the first two years of this project to measure Ca and Mg diffusivities in Mg- and Ca-rich carbonate minerals. We used LLNL's secondary ion mass spectrometer (SIMS) to measure the rates of change of Mg and Ca concentration as a function of depth below the surfaces of carbonate minerals annealed at temperatures of 400 to 600˚C (see Fig.). The SIMS techniques developed in this study enabled us to determine diffusivities at much lower temperatures (200˚C) than in any previous study and to avoid the pitfalls associated with large down-temperature extrapolations. Our data established the rates of chemical diffusion of Mg in calcite and Ca in magnesite and allowed us to set stringent constraints on the formation temperature and thermal history of carbonates in ALH 84001. We found that the diffusion of Mg in calcite at temperatures between 400 and 550˚C is substantially faster than predicted by the extrapolation of existing higher-temperature data, suggesting that different mechanisms govern Mg diffusion at temperatures above and below about 550˚C.

We used our data to model thermal histories that allow the micrometer-length scale variations in Ca–Mg composition in ALH 84001 carbonates to survive diffusive homogenization. For initial cooling rates between 0.1 and 1,000˚C/Ma, our results demonstrate that these Martian carbonates most plausibly formed at temperatures of less than 200˚C.

Our study excludes the possibility that the ALH 84001 carbonates formed by high-temperature fluid or melt-related (igneous) processes on Mars, as was previously believed. While not resolving the controversy over the possibility of fossil life, the low temperature derived from our results agrees well with data on O-isotope compositions and leads to a self-consistent model of carbonate formation through metamorphic and/or hydrothermal processes, such as precipitation from saline fluids in the Martian crust.

A manuscript has been accepted for publication in *Geochimica et Cosmochimica Acta* and is in press.

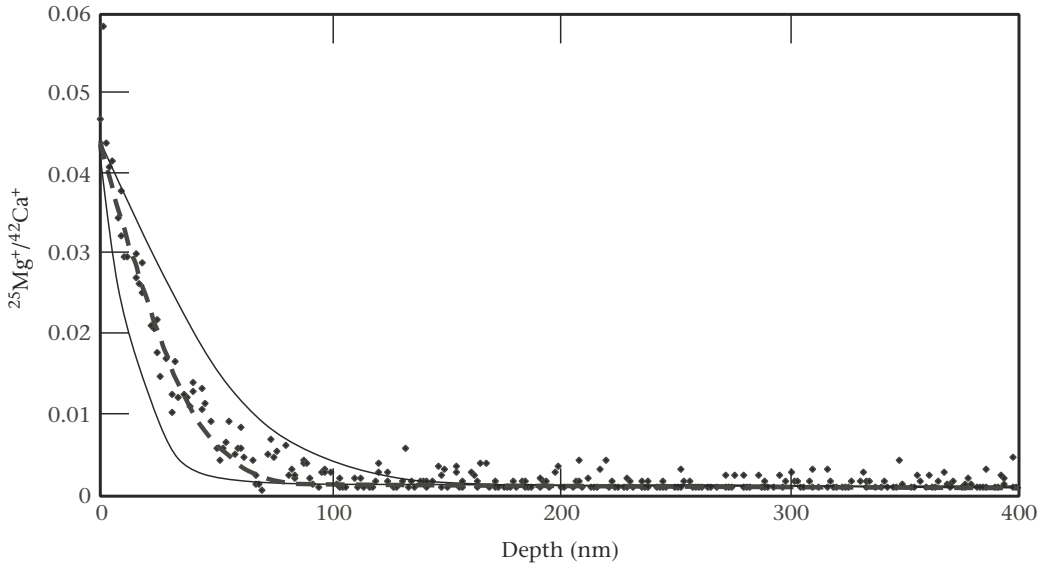

Measured diffusion gradient for chemical diffusion of Mg in calcite for an experiment annealed at 450°C for 152 days. Filled circles represent individual ion microprobe measurements of the $^{25}Mg^{+}/^{42}Ca^{+}$ ratio as a function of depth beneath the sample surface. The dashed line shows the error function fitted to these data and corresponds to a diffusion coefficient of 1.04×10^{-22} m²/s. To emphasize the quality of the error function fitting procedure, the thin solid lines bounding the data show diffusion profiles calculated for a factor-of-2 variation in the diffusion coefficient.

Seasonal to Decadal Variability in Pacific Circulation Using Δ Carbon-14 in Corals

M. Kashgarian, T. P. Guilderson

98-ERI-002

The western tropical Pacific plays a key role in both local and global climate. On interannual and longer time scales, the transport of warm surface water into and out of the western equatorial Pacific is thought to play an important role in El Niño/Southern Oscillation (ENSO) events, the Asian Monsoon system, and global climate through atmospheric teleconnections. Intense surface heating along the Equator, combined with mean easterly tradewind flow, causes warm surface waters to accumulate in the western Pacific; this drives tropospheric circulation by creating deep convection aloft. Compensation of westward-flowing currents occurs via the surface countercurrents, eastward-flowing undercurrents, and the Indonesian throughflow.

Our understanding of the interaction between the atmosphere and surface oceanic circulation has historically relied upon data from ship drifts, drogues, and a relatively small number of moored current meters. Satellite observations provide higher spatial and temporal sampling; however, such data unfortunately are available only for the last ten to twenty years, at best. These records are insufficient either for examining decadal or longer time-scale variability or for adequately addressing questions such as anthropogenic influences on natural climatic variability.

Our work demonstrated the potential to use carbon-14 (^{14}C) time series in corals to study the dynamics of oceanic circulation over multidecadal time scales. Our objective was to (1) document ^{14}C variability in the equatorial Pacific and Indonesian Seaway by making high-resolution measurements on corals, and then (2) determine how that variability relates to the movements of water masses over time scales long enough to study the linkage between surface–water processes and decadal modulation of ENSO and the Asian Monsoon. We chose key sites to monitor variations in the transport of water within the equatorial Pacific and through major pathways of the Indonesian Seaway. Our work used an integrated approach to oceanography and climate change and was part of a collaborative effort involving modeling and data collection at several institutes.

The coral $\Delta^{14}C$ time series that we produced in this study also provided information that can be used to uncover flaws in paramaterization of dynamic processes in oceanic circulation models. The incorporation of ^{14}C as a passive advective tracer is a major component of the International Ocean Carbon Modeling Intercomparison Project as well as a diagnostic and prognostic tracer in several high-resolution models.

In FY1998 and FY1999, we completed "post-bomb" radiocarbon time series from the equatorial Pacific islands of Nauru (166°E, 0.5°S), Guadalcanal (167°E, 7°S), Rarotonga (21°S, 160°W), and Hawaii, and also a partial record from the Galapagos (90°W, 0°).

In FY2000, we completed the most recent part of the Galapagos record and began a study of sites in the Indonesian Seaway, which included a complete record from Padang Bai in Bali (8.5°S, 115.5°E) and a partial record from Bunaken (1.5°N, 125°E). The Figure illustrates $\Delta^{14}C$ records from Bali, Bunaken, and a record from Langkai generated at Center for Accelerator Mass Spectrometry (CAMS) for an earlier study. The $\Delta^{14}C$ results from Bali, which span 1957 to 1990, show the uptake and redistribution of bomb-derived ^{14}C, in addition to strong seasonal (10 to 25‰) and interannual (10 to 15‰) variability. Of particular note is the rapid approximately 50‰ rise in late 1958 and early 1959, which indicates transport of North Pacific surface water recently "spiked" with bomb-derived ^{14}C. Preliminary data from Bunaken imply a larger-than-expected component of low-^{14}C water from the south equatorial current in the surface waters of the Sulawesi Sea. A comparison of the three records suggests that there is clearly modulation of the surface flow through the Indonesian Seaway.

Our work has been published in refereed publications.

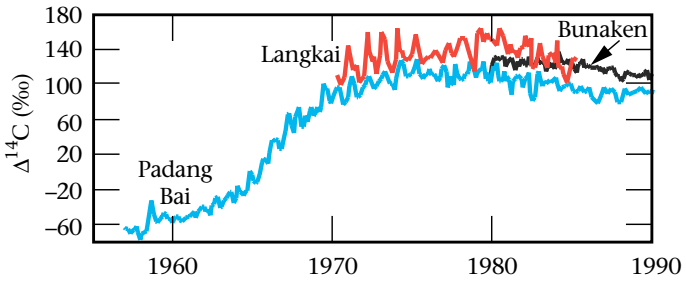

High-resolution $\Delta^{14}C$ records in Indonesian corals: Langkai (1σ error ± 7‰), Padang Bai (Bali), and Bunaken (1σ error ± 3.5‰).

Back to main TOC

Assessing Changes in Solar Activity Using Cosmogenic Radionuclides

R. Finkel, M. W. Caffee

98-ERI-013

In this project, we focused on three aspects of the earth sciences that are of concern to the Department of Energy (DOE): (1) energy use as affected by potential climatic change (i.e., solar effects on climate), (2) landform stability as it relates to the assessment of natural and manmade hazards (e.g., earthquake recurrence rates), and (3) global atmospheric mixing as it influences problems relating to the ozone hole and to emissions by jet aircraft. During FY2000, we focused on research related to aspect (1).

The amount of solar radiation received by Earth rises and falls in step with the 11-year sunspot cycle and also changes over longer time scales. The debate over the existence of a solar effect on climate has deepened as the result of recent work identifying possible atmospheric "amplifiers" that may convert the small changes in solar luminosity (~0.1%) associated with the sunspot cycle to larger climatic effects. This debate is important because potential human influences on climate through greenhouse gases or atmospheric aerosols, are superimposed on a background of natural climatic change. To construct realistic scenarios describing future climate, this background must be fully characterized and considered. During the course of this project, we used cosmogenic beryllium-10 (^{10}Be) and chlorine-36 (^{36}Cl) in polar ice cores from both Greenland and the Antarctic to develop a proxy record for solar activity during the Holocene. Comparison of results from these two regions has shown that they respond to solar activity changes in a similar fashion, although there are some significant differences in the behavior of ^{10}Be and ^{36}Cl in the atmosphere.

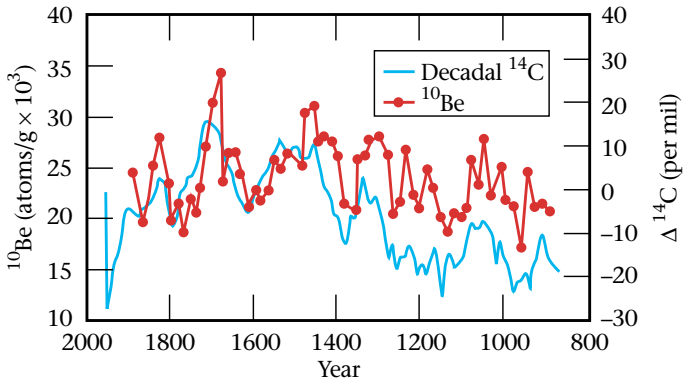

Beryllium-10 (^{10}Be) in ice, from an ice core at Siple Dome, Antarctica, and carbon-14 (^{14}C) in the atmosphere, as obtained from tree rings. The centennial-scale variations observed are due to changes in solar activity. Δ^{14}C is the age-corrected per mil difference from 95% of the National Bureau of Standards (NBS) standard for oxalic acid ^{14}C and gives the relative fluctuation of ^{14}C in the atmosphere.

Toward the close of FY2000, we compared our ice-core record of ^{10}Be with the record of carbon-14 (^{14}C) in the atmosphere, as derived from tree rings and varved sediments. The Fig. shows this comparison for the Siple Dome, Antarctica core. The centennial-scale variations are thought to result primarily from changes in solar activity that affect the production of both ^{10}Be and ^{14}C. We used our ^{10}Be record from a second ice core drilled at the Greenland Ice Sheet Project 2 (GISP2) site to make a detailed comparison of ^{10}Be and ^{14}C variations at the end of the last ice age, about 11,500 yr ago. Our reconstructions of the atmospheric radiocarbon concentration show that temporal variations at that time can be attributed to changes either in the carbon cycle or in the ^{14}C-production rate resulting from heliomagnetic and geomagnetic modulation. A priori, it is not clear which process governed changes in the atmospheric ^{14}C concentration. Strong climatic oscillations occurred near the end of the last ice age that might have influenced the carbon cycle and, therefore, also the radiocarbon content of the atmosphere. Because ^{10}Be is geochemically very different from ^{14}C, a comparison of ^{10}Be in ice cores with atmospheric ^{14}C derived from measurements of tree rings and varved sediments allowed us to differentiate changes in solar activity—which affects both ^{14}C and ^{10}Be—from changes in oceanic circulation or in the functioning of the carbon cycle—which only affects ^{14}C.

Our results show that the large fluctuations in atmospheric ^{14}C concentration observed around the Younger Dryas (YD) cooling event at the end of the ice age could be explained largely by changes in the production rate of ^{14}C. A residual difference between measured and modeled ^{14}C concentrations points to the existence of a smaller effect resulting from changes in global oceanic circulation. Furthermore, by matching the ice-core time scale with tree-ring chronology for the YD event at 13,550 yr ago, we showed that the GISP2 time scale had to be shifted approximately 60 yr towards younger ages. Thus, the relationship between ^{10}Be and ^{14}C concentrations has helped to calibrate the dating of the GISP2 ice core and resolve the origins of the YD cold period.

In addition to the ice-core work, we made significant progress in the course of this project in applying cosmogenic-nuclide surface-exposure dating techniques to determining long-term slip rates on earthquake faults. This success has led us to undertake new studies along the San Andreas fault system in Southern California and at other sites in the Southwest, in collaboration with the Southern California Earthquake Center and the U. S. Geological Survey. Our extensive measurement of ^{10}Be in high-altitude air filters is completed and is being analyzed to derive information about the mechanism of stratosphere–troposphere exchange.

Performance Prediction for Large-Scale, Nuclear-Waste Repositories

W. E. Glassley, J. J. Nitao, T. Bulous, M. Gokoffsky, C. W. Grant, J. W. Johnson, J. Kercher, J. A. Levatin

98-SI-004

Evaluating the suitability of potential sites as high-level nuclear waste repositories requires the capability to conduct simulations of how the site will change over thousands of years. The suitability of Yucca Mountain, Nevada is being evaluated as a potential repository site because of its arid climate and remote location. Yucca Mountain is composed of rock that contains a small volume of water in its microscopic pores. Heat from the repository will cause the pore water near the waste to migrate and chemically interact with the surrounding rock, which will change the local hydrological and mineralogical properties and water chemistry. To conduct realistic simulations of the behavior of such a repository, codes must be able to evaluate heat transfer; the boiling, evaporation and condensation of water; and the evolution of water chemistry and mineralogy. To be useful for predictive and engineering purposes, high spatial resolution is also required in two and three dimensions.

Until a few years ago, such simulations were not possible because a single model could take years to process on a standard workstation, and many simulations are required to evaluate hypothetical scenarios.

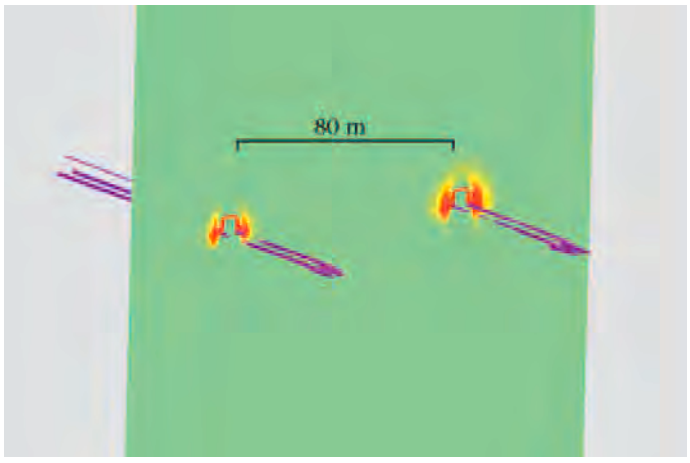

Three-dimensional, perspective view projected 300 yr in the future of salt deposition (red) and decreased porosity (purple) around the end regions of two waste-emplacement tunnels that are 80 m apart. The green surface on which the salt deposition is shown is a 2-D perpendicular cross section. The maximum salt deposition is 5 ppm by volume (red region), decreasing to 0 ppm (green region) away from the tunnels. The purple regions enclose those rock volumes in which the porosity reduction was at least 1%.

In FY1998 we tackled the problem of developing a code that would conduct such simulations on massively parallel computers at LLNL. We developed a coupled thermal-hydrological-geochemical code (NUFT-C) that runs on the IBM ASCI Blue Pacific. In FY2000 we applied the code to the problem of simulating the evolution of the environment around multiple waste packages in a prototype, high-level nuclear waste repository. The Fig. shows a simulation that projects salt deposition (red) and decreased porosity (purple) around two waste emplacement tunnels 300 yr in the future. We have demonstrated that high spatial and temporal resolution of the chemical conditions surrounding waste packages can now be routinely achieved.

Our project considered two important questions for repository studies. The first question, how the present day pore water compositions achieved the properties that are observed, is important because it provides a measure of how well the code is constructed and validates the conceptual model. The results of the simulations matched well the observed water chemistry, and suggest that the water composition variability throughout the mountain reflects the combined influence of the local rock mineralogy, the hydrological properties, and the influence of time. Time is important because of the slow reaction rates of minerals. Our results suggest that the chemical properties of water at a depth of approximately 700 m reflect water contact times with the rock of approximately 10,000 to 20,000 yr, while water at a depth of 100 m has chemical properties consistent with approximately 2,000 yr of contact time. These ages are similar to dates obtained from other, independent methods, and provide good evidence that the code and conceptual model closely represent the natural system.

The second question addressed the chemical conditions that a waste package might experience and the chemical parameters that could be measured to best test these. In FY2000 we have shown that spatial variability will be sufficiently high in the concentrations of certain key chemical parameters to allow measurement of those parameters in the field. These results can be used to design field-testing programs that evaluate the accuracy of predictions, which will provide the means to confirm models and assumptions upon which the long-term predictions of repository behavior have been based.

Multivariate Climatic-Change Detection

B. D. Santer, K. E. Taylor, C. Doutriaux

99-ERD-056

An apparent difference between the thermometer-estimated surface warming of roughly 0.2˚C per decade since 1979 and the much smaller warming trend in the lower troposphere estimated from satellites and radiosondes has received considerable scientific and political attention. Some have used this discrepancy to suggest that the Earth has not warmed over the last several decades. Another contentious issue relates to the consistency between modeled and observed temperature trends. Computer-model experiments driven by historical changes in greenhouse gases typically show larger warming in the lower troposphere than at the surface—the converse of the observed behavior. This apparent disagreement has been used in support of claims that *all* climatic models are fundamentally flawed.

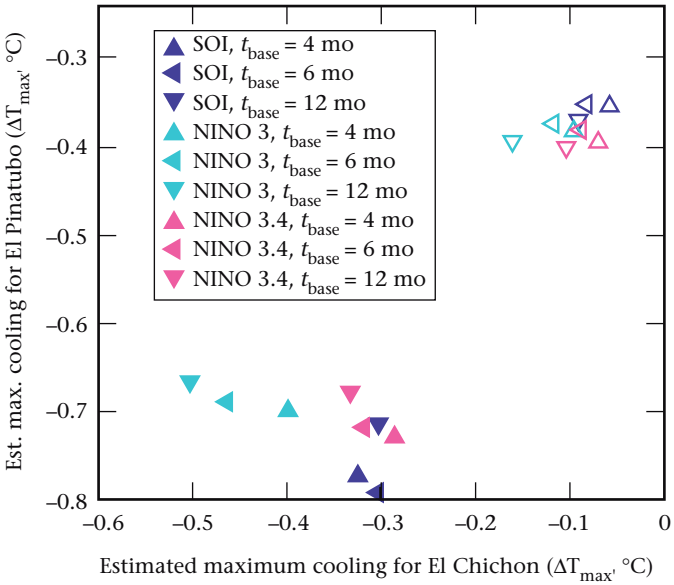

Estimated maximum coolings of surface and tropospheric temperature data caused by the 1982 El Chichon and the 1991 Pinatubo eruptions. The large range of estimates arises from uncertainties in key volcanic parameters, such as t_{base} (the time period, in months, used for determining the average temperature prior to the eruption) and the choice of index used to remove El Niño effects. Here we consider three values of t_{base} (4, 6, and 12 mo) and three different indices for removing El Niño effects (SOI = Southern Oscillation Index; NINO3, NINO3.4 = sea-surface temperatures averaged over different geographical areas of the equatorial Pacific). Note that the estimated coolings caused by El Chichon and Pinatubo are larger in the troposphere (solid symbols) than at the surface (open symbols). This partly explains why the Earth's surface and the lower troposphere have warmed at different rates over the past 21 yr.

This project investigated whether the identification of human effects on climate can be facilitated by examining the joint behavior of a number of different climatic variables rather than a single variable only (typically, surface temperature). Our work focused on one particular "joint relationship"—the covariability between temperatures at the Earth's surface and in the lower troposphere. Specifically, we sought to understand (1) whether the observed difference between surface and tropospheric temperature trends (1979 to present) is real or apparent; and (2) if it is real, can models simulate this behavior?

In FY1999, we found that some of the observed difference in surface–troposphere trends could be explained by accounting for differences in the spatial coverage of temperatures derived from satellites and surface thermometers (the satellite data provide global coverage, whereas the surface data do not). Model experiments suggested that the remaining difference could not be explained by natural climatic variability. We concluded that the observed surface–troposphere trend difference was largely real. However, climatic model simulations driven by changes in greenhouse gases and sulfate aerosols could not fully reproduce the observed behavior. If we also included the effects of stratospheric ozone depletion and aerosols from the June 1991 eruption of Mt. Pinatubo, projections by the model more closely agreed with observations; however, an unexplained residual difference remained.

During FY2000, we tried to explicitly quantify the effects of volcanoes and El Niño on surface and tropospheric temperatures. This was difficult, primarily because of the fortuitous temporal coincidence of the 1982/83 El Niño and the 1982 eruption of El Chichon. To account for such "collinearity," we developed an iterative procedure for separating signals from volcanoes and El Niño. We found that observed El Chichon and Pinatubo eruptions had a larger cooling effect on the lower troposphere than at the Earth's surface. This confirmed our earlier finding that the observed surface–troposphere trend difference probably has a real physical explanation.

During FY2000, we also examined simulations that included more complete estimates of volcanic forcing. These show, for the first time (see Fig.), that models forced by a combination of natural and anthropogenic effects *are* capable of simulating warming of the surface relative to the troposphere—behavior qualitatively similar to that seen in the observations.

Application of Terascale Computing Capabilities to Simulations of Global and Regional Climate

P. B. Duffy

99-SI-001

Most scientists accept that humans have influenced Earth's climate. Understanding these influences is an important scientific challenge with pressing social relevance. Some of the principal tools used to address this problem are climate models—computer representations of the ocean, atmosphere, sea ice, and other aspects of the climatic system. The Department of Energy (DOE) laboratories are involved in climatic modeling because (1) the main human influence on climate is fossil-fuel burning, and (2) the tremendous computational demands of climatic models are well matched to the DOE's outstanding computational resources.

This project had two broad objectives. First, in partnership with other institutions, we wanted to develop a new generation of climatic models that would be state-of-the-art scientifically and numerically and that would effectively use the latest massively parallel computers. A second objective was to perform important research that would maintain or increase LLNL's visibility in climate research. [For example, two studies performed last year as part of this project were featured in the United Nations-sponsored Intergovernmental Panel on Climate Change (IPCC) Third Assessment Report, a summary of the science of climatic change intended as a guide for policy makers.] We aimed to accomplish these objectives by taking advantage of LLNL's high-end computing resources.

During FY2000, we progressed in a number of important areas. First, using LLNL's new 512-processor TeraCluster 2000 computer, we completed the highest-resolution near-equilibrium simulation ever performed with a global oceanic model (see Fig.). Near equilibrium means that the model was run long enough that the solution was determined by the model's physics and boundary conditions rather than being influenced significantly by the initial conditions. This allowed a meaningful comparison between the model solution and observations. We also compared the high-resolution solution to a solution obtained at coarser resolution, which required 32 times less computer time. Although some aspects of the model solutions are noticeably different at the two resolutions, the coarse- and fine-resolution solutions are generally very similar. Thus, we concluded that even finer resolutions (and even more computational expense) would significantly improve the solution.

Second, we demonstrated the successful use of an innovative reduced grid in an oceanic–climatic model. In many climatic models, grid cells get smaller in the East–West direction as one approaches the poles. These small grid cells tend to require the use of a short time step, which slows the execution of the model. We implemented a reduced grid in which the physical size of the grid cells was kept relatively uniform by reducing the number of grid cells in the East–West direction at higher latitudes. This reduced the execution time of the model by roughly four times, primarily because we used a longer time step.

Finally, we completed a modeling study of oceanic uptake of CO_2 that has been released to the atmosphere by fossil-fuel burning. Understanding the oceanic uptake of fossil-fuel CO_2 is important because this process significantly slows the accumulation of CO_2 in the atmosphere and thereby slows global warming. We showed that LLNL's oceanic–sea-ice model simulates an uptake of fossil-fuel CO_2 in the important Southern Ocean region (near Antarctica) that agrees closely with observation-based estimates. This agreement increases confidence in our ability to predict future oceanic uptake of fossil-fuel CO_2, and thus to predict future global warming. Our results were published in *Science*.

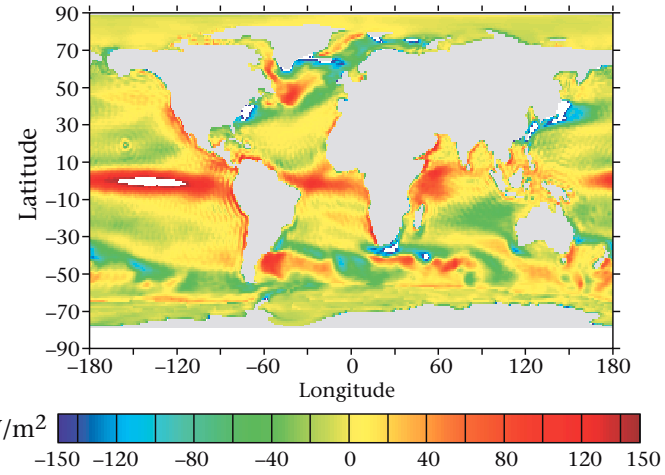

Ocean–atmosphere heat flux obtained from the highest-resolution near-equilibrium simulation ever performed with a global oceanic model.

Back to main TOC

Toward a New Era of Research in Aerosol–Cloud–Climate Interactions at LLNL

C. Chuang, J. Dignon, K. Grant, P. Connell, D. Bergman, D. Rotman

00-ERD-055

ne of the largest uncertainties in simulations of climatic change over the industrial period is the impact of anthropogenic aerosols on the Earth's radiation budget. Much of this uncertainty arises from the limited capability for either precisely linking precursor gases to the formation and size distribution of the aerosols or quantitatively describing the existing levels of global aerosol loading.

In this project, we are building on LLNL's expertise in aerosols and chemistry to address each of these uncertainties by coupling the most advanced chemistry and climate models. Specifically, we are (1) adding a sulfur chemistry mechanism to the Integrated Massively Parallel Atmospheric Chemical Transport (IMPACT) model, a state-of-the-art global-chemistry model; (2) developing an aerosol version of IMPACT with a simplified sulfur chemistry together with other nonsulfate aerosol species for use in chemistry–climate coupling; (3) implementing an aerosol microphysics module in the IMPACT aerosol version to include the important processes of aerosol dynamics; and (4) linking this chemistry–aerosol model to the most current version of the National Center for Atmospheric Research Community Climate model (NCAR CCM) to examine the climatic feedback by anthropogenic aerosols.

This unique modeling capability will enable us to identify and analyze the responsible processes in aerosol–cloud–climate interactions, which will increase scientific understanding of the effects of aerosols on climate. Our models will also be used to address the relative importance of anthropogenic and natural emissions in the spatial pattern of aerosol climatic forcing, and thus to assess the potential role of human-induced climatic change.

In FY2000, we progressed on three fronts. First, we validated the full-chemistry version of IMPACT with data from field measurements. That is, we ran the IMPACT full-chemistry version for a time period that overlapped data from the Subsonics Assessment (SSAS) Ozone and Nitrogen Oxide Experiment (SONEX) project being conducted by the National Aeronautics and Space Administration (NASA). Although the data exhibit large temporal and spatial variations, our model is able to capture their statistical average. The simulated concentrations compare well with observed mean values and are within one standard deviation of observed values.

Second, in FY2000 we compared results from our aerosol version of IMPACT to surface measurements taken at a number of remote ocean sites. Most of the simulated concentrations are within one standard deviation of the mean of the measurements, but discrepancies exist at some locations. During FY2001, we will look for a possible explanation by examining the oceanic source of dimethyl sulfide (DMS) and the mechanism for converting DMS to sulfate.

Finally, we adapted an aerosol microphysics module from the Brookhaven National Laboratory to simulate aerosol properties. We implemented this module into a box model to examine the role of each process (nucleation, condensation, coagulation, and dry deposition) in the evolution of aerosol size distribution.

In FY2001, we plan to (1) use our fully coupled NCAR CCM/LLNL IMPACT-aerosol model to simulate total aerosol optical depths and extinction profiles, and (2) compare our results to those retrieved from satellite measurements. This comparison should validate our emission inventories of aerosols and our treatments of transport and transformation.

In addition, in FY2001 we will perform multiyear simulations to characterize future variations in climate. Our simulations will incorporate the newly developed emission scenarios by the Intergovernmental Panel on Climate Change (IPCC). This work will provide us with a more quantitative range for aerosol effects on climate when compared to climatic effects from greenhouse gases.

Satellite-Based Observation of the Tectonics of Southern Tibet

F. J. Ryerson, J. Van der Woerd, R. Finkel, M. Caffee, P. Tapponnier, A. S. Meriaux, M. Taylor

00-ERI-009

The Himalayas and the Tibetan Plateau, formed as a result of the collision of India and Asia, provide an excellent natural laboratory for the investigation of the mechanical response of the outer 100 km of the Earth (the lithosphere) to tectonic stress. Geophysicists are divided in their views on the nature of this response: one group advocates homogeneously distributed deformation in which the lithosphere deforms as a fluid continuum, while others contend that deformation is highly localized, with the lithosphere deforming as a system of rigid blocks. The latter group draws support from the high slip rates recently observed on strike-slip faults along the northern edge of the Plateau [e.g. the Altyn Tagh Fault (ATF)], coupled with seismic observations suggesting that these faults penetrate the entire lithosphere. These "lithospheric faults" define continental lithospheric plates and facilitate the eastward extrusion of the rigid central Tibet plate. If such an extrusion occurs, then equivalent features must exist at its southern boundary, which has slip rates similar to those in the north.

Because the southern boundary of Tibet, defined by the Main Himalayan Thrust (MHT), has no lateral component of motion, it is kinematically incompatible with motion in the north. However, a series of features to the north of the MHT—the Karakorum Fault, the Karakorum-Jiali Fracture Zone (KJFZ), the Jiali Fault, and the Red River Fault—may define the actual kinematic, southern boundary of this central Tibet plate. We are determining slip rates on these faults, along with those on the ATF in northern Tibet, using a combination of satellite image interpretation, field mapping, and cosmic-ray-exposure dating at LLNL's Center for Accelerator Mass Spectrometry (CAMS) to assess the kinematic compatibility of features in northern and southern Tibet. This investigation supports efforts to understand the structure and mechanical response of the Earth's crust—information that forms the basis for activities such as nuclear test monitoring and resource recovery.

CAMS at LLNL is uniquely suited to surface exposure dating, allowing a number of cosmogenic isotopes to be measured. This year our international team, including Paul Tapponnier from the Institut de Physique du Globe de Paris and his graduate student, Anne-Sophie Meriaux, and Michael Taylor, a graduate student from UCLA, completed the dating of samples from the ATF and began mapping and sample collection at the northern and southern ends of the Karakorum Fault (KF). LLNL team members participated in the sample collection, and will be responsible for all of the sample dating. Our results for the ATF indicate that the slip rate decreases from west to east as slip is transferred to associated strike-slip and thrust faults. The rate on the central ATF (now supported by our own radiocarbon dating at key sites) is as great as 35 mm/yr. Such a high rate supports the hypothesis that these large strike-slip faults play an important role in accommodating Indo-Asian convergence; therefore, the deformation is localized rather than distributed. Similar conclusions can be drawn from our preliminary analysis of the morphological offsets along the KF. Here we have observed what, based on morphological criteria, appear to be glacial deposits associated with the Last Glacial Maximum (~10,000 yrs ago) that have been offset by distances greater than 100 m, implying slip rates of greater than 10 mm/yr. We are currently dating these samples using the beryllium-10 and aluminum-26 decay schemes to quantify both lateral and vertical slip rates. These data will allow us to assess the role of the Karakorum Fault in allowing eastward extrusion of central Tibet.

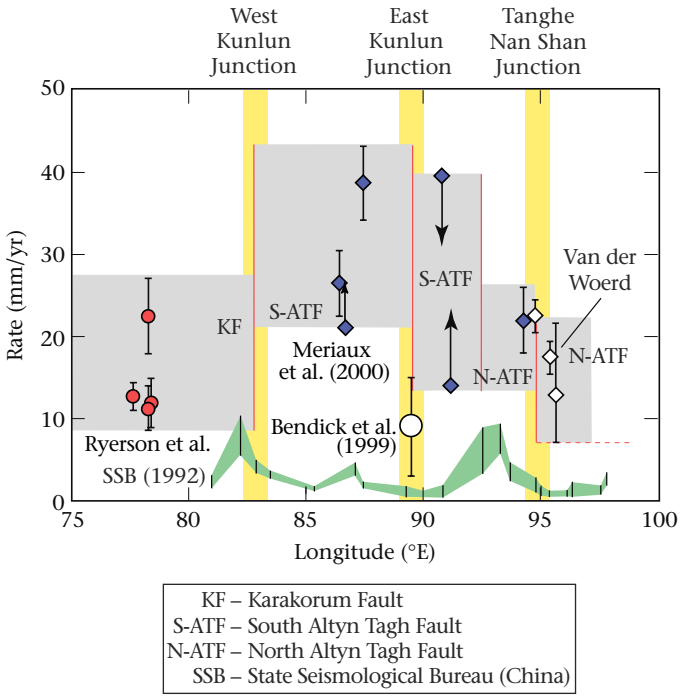

Longitudinal variation in slip-rate along the Altyn Tagh Fault from cosmogenic dating compared with GPS (Bendick et al., 1999) and previous Chinese results (SSB 1992). The decreasing rate indicates that slip on the ATF is transferred to other faults at its eastern terminus, causing uplift and plateau growth.

Stuffing Carbon Away: How Mineralogy and Precipitation Control Long-Term Carbon Sequestration in Soils

J. R. Southon, C. A. Masiello

00-ERI-010

As humans continue to add fossil-fuel CO_2 to the atmosphere, it becomes increasingly important to understand the processes that sequester carbon. One method of carbon sequestration is moving it into plant biomass and eventually into organic matter in the soil. Certainly, any changes in agricultural practices to enhance carbon storage would be far more effective if they were targeted for soil systems capable of sequestering the excess carbon for long periods.

The goal of this project is to improve capabilities for predicting carbon storage in soil by using radiocarbon measurements to help us understand two of the factors that control how efficiently soils store carbon: mineralogy and precipitation.

In FY2000, we collected a first suite of soil profiles from pits dug on uplifted marine terraces located south of the Mattole River, near Eureka, California, and measured organic-carbon inventories and radiocarbon ages. The terraces range in age from 3 to 240 kyr, with the degree of mineral weathering increasing with terrace age. Because carbon cycled through the soil many times over the lifetime of the terraces, the age of the carbon in the soil is much less than the age of the terraces. The mean age of the organic carbon is an excellent indicator of how effectively a soil stores carbon—slower cycling implies better storage.

The results from the Mattole terraces [Fig. (a,b,c)] show that the age of the organic carbon in the soil is most closely related to the content of amorphous minerals. These minerals are intermediate, metastable weathering products that initially increase in soils with time, but later decline as they transform over tens of thousands of years to more stable, more crystalline minerals. In almost all carbon-cycle models, the parameter used as a proxy for carbon storage in soil is clay content (i.e., grain size); however, the carbon-storage data from the Mattole terraces do not correlate well with the clay content, suggesting that current models are seriously deficient. These results confirm work done in Hawaii by our Lawrence Berkeley National Laboratory collaborator Margaret Torn; but the Mattole soils, which are based on sandstone parent material, are a far more common soil type than the volcanic soils in Hawaii.

In FY2001, we will test the relationship between the storage of organic carbon and the amorphous mineral content in the soil at a second suite of terraces located near Santa Cruz, California. Because the Santa Cruz terraces receive 50% less rainfall than the Mattole terraces, the rates of carbon cycling may be quite different, although the ages of the parent material and the terraces are similar. Comparisons between the Mattole and Santa Cruz data will allow us to examine how rainfall affects the ability of soils to store carbon.

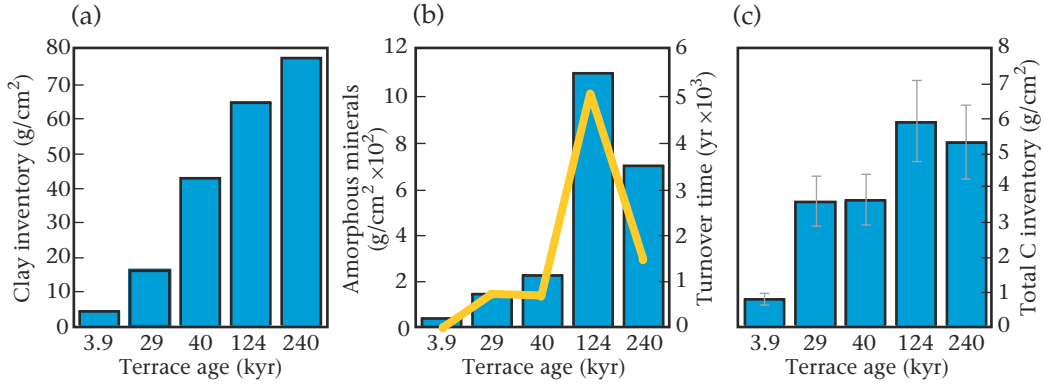

Terrace ages at Mattole River, California vs. (a) soil clay content, (b) amorphous mineral content and ^{14}C ages of organic carbon (in yellow), and (c) carbon inventories.

Biotechnology and Health Care Technologies

3

Section 3—Biotechnology and Health Care

Advanced Imaging Catheter

P. Krulevitch, D. Hilken, J.-U. Kluiwstra, R. Miles, D. Schumann, K. Seward

98-ERD-062

Catheter-based, minimally invasive surgery is performed by making a small incision in a main artery, inserting a long, hollow tube (catheter), and navigating through the artery to the treatment area. Once positioned, the catheter is used to deliver devices such as angioplasty balloons and stents for opening occluded arteries. Over 700,000 catheter procedures are performed annually. The advantages of this technique—reduced patient trauma and fast recovery—make it one of the fastest-growing surgical procedures. In most cases, catheters are positioned using radiography for visualization and manual manipulation for navigation and positioning of the device. However, the procedure has its difficulties: catheters can be as long as 2 m and can taper down to outside diameters of 800 µm, with artery channel diameters of 500 µm.

The objective of this project is to enhance the physician's navigational abilities by producing a compact catheter that offers imaging and active control for guiding and positioning the distal end (i.e., the end inside the body). Clinicians have emphasized that such a device would be a tremendous breakthrough. In addition, this technology has the potential for noninvasive or minimally invasive imaging of explosives or weapons systems.

Over the past three years, we have applied LLNL's expertise in optical and ultrasonic imaging, microfabrication, and modeling toward the development of an advanced catheter. The emphasis for FY2000 was on catheter articulation, mesoscale polymer molding and extrusion, and forward-looking ultrasound. In collaboration with physicians at the University of California, San Francisco (UCSF) and the University of California, Davis (UCD), we observed several catheter-based procedures and discussed how an articulating, imaging catheter could improve their patient's outcomes. Prototype devices incorporating shape-memory alloy (SMA), shape-memory polymer (SMP), and hydraulic actuation were fabricated and tested. The Fig. shows an SMP catheter tip with an embedded SMA spring. Heating the composite device just above the SMP transformation temperature causes it to expand and lengthen; heating above the SMA transformation temperature causes it to contract, enabling advancement of the tip when combined in series and actuated peristaltically. By fabricating and testing a 1-in.-long, 0.16-in. i.d., 0.08-in. o.d., hydraulically actuated, molded silicone catheter tip, we demonstrated repeatable 90° bending. In addition, a fluid-filled, 1/4-in.-diam polymer bellows increased in length 1/2 in. when heated by a laser.

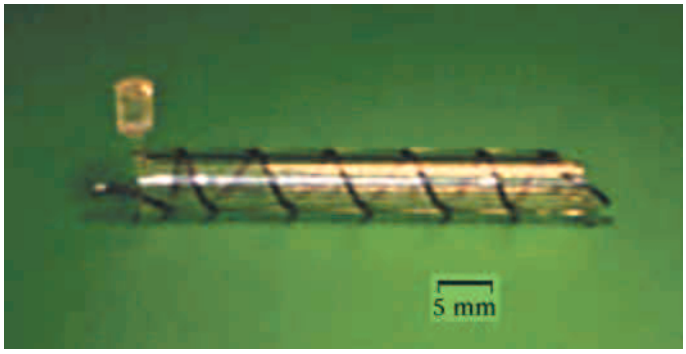

Our advanced, composite catheter tip, showing a prototype shape-memory polymer (SMP) tip with an embedded shape-memory alloy (SMA) spring.

During FY2000, we also investigated using forward-looking ultrasound to aid in guiding a needle during an intravascular liver-bypass procedure known as transjugular intrahepatic portosystemic shunting (TIPS). In this procedure, a single-element piezoelectric transducer is placed at the end of the articulating catheter and periodically pulsed. Harder tissues reflect more acoustic energy compared to blood-filled veins, thus enabling navigation through a diseased liver. To demonstrate the principle, we placed a single-element, circular transducer in a water bath 40 mm from a vessel-mimicking tube. The first interface was the front wall of the tube, and a large amount of energy was reflected back to the transducer. A second, much smaller reflection was observed coming from the back wall of the tube. This demonstrated the ability to use ultrasound to measure both the distance to the vessel and the size of the vessel. Numerical simulations optimized the size and shape of the transducer.

Several patents have been filed from this project, and two have been issued.

Low-Charge-State Accelerator Mass Spectrometer for Biological Research

J. S. Vogel, T. Ognibene

98-ERI-012

Drug companies are developing therapeutic compounds that are effective at very low doses. Some of these drugs are effective at less than one-thousandth the dose of a simple headache pill. Although the health benefits are clear, the manufacturer must study the drug's metabolites to be sure that none of them are toxic. Common analytical methods are unable to quantify the chemical products at such low concentrations in a reasonable amount of the patient's blood. Another problem that has puzzled biochemists for many years has been the exact behavior of nutritional compounds, such as vitamins, that must be consumed every day to maintain health. These chemicals appear in our food at microgram quantities and are stored by our bodies at milligram to gram levels for many months. Again, the overall benefit of the vitamin can be seen in the health of those who receive adequate amounts, but what are these chemicals really doing? Why do some people need more of certain vitamins than other people do? What analytical technique could distinguish the vitamin just taken from those that were swallowed a week ago?

Academic and industrial research scientists use the accelerator mass spectrometer (AMS) at LLNL to quantify isotope-labeled compounds at levels as low as a femtogram (one billionth of a microgram) to resolve drug metabolites and vitamin chemistry in human volunteers. LLNL's building-sized AMS, the most versatile and highest throughput instrument of its kind, is too large and costly for duplication at most research laboratories. This project explored the constraints of designing smaller, less expensive spectrometers that maintain the sensitivity, precision, and throughput required for analyzing isotopes of interest to biomedical research.

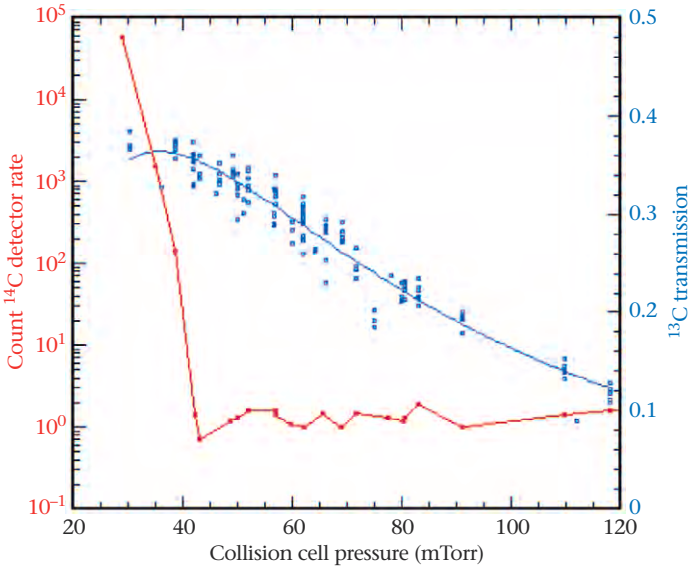

The percentage of ions converted to singly positive ions from negative ions (right axis) and the final isotope count rate (left axis) are shown as a function of the collision-cell gas pressure. High efficiency with complete molecular breakup is possible at 45 mTorr pressure.

To develop an optimal instrument, we obtained acceleration and ion-filtering components from a commercial vendor that are of a size that make them accessible to research institutions. We first modeled methods to couple our ion source to the spectrometer, a task completed in the previous year through adaptation of a "zoom lens" ion transport, which we then constructed and tested. Our design was fully assembled in FY2000, and we tested the complete spectrometer.

The design is successful in transporting a large fraction of the atomic ions through the accelerator and the collision cell, as shown in the Fig. Cell gas pressure must destroy molecules, and the minimum useful pressure is revealed by the detector count rate (left axis of Fig.), which becomes a constant rate at 45 mTorr. A 35% transmission of negative to singly positive ions is achieved at this pressure, even for our full-source output of up to 300 μA (right axis of Fig.). As the gas pressure in the cell increases, more ions are scattered out of the transported beam without any decrease in the detector count rate, indicating complete molecular suppression. Another 30 to 40% of the ions lose more electrons and are rejected by the spectrometer analysis. Our goal of measuring samples on a smaller system as rapidly as with our larger spectrometer is proven. The counting rate of carbon-14 (^{14}C) at natural levels is equivalent (500 to 750 counts/s) to that of the larger spectrometer. The background rate (see Fig.) of about 1 count/s, only marginally higher than more complex and expensive spectrometers, is low enough that it will not limit sensitivity needed in biomedical measurements, but it could be decreased by improved vacuum pumps in the collision cell.

Another feature that promises to enhance the capability of our spectrometer design is counting the final ions with a discrete-anode electron multiplier, a more robust (and less expensive) alternative to the usual solid-state detectors. The electron multiplier also distinguishes ions at a higher count rate, providing a dynamic range of up to five orders of magnitude for quantifying biological samples.

This project shows that room-sized AMS can have the high throughput, high precision, good sensitivity, and very wide dynamic range for biomedical research tracing ^{14}C. The results of this project will support a spectrum of university, industrial, and internal research, and make it possible for larger users to duplicate our design.

Analysis of the *Yersinia Pestis* Genome: A Prototype for Functional Genomics

P. M. McCready, E. Garcia, J. P. Fitch

99-ERD-083

DNA sequencing provides us with a path to understanding the genetic composition of the world around us, from the smallest virus to complex organisms, including humans. Portions of DNA known as genes dictate what a cell is and how it responds to its environment. Today, attention is shifting from mapping the DNA sequence—akin to reading its "parts list"—to understanding the function of the genes—its "wiring diagram." Functional genomics is a collection of methods for observing or inferring gene function for many genes at once. The tools of functional genomics are broadly applicable to many biological problems ranging from agriculture to human health.

We have selected the bacterium *Yersinia pestis*, the causative agent of bubonic plague, as a model organism for developing our functional genomics prototype. *Y. pestis*, considered highly contagious, is a great model for studying pathogen-host interactions because of its importance to human health, agriculture, and counterterrorism. Most importantly, *Y. pestis* has an inducible virulence mechanism. When grown at ambient temperatures (26°C), *Y. pestis* does not express many of the genes that make it virulent in humans. But when the temperature is increased to human body temperatures (37°C) and the calcium concentration is decreased, the bacterium begins to produce the proteins essential to its virulence. Assaying certain molecules present in the bacteria at room temperature and at elevated temperatures indicates which genes of the 4,500 in *Y. pestis* are involved in virulence mechanisms. We can then compare the candidate virulence genes in *Y. pestis* with those in other bacteria to determine what is unique to *Y. pestis*, what is common to other virulent bacteria, and what is shared with all microbes.

Our hypothesis is that the degree and nature of pathogenicity is a complex pathway of interactions among the virulence genes of a pathogen and the defense genes of the mammalian host. Induced changes in the expression of specific pathogen and host genes are critical first steps that determine the degree and nature of the subsequent pathogenicity. By identifying the critical genes involved in virulence mechanisms and host response, we will be better able to design effective detectors, vaccines, and treatments for exposed individuals.

Since June 1999, the functional genomics project has constructed a queriable, relational database containing the 4.9-million base DNA sequence composition of the *Y. pestis*. In collaboration with the Department of Energy Genome Consortium at the Oak Ridge National Laboratory, these data were used to computationally predict where the 4,500 genes in *Y. pestis* are located and which genes may be associated with virulence.

In FY2000, we designed chemical reagents to extract over 300 genes, including all known virulence-associated genes on the plasmids. For a 96-spot initial test microarray, 85 virulence-associated genes were extracted and spotted on a glass microscope slide (along with 11 control spots) to detect gene activity. A protocol was also developed in FY2000 that extracts appropriate biological material from *Y. pestis* at 26°C and 37°C. We verified the performance of the 96-spot array (see Fig.) and began design of a whole-genome microarray with all 4,500 genes.

In FY2000, we also investigated approaches to profiling protein activity and function. A mass spectrometer approach to protein screening was demonstrated and confirmed with two different affinity capture techniques—strong anion exchange and divalent cationic copper affinities. To generate and purify specific *Y. pestis* proteins, we investigated expression systems for both bacterial and insect cells.

This project was completed in FY2000. The protocols and basic biology developed under this project are already being used in our counterbiological terrorism programs.

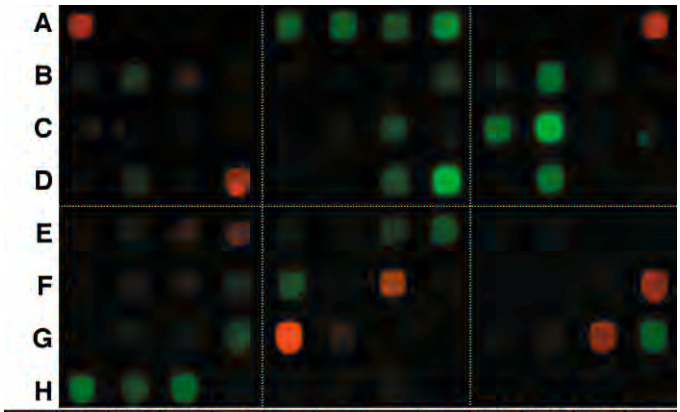

A	λ	BRCA	XRCC	PKC	ypkA	yscC	yscO	lcrV	PKC	XRCC	BRCA	λ
B	yopE	caf1A	sodA	envZ	ompR	yenI	rpoE	yopJ	yscB	lcrH	sycE	caf1R
C	tpx	rfaH	phoP	yenR	g6pd	rpoN	yopH	lcrF	lcrE	yopB	sycH	luxS
D	oxyR	psaA	glts	rpoS	lcrQ	yscW	tyeA	yopD	yadA	katY	hemF	toxR
E	rstB	nqrA	dha4	rpoH	yscL	yscU	sycN	yopM	pst	hns	cbl	flhC
F	nhaB	nadB	rpoD	yscH	lcrD	sycT	pla	catA	gcvA	copR	araC	nhaC
G	dam	yscG	lcrR	yopT	ymt	sodC	lysR	ilvY	tsaA	caf1	tuf	yscD
H	yscP	lcrG	yopK	caf1	sodB	crp	nhaR	fliA	h5	RAD	CDC2	Empt
	1	2	3	4	5	6	7	8	9	10	11	12

A 96-spot DNA microarray with 85* Y. pestis *KIM D14 genes and 11 controls (in yellow). Over expression of genes at 37°C and 26°C is denoted by green and red, respectively.

Chimeric Proteins to Detect DNA Damage and Mismatches

S. L. McCutchen-Maloney, C. Giannecchini, K. Robbins, J. Smessaert, M. Malfatti

99-LW-004

As a result of the Human Genome Project, the sequence and integrity of an individual's DNA can now be analyzed. In nature, DNA is constantly being subjected to damaging agents such as exposure to ultraviolet light and carcinogens from smoke. If such DNA damage is not repaired, mutations and eventually cancer can result. In addition to DNA damage, single nucleotide polymorphisms (SNPs)—variations in the genetic sequence between individuals—may predispose an individual to disease. Therefore, methods to detect DNA damage and SNPs are useful both in basic research and in healthcare and biotechnology. Current methods of detection often use radioactive labeling and rely on expensive instrumentation, which are not readily available in many research settings.

In this project, we have developed chimeric proteins to detect DNA damage and mismatches. These chimeric proteins were produced by fusing two individual proteins into one through genetic engineering, thereby generating a protein with a novel function. Our method to detect DNA damage and mismatches using chimeric proteins can be performed using simple gel electrophoresis, which makes the method suitable for basic research because it alleviates the need for labeling and expensive equipment. In addition, we have developed an SNP detection method based on the ability to detect mismatches that can be performed in multiplex, high-throughput form. This method has application in genomic/proteomic scale analysis of SNPs as well as in genetic testing.

In FY2000, we produced six new chimeric proteins, each of which is comprised of a nuclease (a protein that can degrade DNA) and either a damage- or a mismatch-recognition protein (a protein that can bind to DNA damage or mismatches). The new chimeras were designed to optimize the ability to detect damage and mismatches based on results obtained from the original six chimeras we produced. The polymerase chain reaction (PCR) mutagenesis was used to fuse the two genes of interest, and the fusion sequence was then engineered into an expression system. Proteins were expressed in bacteria and purified by affinity and/or ion exchange chromatography.

To date, we have shown that several of chimeras possess greater affinity for damaged and mismatched DNA than for native DNA. This was detected in assays designed to look at degradation of DNA after the addition of a chimeric protein. In the assays, one sample of DNA contains a site of damage or a mismatch and a second DNA sample (with the same sequence) contains no damage or mismatches. When a chimeric protein is added to the two DNA samples, the damage or mismatch-recognition protein binds to the sample containing DNA damage or mismatch, which allows the nuclease to degrade the DNA. Thus, the damaged or mismatched DNA is preferentially degraded. We have shown this both in gel-based assays and in a multiplex, high-throughput, dynamic liquid-array method. Use of the chimeric proteins in high-throughput assays suggests that the chimeric proteins could have application for detecting SNPs and DNA damage as well as for genetic testing.

In addition, a method using dynamic liquid array has been developed to detect mismatches, which has direct application to SNP detection. Mismatches can be detected on fluorescent beads by specific binding of a thermophilic MutS protein to mismatched DNA. In this method, matched (dsDNA) and mismatched (mmDNA) DNA substrates are coupled to two different beads. Biotinylated MutS protein is added and binding to the DNA substrates is detected by addition of a fluorescent reporter (streptavidin-phycoerythrin). This reporter has a strong affinity for the biotin molecule on the MutS protein. Thus, the reporter is only detected if the MutS protein binds to the DNA substrate on the bead. The amount of fluorescent reporter bound to the bead is recorded as mean fluorescent intensity (MFI). As the Fig. shows, we have detected a fivefold increased affinity of MutS for mismatched DNA both in singleplex mode (analyzed separately) and in multiplex mode (analyzed simultaneously). With this mismatch detection capability, it may be possible to analyze genomic DNA for SNPs.

In FY2001, we are pursuing application of our new technology to SNP detection using dynamic liquid-array, high-throughput assays. If our approach is successful, this work will provide a unique and simplified approach to SNP detection. Two patents for this work are pending.

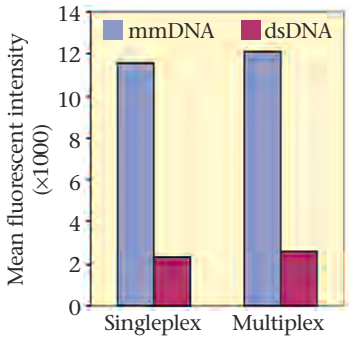

Matched DNA (dsDNA) and mismatched DNA (mmDNA) are attached to fluorescent beads. When MutS protein is added, it preferentially binds to the mmDNA bead rather than to the bead with dsDNA, as shown by the fivefold increase in mean fluorescent intensity for the bead containing the mismatch.

Polarized Light Imaging through Scattering Media

D. J. Maitland, V. Sankaran, R. London, G. Zimmerman

99-LW-011

Imaging through optically turbid media has a variety of applications, including medical diagnostics, underwater imaging, and atmospheric optics. The common goal in these applications is to discriminate weakly scattered photons, which have traveled a near-direct path through the medium, from highly scattered photons, which have traveled a more circuitous path through the medium.

The goals of this project are to (1) experimentally demonstrate that polarized light can be used to optically diagnose or image objects that are embedded in optically turbid media, and (2) increase the physical understanding of polarization propagation in scattering media by means of both experimental phantom studies and numerical simulations that use a Monte Carlo code that has been modified to include polarization. The Monte Carlo model is set up to use an electromagnetic (EM) scattering cross-section to determine polarized photon propagation.

Our experimental results have indicated that polarized light can indeed be used to image through optically turbid samples. For example, our initial research suggests that it may be possible to use polarized light to discriminate cancerous tumors from the healthy tissue in which they are embedded. Our results show that (1) polarized light survives hundreds to thousands of scattering events in tissue and tissue phantoms (microspheres in water suspensions) for a 1- to 3-cm path length (depending on the type of tissue), and (2) embedded objects that have different polarization properties will locally disturb the polarization state.

Most tissues typically contain photon scatterers that are very densely packed. However, most common tissue phantoms are made of dilute scatterers. Therefore, a limited study was conducted of the effects of scatterer density on polarized light propagation through aqueous suspensions of polystyrene microspheres. Depolarization by tissue phantoms was studied using suspensions of 0.48 mm, 0.99 mm, 2.092 mm, and 9.14-mm-diameter polystyrene microspheres in water with concentrations ranging from 0.065 to 19.3 volume percent microspheres. For dilute concentrations of each suspension, as the scatterer concentration increases, the degree of linear and circular polarization both decrease.

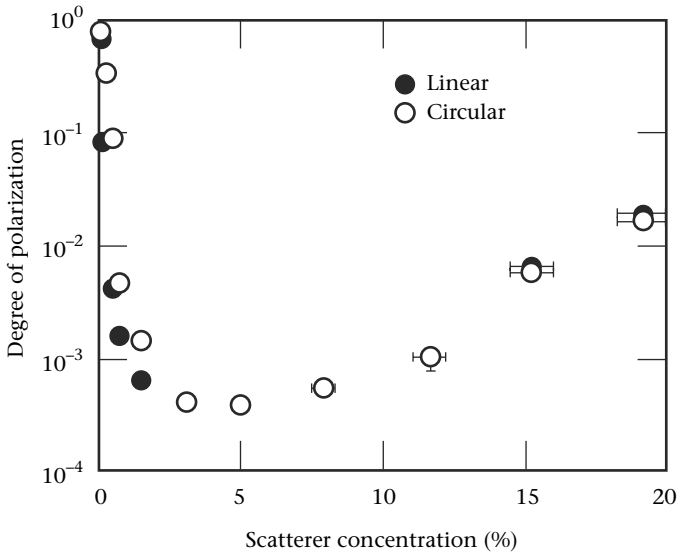

Degree of linear and circular polarization in suspensions with sphere diameters of 0.99 μm

Beyond a critical concentration of scatterers, however, the degree of linear and circular polarization begins to increase with increasing scatterer concentration. This critical scatterer concentration, at which there is an inflection in the degree of polarization, follows trends seen in previous studies that report on changes in unpolarized light attenuation through densely packed microsphere suspensions. For these dense suspensions, circularly polarized light is depolarized similar to or more quickly than linearly polarized light, which is comparable to results seen in adipose and myocardial tissue. We believe this increase in polarization is due to correlated scattering effects occurring between scatterers that are located very close to one another. This result is novel in that it is the first step towards an explanation of why polarized light propagates as it does in tissue.

The experimental results of this LDRD project have been published in three journal papers and two conference proceedings. The work started with this two-year LDRD project has been awarded an extramural NIH grant for applying this technology to cancer research.

Back to main TOC

High-Efficiency, Multilayer X-Ray Optics for X-Ray Crystallography

S. M. Lane, T. W. Barbee, Jr.

99-LW-013

The goal of this project has been to develop a novel x-ray lens that can concentrate ten to one-hundred times more x rays from a laboratory x-ray source onto a protein crystallography sample than is currently possible with commercially available equipment. This new lens will be a significant advancement because (1) most biological-structure information is obtained from protein crystallography measurements and (2) acquisition of these data takes one to two weeks for a single measurement.

The lens is designed to collect 8-keV x rays from either a copper rotating anode x-ray tube or a high-brightness fixed anode x-ray tube. The lens consists of a tube-like truncated ellipsoidal shell (~1-cm diam) whose inner surface is a precision x-ray mirror. The lens is especially efficient because it uses a multilayer mirror to reflect x rays by the Bragg mechanism (reflection angles of 3 deg) compared to conventional specular reflection mirrors (reflection angles of 0.3 deg). In addition, the fully enclosed tubular geometry of the lens allows a much large collection solid angle than conventional mirrors that consist of two orthogonal cylindrical sections.

The lens is fabricated using a method known as optical replication, in which a superpolished negative form of the optic (in this case a solid truncated ellipsoid) is fabricated with high accuracy (<1-mm radial error per cm length) and an ultrasmooth surface (3 to 5-Å-rms roughness) formed by high-velocity water-flow polishing. The lens is then formed by dc sputter coating the mandrel with multilayer reflecting surfaces and a stress-relieved supporting structure. The shell (lens) is separated from the mandrel and its inner surface retains the surface smoothness and figure of the mandrel with high fidelity. This fabrication technique results in dramatically reduced cost because of the relative simplicity and improved quality of external polishing of the mandrel, compared to conventional inside polishing of small-diameter tubular structures. Moreover, multiple shells can be produced from a single mandrel.

Accomplishments in FY2000 included the development of a new sputter coating system capable of producing accurate variable-thickness multilayer structures on small-diameter mandrels. This system consists of a planetary arrangement of three equally spaced rotating fixtures, each capable of mounting a mandrel, that themselves revolved around the central axis of the coating system. This arrangement allows the mandrels to be in close proximity to the sputter sources and results in accurate position-dependent deposition.

With this new deposition system and smooth substrates, we demonstrated that a precision variable-thickness multilayer mirror can be fabricated that has x-ray reflectivities within 85 to 90% of the theoretical maximum.

The remaining goal of the project was to improve the smoothness of the mandrels to allow for efficient reflection by the multilayer surfaces. By optimizing mandrel polishing methods and using new cleanroom handling techniques to minimize surface contamination, we have increased the reflectivity in the past year by over an order-of-magnitude and are within a factor of 2 of the theoretical maximum reflectivity.

The project ended in FY2000. However, an experimental demonstration of the effectiveness of this lens is still required. An industrial partner has been selected to commercialize lenses manufactured using this technology.

Back to main TOC

Development of Nuclear-Magnetic-Resonance Pulse Sequences and Probes to Study Biomacromolecules

M. Cosman, V. V. Krishnan, R. Maxwell

99-LW-031

Nuclear magnetic resonance (NMR) spectroscopy is a powerful method for determining biomolecular structures and dynamics in the solution state. In this project, we developed new and improved NMR probes and pulse sequences that we tailored to tackle specific problems that are not adequately addressed by current technology. Probes are the hardware containing the radio frequency (rf) circuitry used to both excite and detect the NMR signals; pulse sequences are composed of a series of rf pulses and delays that manipulate the nuclear spins.

The nature of our work requires an interdependent, multidisciplinary approach that brings together knowledge of spin physics (pulse sequences), engineering (probes), and structural biology (sample preparation and structure determination).

We focused on designing and constructing (using microfabrication techniques) a high-sensitivity microprobe, with specific applications directed toward enabling the more effective use of the phosphorus nucleus. Phosphorus (^{31}P) is a very important biological element that is strategically located in nucleic acids, where it imparts negative charge and flexibility to RNA and DNA. Phosphorus-31 is also a component of the cellular membrane: it is used in mechanisms to signal, activate or deactivate enzymes; and participates in energy storage and release. However, the phosphorus nucleus exhibits certain properties—(1) poor magnetic resonance spectral dispersion, (2) low sensitivity of detection, and (3) fast relaxation—that limit its effective use in NMR studies of biomolecules. Our unique combination of expertise allowed us to tackle each negative feature of ^{31}P-NMR in a three-pronged, concerted effort.

In FY2000, we synthesized DNA molecules that were modified by environmental carcinogens and food mutagens so that the phosphorus-containing backbone was severely distorted. Using these samples, we obtained an order-of-magnitude better signal dispersions in the phosphorus spectra, thereby overcoming the first of the three major shortcomings of ^{31}P-NMR spectroscopy mentioned above.

To overcome the second shortcoming, sensitivity of detection, we designed and tested—in collaboration with the University of California, Davis (UCD)—several novel rf microcoils. These microcoils increase the effective sample-to-coil ratio, and thereby increase the sensitivity of signal detection. A record of invention has been filed for a new type of microprobe cassette design that integrates these microcoils together with the rf circuitry and sample chamber to enable easier handling and storage of samples of less-than-microliter volume.

To overcome the fast-relaxation property of ^{31}P, we used our modified DNA samples to test two new pulse sequences that we designed to facilitate determining NMR structures. Our work was published. One sequence provides an improved experimental scheme for measuring self-diffusion coefficients of biomolecules with an advantageous use of radiation damping. The other is a novel, relaxation-compensated method that uses the decorrelation of heteronuclear two-spin order to enable the measurement of amide proton exchange rates in biomolecules. These new methods will greatly aid the optimization of our prototype microprobes and their application to studies of real biomolecules under physiologically relevant conditions.

Broad-Base Biological Assay Using Liquid-Based Detection Arrays

F. Milanovich, J. Albala, B. Colston, R. Langlois, K. Venkateswaran

99-SI-016

The release of biological agents by terrorists represents a serious threat to the safety of U.S. citizens. At present, over 50 pathogens and toxins appear on the threat lists of various agencies. Because most of these pathogens are rarely seen in this country, public health personnel have limited ability to rapidly identify infection by these pathogens. Many pathogenic infections have symptomatic delays as long as several days, which often compromises effective treatment. This translates into two major requirements for countering biological terrorism: we need credible detection technology to rapidly (1) detect and identify all the pathogens or toxins on current threat lists, and (2) diagnose thousands of potential victims.

In this project, we are developing a rapid, flexible, inexpensive, high-throughput, and deeply multiplex-capable biological-assay technology. Our liquid array (LA) technology, uses optical encoding of small-diameter beads that serve as the templates for biological capture assays. Once exposed to a fluid sample, these beads can be identified and probed for target pathogens at rates of several thousand beads per second. Because each bead can be separately identified, one can perform parallel assays by assigning a different assay to each bead in the encoded set. Our goal is a detection technology capable of simultaneously identifying hundreds of different bioagents and/or rapidly diagnosing several thousand people.

Our research has three emphases. In the first, we are exploring the fundamental interactions of the beads with proteins and nucleic acids in complex mixtures. This will provide us with a complete understanding of the limits of the technology with respect to throughput and complex environment. A major spin-off of this activity is in the rapidly emerging field of proteomics, where we may be able to rapidly assess the interactions responsible for cell metabolism, structural organization, and DNA replication and repair. Understanding the complexities of these interactions is a fundamental step towards comprehending key aspects of the biochemistry of disease. During FY2000, we used our LA technology to confirm the dynamics of a well-characterized, three-protein, bacterial DNA repair mechanism—UvrABC. In FY2001, we will begin studying the less-characterized mammalian homologous recombinational DNA repair pathway by examining the protein/protein and protein/DNA interactions of RAD51B/C.

We are also studying a model human disease state to assess the application of the LA in highly parallel and rapid medical diagnostics. In collaboration with researchers at the University of California, San Francisco (UCSF), and the California Department of Public Health, we are developing a multiplex assay for determining exposure to Human Herpes Virus 8 (a cancer-inducing virus) in AIDS patients. We have successfully demonstrated an 8-plex assay. During FY2001, we plan to extend the 8-plex detection capability to a 20-plex assay and, in parallel, develop an 18-plex assay for detecting antibodies to all vaccine-preventable childhood viral infections.

Finally, we are developing a microbead immunoassay dipstick system (MIDS) [see Fig. (a)] that would use the bead assay in the simplest possible form. In this method, after the microbeads and a fluorescent reporter have been captured in solution, the beads are trapped on an ordered dipstick array [Fig. (b)]. The color of each bead identifies the biomarker; the fluorescent reporter measures its concentration. MIDS would enable widespread use of our LA technology by reducing the capital investment required while greatly simplifying operation and maintenance. In FY2001, we plan to build a brassboard system capable of addressing major design and performance elements for the MIDS concept.

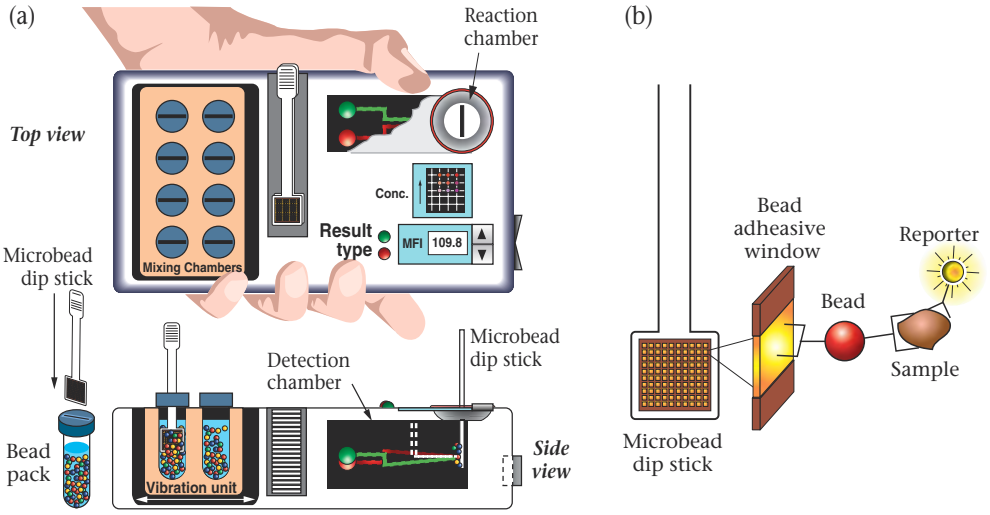

The microbead immunoassay dipstick system (MIDS), showing (a) the conceptual design, and (b) how biological-sample and fluorescent molecules are trapped and detected on a disposable dipstick.

Using Mass Spectrometry to Probe Noncovalent Interactions between Biomolecules

S. J. Shields

00-ERD-006

To counter bioterrorism and to understand, treat, and prevent human disease (e.g., by developing therapeutic inhibitors for proteases involved in DNA repair), we must be able to probe protein conformation, characterize noncovalent interaction sites between biomolecules, and investigate the dynamic change in protein conformation upon ligand binding.

Research efforts implemented by LLNL and the Department of Energy include the design, synthesis, and characterization of small-molecule ligands that act to inhibit the function of biological toxins such as tetanus, botulinum, and cholera by blocking the protein's active site. For studying noncovalent interfaces between biomolecules, mass spectrometry (MS) offers several advantages over traditional analytical methods, e.g., nuclear magnetic resonance (NMR), and x-ray crystallography. Most importantly, MS consumes biologically relevant concentrations of protein, 1 to 10 µM, compared to the 1 to 10 mM consumed by NMR and x-ray crystallography. Mass spectrometry also offers (1) high throughput capabilities, where data-collection times are measured in seconds (rather than in hours or days); and (2) a detection limit of a molecular weight of 1 million amu.

In this project, we are developing MS methods that are needed to characterize solution-phase, noncovalent interactions between biological toxins (molecular weight of 50,000+) and small-molecule inhibitors (molecular weight of 300 to 1000). Our research goals for this project include (1) developing MS methods for screening libraries of small molecules that are predicted to bind to tetanus toxin, (2) determining protein region(s) in which ligands bind, and (3) determining specific interactions between amino acids and ligands.

During FY2000, we developed an MS method for screening potential polar inhibitors of tetanus toxin. Figure (a) shows a mass spectrum of tetanus toxin C-fragment (51.8 kDa) complexed to one doxorubcin molecule (52.3 kDa) and two doxorubicin molecules (52.9 kDa). From these data, we determined that doxorubicin interacts noncovalently with tetanus toxin, and doxorubicin has more than one binding site when the molar ratio of doxorubicin:tetanus toxin is 2:1.

At the end of FY2000, we performed kinetic experiments on the enzymatic degradation of tetanus toxin and tetanus toxin:doxorubicin complex to determine ligand-binding regions. We investigated the dissociation of the two systems, over 24 h, by proteolysis with specific enzymes. In the toxin:doxorubicin complex, doxorubicin prevents the enzyme from cleaving the protein at the binding site by limiting access to those amino acids. Figure (b) shows the crystal structure of tetanus toxin C fragment, where amino acids in yellow indicate experimentally determined doxorubicin binding region(s). These binding regions agree with the data in Fig. (a) that suggest two potential doxorubicin-binding sites.

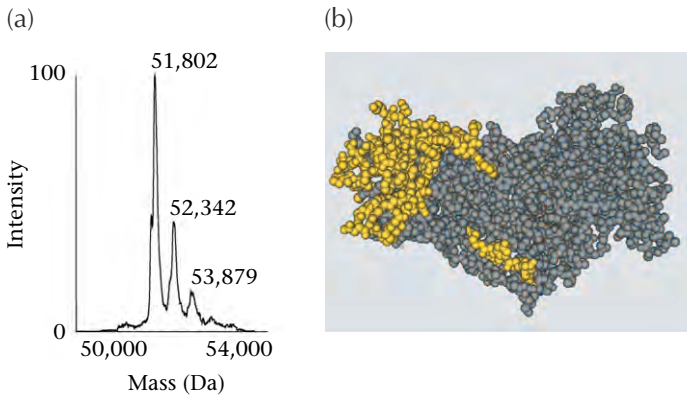

Results of work on the tetanus toxin C-fragment protein, showing (a) the mass spectrum of the protein complexed to doxorubicin; and (b) crystal structure of the C-fragment, with yellow indicating the doxorubicin binding regions.

Due to concerns about specific and nonspecific binding of ligands to proteins, in FY2001 we will investigate the dependence of ligand concentration on the number of observed binding sites. In other words, as doxorubicin concentration increases, are more nonspecific binding sites observed or does doxorubicin compete for the same site(s)? Results from our initial enzymatic-degradation experiments show subtle changes in tetanus toxin's tertiary structure upon complex formation, suggesting that the protein envelopes doxorubicin. To interrogate this conformational change, we will perform hydrogen–deuterium-exchange MS experiments, which should reveal (1) a shift in mass of the protein resulting from a reduction in the amount of deuterium incorporation in the protein at the binding site, and (2) an increase or decrease in exchange in regions of the protein not associated with the binding site.

Application of Carbon-Nanotube-Based Atomic Force Microscopy to Proteomics and Biological Forensics

J. De Yoreo, A. Noy, A. Malkin

00-ERD-008

Due to the difficulty of growing protein crystals for x-ray diffraction, scientists have determined the atomic structures of less than 1% of the approximately 100,000 proteins in the human body. Given the current rate at which structures are being solved, it will take more than 100 years to determine the rest. Consequently, techniques that can help to elucidate the factors controlling macromolecular crystallization, increase the amount of structural information obtained from crystals, or eliminate the need for crystallization are of enormous importance. In addition, potential applications for those techniques extend well beyond the challenges of protein-structure determinations. The global spread of modern technology has brought with it an increasing threat from biological agents such as viruses. As a result, developing techniques for identifying and understanding the operation of such agents is becoming a major area of forensic research for the Department of Energy.

Over the past few years, we have shown that atomic force microscopy (AFM) can be used to image the surfaces of growing macromolecular crystals with molecular resolution and can even provide structural information not obtainable from x-ray diffraction. For some viruses, AFM can resolve gross structural features of the virions themselves, even in the absence of crystallization. The limitation on the application of AFM to structural studies of viruses and proteins is the size of the AFM probe, which currently restricts the lateral resolution to about 10 nm.

The purpose of this project is to develop the use of carbon nanotubes as AFM probes in fluids for in situ imaging and identification of viruses with subvirion resolution and for single-molecule investigations of protein crystallization.

During FY2000, we constructed a micromanipulation system for attaching carbon-nanotube bundles to the tips of conventional AFM cantilevers. We also set up a pulser for shortening and sharpening the bundles. The Fig. shows an example of a carbon-nanotube tip along with images of a titanium surface before and after attachment of the nanotube. Using this system, we fabricated numerous carbon-nanotube probes and collected images of proteins, RNA, DNA, and viruses in air. Unfortunately, these tips were not robust enough to survive fluid environments. Consequently, we took a two-pronged approach to making nanotube tips for fluid environments. First, we constructed a chemical vapor deposition (CVD) system for growing carbon nanotubes directly onto the AFM cantilevers. In addition to producing single-walled carbon nanotubes that have maximum sharpness, this technique should result in much better contact between the nanotubes and the cantilever. Our second approach to making nanotube tips that operate in fluid is to, in essence, weld them on by using a scanning electron microscope (SEM) to deposit a layer of carbon over the nanotube–cantilever junction. At the close of the year, we were testing these two methods.

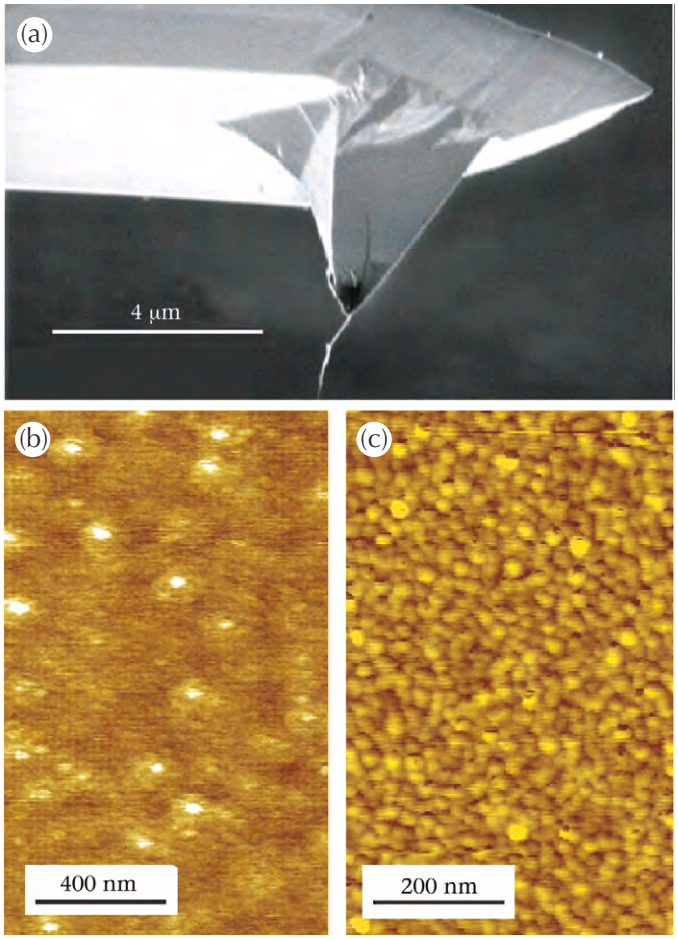

Imaging results obtained using bundled carbon-nanotube tips attached to a conventional atomic force microscopy (AFM) tip, showing (a) a scanning electron microscope (SEM) image of the attached nanotube bundle, and AFM images of titanium using (b) a conventional tip and (c) a nanotube tip.

During FY2001, we will perfect the use of carbon-nanotube tips in fluids and turn our attention to imaging viruses, both during crystallization and following direct adsorption onto the substrate. After a sufficient database has been collected, we will use an image-recognition software package to develop an automated routine for categorizing and identifying viruses.

Development of Tritium Accelerator Mass Spectrometry for Biomedical Sciences Research

K. H. Dingley, A. Love, M. L. Chiarappa-Zucca

00-ERI-001

Tritium (^{3}H), a radioisotope that is extensively used in biological research, normally is quantified by liquid scintillation counting. However, for the most sensitive measurements, liquid scintillation counting requires large samples and counting times of several hours. In contrast, provisional studies at LLNL's Center for Accelerator Mass Spectrometry (CAMS) have demonstrated that AMS can be used to quantify ^{3}H in milligram-sized biological samples with a hundred- to thousandfold improvement in detection limits when compared to scintillation counting. This increased sensitivity is expected to have great impact in the biological research community.

However, before ^{3}H AMS can be used routinely and successfully, two areas of concern need to be addressed: (1) only a preliminary ^{3}H AMS sample preparation method has been developed, which lacks the robustness and reproducibility needed for routine ^{3}H AMS analyses; therefore, sample preparation methods need to be refined and standardized; and (2) few institutions in the world can afford to build and maintain a facility as large as the LLNL CAMS, consequently smaller and simpler AMS instrumentation must be developed. The goals of this project are to (1) characterize a small dedicated ^{3}H AMS spectrometer [built in collaboration with AccSys Technology, Inc. of Pleasanton, California, this relatively low-cost system is based on a LLNL ion source and sample changer, and injects ions into an AccSys radio frequency quadrupole (rfq) linac]; (2) develop routine and robust biological sample preparation methods that can be used for a variety of sample forms and sizes likely to be generated in a biological study; and (3) demonstrate the application of ^{3}H AMS in the biomedical sciences, with the aid of our external collaborations.

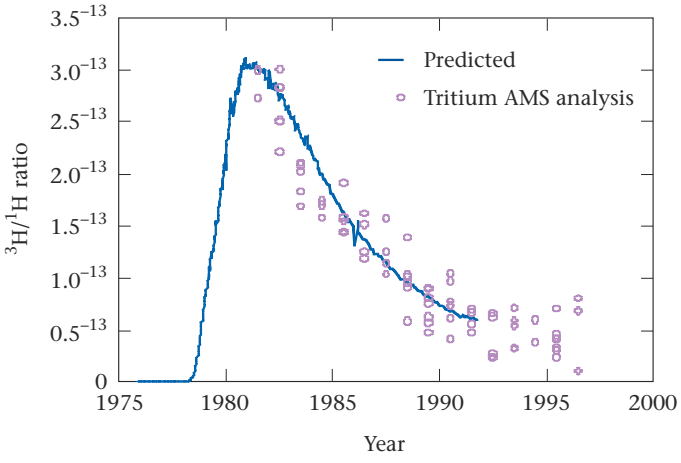

Tritium AMS has been used to measure the tritium content of tree-ring samples collected from the Nevada Test Site. (courtesy of A. Love and J. Hunt, U. C. Berkeley)

In FY2000, we made significant improvements in the performance of the ^{3}H AMS spectrometer: (1) optimization of control parameters, which resulted in a threefold increase in ^{3}H count rate and an order-of-magnitude improvement in the detection limit; and, more importantly, (2) a linear response of at least four orders of magnitude. To understand possible sources of contamination and variation in the samples, we characterized the combustion and transfer steps of the sample-preparation procedure. Results provided a better understanding of the process and led to a drastic improvement in the quality of the samples and the consistency of the results.

A number of collaborative biological studies that require ^{3}H AMS are underway at the University of California, Berkeley (UCB) and LLNL. For example, we have developed a novel method for the measurement of cell turnover using ^{3}H AMS in collaboration with Dr. M. Hellerstein (UCB). This method should provide significant improvements over current methods, which either use toxic chemicals or high levels of radioactivity, or lack the sensitivity necessary for measuring low rates of cell turnover. In addition, we are collaborating with Dr. J. Hunt (UCB) to analyze ^{3}H in tree-ring samples (see Fig.), which will facilitate monitoring ^{3}H contamination near residential or agricultural areas. Work in FY2001 will continue to optimize sample preparation methodology for biological samples and analysis methods to measure samples from these projects.

Results gained through this project demonstrate the availability of a compact, sensitive, and cost-effective instrument to perform accurate measurement of ^{3}H from small samples. Tritium AMS will enable LLNL biologists and our university collaborators to conduct studies of national interest that would otherwise be impossible and will strengthen LLNL's position as a center for university-based biological research.

Back to main TOC

Engineering Titanium for Improved Biological Response

C. A. Orme, J. P. Bearinger, J. Gilbert

00-ERI-006

The fundamental science of corrosion affects many practical problems when metals are used in humid or wet conditions. These uses range from nuclear-waste containers to biomedical implants. Titanium (Ti) is the material of choice for many of these uses because the metal is both lightweight and strong. For biomedical applications, titanium's native oxide film is just as important, serving both as a barrier to resist corrosion and as a biocompatible surface. We are working to establish the basic science of Ti interfacial dynamics and oxide behavior in its native, hydrated state, with the goal of optimizing its biological integration and its performance in other environments.

The human body's electrolytic solution, which is responsible for transport, healing, integration, or attack, provides a first point of contact with an implant. This solution presents an aggressive environment that challenges the survival of implanted foreign materials through biological, chemical, electrical, and tribological factors. In this project, we are testing the reaction of titanium and TiO_2 to a subset of these factors in electrolytic solution. Specifically, we use an electrochemical atomic-force microscope (AFM) to (1) directly observe morphological changes of TiO_2 upon its exposure to physiological environments, (2) compare hydration kinetics at voltages relevant to implant tribology, and (3) compare the electrical characteristics of oxide films in relevant solutions.

Hydration experiments were performed in phosphate-buffered saline solutions. Oxide domes, present on all the forms of Ti that we examined (commercially pure Ti_6Al_4V and vacuum-sputtered Ti), swelled upon immersion in solution and grew over time, showing impingement and coarsening. Under open-circuit potential (OCP) conditions, the oxide domes of commercially pure Ti expanded at 1098 nm^2/min. Application of a –1-V overpotential decreased the kinetic growth rate to 185 nm^2/min, six times slower.

Bone can abrade TiO_2 on an implant, with the result being an OCP drop close to 1 V. To mimic this effect, we examined the morphology of TiO_2 and its electrical response in the ±1-V range. Both the imaging and electrical response were monitored simultaneously. As the voltage was ramped in the positive direction, early (oxide) resistance increased and capacitance decreased; both are consistent with growth of an oxide film. We found that electrical properties approached starting values when the voltage was looped back down, although hysteresis was present. In contrast, the size of the oxide dome continually increased with increasing voltage, but did not decrease with decreasing voltage. Although we had not initially expected the morphological and electrical properties to be independent, this relationship can be explained by the classification of TiO_2 as an n-type semiconductor. Thus, the oxide grows and changes at the metal–oxide interface, but not at the oxide–solution interface. This decoupling may in fact result in a more stable interface between an implant and the biological milieu.

In FY2001, we will examine the effect of solutions modified to mimic aspects of wound healing and osseointegration events. In particular, we will look at hydrogen peroxide and calcium phosphate solutions. Hydrogen peroxide is an oxidizing molecule secreted by cells that are associated with wound healing; it is present in significant quantities in fresh implant environments. Calcium phosphate is the mineral component in bone.

In collaboration with Brookhaven National Laboratory, we will also perform surface x-ray scattering experiments to obtain structural information about the oxide layer and the initial stages of ordering in the solution phase.

This work is directly relevant to the medical technologies program, which creates devices for implantation, and to the Yucca Mountain project, which needs to understand the growth and adhesion properties of oxide films on metals.

Acoustic Filtration, Fractionation, and Mixing in Microfluidic Systems

A. Wang, K. Fisher, M. O'Brien, L. Tarte, W. Benett

00-LW-032

Sample pretreatment is a critical aspect in the development of miniaturized microfluidic biological analysis systems, yet it remains largely an unsolved problem. Integrated sample preparation requires a high degree of functionality to perform biological or chemical analysis in a miniaturized system. Typically the cost of a sample chamber part increases with its functionality, yet the danger of sample-to-sample contamination makes inexpensive, disposable parts attractive. By using acoustic energy remotely coupled into a plastic or glass chamber we have combined high functionality with an inexpensive, disposable sample chamber.

In FY2000, we demonstrated a noncontact method that uses acoustic radiation pressure to concentrate and mix particles in a plastic microfluidic chamber. We developed plastic fabrication processes, designed a removable method of coupling acoustic energy into the sample chamber, and designed and characterized mixing chambers. Our prototype devices for acoustic-based particle manipulation that indicate preferential geometry for mixing versus concentrating functions. Typical devices consist of a single half-wavelength-wide fluid channel fabricated from laser-cut acrylic sheets. The fluid channels are formed from a bonded acrylic laminate. Bulk PZT-4 piezoelectric transducers with a half-wavelength resonance thickness and a primary resonance peak of 365 kHz were used as the acoustic source. A flow cell package has also been designed that integrates reusable liquid sample interconnects, electrical contacts and a removable plastic sample chamber.

Results show that we are able to induce mixing and concentration of polystyrene and glass beads suspended in deionized water. Piezoelectric transducers were driven at 15-40 Vpp. Bead mixing was achieved at drive frequencies that correlated to observed piezolelectric resonance frequencies. Mixing speed increased with drive voltage. Figure (a) illustrates a series of experimental observations that correlate the improvement in binding of bacteria spores to magnetized glass beads as a function of mixing speed. We also demonstrated bead concentration and bead separation based on size. Bead concentration was accomplished when transducers were driven so that a standing wave was set up in the channel. Figure (b) shows concentration of 10-µm polystyrene beads at the center of the fluid channel, an expected pressure node of the standing wave. Also demonstrated in Fig. (b) is separation of particles based on size. The larger, 5-µm beads collect at the central node of the channel, while smaller, 3-µm beads remain dispersed in solution. Two finite element modeling packages (ABAQUS and ALE3D) have been applied to characterize the standing-wave pattern with excellent results. Figure (b) gives a sample of the radiation pressure contours.

In FY2001 we plan to (1) apply analytical and finite element models to aid in design optimization of our devices, (2) use particle-image velocimetry to measure the force and velocity of particle motion, and (3) test biological samples for feasibility in future applications.

(a)

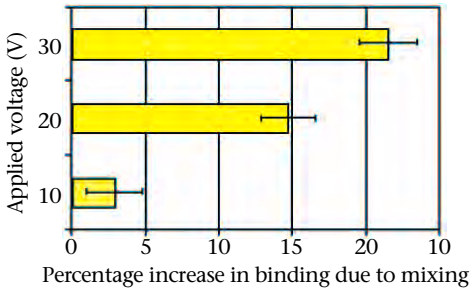

(b)

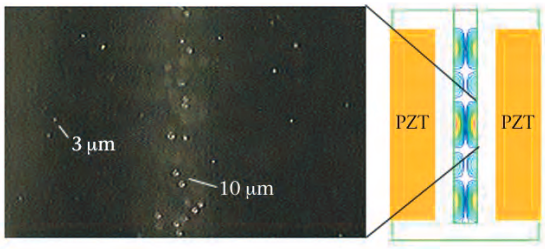

(a) Mixing speed increases the binding of bacteria spores to 5-µm magnetized glass beads; (b) 10-µm polystyrene beads focused to the center of the fluid channel (left) and a 3-D finite element model of the acoustic energy in the chamber (right).

Nonlinear Optical Tissue Diagnosis and Imaging In Vivo

B.-M. Kim, K. M. Reiser, P. C. Stoller, A. M. Rubenchik

00-LW-063

Second-harmonic generation (SHG) is a second-order, nonlinear optical phenomenon that results from the interaction between high-intensity light and an object with nonlinear susceptibility. Recently, there has been interest in developing nonlinear optical-imaging methods suitable for studying biological materials. Techniques using special dyes or other enhancements have been reported for analyzing membrane depolarization.

The overall goal in this project was to develop a more comprehensive understanding of the molecular basis of SHG in collagen. Such understanding would enable us to develop noninvasive imaging modalities applicable to disorders as diverse as malignant transformation in dysplastic nevus syndrome, vascular stiffening, diabetic complications, and preclinical stages of hypertrophic scarring.

Our work was based on analysis of the second-harmonic signal generated by collagen. Collagen is an attractive target for several reasons. First, because of their helical structure both at the molecular and supra-molecular level, collagen molecules possess second-order nonlinear susceptibility. Second, even though phase matching is not possible in collagen fibers, significant SHG can occur because fiber diameters are comparable to the coherence length for non-phase-matched SHG. Third, collagen is unique among biologically important molecules in that it generates an exceptionally strong second-harmonic signal, resulting in little noise even in complex tissues. Fourth, as the most abundant protein in almost all tissues, collagen can serve as a signal source in virtually all organ systems. Finally, many pathological processes are associated with derangement in collagen structure, sometimes at very early stages.

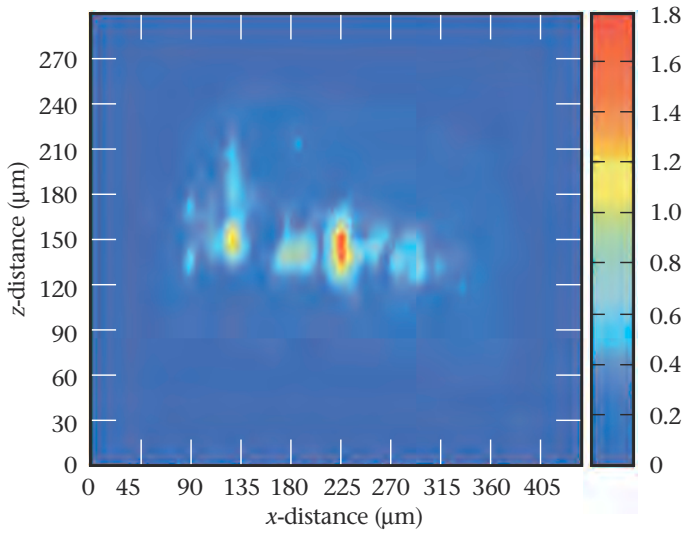

Cross-sectional image of a rat-tail tendon fascicle at a fixed light polarization. Non-uniform second-harmonic generation (SHG) is observed even if the collagen fibers are distributed uniformly. This may be related to the phase-matching condition and the size of the fibers.

During FY2000, we developed methods for SHG analysis in unmodified biological samples, including tendon, muscle, cartilage, and skin tissues from rat, cow, and chicken. We devised a confocal microscope that measures the second-harmonic light generated from biological tissues. Our setup, which includes a confocal lens, allowed us to perform 3-D scans capable of identifying structural features of 10 to 50 μm (1-μm maximum resolution) and to assess the polarization-dependence of SHG (see Fig.). We also investigated correlations between SHG and perturbations of collagen structure, including glycation and degradation.

Primary structure may play a role: we found differences in SHG between type I and type II collagens, and we investigated SHG in some of the 17 or so other genetically distinct collagens. Supramolecular architecture may also be a major determinant. We analyzed some of these aspects of molecular packing with SHG by investigating polarization dependence, and showed that the signal intensity in rat-tail tendon fibrils is proportional to the angle of polarization. We developed a mathematical model for understanding this phenomenon. A least-square fit of the experimental data to the model enabled us to extract an independent parameter that is directly related to the nonlinear optical susceptibility of the collagen fibers of rat-tail tendon.

Results of our project have been published.

Computing, Modeling and Simulation

4

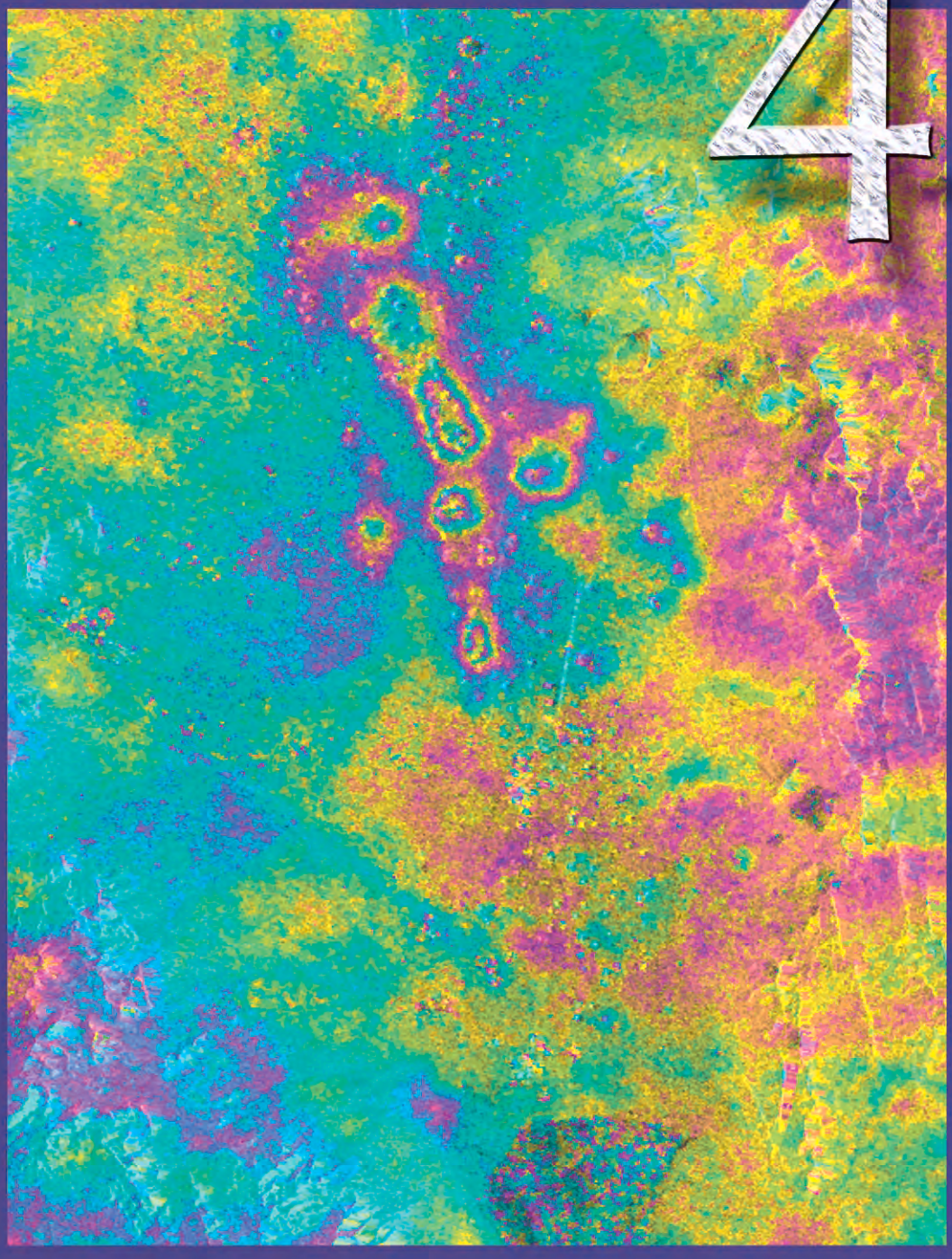

Section 4—Computing, Modeling, and Simulation

Novel Parallel Numerical Methods for Radiation and Neutron Transport

P. N. Brown, B. Chang, K. Grant, U. Hanebutte, C. S. Woodward

98-ERD-022

In many of the multiphysics simulations performed at LLNL, transport calculations can take up 30 to 50% of the total run time. If Monte Carlo methods are used, the percentage can be as high as 80%. Thus, a significant core competence in the formulation, software implementation, and solution of the numerical problems arising in transport modeling is essential to Laboratory and Department of Energy research.

In this project, we worked on developing scalable solution methods for the equations that model the transport of photons and neutrons through materials. Our goal was to reduce the transport solve time in these simulations by means of more advanced numerical methods and their parallel implementations. These methods must be scalable—the time to solution must remain constant as the problem size grows and additional computer resources are used. For iterative methods, scalability requires that (1) the number of iterations to reach convergence is independent of problem size, and (2) the computational cost grows linearly with problem size.

We focused on deterministic approaches to transport, building on our earlier work in which we performed a new, detailed analysis of some existing transport methods and developed new approaches. The Boltzmann equation (the underlying equation to be solved) and various solution methods have been developed over the years. Consequently, many production codes are based on these methods, in some cases decades old. For the transport of x rays through partially ionized plasmas in local thermodynamic equilibrium, the transport equation is coupled to nonlinear diffusion equations for the electron and ion temperatures via the highly nonlinear Planck function. We investigated the suitability of traditional-solution approaches to transport on terascale architectures and also designed new scalable algorithms; in some cases, we investigated hybrid approaches that combined both.

During FY2000, we performed large-scale neutron-transport calculations with our Boltzmann 3-D code. The code utilizes a generic solver for time-dependent systems of differential/algebraic equations and employs multilevel methods for scalability. Our code is also capable of performing first-scatter solutions for problems with point sources, both constant and pulsed in time. Using a model of a target bay, we performed steady-state and time-dependent simulations (see Fig.). The purpose of these calculations was to simulate the flux of fusion neutrons discharged from the target chamber during an actual experiment. These preliminary computations (200 million unknowns) were carried out on 128 central processing units (CPUs) of the LLNL Compaq TeraCluster. For the steady-state problem, we assumed a constant neutron source at the center of the target sphere; for the time-dependent problem, we modeled a neutron pulse originating at the center of the sphere.

In FY2000, we also developed a parallel multigrid code that uses the method of first-order-system least squares (FOSLS) to solve a spherical-harmonics discretization of the multigroup transport equation. We found that simple spatial finite elements are adequate for solving nondiffusive problems. This class of problems includes the transport of x rays through partially ionized matter. As the theory predicts, the code scales with multigrid efficiency for nondiffusive problems, while not scaling as well for highly diffusive problems. The latter will be the focus of our future FOSLS research.

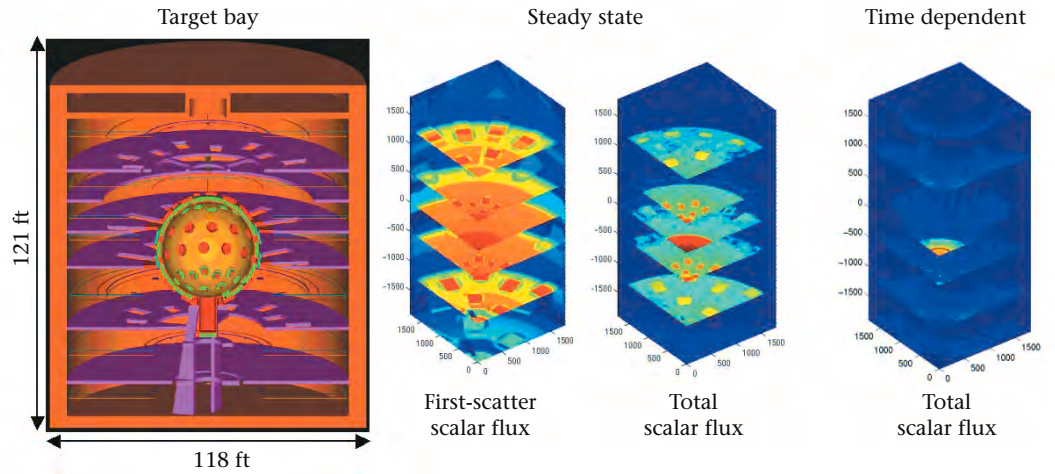

Using a model of a target chamber (left), which includes the surrounding floors and concrete bunker, large-scale neutron-transport calculations simulated the flux of fusion neutrons discharged from the chamber during an actual experiment. Scalar flux values are shown with logarithmic color scales.

Computational Theory of Warm, Condensed Matter

T. W. Barbee, III, M. P. Surh, L. X. Benedict

98-ERD-052

Laboratory missions such as the Stockpile Stewardship Program (SSP) demand accurate materials-modeling capabilities. Among these, calculations of the equation of state (EOS) and opacity play important roles. The SSP requires knowledge of these properties over an extreme range of densities and temperatures. In the low-density/high-temperature limit, models based on plasma physics are very accurate, whereas models based on condensed-matter physics perform best in the high-density/low-temperature regime. Current models for the EOS of warm, condensed matter are primarily based on theoretical models that are most accurate in the low-temperature limit and that treat the effect of finite temperature as a perturbation of the zero-temperature solution. These models are largely untested above the melting point, especially approaching the Fermi temperature T_{Fermi} —the characteristic energy scale for the interacting electrons in a material.

In this project, we focused on "warm" condensed matter—the region of intermediate temperature and density where the high-temperature or low-temperature approximations may no longer be valid. Our specific goal was to develop rigorous extensions of existing state-of-the-art condensed-matter techniques that are valid in this intermediate-temperature regime. Our approach emphasized three areas: (1) improving theoretical treatments of the thermal contributions to the EOS; (2) calculating optical properties (e.g., opacity) at finite temperature; and (3) developing a new theoretical formalism for solving the quantum-mechanical, many-electron problem at finite temperature.

In FY2000, we continued our extensive calculations for the shock Hugoniot of aluminum (Al) using the final-state pseudopotential scheme we had developed earlier. We discovered that the molecular-dynamics (MD) simulations at high temperatures could be performed with very small simulation cells, encompassing just four atoms, which is sufficient to describe the ion–ion pair correlation function out to the average nearest-neighbor separation. This minimal simulation cell permits calculations into the million-degree range. We used electronic wave functions from the MD simulations to calculate plausible dielectric functions for the optical properties of hot, dense Al and submitted our results for publication.

During FY2000, we also made significant progress in understanding the optical properties of warm, condensed matter. First, we computed the optical absorption spectrum of laser-pumped GaAs for a model in which excited electrons and holes occupy the extreme of conduction and valence bands (see Fig.). Comparisons with experimental results obtained by a group at Harvard University demonstrated that their earlier interpretation of the short pump-probe delay time results is largely correct. Such comparisons also shed light on ways to improve our theoretical approach. A paper discussing these issues has appeared in *Physical Review B*.

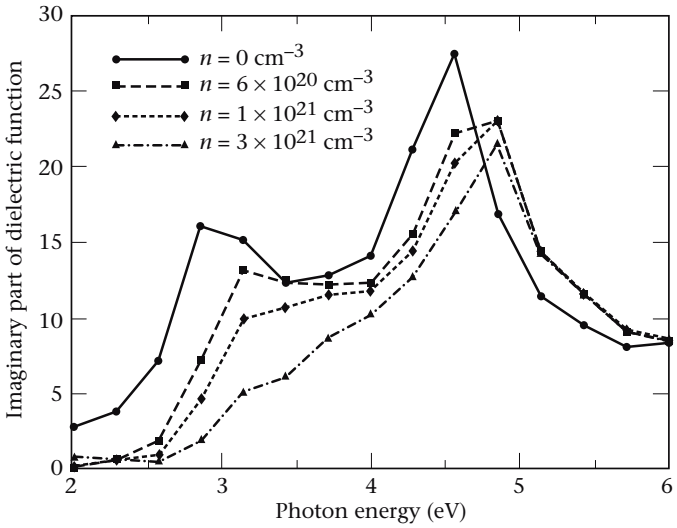

Imaginary part of dielectric constant $\varepsilon_2(\omega)$ vs. frequency ω for GaAs at different carrier concentrations n. At higher carrier concentrations (higher laser fluence), the peak at 2.5 eV is strongly screened.

Second, we computed the optical properties of solid-or-greater density Al for temperatures approaching T_{Fermi} using the output (one-electron wave functions and energies) from our high-temperature quantum MD code. These computations show that the resulting optical properties are quite far from results for electron gas because of electron–ion scattering, although the density of single-particle states looks very free-electron-like for the high-temperature fluid.

In addition, we investigated the extent to which the quasiparticle approximation is valid at these high temperatures by computing electron lifetimes and band-energy renormalization caused by the emission and absorption of plasmons. At the close of FY2000, we were using the electron lifetimes determined in this way to broaden the calculated absorption spectra and preparing to predict the results of Al thin-foil experiments being performed at LLNL.

LambdaConnect: Multiwavelength Technologies for Ultrascale Computing

S. W. Bond, M. D. Pocha, R. R. Patel, E. M. Behymer, G. A. Meyer, P. L. Stephan, G. A. Cooper

98-ERD-057

Ultrascale computing—the integration of large numbers of processors into a single, highly capable multiprocessor system—is of great interest for several national security missions. Scalability of these systems, with upwards of hundreds of central processing units (CPUs), is hampered by the communication bottlenecks imposed by latency, bandwidth, and congestion in electrical interconnection and switching networks. To alleviate these bottlenecks, we leveraged the recent emergence of low-cost byte-linear arrays of multimode optical fiber in ribbon-cable assemblies. We showed that the addition of multiple wavelengths over this byte-wide medium can enable source-routed optical switching, which greatly relieves communication congestion and improves bandwidth.

During the course of this project—dubbed LambdaConnect—we focused on implementing byte-wide, multiwavelength, multimode optical interconnects for ultrascale computers. We developed novel components, including transmitters capable of fast wavelength tuning and fixed-wavelength optical filters, all compatible with multimode fiber-ribbon cables. Our system uses an *N* by *N* optical star coupler (an optical mixer that makes a portion of all inputs available to all outputs) as a broadcast element, with the byte-wide, wavelength-selectable transmitters as inputs and with fixed-wavelength optical receivers as outputs. Switching is achieved by predetermining the output port through appropriate selection of the transmitter wavelength.

Previously demonstrated, four-wavelength optical transmitters, which used proximity coupling to large-core multimode fibers, required vertical-cavity, surface-emitting laser (VCSEL) die to be cleaved and aligned manually to ensure good coupling. During FY2000, we simplified this labor-intensive packaging process through the development of passive alignment techniques in which we used a silicon microbench and deep, silicon-trench etching processes common in microfabrication and microelectromechanical systems (MEMs). The precisely cleaved VCSEL devices are aligned to the fibers using mechanical stops and the ribbon-cable alignment pins.

During FY2000, we also investigated postgrowth, process-tunable VCSELs and filters. Selectively oxidized, monolithic, multiwavelength VCSELs were a crucial element for scaling our transmitter to higher wavelength counts. Monolithic, multiwavelength VCSELs were demonstrated with three individual wavelengths spaced 4- to 16-nm apart. We also investigated multicavity filters that use lateral oxidation to allow postgrowth tuning of a single epitaxial wafer.

In addition, we explored the scalability of our system for application in an Accelerated Strategic Computing Initiative-(ASCI-) scale machine, one designed for 100-Tflops computations. We investigated the strictly nonblocking, five-stage Clos switching architecture shown in the Fig. The interface to each stage of the network (the dashed vertical lines) uses an optical-to-electrical and electrical-to-optical conversion, allowing wavelength "re-use" of the coarse wavelength space of LambdaConnect, which is fundamental to allowing scaling of this low-cost optical switch. An advanced, fully functional LambdaConnect system—with fiber parallelism of 36 and with 19 wavelengths per fiber, each operating at 5 GB/s—functions as a fully nonblocking crossbar switch (no internal contention) with a potential bisection bandwidth of 10.2 TB/s. Although this is impressive, ASCI performance requirements for balanced computing (where the bisection bandwidth of the interconnect fabric scales linearly with the overall computing power of the machine) require 1 B of communication for every 10 flops, a bisection bandwidth of 80 TB/s for a 100-Tflops system.

Although we found the cost of an ASCI-scale solution using the Clos network prohibitive, the components and packaging techniques developed within this project are useful for smaller switching networks and for "fat-pipe" applications, where all wavelengths are used concurrently for byte-wide, high-bandwidth communication.

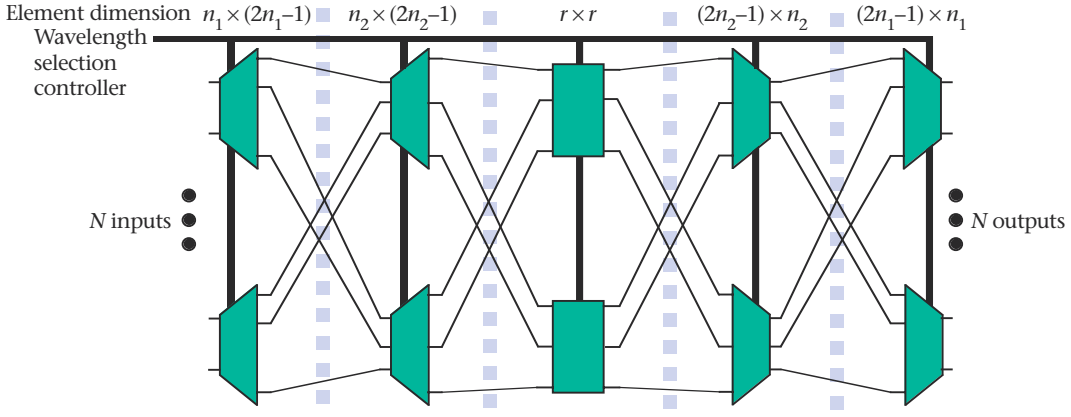

Five-stage Clos network investigated for a 100-Tflops Accelerated Strategic Computing Initiative (ASCI) machine with 500 symmetric multiprocessor (SMP) nodes. Key parameters are N = 500, n_1 = 10, n_2 = 5, and r = 10—where N is the total number of input nodes and output nodes to achieve N by N switching, n_1 and n_2 are inputs to individual switching stages, and r gives the dimensions of the innermost switch.

Coupling Atomistic to Continuum Mechanics Simulation with Application to Stress-Corrosion Cracking

A. A. Quong, T. Lenosky

98-ERD-087

In a variety of problems in materials science, processes that occur over atomistic distances—those measured in nanometers—generate processes and interactions over macroscopic distances. Two examples are cracks and dislocations in crystalline solids. Although good atomistic Hamiltonians are now available for computer simulation of atomistic systems, modern computers are limited in the number of atoms they can handle practically. Depending on the desired accuracy and the type of interatomic potential, only a few hundred to a few hundred million atoms can be treated using these computational methods.

Our goal in this project was to extend current atomistic simulation capabilities to mesoscale properties by (1) treating the core of the problem with an atomistic potential and then (2) using linear elasticity for long-range behavior. For cracks, large deformations and bond-breaking at the crack tip were treated atomistically; for dislocations, the core reconstruction was treated atomistically. The remainder of each problem was then treated as an elastic medium that was bonded firmly to the atomistic region.

In FY2000, we implemented the boundary-element method for orthotropic elasticity in two dimensions and an embedded atomistic region in the continuum elastic region. We located arbitrary loads and displacements on the outer boundary of a homogenous elastic medium (its elastic constants do not depend upon position). Our methodology for the elastic region used Green's function-based boundary-element method for treating the response of the elastic region given arbitrary tractions and displacements imposed upon its boundary. For an atomistic Hamiltonian, we used the silicon (Si) modified embedded atom method (MEAM) potential. In practice, any atomistic potential could have been used, including more accurate tight-binding or density functional theory approaches.

The geometry of the test case, a crack in Si, is shown in Fig. (a). The quasiatoms were embedded in the elastic medium and moved along with it as it was deformed. The forces and energy for the atoms were evaluated using the atomistic Hamiltonian by including atoms in all three regions. Thus, the quasiatoms served as a buffer region for the rest of the atoms. As long as the thickness of the quasiatom region was greater than the range of the potential, the quality of the matching was perfect.

As a demonstration of the method, we plotted the crack-opening displacement as a function of the applied load for several different systems. In all cases, the total dimensions of the system were the same, but the numbers of atoms in the atomistic region varied from 180 to 4380. As Fig. (b) shows, we obtained very similar behavior even for the smallest system. All systems showed a discontinuous jump in the displacement at a load of approximately 1.15, which was due to the movement of a single atom in the simulation region. It is remarkable that such a jump could be achieved with such small numbers of atoms—a demonstration of the power of the method when coupled with more accurate quantum-mechanical-based atomistic simulation techniques.

The project, completed in FY2000, demonstrated that, with the proper boundary conditions, small atomistic simulations can be used to study complicated problems like crack growth. This opens the possibility of studying such problems with quantum mechanical techniques.

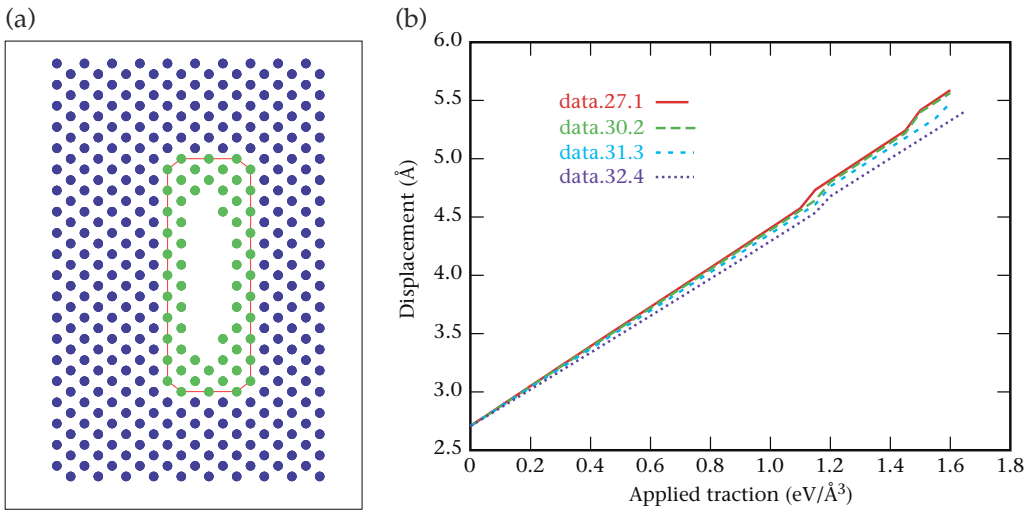

(a) Simulation cell with different regions: atomistic (green), boundary (red lines) and quasiatoms (blue); (b) Crack-opening displacement as a function of applied load.

Effects of Radiation on the Mechanical Properties and Structural Integrity of Nuclear Materials

T. Diaz de la Rubia, B. D. Wirth, M. J. Caturla

98-ERD-090

When deformed after irradiation with energetic particles, metals exhibit increased yield stress and often undergo plastic flow localization and significant degradation of their mechanical properties. The effect limits pressure vessel lifetime in most of the world's nuclear power plants, and threatens to severely limit the choice of materials for the development of fusion-based alternative energy sources. While these phenomena have been known for many years, an explanation of the underlying fundamental mechanisms and their relation to the irradiation field is lacking. We have developed a multiscale computer simulation that provides a physical description of the underlying mechanisms that govern plastic flow localization and mechanical failure in irradiated metals. New molecular dynamics (MD) simulations demonstrate the mechanism of absorption of radiation-induced vacancy, stacking fault tetrahedra (SFT) by moving-edge dislocations in copper (Cu).

The Fig. shows a comparison between an MD simulation of a moving-edge dislocation in Cu interacting with a vacancy SFT and an in situ transmission electron micrograph (taken by Ian Robertson at University of Illinois) of a dislocation in Cu interaction with a vacancy SFT induced by ion irradiation. The similarity and qualitative agreement between the simulation and the experiment is remarkable. Additional work is underway to further quantify this finding. Our 3-D dislocation dynamics (DD) simulation couples these atomistic simulations and experiments to a mesoscale description of mechanical behavior. The results show that flow localization results from a combination of dislocation pinning by irradiation-induced defect clusters, unpinning by unfaulting and absorption of the defect clusters, and cross slip of the dislocation as the stress is increased. Double cross slip results in dipole formation, which in a natural way self-limits the width of the channels. The plastic instability results in catastrophic mechanical failure.

(a) (b)

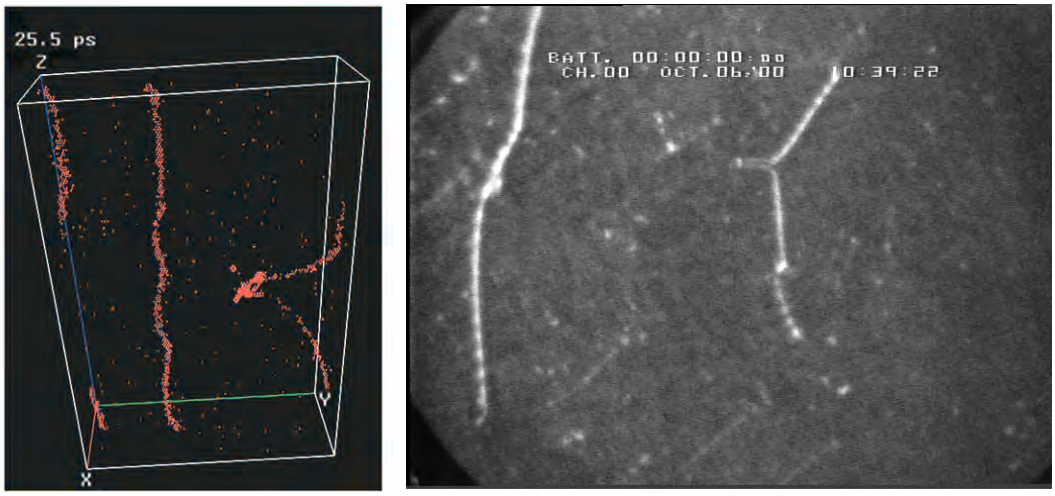

Comparison between (a) a molecular dynamics simulation and (b) an in situ transmission electron micrograph of a dislocation interacting with a defect in copper.

Strategic Initiative in Computational Biology

M. E. Colvin, F. Gygi, G. Galli, F. C. Lightstone, E.R. Schwegler, D. Barsky

98-SI-008

The biological sciences are undergoing a rapid transformation that promises to alter almost every aspect of human endeavor, from food production to health care. The sequencing of the full genomes of humans and many other organisms, in combination with a molecular-level understanding of biological phenomena, is increasing the role of predictive models in biological research. This transformation will be largely dependent on computer simulations to do everything from predicting macromolecular structure to designing new drug molecules. Because of its capabilities in advanced simulation and high-speed computing, LLNL is well positioned to play a major role in the emerging field of computational biology.

The goal of this project has been to develop new, state-of-the-art biological-modeling methods and to test them on problems in biology. This project has been very successful, as demonstrated by several dozen scientific papers, as well as numerous invited talks and fruitful collaborations. The simulation tools developed here have also proved valuable to emerging Laboratory programs in biological defense and advanced sensors.

One of our primary goals in this project has been to create methods for simulating the dynamics of biochemical processes using a quantum mechanical description of the molecular interactions. In FY2000, we applied such first-principles-molecular-dynamics simulations to investigate the flexibility of the DNA backbone in solution. This property is central to the formation of DNA protein complexes that mediate the replication, transcription, and packing of DNA. We simulated the simplest plausible model of the DNA backbone, dimethyl phosphate (DMP), in water along with a sodium counter ion, included to mimic actual biological conditions (see Fig.). From these simulations, we found that the structure of DMP is altered by the presence of the sodium ion, causing a redistribution of charge, which in turn leads to a sudden change in the DMP conformation. This result differs from earlier, nondynamical simulations and demonstrates the need for such computationally intensive methods to answer certain biological questions.

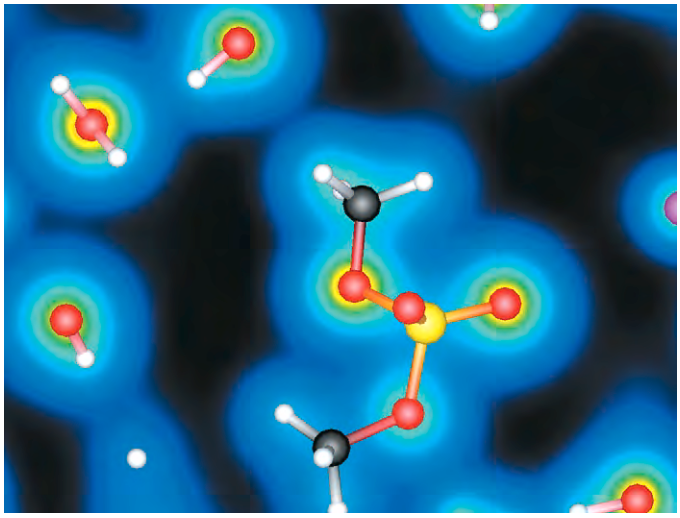

Plot of the electron density of dimethyl phosphate (molecular structure shown in center of image) in water as simulated by first-principles molecular dynamics. The atoms are shown as solid spheres with the surrounding electron clouds colored by density (yellow = highest density, dark blue = lowest).

A second major goal has been to develop a homology-based algorithm for predicting the folding of proteins based on known protein structures. This capability is essential for the structural characterization of the many new proteins discovered by genomic DNA sequencing. In FY2000, we applied these methods to making the novel prediction that a newly identified DNA clamp protein is formed as a trimer of three different proteins.

This year we also demonstrated the utility of a range of other chemical simulation methods in biological applications. We used large-scale, static, quantum-chemical simulations to demonstrate that accurate chemical properties could be calculated for biological molecules. We applied classical molecular dynamics to investigate (1) the structure of a basic DNA and the nuclease that binds this form of damaged DNA, and (2) the interactions of antifreeze proteins. We also applied computational docking methods to develop inhibitors of enzymes that control DNA repair and cell-cycle checkpointing.

Back to main TOC

Computational Modeling of Plasma Polymerization

C. K. Westbrook, A. Kubota

99-ERD-006

Plasma polymerization is a technologically important process in many different areas ranging from microelectronics to biotechnology and protective coatings. However, fundamental understanding of the interactions of energetic and reactive plasmas with bulk materials and surfaces is still lacking.

We have been studying the various aspects of plasma polymerization by developing the computational modeling tools necessary to understand this inherently multiscale process. Earlier work on this project focused on Monte Carlo simulations of growth under equilibrium conditions, together with molecular-dynamics simulations of hydrocarbon systems under conditions far from equilibrium.

During FY2000, we developed sophisticated bond-order potentials capable of modeling systems that incorporate carbon (C), hydrogen (H), and oxygen (O) atoms. These potentials were parameterized to a large body of thermochemical data for species involving the C/H/O elements, derived primarily from ab initio and density-functional-theory (DFT) thermochemical calculations. The ability of these potentials to reproduce most of the thermochemical data to within a few percentage points demonstrates the robustness of our bond-order formalism, and our potential capability to study many industrially and programmatically relevant applications.

During FY2000, we also investigated several such applications, including a problem in the area of microelectronics processing. In photolithography of electronic materials, a substrate is coated with a polymeric material, patterned, and finally exposed to reactive plasma to ultimately produce the microtopographical feature of the electronic devices. To obtain the final electronic product, the plasma etches away material that is not protected by the chemical resist material. With industrial progress requiring smaller and smaller devices, smaller-wavelength irradiation is needed for the patterning process. The resist material must have a number of qualities, including transparency to the radiation, sufficiently high glass-transition temperature, and erosion resistance to a variety of plasma conditions. However, the least understood and least controllable process in the selection of photoresist material is its erosion resistance. The C/H/O potentials described make it possible to study this erosion in photolithographic materials—particularly for the case of erosion produced using radiation at wavelengths, such as 193 nm, that are close to the current limit of experimental photolithography.

Our new modeling capabilities have also enabled us to study other classes of applications. In particular, we are using our ab initio thermochemical calculations to investigate highly oxygenated hydrocarbon compounds and their importance in the combustion of alternative fuels in diesel engines. In addition, we are using bond-order potentials for the silicon (Si)/O and Si/O/C systems to expand our understanding of the laser-absorption, damage-initiation, and damage-growth processes related to the silica optics that are important to laser applications. The Fig. illustrates an application in which a shock wave is moving through a silica matrix, changing the bonding pattern of the Si and O in a way that may help explain how local deposits of energy damage the material.

We successfully achieved our goal of developing new computational modeling capabilities and then applying them to an important problem in photolithography. Several journal papers are in preparation.

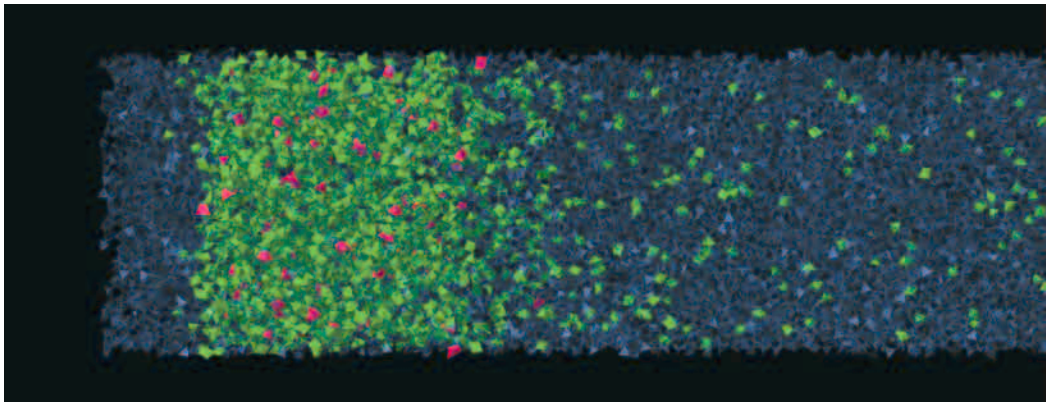

Shock wave in amorphous silica, showing the generation of different valence states in silicon (Si) caused by the shock wave. The high-density region shows fivefold (green) and sixfold (red) coordinated Si, and normal fourfold coordinated Si (violet).

Quantitative Tomography Simulations and Reconstruction Algorithms

H. E. Martz, M. B. Aufderheide, D. M. Goodman, A. Schach von Wittenau, C. M. Logan, J. M. Hall, J. Jackson, D. Slone

99-ERD-015

X-ray, neutron, and proton-transmission radiography and computed tomography (CT) are important diagnostic tools for nondestructive testing of complex structures. However, current radiographic accuracy does not allow satisfactory separation of experimental effects from the true features of an object's tomographically reconstructed image. This can lead to difficult and sometimes incorrect interpretation of the results. By improving our ability to simulate the whole radiographic and CT system, it would be possible to examine the contribution of system components to various experimental effects, with the goal of removing or reducing these effects.

In this project, we are merging the existing simulation capability with a maximum-likelihood (constrained-conjugate-gradient—CCG) reconstruction technique to yield a physics-based, forward-model, image-reconstruction code. In addition, we seek to improve the accuracy of CT from transmission radiographs by studying the x-ray, neutron, or proton physics required in the forward model to obtain the best recovery of the object under inspection.

During FY2000, we coupled an improved version of LLNL's ray-tracing code HADES with a recently developed LLNL CT algorithm known as CCG. The combined code is called HADES–CCG. The problem of image reconstruction is expressed as a large matrix equation in which a model for the object being reconstructed is related to its projections (radiographs)—the forward model. Using a CCG search algorithm, we search for a maximum-likelihood solution until the difference between the input—measured radiographs or projections—and the simulated or calculated projections is satisfactorily small.

The 2-D HADES–CCG CT code uses full ray-tracing simulations from HADES as the projector. Often, an object has axial symmetry, and it is desirable to reconstruct into a 2-D *r*–*z* mesh with a limited number of projections. The physics (e.g., source energy spectrum, scattering, and detector response) required in the HADES code is determined from Monte Carlo simulations. The current version of HADES–CCG reconstructs into a volume–density mesh made of one material and assumes a monochromatic source.

We used both 10-MeV neutrons and 9-MV x rays to image a British test object (BTO). A BTO consists of a set of nested carbon, tungsten, and polyethylene shells and is used for verifying tomographic algorithms. The neutron and x-ray radiographs (Fig. (a,c)] of the BTO show some of the joint and different material details. However, it is difficult to use the radiographic projection data to obtain detailed quantitative measurements of the joint thickness, material boundaries, etc. To extract more details from the BTO radiographs, we used a single radiographic projection and the current HADES–CCG code to obtain 2-D CT cross sections of the BTO [Fig. (b,d)]. If the x-ray and neutron CT reconstructions in Fig. (b,d) are compared, it is apparent that spatial resolution is superior in the x-ray image. This is expected and is largely because of the unsharpness of the neutron source.

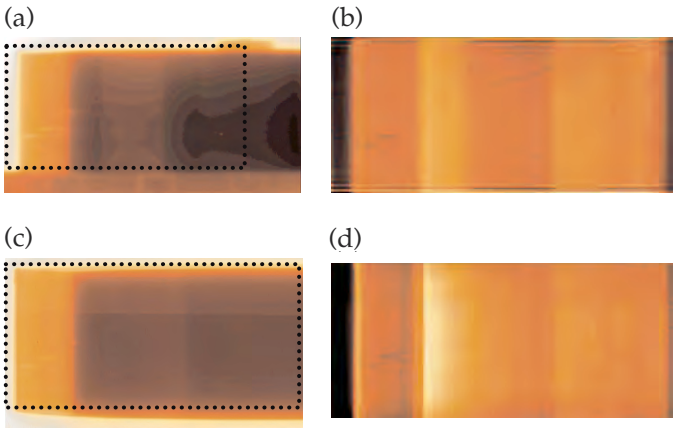

Radiation images of a British test object (BTO), showing (a) a 10-MeV neutron radiograph, (b) a 2-D computed tomography (CT) image, (c) a 9-MV x-ray radiograph, and (d) a 2-D CT image. Each reconstruction—(b) and (d)—used the single radiograph to its left. The dotted lines enclose the portion of each radiograph that was used to obtain the CT image. The CT images reveal more internal details than the radiographs; the neutron CT has more internal details, whereas the x-ray data do not image beyond the first few layers.

Our current implementation of HADES–CCG has shown interesting potential, but more work is needed to make a fully viable reconstruction code. In FY2001, we will (1) study the treatment of multiple materials and polychromatic sources in a reconstruction; and (2) expand the HADES–CCG code to include 3-D reconstructions, thereby broadening its applicability.

Lattice Boltzmann Simulation of Microfluidic Devices

D. S. Clague, E. K. Wheeler, D. Hilken

99-ERD-016

The design and manufacturing of microfluidics and biological microfabrication and microelectromechanical (Bio-MEMS) devices at LLNL have application to a number of important programs of national interest. For example, biomedical and biotechnology applications include subsystems designed for preparing miniaturized samples and for detecting target species. However, before such devices can achieve desired functionality and ultimately lead to potentially new technologies, many challenging scientific issues must be addressed.

(a)

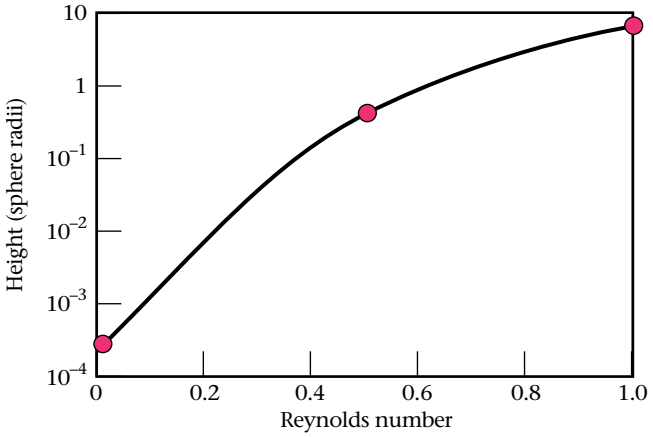

(b)

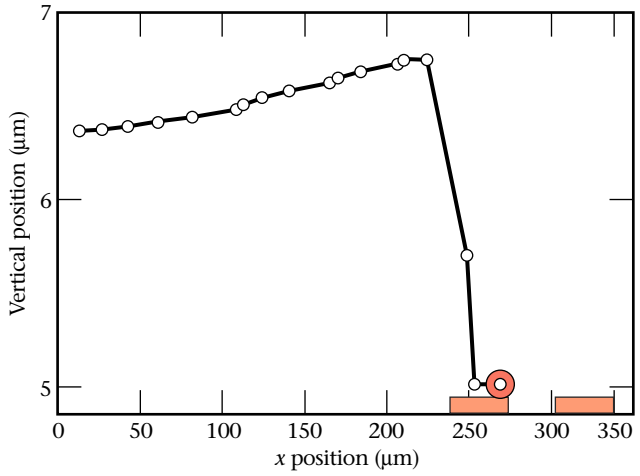

Results of our investigation into coupling hydrodynamic and dielectrophoretic (DEP) forces: (a) inertial lift as function of Reynolds number, and (b) coupled inertial lift and DEP capture, where the rectangles and the sphere represent an electrode array and a target species, respectively.

Our project focuses on developing simulation tools to address these fundamental scientific issues to augment and guide device designs. Specifically, we are developing lattice Boltzmann (LB) simulation capabilities to study the transport properties of particulate species in microflows. At micrometer-length scales, forces that act on short-length scales become important. As a result, we are developing simulation capabilities to study coupled physical effects.

During FY2000, we focused on the coupling between hydrodynamic and dielectrophoretic (DEP) forces. We (1) performed LB simulations to explore inertial lift effects as a function of the effects Reynolds number, and (2) coupled inertial effects with DEP forces for systems with length scales of actual interest.

Figure (a) shows the extent of lift as a function of Reynolds number; Figure (b) shows a dielectrophoretic capture. In Fig. (a), the lift height is made dimensionless with the sphere radius, and the Reynolds number is based on the maximum fluid velocity. According to Saffman's theory (1964), the lift force is proportional to the magnitude of gradient in the velocity profile of the fluid. As the Reynolds number increases, the gradient in the fluid velocity steepens, and the theory predicts an increase in the lift force. Typical Reynolds numbers range from much less than 1 to about 5 in microfluidic systems. As expected, our LB simulations capture the weak inertial forces and predict an increase in lift with an increase in the Reynolds number.

As depicted in Fig. (b), we built a time-averaged electric field into the LB capability to study coupled hydrodynamic and DEP forces on suspended species. As Fig. (b) shows, the sphere initially experiences inertial lift forces; however, when it encounters the electrode array, it is pulled to the electrode surface and captured. Often, device designers want to position target species in the central region of microchannels for detection purposes. Our results in this project now enable the rapid prediction of optimal flow rates for either suppressing or using inertial lift effects to cause the desired repositioning of the particles.

In FY2001, we will (1) continue investigating the forces influencing DEP manipulation in flow conditions that are relevant to LLNL's device designers, and (2) explore the inclusion of representative particle geometries in the LB capability. In particular, we will extend our ability to study the transport behavior of macromolecules using ellipsoidal and bead-and-spring models, which are representative of proteins and long-chain polymers (e.g., DNA fragments), respectively.

Improved Implicit Finite-Element Dynamics

M. A. Puso, E. Zywicz

99-ERD-018

Implicit finite-element methods have been primarily applied to linear dynamics and to problems in mildly nonlinear, static structural mechanics. Explicit finite-element codes, however, have typically been used for highly nonlinear dynamics problems. Numerical difficulties encountered with implicit analysis have forced the use of explicit rather than implicit finite-element codes for many problems. This is unfortunate because implicit methods promise better accuracy for nonlinear statics and for long-time, nonlinear dynamics problems such as those encountered in analyses of seismic events, reentry vehicles, and transportation-container vibrations.

The goal of this project was to develop implicit, finite-element algorithms that solve the aforementioned problems reliably by attacking the two main obstacles inherent to the implicit method: (1) for nonlinear problems, the classical implicit-integration schemes are numerically unstable; and (2) convergence of the implicit, nonlinear-solution algorithm is severely affected by unilateral constraints on contact surfaces.

During FY2000, we developed time-integration schemes that are unconditionally stable for the general setting of coupled (flexible) finite-element and rigid-body analysis. For example, we used a random input to excite a vibration in the transportation container shown in Fig. (a); Fig. (b) compares the simulated kinetic energy using the old method with that using our new method. Gaps between the foam and cylinder walls cause contact-impact during the motion. With the classical trapezoidal simulation, this contact nonlinearity causes the energy to grow; however, with our new method the energy is controlled. Our work is the first for the general 3-D multibody implicit-dynamics setting and has been the subject of three journal publications.

Contact surfaces are used to interface disjoint objects that impact during analysis. This contact interaction is highly nonlinear and is the major cause of convergence problems. In particular, the non-smooth contact surface causes jumps in contact forces at facet edges and vertices when objects slide past each other. To eliminate this problem, 3-D Gregory patches were used to smoothly interpolate the bilinear surface mesh so that objects now slide smoothly past each other. The major technical hurdle overcome in FY2000 was the ability to smooth arbitrary, irregular meshes such as that in Fig. (c). Smoothing allows the solution to many problems that would have diverged in the past and is the topic of a recently submitted journal publication.

In summary, we have developed state-of-the art algorithms that are more robust, accurate, and efficient than those previously available. Consequently, we can now better handle long-term dynamics and highly nonlinear statics problems using the implicit method.

(a)

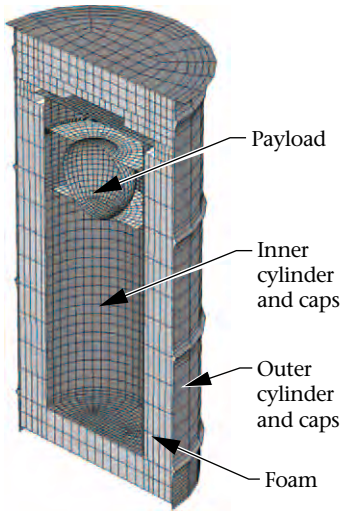

(b)

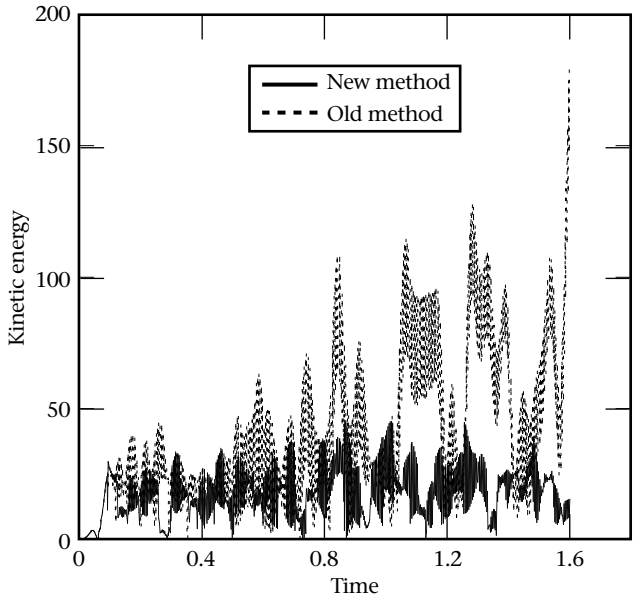

(c)

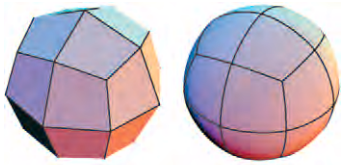

Application of our new method for stable implicit analysis, showing (a) a typical transportation container, and (b) the kinetic energy resulting from a random input as simulated by the old (unstable) method and our new (stable) method. In (c), we compare a conventional finite-element sphere with our smoothed sphere.

Updating Finite-Element Models Using the Extended Kalman Filter

R. R. Leach, Jr., L. Ng, D. B. McCallen

99-ERD-057

The motivation for this project is to provide a method to update finite element models (FEM) of large structures based on recording structural motions with an array of motion sensors such as accelerometers. Previous attempts to quantify computational structural models using Kalman filtering were poor, due to the exclusion of critical second-order terms in the calculations. Inclusion of these terms yielded extremely accurate stiffness, displacement, and velocity estimates for most of the sensor-placement scenarios in a five-story building with a simple 10-degrees-of-freedom (DOF) model. The primary goal of this project is to develop and apply state-space-based signal processing techniques to locate the existence and type of model mismatches common in FEM by using an extended Kalman Filter (EKF).

A simple, 10-DOF FEM of a five-story building is shown in Fig. (a). Each floor is represented as a node with mass, M; the nodes are connected by single-column elements of stiffness, *K*, and damping, C. The stiffness elements, *K*, are estimated by the Kalman filter; the mass and damping values are considered constant. Measurement occurs at the nodes, while the stiffnesses of the columns are the quantities to be identified.

A force was applied to Node M1 consisting of Gaussian noise (0 to 50 Hz). Initial stiffness parameters were set to 7/8, 3/4, 9/10, 1/3, and 1/2 of *K*, representing a perturbed or "damaged" structure. In the first experiment, the model was fully measured and the stiffness identification errors were essentially zero. Other experiments (27 total) were then completed with various number of sensors and their locations.

Results are shown in Fig. (b). Each column of five boxes represents one experiment. The numbers inside the boxes indicate the error for that node or floor. The number at the top of the boxes corresponds to the average error for all five floors.

In almost all but those experiments with two or more measurement points, the Kalman filter converged very near to the correct stiffness. This is particularly promising in that estimates in many cases converged to the correct value even with floors having poorly modeled stiffness parameters (such as the fourth one). The largest error tended to occur when the uppermost floors (furthest from the vibration source) were unmeasured. The Kalman filter state-space-based parameter-identification method works relatively well in this simple 10-DOF identification problem, does not require excessive computational time, and performs consistently for situations where only partial measurement of the system is available.

Our results indicate that the EKF method can be used to (1) update FEMs, (2) identify optimum placement and density of sensors, and (3) detect damage in previously tested structures. Having completed the project, we can begin practical application of the technique to conducting experiments on a shaker table with a fixed, aluminum tower for controlled testing. The work also can be extended to high-DOF (≥400 DOF) simulated systems.

(a)

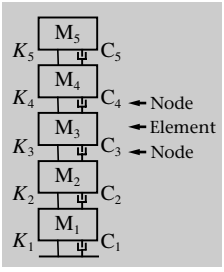

(b)

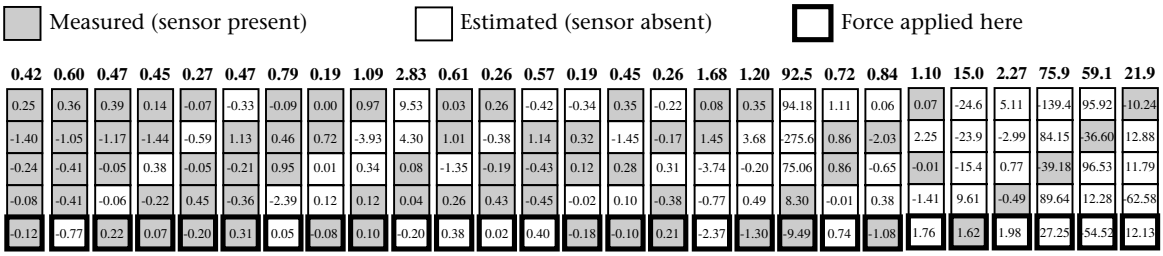

(a) A 10-degrees-of freedom (DOF) finite element model (FEM) of a five-story building. (b) Mean identification error (bold) using extended Kalman filter (EKF) with Gaussian noise input for 27 sensor-placement scenarios.

Back to main TOC

Model Development for the Interaction of Ultrahigh-Intensity Lasers with Matter

A. B. Langdon

99-ERD-063

Recent experiments and modeling of laser-target physics at ultrahigh-intensity (>10^{20} W/cm^2) have enabled advances in the basic understanding and predictive capability of laser–plasma interaction in this unprecedented regime of intensity. The goal of this project is to accurately model laser–target interaction and the associated physical phenomena. This will enable LLNL to exploit ultrahigh-intensity lasers in novel ion sources and in opacity and equation-of-state studies.

Design and interpretation of ongoing experiments and advancement of code modeling capabilities are the two components of our project. In modeling development, we obtained preliminary results from two new 3-D massively parallel plasma codes, z3 and pF3d, that would replace the serial codes we previously used. We made the first physics applications with the z3 particle-in-cell (PIC) code. This code builds on our experience in PIC algorithms with the 2-D serial Zohar code used in other LDRD applications. The pF3d code provides an intermediate level of description between the PIC and radiation hydrodynamic codes such as LLNL's LASNEX. We made extensions to the pF3d code to model relativistic and charge-separation effects that occur at petawatt intensities. We also made proof-of-principle runs with the extended pF3d, which is the only code capable of modeling the entire Petawatt beam, including a realistic description of the laser beam and its aberrations.

The project resulted in several published papers in refereed journals, which document the experimental and theoretical understanding of a very intense collimated proton source discovered in FY1999. A patent application is pending. This LDRD project lays a foundation for future applications of this novel source.

Furthermore, the project (along with project 98-ERD-079) generated much favorable visibility for LLNL. These two projects were recognized by two invited papers that were presented at the American Physical Society Division of Plasma Physics and published in prominent refereed publications, and a *Physical Review Letter* that was written with a student as lead author. Moreover, these projects led to a Department of Energy Office of Fusion Energy Sciences grant in FY2000.

Back to main TOC

SAVAnTS: Scalable Algorithms for Visualization and Analysis of Terascale Science

M. A. Duchaineau

99-ERI-009

During a given run, multiphysics simulation codes on LLNL's supercomputers produce dozens of terabytes of data that form a vital component of the Stockpile Stewardship Program and other programs. Great strides are being made to increase the efficiency and accuracy of the codes by harnessing thousands to tens of thousands of processors using scalable algorithms. However, the efficient and accurate post-computation data handling and interactive exploration must also scale efficiently to reach LLNL's goal of a capability for productive, terascale simulation.

Our goal is to offer multiresolution data-selection and compression algorithms coupled with optimal data access during interaction to provide thousandfold increases in interactive performance and hundredfold more efficient storage than current best practice. These output-sensitive algorithms make it possible to store and compute exactly the amount of information needed by the scientist who is using the results of a simulation.

Our focus is on devising (1) new wavelet transforms, and (2) other hierarchies for compression and for the accelerated access and display of volumetric field data and boundary or contour surfaces. We have found that the useful information content of a 3-D field such as pressure or density tends to be quite sparse. Because wavelets automatically find and exploit coherence in both space/time and frequency/scale, this sparse information content is readily compressed after the application of an appropriate wavelet transform.

Wavelets are well understood for regularly spaced grids filling a complete volume of space. However, the innovations required for large-scale applications at LLNL include the extension to (1) highly adaptive or unstructured settings, and (2) arbitrary surfaces that typically cannot be represented as anything resembling a regularly spaced grid. Fundamentally, the work performed should be proportionate to the sparse, post-transform information content at as many stages as possible of the end-to-end data flow going from simulation to scientist. This requirement leads to a suite of connected optimization problems that we are addressing.

During FY2000, we devised a new type of wavelet for general surfaces that is the first to have bicubic precision while allowing sparse, local transforms using small filters at all steps in the transform. Thus, our methods offer the first practical, high-precision wavelets that can be used to store the surfaces arising in large-scale simulations. To support the wavelet transform, we devised new conversion procedures that automatically shrink wrap to a semiregular form the arbitrarily-shaped geometry that contains any number of topological handles and connected components.

For example, the Fig. shows 0.3% of the total surface from a record-breaking simulation of a Richtmyer–Meshkov instability forming in a shock-tube experiment. (For this work, two members of our team were co-recipients of several awards, including the Gordon Bell Prize in the Performance Category at the IEEE SuperComputing conference in November 1999.) Our experiments indicate that the combination of our shrink-wrap and wavelet compression will reduce the storage size of this 460-million-triangle surface from 13 GB of disk space to under 260 MB—a fiftyfold space reduction. This new approach is at least ten times faster than unstructured surface-mesh compression schemes and previous wavelet surface-compression methods based on infinite-width filters.

In FY2001, we plan to (1) increase performance on per-view surface optimization time by two or more orders of magnitude using pre-optimization on subregions, and (2) complete a working prototype of our wavelet surface-compression method.

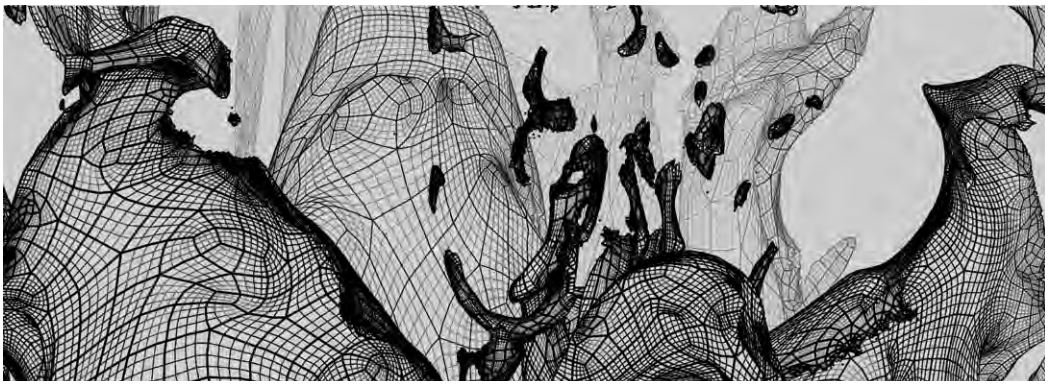

Shrink wrap of 0.3% of the mixing-layer boundary of an eight-billion-cell, turbulent-mixing simulation. Experiments show that combining shrink-wrap and wavelet compression will reduce disk storage size by a factor of 50.

Back to main TOC

Sapphire: Scalable Pattern Recognition for Large-Scale Scientific Data Mining

C. Kamath, E. Cantu-Paz, I. Fodor, N. Tang

99-ERI-010

Because of the rapidly widening gap between our ability to collect data and our ability to explore, analyze, and understand the data, useful information is overlooked, and the potential benefits of increased computational and data-gathering capabilities are only partially realized. This problem of data overload is becoming a serious impediment to scientific advancement in areas as diverse as counterproliferation, the Accelerated Strategic Computing Initiative (ASCI), astrophysics, computer security, and climatic modeling—all areas where vast amounts of data are collected through observations or simulations. Data mining—the semi-automated discovery of patterns, associations, anomalies, and statistically significant structures in data—is being developed to improve how scientists extract useful information from their data. Data mining consists of two steps: (1) data preprocessing: high-level features are extracted from the data; and (2) pattern recognition: the features are used to identify and characterize patterns in the data.

In this project, we are developing a new generation of tools and techniques for the pattern-recognition task of data mining. Specifically, we are developing scalable algorithms with the goal of improving the performance of these algorithms without sacrificing accuracy. We are demonstrating these techniques by applying them to the detection of radio-emitting galaxies with a bent-double morphology in the Faint Image of the Radio Sky at Twenty Centimeters (FIRST) survey.

In FY2000, we focused on three tasks: (1) improving the performance of decision-tree algorithms, (3) identifying bent-double galaxies in the FIRST survey, and (c) incorporating our research into software to make it easily accessible to LLNL scientists. For decision trees, we considered oblique trees, where a decision at a node uses a linear combination of the features instead of a single feature. As this is essentially a search in a high-dimensional space, we investigated the use of evolutionary algorithms to solve the optimization problem. Our research showed that combining evolutionary algorithms with decision trees resulted in better and faster classifiers. On a data set with 50 features or dimensions, one of our new algorithms, Oblique-ES (where ES means the algorithm uses evolutionary strategy), was more accurate (79% vs. 73%) and four times faster than the current best oblique classifier. Another algorithm, Oblique-GA (where the algorithm is based on genetic algorithms), gave the most accurate results (85%), and was twice as fast. In contrast, the traditional axis-parallel tree, while fast, resulted in accuracy (58%) that was just a bit better than making a random decision.

For the bent-double problem, we focused on galaxies composed of three blobs. Using features from the FIRST catalog, we completed six inner iterations of data mining, improving the features extracted with each iteration. We completed two outer iterations, in which we increased the size of the training set from 195 to 495 examples. In the process, we reduced the classification error by 50%.

In FY2000, we released the alpha version of our software—which includes serial, object-oriented versions of decision trees; wavelets and wavelet-de-noising techniques; evolutionary algorithms; and support for a parallel infrastructure. In addition, we published twelve papers, made presentations at eight conferences and workshops, and filed three records of inventions. We also co-organized two data-mining workshops and actively participated in university collaborations.

During FY2001, we will (1) complete our work on parallel, scalable decision-tree algorithms and software; (2) complete the detection of bent-double galaxies using the techniques developed during FY2000; and (3) focus on the use of evolutionary algorithms to improve the performance of neural-network algorithms for classification.

Back to main TOC

Modeling and Simulation for Critical Infrastructure Protection

D. E. Sackett

99-SI-005

With the rapid growth of global computing and communications, information assurance is crucial to our national security and to security at Department of Energy facilities. Addressing this important issue requires the ability to predict, recognize, and react in real time to potential intrusions. This requirement in turn gives rise to a number of complex technical challenges, including automated characterization of computer networks, network modeling, analysis of network structure, identification of vulnerabilities, simulation of network behaviors, and assessment of the consequences of intrusions.

In this project, we are developing an integrated suite of simulation engines, computer visualization tools, analysis techniques, and assessment methods for understanding and evaluating issues pertinent to information security.

During FY2000, through our Open LabNet Mapping effort, we collected a great deal of information about LLNL's unclassified network and how it interacts with the Internet. For example: (1) within a two-week period of monitoring the network traffic going in and out of LLNL, we could identify almost all the 12,300 hosts that regularly communicate externally; and (2) within a one-week period, we could identify over 80% of these 12,300 hosts. We also found that about 2,500 hosts on Open LabNet do not normally communicate outside the Lab but do respond to a probe from outside. The network analysis tools that we have developed demonstrated how LLNL's network configuration was changed and significantly improved in mid-FY2000.

We also developed a risk-assessment technique supported by an analytical tool that we applied to a case study of a medium-sized organization with many of the characteristics of LLNL. Using a risk-benefit analysis, we determined an appropriate level of computer security for our example organization.

During FY2000, we also developed a prototype, rule-based expert system (called Oklahoma) with which we assessed vulnerabilities in a set of sample computer networks that we obtained from actual local-area networks (LANs) at LLNL. We derived the vulnerability knowledge base from LLNL's Nevada Vulnerability DataBase.

However, the fundamental difficulty with using rule-based, expert-system techniques such as Oklahoma to perform reasoning about the existence and exploitation of vulnerabilities is that the details that are known about a large, complex network may not be sufficient to support conventional artificial intelligence techniques. Thus, any vulnerability assessment of a possible scenario requires that some details be assumed. However, making assumptions degrades the quality of an assessment.

The central thrust of this aspect of our research is establishing an innovative approach to making the appropriate assumptions so that we can make an assessment, while simultaneously keeping the attendant degradation of the assessment to a minimum and maintaining a record of those assumptions. We are focusing on a state-space approach wherein the state-transition operators ASSERT and ASSUME have been defined. ASSERT is an operator that states conclusions from known facts, and ASSUME is an operator that states assumptions that enable further conclusions.

By the close of FY2000, we had begun adding active-discovery techniques to our tools. These techniques will enable us to generate the more detailed network database that is required for vulnerability assessment and for various other applications such as intrusion detection and prevention.

In FY2001, we plan to (1) complete a prototype capability to demonstrate the usefulness of integrating active-discovery techniques into our toolset and (2) generate an approach to extending the vulnerability-characterization activity to larger, more complex networks.

Coupled Ab Initio Molecular Dynamics and Poisson-Boltzmann Solvation Model

F. Gygi, J.-L. Fattebert

00-ERD-007

First-principles molecular dynamics (FPMD) is an atomistic simulation method that couples a quantum mechanical description of electrons with a classical description of nuclei. Over the past decade, this method has reached a level of accuracy that makes it a promising simulation tool for biological applications. The progress made in Density Functional Theory is mostly responsible for this advance, through the development of density functionals that provide an accurate description of hydrogen bonds, which play a key role in many biochemical processes. These advances combined with the availability of large-scale computers at the Laboratory have open the way to first-principles simulations of biomolecules in solution.

Direct molecular dynamics simulations of biomolecules in solution using explicit solvent molecules are extremely time-consuming, even on large supercomputers. This has motivated research in the area of continuum solvation models, in which the water molecules surrounding a solute are replaced by a dielectric medium having the same polarizability as water. Such models, if successfully coupled to FPMD algorithms, could extend considerably the scale of FPMD simulations of biomolecules.

Our goal is to investigate and implement a new approach to the simulation of solvated molecules by coupling a Poisson-Boltzmann solvation model to the FPMD method. We plan to apply this method to the study of simple biochemical process involving receptor-ligand binding.

During FY2000, we have focused on the development of a robust and efficient Poisson-Boltzmann solver that can be coupled to existing FPMD simulation codes. We have also developed a simple continuous dielectric model to simulate the solvation effects of molecules in solution. The model, based on a Poisson-Boltzmann equation with a smooth dielectric function, is integrated in the Density Functional formulation of the electronic structure calculation. The model has been designed to simplify the calculation of accurate ionic forces needed for molecular dynamics. In particular, no explicit dependence on ionic positions appears in the definition of the dielectric function.

Several finite difference discretization schemes have been tested for the Poisson-Boltzmann equation to find the optimal accuracy compatible with current ab initio molecular dynamics simulations. An object-oriented multigrid Poisson solver has been developed for an efficient iterative solution. Its coupling with a real-space ab initio molecular dynamics code has already allowed us to run tests on small molecular systems (see Fig.). The results of these tests will be used to define the optimal parameters used in the solvation model, in particular the thickness of the transition region between the cavity containing the molecule and the dielectric medium, as well as the size and shape of the cavity surrounding the molecule.

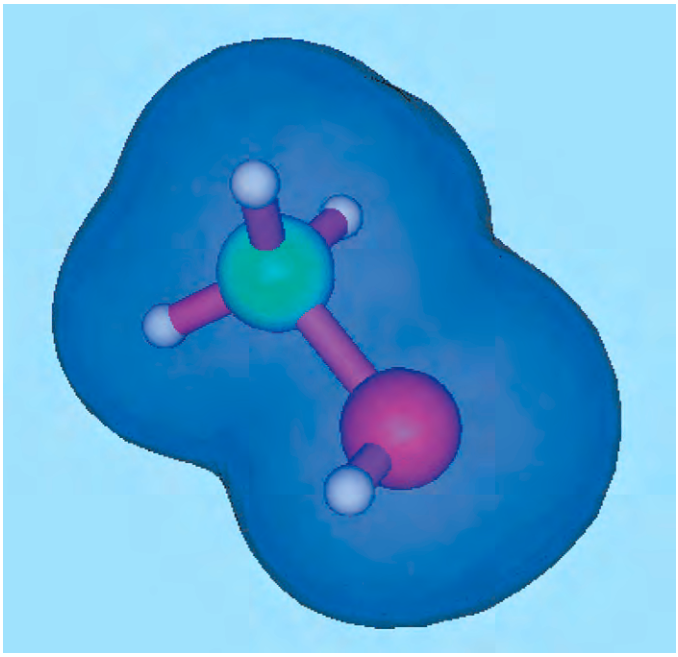

Illustration of a dielectric cavity around a methanol molecule in solution. The cavity is defined by a surface of constant electronic density.

In FY2001, we plan to develop a parallel implementation of the multigrid Poisson-Boltzmann solver. We will investigate the accuracy of our solvation model on larger molecules for which strong solvation effects can be observed. The Poisson-Boltzmann solver will also be coupled to the JEEP first-principles molecular dynamics code.

Negating Chemical Agents in Theater Missile Defense

G. N. Nakafuji, C. K. Westbrook, P. S. Fiske, T. Theofanous, R. M. Greenman

00-ERD-014

The need for theater missile-defense systems was illustrated graphically during the Persian Gulf War when Iraq launched SCUD missiles against Israeli and U.S. forces in Kuwait. The threat of future use of ballistic missiles carrying nuclear, biological, or chemical (NBC) payloads has driven the development of new theater missile-defense systems. These new systems, which intercept ballistic targets at altitudes in excess of 30 km, are designed to protect military ground forces from tactical ballistic missiles carrying NBC payloads. Military personnel in combat areas are typically provided some level of training and equipment to deal with possible ground deposition of a biological or chemical agent after a successful missile intercept. However, the protection of civilians from the same post-intercept effects is not guaranteed if lethal amounts of an agent reach the ground.

Key pieces of knowledge required for understanding the post-intercept agent survival and fallout are needed to augment the current technical knowledge base in the theater-defense community. For example, the extreme conditions that a dispersed drop will experience during reentry lie in a flow regime in which no experimental data exist. This knowledge is vital for assessing the effectiveness of various high-altitude missile-defense systems.

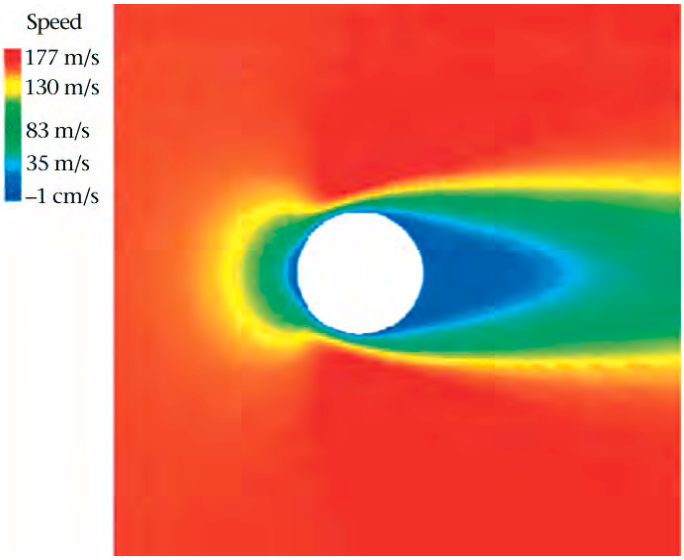

Contours of axial velocity show the wake for a 2-mm-diameter rigid sphere at a Mach number of M = 0.5 in a rarefied air stream.

Our goals in this project are to characterize and evaluate the threat of lethal chemical-agent fallout by scientifically addressing the hydrodynamic breakup and chemical evolution of a chemical agent following a successful missile intercept at high altitude (>30 km).

For this purpose, we are using unique hydrodynamic and shock-physics experiments coupled with advanced chemical-kinetic and hydrodynamic computer codes to directly simulate the supersonic, rarefied flow environments that reentering droplets of a chemical agent will experience. Specifically, we are characterizing the post-intercept fate of a chemical agent by (1) determining the range of stable droplet sizes of a surviving agent during reentry into the troposphere; and (2) modeling the reaction chemistry of the agent for pyrolysis, hydrolysis, and oxidation to estimate the mass of the surviving agent during intercept and reentry. In parallel to the droplet-breakup work, we are developing chemical-kinetics models for specific chemical agents and their simulants.

During FY2000, we constructed a large vertical-wind-tunnel facility—instrumented with fast framing cameras and laser photography—that achieves the supersonic, rarefied conditions required for characterizing droplet breakup. The facility has achieved operating conditions in the 5-Torr (~667-Pa) pressure range with Mach 3 flow conditions. We validated the ALE3D code for predicting the drag on rigid spheres in subsonic and supersonic rarefied flows (see Fig.). We also validated a new surface-tension model in the ALE3D code; at the close of FY2000 we were testing a deformable-drop simulation in representative test conditions.

In FY2001, we plan to (1) further develop our chemical-kinetics modeling capability for organophosphorous agents and simulants and (2) continue using both the vertical wind tunnel and LLNL's light gas gun to obtain the critical hydrodynamic and chemical data needed for model validation. Validated chemical-kinetics models will then allow us to estimate the negated fraction of an agent resulting from both missile intercept and subsequent atmospheric dispersal.

Back to main TOC

Adaptive Methods for Simulating Laser–Plasma Interaction

M. R. Dorr, F. X. Garaizar

00-ERD-016

The ability to model, predict, and control the interaction of intense laser light with plasmas is important in the design of large-scale, laser-driven fusion experiments. Of particular interest are phenomena such as filamentation and parametric instabilities, which can significantly affect the transport of laser energy to the target capsule. A major challenge in modeling these interactions is the need to accommodate a wide range of scales. The numerical propagation of laser light in a plasma typically requires wavelength-scale resolution, whereas the diameter of a single laser beam might span 2000 wavelengths. Moreover, we often want to model a region of plasma that extends outside the beam and does not require such high resolution. Present-day simulators, based solely on uniform grids, must use the same fine gridding everywhere. Such inefficiency ultimately limits the size of the simulations that can be performed and the number of simulations that can be completed in a given time period.

The goal of our project is to investigate the use of parallel adaptive-mesh refinement (AMR) as a means of spanning these diverse scales in the simulation of laser–plasma interaction. We are developing a research code called Adaptive Laser Plasma Simulator (ALPS), which employs parallel AMR to solve a coupled system of equations that models laser–plasma filamentation. ALPS simulates problems in two or three spatial dimensions and runs on any platform that supports the message-passing interface (MPI) standard, including the Compaq symmetric multiprocessor (SMP) clusters and the Accelerated Strategic Computing Initiative (ASCI) Blue Pacific machine at LLNL. The mathematical model solved by ALPS consists of a fluid approximation of the plasma combined with paraxial models of the light propagation. The mesh-refinement strategy is block-structured, and involves the synchronized integration of the plasma and light equations on a hierarchy of refinement levels.

In FY2000, we used the Structured Adaptive-Mesh Refinement Applications Infrastructure (SAMRAI) system, being developed at LLNL, to obtain an object-oriented, parallel implementation of the ALPS algorithm. The Fig. shows a 2-D example of an ALPS calculation. Here, a beam of light emerging from a random phase plate illuminates a 500-wavelength-wide spot on the left-hand boundary of the 2,000-wavelength-square computational domain. The domain contains initially quiescent plasma modeled on a coarse, 256 × 256-cell grid. Using AMR, we dynamically introduced a locally refined mesh where the light intensity exceeded a prescribed threshold. In the Fig., each of the fine grid patches (indicated by the yellow boxes) is refined by a factor of 8 in each coordinate direction relative to the underlying coarse grid. When we compared our results with a calculation performed using a fine uniform mesh over the entire domain, we observed a factor of 3 savings in execution time and memory requirements. This is consistent with the fact that the refined region occupies only about one-third of the computational domain. We obtained larger adaptive speedups for analogous 3-D problems, where the ratio of the refined grid volume to the volume of the entire domain was higher.

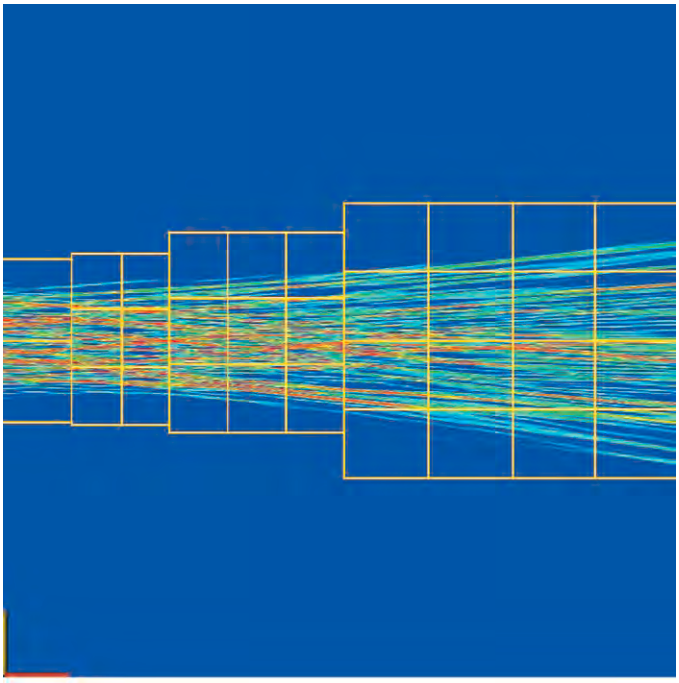

Adaptive-mesh calculation of light intensity resulting from the propagation in a plasma of a laser beam smoothed by a random-phase plate. The color map indicates the range of intensity level from highest (red) to lowest (blue).

In FY2001, we will continue to investigate the development of practical mesh-refinement criteria, as well as apply ALPS to larger laser–plasma interaction problems.

Rapid Problem Setup for Mesh-Based Simulation

W. D. Henshaw

00-ERD-017

Many of the computational simulation projects at LLNL involve the solution of partial differential equations (PDEs) in complex, 3-D geometrical configurations. A significant, recognized area of deficiency in our capability to perform these simulations arises from an inability to rapidly set up and easily modify the computational geometries. The problem-setup process consists of all the steps that must be taken to convert some specification of a geometry to a computationally appropriate 3-D volumetric mesh that can be used for simulation and analysis. Currently, using state-of-the-art mesh-generation software, Laboratory scientists must spend person-weeks or person-months to generate a new computational mesh from scratch. Thus, setting up the problem can often take much longer than performing the computational simulation. This grid-generation bottleneck is a severe problem in many areas of investigation.

The objective of this project is to reduce setup time by developing algorithms and a set of object-oriented tools for the semi-automatic creation of high-quality computational grids. We are leveraging the infrastructure supplied by the Overture object-oriented framework, developed at LLNL, and using a component-based approach whereby a complicated configuration is divided into separate, more simple, parts. Grids are first built for the simple parts and then are automatically connected together. This requires improved techniques for building component grids, improved algorithms for automatically joining the components together, a sophisticated graphical user interface, and the ability to access computer-aided design (CAD) geometry from a variety of sources.

Our accomplishments during FY2000 include the development of (1) a new hyperbolic surface-grid-generation algorithm for creating component grids on general surfaces such as those from CAD packages (see Fig.); (2) improved algorithms for evaluating networks of trimmed, nonuniform rational B-splines (NURBS), including algorithms for the automatic determination of the connection topology and more rapid and robust evaluation of trimmed surfaces; (3) algorithms and data structures for the generation of hybrid meshes, starting from a collection of overlapping, structured, component meshes; our advancing-front algorithm includes improved mesh-quality features such as the use of an influence function to specify the appropriate local-element size; (4) extension and enhancement of our capabilities for handling a wider range of CAD surface descriptions, such as those required by some LLNL applications; (5) a new volume-partitioning algorithm based on simulated annealing—we have demonstrated its effectiveness on 2-D geometries; and (6) a new, fast, approximate Voronoi tessellation algorithm for 2-D and 3-D geometries.

In FY2001, we plan to improve our problem-setup toolkit by continuing the development of (1) the hybrid-mesh grid generator, including obtaining results for 3-D geometries and for generation of hybrid grids on surfaces; (2) algorithms for building grids from their components and for incrementally adding new components to a geometry; and (3) hyperbolic mesh-generation algorithms, which will improve robustness and automatic selection of parameters. We also plan to evaluate and select strategies for CAD repair and feature suppression and to investigate the use of PDE-based metrics for analyzing mesh quality.

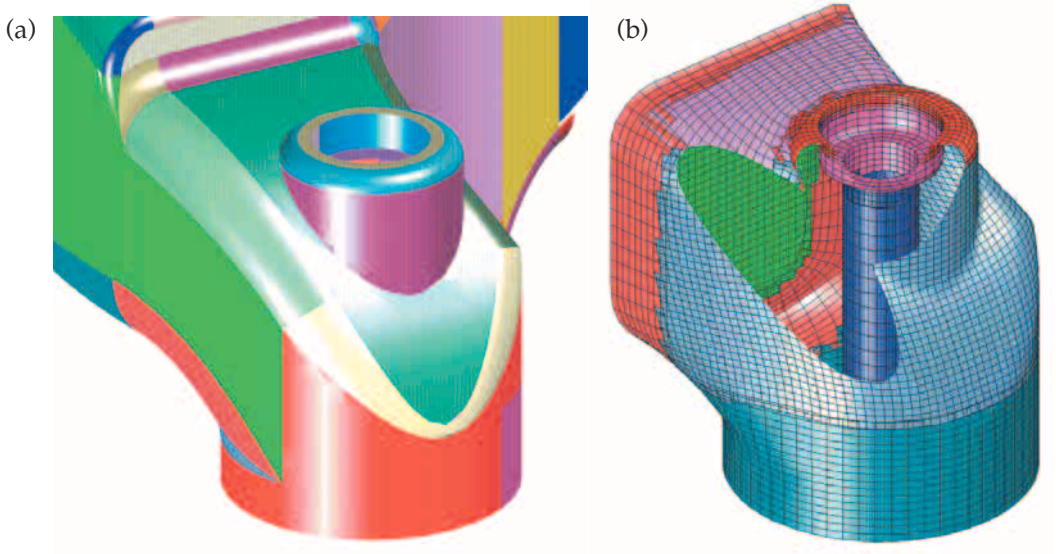

Techniques developed in this project have permitted us to use a computer-aided design (CAD) description of a surface (a) for the creation of a high-quality computational volume grid (b).

Back to main TOC

New Directions for Algebraic Multigrid: Solutions for Large-Scale Multiphysics Problems

V. E. Henson

00-ERD-018

Many problems of interest to the Department of Energy require parallel methods of solution that use hundreds or thousands of processors. These methods can succeed only if the algorithms are scalable—if the runtime remains constant as both the number of processors and the problem size grow. Increasingly, traditional methods are not applicable to large, unstructured grids in multiphysics simulation packages. For this situation, the algebraic multigrid (AMG) algorithm is the method of choice. However, for certain important problems, such as multiphysics codes used in Accelerated Strategic Computing Initiative (ASCI) simulations, standard AMG is also insufficient.

To address these difficult problems, in this project we are researching a new type of AMG, known as element-based algebraic multigrid (AMGe). AMGe is based on the use of individual finite-element stiffness matrices to create interpolation schemes that lead to effective multigrid cycling routines. As these methods are discovered, we implement them into BoomerAMG, an advanced AMG code for massively parallel processors (MPPs), and make BoomerAMG available to our customers. Our research is at the leading edge of AMG technology; it has immediate applicability to high-profile codes and solidifies LLNL's status as a leader in computational mathematics and computational simulations for physics.

To build a useable algorithm, we need an automatic way to determine the coarse-grid elements. In FY2000, we discovered a new form of element agglomeration, which creates the coarse-grid elements in a novel, two-step graphical-theoretical algebraic process. Using this algorithm, we implemented AMGe in a sequential code and applied it to several difficult problems. We showed that the AMGe method—although expensive in terms of computation and storage—can for certain problems (e.g., 2-D thin-beam elasticity) yield dramatic improvements in performance over previous methods.

Another major achievement during FY2000 was the discovery of the so-called "element-free AMGe" method. For some problems, we can use this method to simulate the effect of AMGe without having access to the element-stiffness matrices. Where this method works, we have shown it to be as effective as AMGe; moreover, it is much less expensive in terms of both operation count and data storage.

During FY2000, we also integrated the BoomerAMG code into the simulation codes of two of the main code groups at LLNL. Members of one code group find that BoomerAMG is the solver of choice for many of their problems.

We have three main goals for FY2001. First, we showed in FY2000 that element-free AMGe performs comparably to AMGe (and generally better than AMG) for many problems in terms of convergence and computational cost. During FY2001, we plan to perform the additional research required to (1) develop a full-fledged theory for this new method, and (2) explore several avenues regarding the effectiveness of variations to the method.

Second, both AMGe and element-free AMGe can be of general use only if they can be run efficiently on MPPs. Parallelizing these two methods, a high priority for us in FY2001, will involve fundamental research in both mathematics and computer science.

Finally, having focused thus far on the interpolation part of AMG, in FY2001 we plan to (1) develop an effective parallel algorithm for selecting coarse-grid points, and then (2) form the coarse-grid elements based on these points.

Numerical Technology for Large-Scale Computational Electromagnetics

R. M. Sharpe, D. A. White, N. J. Champagne

00-ERD-021

The key bottleneck in applying implicit computational electromagnetics (CEM) tools to large, complex geometries is the solution of the resulting linear system of equations. This encompasses virtually all frequency domain solutions of Maxwell's equations. The mathematical operators and numerical formulations used in this arena of CEM yield linear equations that are complex valued, unstructured, and indefinite. Also, simultaneously applying multiple mathematical formulations to different portions of a complex problem (hybrid formulations) results in a mixed-structure linear system, further increasing the computational difficulty. Typically, these hybrid linear systems are solved using direct-solution methods, which were acceptable for Cray-class machines but which do not scale adequately for Accelerated Strategic Computing Initiative (ASCI)-class machines. Approaches that combine domain decomposition (or matrix partitioning) with general-purpose iterative methods and special-purpose preconditioners are being investigated. Special-purpose preconditioners that take advantage of the structure of the matrix will be adapted and developed based on intimate knowledge of the matrix properties. In addition, LLNL's existing linear solvers are not well suited for the linear systems that are created by hybrid, implicit CEM codes.

The goal of this project is to research and develop critical numerical technology that alleviates this bottleneck for large-scale CEM.

During FY2000, we first developed a CEM matrix testbed by collecting a variety of linear systems of equations. Our purpose was to offer a means of evaluating combinations of preconditioners and solvers for their applicability with different formulations (dense, sparse, hybrid, etc.) and with different combinations of operators. We organized this information (http://cce.llnl.gov/solver) so that it can be used both as a resource by the electromagnetics community at large and to facilitate our collaboration with other researchers.

Next, we began developing a solver framework to provide (1) applications with a common interface to a variety of solvers and preconditioners, and (2) developers with flexible and extensible system for incorporating new algorithms. We evaluated a variety of existing solver libraries and chose to build upon Sandia National Laboratory's Iterative Scalable Implicit Solver (ISIS++) library rather than start entirely from scratch. We rewrote the ISIS++ software so it could be used for complex-valued linear systems. By doing so, at the close of FY2000 we had generic (type-independent), message-passing-interface (MPI) based, parallel versions of the following Krylov methods: conjugate gradient, conjugate gradient squared, bi-conjugate gradient stabilized, conjugate gradient normal equations, conjugate gradient normal residual, quasi-minimal residual, generalized minimal residual, and flexible generalized minimal residual. The modified library is known as ISIS++2.0 and is written in the C++ language. To support legacy C and Fortran codes, we developed a set of tools, written in the Perl scripting language, that automatically write C and Fortran interfaces to the ISIS++2.0 library. This way, new algorithms can be developed in a modern object-oriented programming language, yet legacy codes can still take advantage of the algorithms.

The next step was to incorporate solution strategies for the hybrid matrices. Initially, our algorithms are based upon applying the best solution procedure to each partition of the overall hybrid system. For example, using the direct solver ScaLAPACK on *only* the dense partition of the matrix (e.g., the Schur Complement method) yields a significant memory savings. Specifically, for a computer with 8 GB of memory, the direct approach restricts us to problems of order 30,000 unknowns; whereas, with the Schur Complement approach we can solve systems of order 5,000,000 unknowns.

Even though this is a dramatic memory saving, the ill-conditioning of the overall hybrid systems will require advanced preconditioners to be developed to yield a corresponding reduction in overall solution time. Work in FY2001 will focus on identifying and evaluating advanced preconditioners for the hybrid system and demonstrating the resulting tools on ASCI-class demonstrations.

Back to main TOC

Hydrogen Bonding and Molecular Dissociation at High Pressure: Low-*Z* Liquids and Liquid Mixtures

G. Galli, E. R. Schwegler, R. Q. Hood

00-ERD-031

Hydrogen bonds are the most prominent "weak" interactions in solids, liquids, and gases. They determine the crystal packing of many organic molecules, the 3-D structure of biological macromolecules, and the bonding properties of water—the most important liquid in physical sciences and biology.

Despite many investigations that have been reported in the literature, the nature of hydrogen bonds is poorly understood, and the evolution of and the changes in hydrogen bonds under pressure are largely unknown. Furthermore, at high pressure, changes in hydrogen bonding may be accompanied by molecular dissociation phenomena, thus giving rise to a variety of complex chemical bonds that differ from those encountered at ambient conditions.

In this project, we are investigating the structural and dynamical properties of low-*Z*, hydrogen-bonded liquids and liquid mixtures under pressure, using computer simulations and quantum molecular dynamics (MD) techniques.

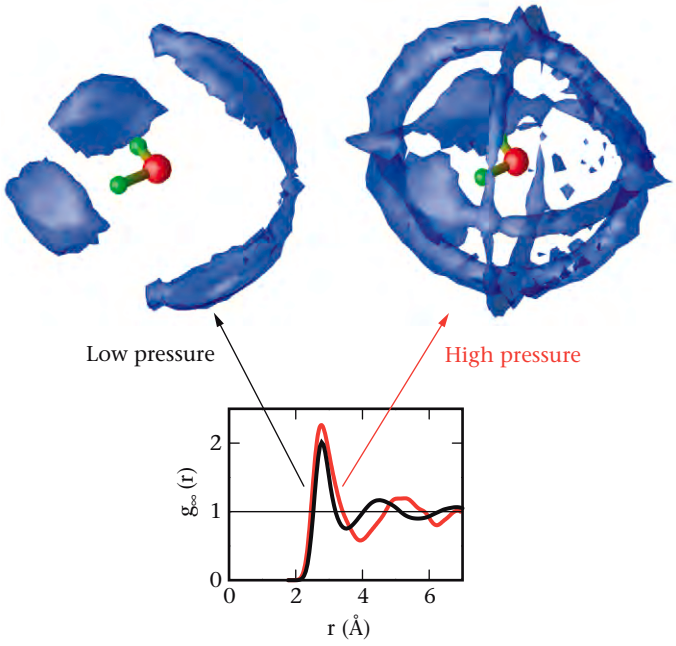

Radial distribution functions [$g_\infty(r)$] and spatial distributions (blue) of low- (black) and high-pressure (red curve) water, showing different geometrical arrangements of water molecules. Spatial distribution functions represent the probability of finding water molecules in the vicinity of a given one [represented by red (oxygen) and green (hydrogen) spheres]. The coordination of oxygen atoms varies from 4.7 at low pressure to almost 13 at 10 GPa, as indicated by the integrals of the functions $g_\infty(r)$ up to their respective first minima.

For several reasons, using a quantum-mechanical description of the interatomic interactions is crucial to describing compressed, low-*Z* molecular fluids. First, few reliable empirical potentials (none, in some cases) are available for mixtures of water with low-*Z* elements. Second, most semi-empirical descriptions make definite assumptions about the chemical reactions that occur under pressure. Instead we intend to predict the bonding properties of the mixture without any input from the constituent liquids other than the atomic species. Finally, ab initio MD simulations give direct access to bonding and electronic properties (e.g., electrical conductivity).

In FY2000, we had four main research achievements (also, see Fig.). First, we predicted, from first principles, the microscopic structure of water and hydrogen fluoride (HF) under pressure. Although both are composed of tightly bound molecules, these fluids differ substantially from each other. Whereas water molecules are arranged into an open, 3-D network, HF molecules form 1-D, chain-like structures. In our study, we obtained data on the equations of state (EOS) of water and HF that can be used to derive effective potentials for the simulation of energetic materials. Furthermore, we interpreted both recent and older experiments on hydrogen-bonded liquids and liquid mixtures, in particular HF/H_2O. Finally, we predicted structural and thermodynamic properties of several low-*Z* molecular systems that are not hydrogen bonded—in particular, hydrogen and CO_2. These fluids were included in our study—thus widening the scope of our project—to make contact with recent, interesting experiments carried out at LLNL. In particular, we studied some crystalline phases of solid CO_2 and helped identify a newly discovered compressed phase. For the latter, G. Galli and F. Gygi received a Defense and Nuclear Technology award in 1999.

During FY2000, some of our results were published in three papers and also presented fully or in part in nine invited talks given at international conferences.

In FY2001, we plan to develop (1) tools to define formation and breaking of bonds under pressure based on the electronic properties of the fluids, and (2) a formalism to sample longer time scales in our MD simulations. Concurrently, we will carry out simulations of compressed hydrogen under conditions similar to those obtained in laser-shock experiments, of water in the dissociative regime, and of other fluids such as methane and oxygen under pressures in the 50- to 100-GPa regime.

Analysis of Radionuclide Migration through a 200-Meter Vadose Zone Following a 16-Year Infiltration Event

A. F. B. Tompson, D. K. Smith, S. F. Carle

00-ERD-054

Beginning in 1975 at the Nevada Test Site (NTS), groundwater adjacent to the CAMBRIC nuclear test of 1965 was pumped steadily for 16 years to elicit information on radionuclide migration in the saturated zone. The effluent was monitored, discharged to an unlined ditch, and allowed to infiltrate into the ground as it flowed towards Frenchman Lake, about a kilometer away. Later, in 1991, regular tests of groundwater from monitoring well Ue5n, located 106 m away from the ditch, began to show rising levels of tritium, apparently confirming that infiltrated radionuclides have reached the water table, roughly 200 m beneath the ground surface.

The goal of this project is to use the data from this unprecedented field experiment to improve our understanding of the migration of water and radionuclides and other contaminants in unsaturated geological media above the water table (in a deep vadose zone) by coupling advanced numerical simulation techniques, available characterization data, and radioanalytic measurements. This migration is a subject of increasing relevance at many sites in the Department of Energy complex.

During FY2000, we developed a simple, 2-D numerical model of infiltration underneath the ditch [Fig. (a)]. The simulations correspond to flow along a vertical plane, perpendicular to the ditch, that extends from the ditch to monitoring well Ue5N. The ditch is considered to be a ponded source of water for the 16-year duration of the experiment and to be dry thereafter. Recharge from the ditch will descend under unsaturated conditions, collect ("mound") above the water table, and change the hydraulic gradients to drive outflow through the saturated-zone boundary farthest from the ditch. Our flow model is being developed to account for two-phase flow (water and air) and for the transport of dissolved radionucludes (tritium, ^{14}C, ^{36}Cl, ^{85}Kr, ^{129}I, ^{99}Tc, and ^{106}Ru) that are entering the system from the ditch effluent.

We also collected additional water samples from well Ue5n and analyzed them for these same radionuclides and for other, stable isotopes (e.g., ^{3}He), many at environmental levels that were unavailable at the time of the pumping experiment. As shown in Fig. (b), tritium concentrations in the monitoring well have been steadily increasing with time; the data that we collected during FY2000 provide the highest tritium concentration to date. Model results of tritium arrival in the well (corrected for radioactive decay) agree favorably with the record of observations and suggest that tritium concentrations (decay corrected) will continue to rise for the next 30 years. The water-sample data also reveal the presence of several previously undetected radionuclides (^{14}C, ^{36}Cl, ^{99}Tc).

During FY2001, we plan additional 2-D and 3-D calculations that will exploit larger-scale computing resources and provide further insights into the complexity of fluid infiltration in nonuniform geological media. Heterogeneity will be incorporated either in the modeled unsaturated 2-D sedimentary section or in an analogous 3-D block. Our simulations will analyze whether the increase of ^{36}Cl/tritium ratios in water collected in the vadose zone results from preferential evaporative loss of tritium. We will compare estimates of the groundwater age calculated for the monitoring well with measurements of the age of the tritium/^{3}He-based groundwater. This reconciliation will provide an additional calibration point for the model as well as test the validity of apparent tritium/^{3}He-based ages inferred from water samples that have traversed an unsaturated zone.

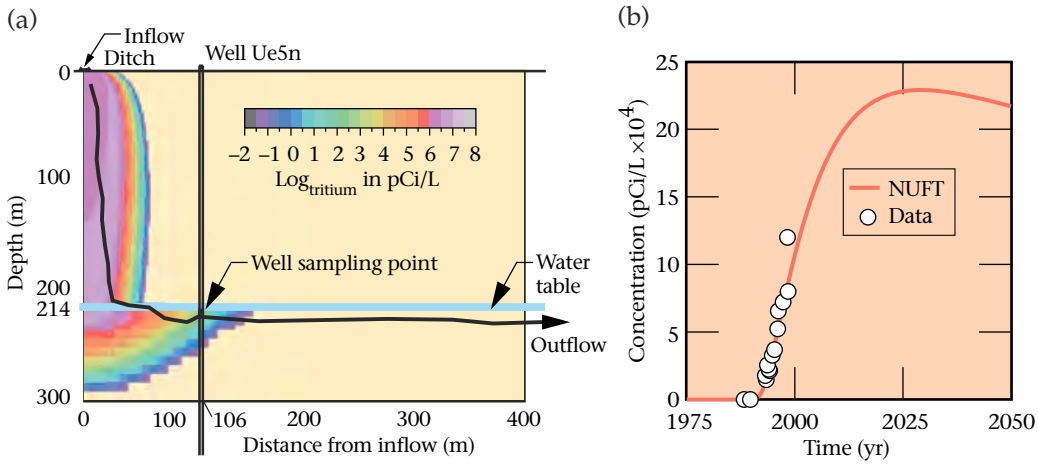

Application of long-term data to radionuclide migration through the vadose zone: (a) shows the simulation domain for current infiltration simulations, with a monitoring point in well Ue5n at just below the water table and contours that represent predicted tritium concentrations in 1990; (b) shows measured tritium concentrations and predicted concentrations using LLNL's nonisothermal unsaturated-saturated flow and transport (NUFT) code.

Back to main TOC

MEDIOS: Modeling Earth Deformation using Interferometric Observations from Space

J. J. Zucca, P. Vincent, W. Foxall, W.R. Walter, J. Swenson, S. Larsen

00-ERD-056

Satellite radar interferometry (InSAR) has become the new geodetic standard for measuring deformation from subsurface processes such as fault movements, fluid reservoirs (oil, gas, geothermal, volcanic), and soil and aquifer compaction. The continuous maps of surface deformation allow for more sophisticated modeling of these sources by providing improved model constraints. Since point-based geodetic measurements [e.g., Global Positioning System (GPS)] did not provide the constraints necessary for the development of more accurate models, only simple homogeneous elastic models were used. LLNL has developed superior expertise in modeling complex subsurface processes through its containment studies associated with underground nuclear testing, contaminant transport and flow, and hazardous materials storage. The purpose of this project is to couple LLNL's superior underground source-modeling expertise with InSAR data-processing capability to produce the next generation of sophisticated, highly accurate models of subsurface processes. These models can be used to invert for parameters that align with LLNL's missions: (1) nonproliferation and defense, (2) energy resource exploitation, and (3) seismic hazards.

We made significant progress in all three categories during FY2000. In category (1), we completed an InSAR study of surface deformation signals of underground nuclear tests at the Nevada Test Site (NTS). This study resulted in new discoveries about how the surface above underground nuclear tests deforms and what can influence this deformation, and about how InSAR can be used as a new tool for monitoring global underground nuclear tests. For example, the Fig. shows InSAR signals associated with clusters of past underground tests in Yucca Flats, NTS, where emplacement depths were at or near the depth of a confined aquifer unit. We interpret the deformation to be caused by stress-related draining of the over-pressured aquifer originally perturbed by underground nuclear testing that ended in 1992. Our models of these and other InSAR signals incorporate various aspects of subsurface processes responsible for the signals, including such hydrologic effects. We are in the process of submitting an article that is based on this work to the journal *Nature*.

In category (2), we applied LLNL's heterogeneous, fully dynamic E3D modeling code to model underground mine collapses in the Solvay mine in Wyoming. The goal of this study is to invert InSAR and GPS data for the mine collapse source parameters (size, depth, geometry, mechanism, elastic moduli). The benefit to the mining company is that by understanding the mechanism by which a mine collapse occurs, they can work to prevent them in the future. We have InSAR results for the Dixie Valley Geothermal Field in central Nevada which show both shallow and deep reservoir-related deformation sources. We are collaborating with University of Utah researchers who have done several GPS surveys of the field and have heat flow, hydrologic, and other data that will be combined with our InSAR results to constrain our models.

In category (3), we completed an InSAR study of anomalous slip events along the southern San Andreas and Superstition Hills faults, which is also in the process of being submitted to *Nature*. Preliminary results for the San Francisco Bay region faults are underway.

Plans for FY2001 include developing inversion routines for our forward models in each of the three source categories. We expect continued layers of sophistication in our forward models and continued adaptation of our inversion routines to these models.

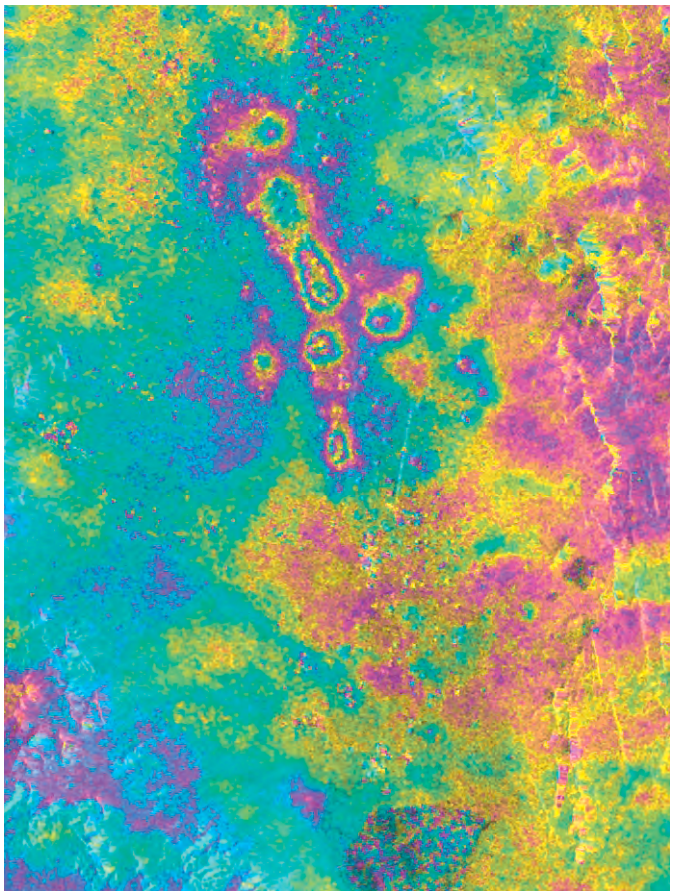

InSAR surface subsidence signals from clusters of past underground nuclear tests conducted in Yucca Flats, Nevada Test Site. One color cycle = 28 mm of near-vertical surface deformation.

Reactive Transport Modeling of Geologic CO_2 Sequestration to Identify Optimal Target Formations

J. W. Johnson, C. I. Steefel, J. J. Nitao

00-ERD-057

The industrial revolution's most insidious environmental legacy—dangerous atmospheric concentrations of CO_2—can no longer be ignored. With "business-as-usual" projections rapidly approaching a grim horizon of climatic consequences, there is an urgent need to develop innovative strategies for CO_2 stabilization that either reduce emissions through improved energy efficiency or eliminate them through waste-stream capture and sequestration. The latter approach stands alone as a potential near-term means of significantly curbing atmospheric CO_2 emissions.

Among proposed sequestration strategies, injection into confined geological formations represents the most promising alternative. Scientific viability of this approach hinges on the relative effectiveness of CO_2 migration and sequestration processes in the subsurface; successful implementation relies on our ability to predict sensitivity of this migration/sequestration balance to key physical and chemical characteristics of potential target reservoirs. By quantifying this sensitivity, we can establish geochemical, hydrologic, and structural constraints on maximizing sequestration performance (storage capacity and isolation security) that can be used to identify optimal target formations.

In this project, we are developing a new modeling capability for implementing this approach by integrating a set of reactive transport simulators (NUFT, CRUNCH), supporting geochemical software (SUPCRT92), and thermodynamic/kinetic databases (GEMBOCHS) developed by the research team.

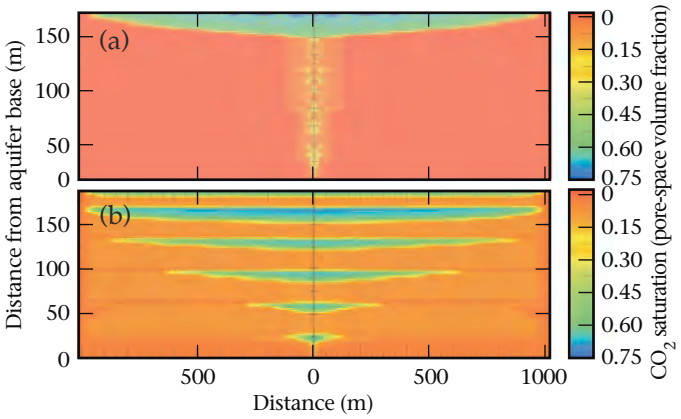

Reactive transport simulations of CO_2 injection at the base of a confined aquifer, illustrating the effect of low-permeability, intra-aquifer shales on migration of the immiscible CO_2 plume: (a) without shales, this plume interacts with the aquifer to a minimum extent while rising to the cap rock; (b) when five 3-m-thick shales are present, the volumetric extent of plume-aquifer interaction is greatly expanded. In (b), note higher background CO_2 saturation, which significantly increases the potential effectiveness of solubility and mineral trapping. The CO_2 injection rate (10,000 tons/yr), duration (1 yr), temperature (37°C), and hydrostatic pressure (90 to 110 bar) are identical in both simulations.

Our initial model development has focused on simulating CO_2 injection at Statoil's North-Sea Sleipner facility. Here, excess CO_2—a million tons annually since 1996—is stripped from recovered natural gas to meet export regulations, then injected into a confined saline aquifer 800 m below the seabed. Such injection for the sole purpose of environmental isolation is unique to Sleipner. Because deep saline aquifers have enormous potential sequestration capacity, this pilot implementation has been the subject of intense scientific study by the International Energy Agency's Saline Aquifer CO_2 Storage (IEA-SACS) project.

During FY2000, we established a working collaboration with IEA-SACS and obtained sufficient site-specific data to carry out initial reactive transport modeling of CO_2 injection at Sleipner. Preliminary results suggest that the local permeability structure of the target formation controls both CO_2 movement by all migration processes (immiscible displacement, gravity segregation, and viscous fingering) and the potential effectiveness of all sequestration processes (structural, solubility, and mineral trapping). For this typical sandstone aquifer, at least 90% of the injected CO_2 migrates as an immiscible plume, which rises relative to surrounding formation waters owing to its lower density. Hence, potential structural trapping beneath the cap rock represents the dominant sequestration mechanism. However, upward migration of this plume is strongly influenced by the absence [Fig. (a)] or presence [Fig. (b)] of thin, low-permeability shale layers within the aquifer. When present, these shales retard vertical and promote horizontal CO_2 migration, thus expanding the volumetric extent of CO_2–aquifer interaction. This interaction increases the potential effectiveness of solubility trapping (whereby CO_2 dissolves into formation waters) and mineral trapping (whereby CO_2 precipitates as carbonate minerals). Relative impermeability of intra-aquifer and cap-rock shales may be enhanced by heightened mineral trapping within these clay-rich lithologies, thus improving cap-rock integrity, the most important constraint on long-term sequestration performance.

Our unique methodology and simulation capabilities that address geologic sequestration represent important advances—and explicitly stated Department of Energy (DOE) technical needs—in the emerging field of carbon-sequestration science. In FY2001, we will determine key physical and chemical constraints on maximizing sequestration performance—DOE's screening criteria—that can be used to identify optimal target formations.

Back to main TOC

Compensation for Thermally Induced and Geometric Errors of Machines Using an Open-Architecture Controller

D. K. Born

00-ERD-062

In a well-controlled laboratory environment, the dominant errors in machine tools and coordinate-measuring machines are geometric; that is, they are induced by imperfections in the geometry of the machine. Because these errors are repeatable with machine position, they can be removed in the machine controller. However, conventional methods for measuring these errors are time intensive and require expensive equipment and highly skilled labor.

In contrast to a well-controlled laboratory setting, most manufacturing environments experience daily and yearly temperature fluctuations as well as heat loads caused by the manufacturing process itself. These internal and external heat flows cause deformations in the structure of the machine, which result in dimensional errors on the part. In a typical manufacturing environment, thermally induced errors can contribute as much as 70% of the overall error.

One approach to improving accuracy in machines is to compensate for the thermally induced errors in process. This procedure, known as thermal-error compensation, has not been practical commercially because no method to date has successfully predicted these errors in real time, and the machine controllers are closed, which prevents making the compensating correction.

The purpose of this project is to improve the accuracy of machine tools and coordinate-measuring machines in a typical manufacturing environment—with minimal increase in both capital and operating costs. We are applying a rapid and inexpensive technique for measuring geometric errors that was developed at LLNL; we are then using an open-architecture controller (OAC) to remove both the geometrically and thermally induced errors.

During FY2000, we developed a simple, 1-D structure model with analytical foundations using statistical techniques and experimental data to fit the model. Our model uses a finite number of temperatures that are measured at critical locations on a machine's structure. Using numerical-integration techniques, we estimate the *integral* of the temperature profile, which is then proportional to the thermally induced deflections. Unlike most thermal models used for compensation that appear in the literature, our model has a theoretical basis, which makes our methodology robust enough to perform under a variety of operating conditions.

We then used a simulation of thermal-error compensation to verify that our strategy works for the 1-D case under certain defined conditions. These conditions determine how many temperature measurements are needed and the time-response characteristics of the system. In FY2000, we built a test stand to study 3-D heat flow and modeled this test stand with finite-element analysis (FEA) to predict its thermally induced deformations.

During FY2001, we will use the test stand to verify our methodology and to refine the FEA model. Our FEA model can then be used as a virtual testbed that will allow us to research our methodology under a variety of conditions. To demonstrate the implementation of compensation on a machine tool, we will also implement geometric-error compensation on an OAC that is based on a personal computer.

New Approaches to Quantum Computing Using Nuclear Magnetic Resonance Spectroscopy

M. E. Colvin, V. V. Krishnan

00-LW-068

Quantum computers are based on quantum systems such as individual atoms or molecules. Theoretically, quantum computers are capable of handling challenging problems at an exponentially faster rate than are classical computers. The development of practical quantum computers would bring about a dramatic revolution in the way computation and information processes are performed and perceived today.

Quantum computing relies on the fundamental superposition principle of quantum mechanics; that is, until it is measured, any quantum system can exist in all possible states at once. Although a classical bit must be either 0 or 1, a quantum bit (qubit) simultaneously contains a 0 component and a 1 component. If the classical bits are denoted by $|0\rangle$ and $|1\rangle$, a qubit can be in any state $a|0\rangle+b|1\rangle$, where a and b are complex numbers called amplitudes that are subject to the condition $|a|^2 + |b|^2 = 1$. In classical computers, a single string of n zeros and ones would be needed to describe the state of n bits, whereas n quantum-mechanical bits can simultaneously represent $2n$ numbers. Since qubits can evolve concurrently along many paths at once, they could be used to perform many calculations on all the bits at once, hence their speed relative to that of classical computers.

Nuclear magnetic resonance (NMR) spectroscopy offers an attractive method for testing theoretical predictions and facilitating the development of better protocols for quantum computing algorithms, as well as for studying the feasibility of practical quantum computers. Each line in a NMR spectrum represents the complex interplay between the various interacting spins of the molecule, and these transitions can be designed to perform quantum computing.

The advantage of using NMR to develop new quantum computing protocols is the long history of development of experimental techniques for manipulating nuclear spins using radio-frequency (rf) pulses and delays. In particular, areas of potential development include ways to increase the number of qubits, development of more cost- and time-efficient methods of computation, and evaluation of the performance of quantum algorithms.

During FY2000, we reached several important milestones on research that forms the necessary basis for a quantum-computing platform. Using NMR spectroscopy and two- and three-qubit systems, we began working on ensemble quantum computing. In particular, we implemented several fundamental quantum logical operations that are needed to build a wide range of quantum algorithms. We also implemented (1) two quantum algorithms—Grover's database-search quantum algorithm and the Deutsch-Jozsa algorithm—in a two-qubit NMR quantum computer, and (2) the quantum Fourier transform, which is a basic element in Shor's algorithm for the factorization of numbers. In addition, we began working on the use of molecules dissolved in an anisotropic solvent system (such as liquid crystals) and identified possibilities for increasing the quantum computation speed by a factor of 5 to 8 relative to conventional NMR samples.

During FY2001, we will develop NMR techniques to increase the number of qubits and to evaluate the theoretical models currently available. We plan to accomplish our goals by developing and combining novel molecular systems and experimental NMR protocols. We will also modify currently available methods to increase the efficiency of data acquisition and processing.

Back to main TOC

Improving Advanced Simulation Software through Scientific Component Technology

S. Kohn, T. Dahlgren, T. Epperly, G. Kumfert

00-SI-002

Numerical simulations play a vital role in the Department of Energy's (DOE's) science mission as a basic research tool for understanding fundamental physical processes. However, as simulations become increasingly sophisticated and complex, no single person—or single laboratory—can develop scientific software in isolation. Instead, physicists, chemists, mathematicians, and computer scientists concentrate on developing software in their domain of expertise—computational scientists then create simulations by combining these individual pieces of software.

Although the DOE has invested significant resources in the development of high-performance simulation software, it is often difficult to share these sophisticated software packages among applications because of differences in implementation language, programming style, or calling interfaces.

In this project, we are addressing problems of complexity, re-use, and interoperability for DOE scientific software by developing scientific component technology for high-performance, parallel, scientific computing. Our component technology will provide a means for managing the complexity of modern, scientific simulation software and will also enable new simulation capabilities that were previously unavailable because of limited interoperability.

During FY2000, we focused on developing three enabling technologies: language-interoperability tools; a component-software repository; and a collaborative online-voting application.

As part of our language interoperability work, we developed a tool called Babel that enables the creation and distribution of language-independent software libraries. To use Babel, library developers describe their software interfaces in a special, scientific interface-definition language (SIDL). Babel then uses this SIDL description to generate "glue code" that enables the software library to be called from any supported language.

We tested our Babel technology in high-performance preconditioners (HYPRE), which is a scientific library of linear solvers and preconditioners. Our experiments demonstrated that, in addition to language interoperability, Babel also provides useful tools for designing scientific software libraries and the ability to experiment with different solver techniques. The Babel modifications did not introduce measurable parallel computing overheads.

As our second enabling technology, we designed and implemented a Web-based repository called Alexandria to encourage the distribution and reuse of software components and libraries used in scientific computing. Alexandria provides (1) a convenient, Web-based delivery system, thereby lowering the barrier to adopting component technology; (2) a convenient Web-based interface to the Babel interoperability tool; (3) a repository of SIDL interface-description information; and (4) a calling interface to support queries by component software tools. We are working with the DOE's Common Component Architecture (CCA) forum to establish common schema for accessing Alexandria from component tools developed by collaborators at other DOE laboratories and in academia.

Finally, we designed and developed a Web application called Quorum that manages online voting on proposals by providing the online equivalent of a parliamentary voting system. This voting mechanism facilitates the development of software standards by distributed teams and is being used by the DOE's CCA and Equation Solver Interface working groups.

In FY2001, we will focus on three areas. First, we will expand the languages supported by our Babel language-interoperability tool. Babel now supports Fortran 77, C, and C++; we plan to extend support to Java, Python, Yorick, Fortran 90, and MATLAB. Second, we will research and develop support for parallel data redistribution among distributed components. Finally, we will continue to collaborate with the CCA working group and with other library developers to demonstrate and deploy component technology for scientific software.

DJEHUTY: A Next-Generation Stellar-Evolution Model

D. S. Dearborn, P. P. Eggleton

00-SI-004

Stars provide the standards of reference for measuring the size, age, and chemical evolution of the universe. They have also become laboratories, providing observational signatures that challenge our understanding of complex physical processes. Many stellar-evolution processes are intrinsically 3-D phenomena. To date, these processes have been modeled through coarse approximation. Now, because of LLNL's massively parallel processor (MPP) systems and the intense Accelerated Strategic Computing Initiative (ASCI) coding efforts, we are uniquely equipped with a quantitative capability to improve our physical understanding of 3-D stellar phenomena.

Our goal in this project is to develop DJEHUTY—a 3-D, stellar-evolution code named after the Egyptian god of astronomy—as a unique tool for studying global, 3-D processes in stellar structure and evolution. We are designing DJEHUTY to operate on massively parallel processors (MPPs) with the best available physical data and with new algorithms tailored specifically for the MPP environment.

During FY2000, we took the first steps toward developing DJEHUTY. We (1) improved an analytical equation of state (EOS) so that it is consistent with the best LLNL tabulations and tested it against helioseismological data in our 1-D evolution code; (2) wrote software that uses our 1-D code to generate small (1.6-million zone), 3-D spherical models; and (3) combined this EOS plus an elementary gravity routine with other LLNL components to form the core of a 3-D stellar-structure code.

Late in FY2000, we successfully followed the hydrodynamic behavior of a four-solar-mass, pre-main sequence star on the TC2K, an alphaserver supercomputer with 512 processors. At year's end, we were running additional tests to ensure the accuracy of our simulation and to develop methodologies for efficiently performing and analyzing calculations of 3-D stellar structure. The experience gathered implementing an astrophysical EOS will facilitate our ability to add other physics in FY2001.

During FY2000, using the power of the Livermore Computer Center (LCC) TeraCluster with standard 1-D approximations, we conducted the first complete survey in which the final configurations of binary stars are linked to their formation. The number of binary-star simulations completed on our survey exceeds all previous computations on this subject. Analysis of our results provided insight into the most interesting binary problems for DJEHUTY. This survey, along with a description of LLNL's effort to revolutionize stellar-evolution calculations by developing DJEHUTY, were well received at two international conferences. In addition, academic researchers have shown interest in a collaboration.

We also began developing our ability to work with distorted potentials for modeling nonspherical (binary) objects. Although our FY2000 work utilized a 1-D code as a platform for testing physics modules and generating models, we took a preliminary step towards developing a 3-D hydrostatic code by testing a multiresolution solution method.

Early in FY2001, DJEHUTY will include astrophysical opacities, nuclear-energy generation (as tested in the 1-D code), and diffusive energy transport. Then, we will be able to begin the first calculations aimed at investigating the long-standing problem of convective-core overshoot. Massive stars possess convective cores driven by the temperature-sensitive carbon-nitrogen-oxygen (CNO) cycles. The treatment of this convection is a critical determinant of the course of stellar evolution. Observations assure us that our best 1-D approximation of steady-state convection is flawed. To address this problem, we are enhancing DJEHUTY to produce large (100-million zone) models for MPP operation.

Dislocation Dynamics: Simulating Plastic Flow of Body-Centered-Cubic Metals

D. H. Lassila, V. V. Bulatov, T. Diaz de la Rubia, L. L. Hsiung, T. G. Pierce, M. Rhee, M. Tang

00-SI-011

The principal mechanism for plastic deformation in metals is the generation and motion of dislocations. Dislocations are atomistic defects in a crystal structure that move and interact with each other when materials are stressed. The aggregate behavior of millions of dislocations per cubic centimeter results in interesting and important mechanical behaviors such as the ductile behavior of lead and the brittle fracture behavior of iron at low temperatures.

A multiscale-modeling approach can be used to model and understand the effects of dislocations on mechanical behavior. The subject of this project was the development of an experimentally validated, 3-D, dislocation-simulation capability that would (1) utilize information generated at the atomistic length scale, and (2) predict strength properties used in larger-scale simulations. The simulation and experimental work were highly coupled and focused on the mechanical behavior of molybdenum (Mb), which is representative of many body-centered-cubic (bcc) metals of interest to Laboratory programs.

(a)

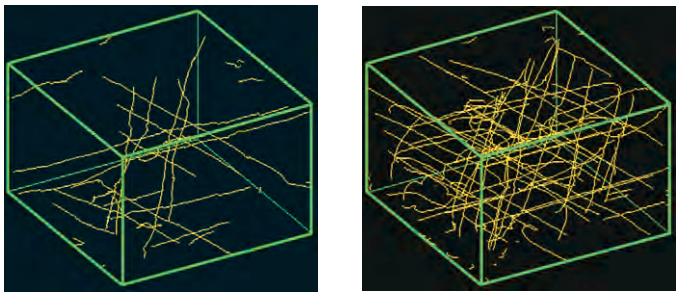

(b)

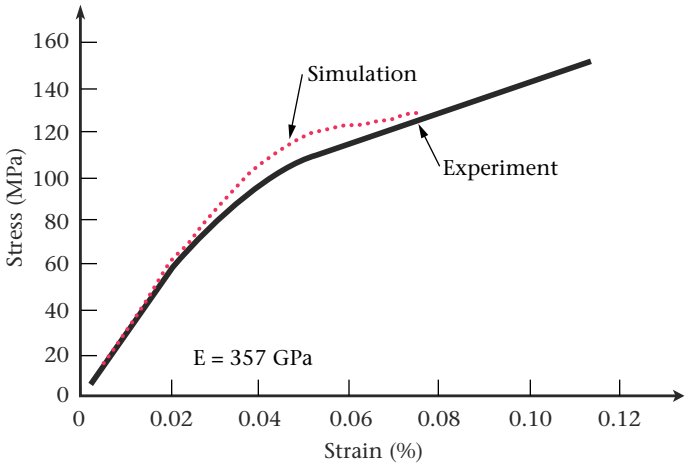

Analyses of dislocation dynamics in single crystals of annealed molybdenum (Mb) subjected to an applied stress of 357 GPa, showing (a) simulated evolution of a dislocation structure and strength response, in which the initial structure was based on experimental observations of dislocations; and (b) close agreement between simulated and experimental responses.

During FY2000, we performed large-scale, 3-D simulations on a massively parallel processor (MPP) supercomputer [the Accelerated Strategic Computing Initiative (ASCI) Blue computer] and obtained predictions of strength properties and dislocation structure evolution, as shown in Fig. (a). Our experiments were specifically designed to validate our simulations.

Simulations of dislocation dynamics (DD) are only as reliable as the rules they employ to describe dislocation mobility. Such rules are external to the DD method and must be obtained either from experimental data or from detailed atomistic calculations. Experimental measurements of dislocation mobility are difficult and limited to a narrow subset of temperature and stress conditions of interest. Atomistic simulations, on the other hand, have no such limitations and can be used to parameterize dislocation mobility under conditions of very high strain rates and/or pressure. Until recently, such atomistic-DD connections had not been implemented. Our work is the first realistic attempt of this kind, where accurate rules for dislocation mobility for bcc Mb are extracted from the atomistic calculations and are then directly incorporated into large-scale DD simulations of macro-scale crystal plasticity.

We developed a new experimental capability to directly observe dislocation mobility and thereby validate the rules for mobility derived from our atomistic simulations. Our experiment involved a special, in situ transmission electron microscopy (TEM) loading stage that can precisely measure the load on a 0.20-μm-thick foil. With this loading stage, we could directly observe and determine, as a function of applied stress, the velocity of the dislocations imaged with the electron beam. We have applied for a patent on the design of the TEM stage.

For our deformation experiments, we used single crystals of high-purity Mb and tested them over a wide range of temperatures and deformation rates. These experiments were central to the project because they provided both strength properties and dislocation structures that were necessary to validate the simulations. Comparison of simulated results with highly accurate experimental data, as shown in Fig. (b), led to the further development of simulation codes. For example, we believe that the boundary conditions in the simulations have been responsible for the underestimation of both dislocation accumulation and strength compared with experimental data. By the close of FY2000, we had implemented new boundary conditions—our improved predictive capabilities showed significantly enhanced multiplication of dislocations in the initial stages of yielding.

Energy and Environmental Technologies

5

Section 5—Energy and Environmental Technologies

Back to main TOC

Printed Wiring Board Fabrication and Lead Elimination via Single-Bath Electrodeposition

M. P. Meltzer, C. P. Steffani

97-ERD-032

Hot-air solder leveling (HASL), the most common method of finishing printed wiring boards (PWBs), is one of the main uses of lead in traditional PWB manufacturing. Replacing this method would benefit both employee health and the environment. Because HASL provides a fairly uneven surface that is problematic for mounting very small components, eliminating HASL would result in a production advantage.

In this project, we investigated single-bath electrodeposition as a potential HASL replacement technology for many applications. The single-bath electrodeposition process alternates deposition of one or the other metal component of a bimetal bath by controlling the plating potential and mass transport. The process employs a nickel layer as both etch resist and finish coat and has the potential for lowering environmental and human-health risks associated with PWB manufacture. Single-bath electrodeposition is also more efficient and profitable than HASL for PWB fabrication.

During FY2000, for the PWB application developed in this project, we adapted techniques from layered electroforming methods that are used to build up copper-nickel composite materials of high tensile strength. These materials typically contain many alternating, extremely thin layers of each metal. We altered the electroforming process parameters so that we could deposit thicker layers of copper that are required for PWB circuitry.

The single-bath process generates copper deposits from a very dilute solution of copper ions (from 0.05 to 0.1 *M*, vs. 2.0 *M* for traditional PWB applications). In our single-bath approach, nickel concentrations are an order of magnitude greater than those of copper, and special complexing agents are used to modify reduction potentials. Solution pH is also controlled very closely. Amperometric manipulation is performed concurrently with agitation variations to ensure the deposition of distinct layers of copper and nickel. Copper thicknesses on the order of 12 µm (0.0005 in.) and nickel thicknesses of 1 µm (0.00004 in.) are achieved by this approach.

Single-bath electroplating is applied to PWB fabrication as follows: copper is plated first, to the desired thickness for the PWB circuitry, typically 12 µm (0.0005 in.). Next, a nickel layer is deposited as an etch resist to protect copper circuitry. The etch-resist layer is left in place rather than stripped (as tin and tin/lead etch resists generally are) and serves as a finish coat for the PWB, onto which components are soldered. Our analyses demonstrated that this nickel layer, which contains a significant percentage of copper because of the chemistry of the process, provides a good solderable surface.

Our process (1) meets PWB-manufacturing requirements for level, bright, durable deposits and for a solderable nickel layer; (2) eliminates a costly, labor-intensive operation that also generates significant hazardous waste because our nickel etch-resist layer does not have to be stripped and discarded; (3) eliminates the of use of highly toxic lead-bearing materials from several PWB manufacturing steps, including etch-resist deposition, finish coating, and tinning; and (4) can reduce equipment requirements and the floor space needed for manufacturing PWBs by combining several fabrication steps into one tank—that is, by depositing either copper (for circuitry) or nickel (for an etch-resistant finish) from the same bath without intermediate rinsing.

High-Power-Density, Solid-Oxide Fuel Cells

A. Q. Pham, B. Chung, J. Haslam

98-ERD-031

Fuel cells are electrochemical devices that have received great interest recently because of their promise for generating clean and efficient power. Because fuel cells generate electricity directly through electrochemical processes that do not involve combustion, they are not limited by the Carnot cycle; thus, they can achieve very high efficiency. For instance, current state-of-the-art fuel cells can reach 50 to 60% efficiency, whereas efficiencies for conventional power-generation devices are generally well below 30%. The high efficiency of fuel cells will enable the use of fossil fuels at reduced levels of greenhouse-gas emissions. For this reason, the development of solid-oxide fuel cells (SOFCs) has become a high priority for the Department of Energy, as exemplified by the recent formation of the Solid State Energy Conversion Alliance (SECA) for bringing SOFCs to market. However, the success of the SECA program will require several breakthroughs in SOFC technology, especially in cell manufacturing and stack performance.

Since FY1998, we have been working on developing low-cost, high-power-density SOFCs that will operate at intermediate temperatures (below 800°C). Our approach is based on developing and demonstrating low-cost, thin-film processing techniques and on optimizing the material and the stack design to increase the power density of the fuel cells. This approach would reduce the overall cost of fuel-cell production.

In FY1998, we successfully developed a novel, low-cost, thin-film deposition technique, for which we filed a U.S. patent. Our technique is as simple as spray painting, yet is highly versatile and can produce high-quality thin films ranging in thickness from one micrometer to several hundred micrometers.

In FY1999, we worked on optimizing the fuel-cell cathode and anode. The result was a single-cell power density of 0.9 W/cm^2 at 800°C in air and hydrogen gases.

In FY2000, we continued improving single-cell performance. Through a systematic evaluation of the effect of the electrode microstructure on electrode polarization cost, we demonstrated very high power density—up to 1.2 W/cm^2 at 800°C—for single cells using only conventional electrode materials. For comparison, the highest power density reported in the literature is typically lower than 700 mW/cm^2 for the same cell materials and for similar testing conditions. Using a multilayer thin-film approach, we further improved the power density of a single cell up to 1.4 W/cm^2. This value sets the world record for power density at 800°C.

Our major goal for FY2000 was to demonstrate that the high power density achieved for a single cell can be scaled up to a stack. Because each single cell provides a voltage of only about 1 V, several cells must be stacked to yield higher voltage. The Fig. shows our first prototype three-cell stack. The stack has a conventional cross-flow design with an external gas manifold. The peak power output of the stack was 61 W, exceeding the project goal of 50 W. The power density of the stack was 1.05 W/cm^2 (at 800°C in air/hydrogen), which is at least 50% higher than any stack power density reported to date.

We have formed a team that includes several industrial partners to respond to the DOE SECA program to bring the SOFC development effort to the next level.

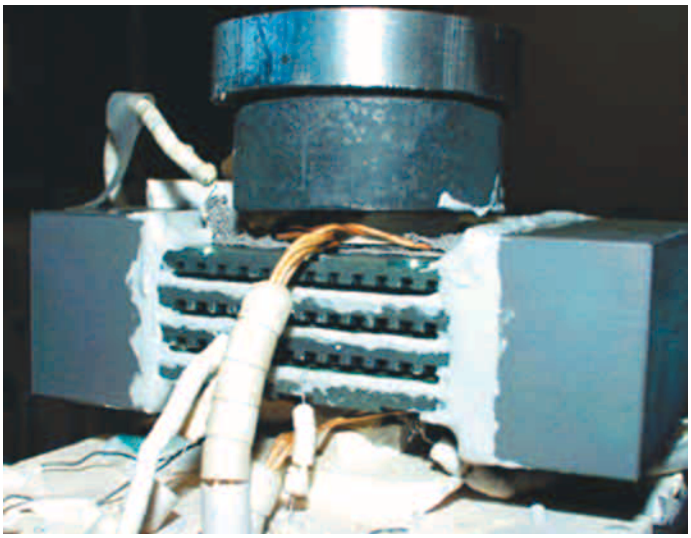

A stack of three solid-oxide fuel cells with cross-flow design.

Diagnostics Systems Approach to Watershed Management

M. L. Davisson

98-ERD-046

Water quality of rivers, streams, and shallow groundwater is adversely affected by agricultural activities, natural habitat changes, and urban runoff. Together these comprise most of the growing non-point-source pollution (NPSP) problem plaguing world water supplies. However, sources of NPSP are difficult to determine using traditional water-quality investigations. Isotopic measurements offer a new tool for delineating sources of NPSP. Natural isotopic abundances of dissolved and suspended constituents in surface and groundwater are intrinsic to their geographic origins and the process that generated them. In using these isotopic measurements, the goal of this project is to develop and demonstrate new measurement and investigative approaches in environmental studies of surface water and groundwater. Our particular focus is to relate these results to contaminant fate and transport issues, and show their applicability to DOE programs and to the needs of public water utilities.

Surface water and shallow groundwater are regionally confined to watersheds. A watershed is an area constrained by topographic boundaries, where all stream flow converges at a single point. The quality of surface water and shallow groundwater is ultimately dictated by land use and climate within a watershed.

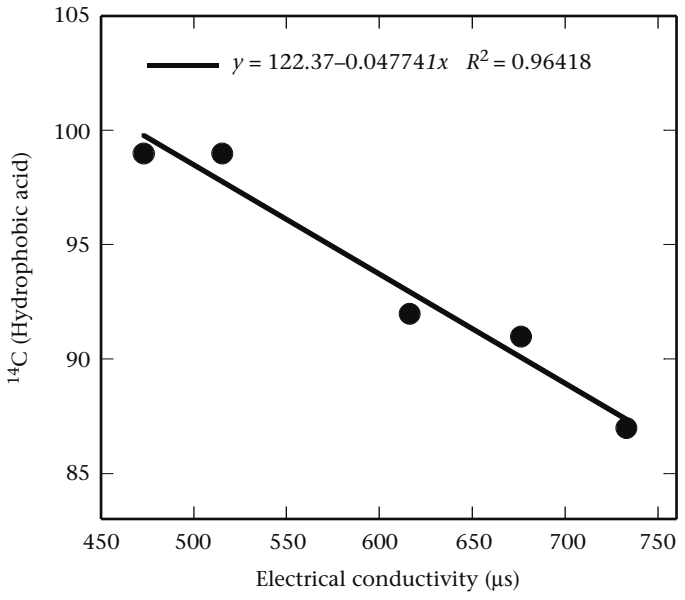

Measurements taken of the Missouri River at St. Louis show that older dissolved organic carbon (lower ^{14}C) and saltier runoff (higher electrical conductivity) originate in the drier upstream Missouri River. Young dissolved organic carbon and dilute runoff originate from the humid downstream.

One NPSP of major concern in watersheds is dissolved organic carbon (DOC). By itself, DOC presents no risk. However, during microbial disinfection of drinking water by chlorination, DOC can be converted to carcinogens such as tri-halomethanes. Increased land use and habitat change in watersheds typically leads to higher DOC concentrations, and regulatory mandates for treating DOC are imminent.

To test if isotope methods could distinguish sources of DOC, measurements were performed on several DOC isolates from major surface waters throughout the Western Hemisphere, representing a range from semi-arid to tropical climates. Measurements were made using standard isolation techniques for DOC and its functional components, followed by accelerator mass spectrometry. Carbon-14 measurements showed that mean radiocarbon ages of the hydrophobic acid (precursor to trihalomethanes) portion of the DOC formed a positive correlation with local mean annual precipitation in the vicinity of sample collection. Bomb-pulse ages (<50 yr) were consistently observed for hydrophobic acids in humid to tropical climates, whereas temperate to arid climates mean ages were as high as 1500 yr. The mean age is proportional to primary productivity rates of local vegetation. However, soil weathering and mineralogy, as well as the amount and solubility of soil organic matter also control carbon sequestration and dissolution rates. The latter is further suggested by an increased aromaticity of the hydrophobic acids with decreasing age, suggesting greater solubility and lower residence times in soil for humid climates.

This relationship is further illustrated for the Missouri River watershed, where downstream precipitation averages ~40 in./yr in a predominantly woodland area, and upstream is dominated by grassland and alpine areas averaging ~20 in./yr. The mean age of hydrophobic acids collected and measured on time series samples at St. Louis inversely correlated with the water's electrical conductivity (EC) (see Fig.). The EC also inversely correlates with the relative proportion of downstream versus upstream runoff, indicating a geographic dependence on DOC source and concentration. The drier upstream climate produces runoff with a higher dissolved salt concentration, has a less weathered soil, and results in higher retention times for soil organic matter. The wetter downstream climate produces runoff with low dissolved salts, but with higher DOC concentration. Because soil is more weathered in the downstream area, DOC is not sequestered as readily and is more soluble.

MEMS-Based Fuel Cell for Micropower Conversion

J. D. Morse, A. F. Jankowski

98-ERD-091

Our new, miniature fuel cell is based on an LLNL-developed technology that combines thin-film expertise with microfabrication and microelectromechanical systems (MEMS). This fuel cell offers a highly compact, lightweight, long-lasting power source with high specific energy compared to existing battery technologies. It will be scalable over a broad range, easily recharged, and compliant with all environmental and safety requirements.

During FY2000, we concentrated on further optimization of the fabrication of high-surface-area, porous-thin-film anodes and manifold. Figures (a) and (b), show thin-film, solid-oxide fuel cells (SOFCs) that were fabricated on silicon substrates. The manifold structures were formed by etching with a deep, anisotropic, silicon-etch process tool. This process has enabled us to use standard integrated-circuit processing to achieve very large-surface-area, porous anode structures for the fuel cell. In developing the fabrication process, we addressed several issues associated with the integration and performance of a fuel-cell stack, micromachined fuel manifold, and flow-field structure. We used photolithographic and etching techniques to create a thin-film, porous-anode structure and then micromachined silicon to form a freestanding fuel-cell membrane. By comparable means, we formed similar structures in the cathode layer. The porous electrode structures enable the rapid diffusion of fuel and oxidant through the electrode structures to the electrolyte interface, and the exhaust of reaction byproducts (water).

To enable manifolding of fuel and oxygen to the anode and cathode, respectively, we constructed a high-temperature test fixture to position the entire assembly in a furnace. Thus, the fuel-cell structure on the micromachined silicon chip was mechanically stabilized as the temperature increased. We measured the performance of the fuel cell by sweeping the voltage. The operation of a thin-film SOFC over the temperature range 300 to 400°C is illustrated in Fig. (c). The SOFC had a porous nickel anode, an yttria-stabilized zirconia electrolyte, and a silver cathode, all deposited using vacuum sputter-deposition techniques. We tested the free-standing SOFC membrane using dilute (4%) hydrogen fuel; the result was the lowest operating temperature reported to date for an SOFC. This low temperature is the advantage offered by utilizing thin-film components for the electrode and electrolyte materials.

In FY2001, we plan to fabricate and evaluate additional electrolytic materials, fabricate manifolding systems with a substrate that will deliver hydrogen-based fuel from a common reservoir to electrode–electrolyte membranes, and evaluate fuel storage and delivery systems.

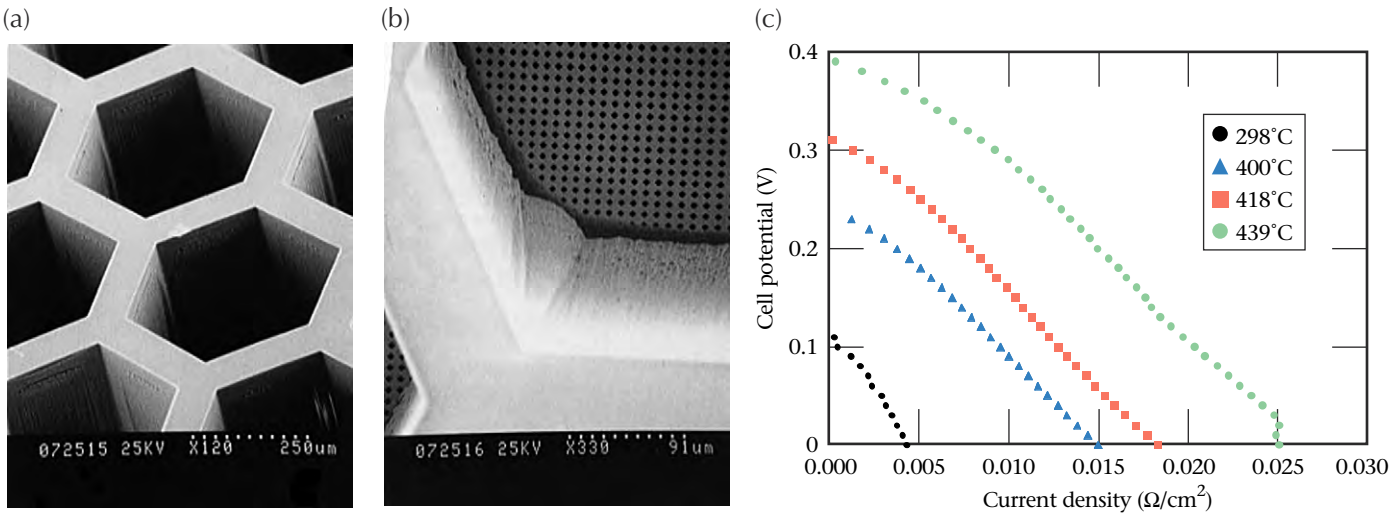

Our new, miniature, thin-film, solid-oxide fuel cell (SOFC), showing (a) the manifold channel, (b) the porous anode (formed by deep, anisotropic, reactive-ion etching), and (c) the present voltage output of the cell.

Chemical Aspects of Actinides in the Geosphere

P. G. Allen, E. R. Sylwester

98-ERD-094

Synchrotron-based x-ray absorption spectroscopy (XAS) is an element-specific, nondestructive, in situ structural probe that determines the oxidation state and local structure (speciation) for the element under study. These properties of XAS make it particularly useful for evaluating and characterizing the fate and transport of actinides [uranium (U), neptunium (Np), and plutonium (Pu)] in environmental samples and for analysis of the bulk phases of metals and alloys. This information is important, because an element's speciation ultimately dictates physical characteristics such as toxicity and solubility. Actinide XAS can provide key chemical information for basic research performed within Department of Energy nuclear-materials stewardship programs (e.g., waste processing and separations, spent fuel and waste forms, aqueous geochemistry, and metallurgy).

We have focused on developing XAS for actinide environmental and materials research. This project serves the dual purposes of developing a fundamental characterization tool for actinide behavior in research relevant to DOE missions (i.e., repositories such as Yucca Mountain, remediation efforts, and Pu disposition) while enhancing LLNL's future capabilities for spectroscopically analyzing actinide elements.

During FY2000, we completed the construction of a new germanium (Ge) x-ray detector and successfully performed XAS experiments in which we investigated Pu speciation in ground water and mineral colloids, U and thorium (Th) complexation with the chelating agents, and the characterization of actinide ceramics and oxides.

Recently, mineral colloids were identified as an important vector for Pu transport at the Nevada Test Site (NTS). To characterize this vector, we investigated the speciation of Pu associated with clinoptilolite (clay mineral) colloids. The Fig. shows that colloidal Pu was observed to be reduced from PuO_2^+ to Pu^{4+} and to form mononuclear surface (inner sphere) complexes with the SiO_4 tetrahedra of clinoptilolite. In the absence of colloids but under the same conditions, Pu remains in the aqueous Pu_2^+ form. These results show that Pu_2^+ is sorbed as Pu^{4+} onto mineral colloids present in the environment. The mechanism for Pu sorption also clearly involves a 1-electron reduction of Pu(V) to Pu(IV), and does not involve precipitation of intrinsic Pu colloids with the form PuO_2. This mechanistic insight into Pu sorption, reduction, and transport is a vital step towards understanding Pu migration away from NTS and its transport in the far field of Yucca Mountain.

We also determined the structural characteristics of UO_2^{2+} and Th^{4+} complexes with the organic ligand Tiron. Tiron complexation is a potential soil-remediation method, and Tiron is known to be an effective complexing agent. Uranyl (UO_2^{2+}) was found to form a 3:3 UO_2^{2+}:Tiron trimer at near-neutral pH conditions that is characterized by inner-sphere, bidentate catechol bonds and oxygen bridging. Thorium forms a 2:3 Th:Tiron dimer where both bidentate catechol and monodentate sulfate bonds are important. The structural determination of these complexes is crucial for the correct thermodynamic modeling of actinide-Tiron complexation and identifies the catecholate groups as active chelating agents.

We achieved our project goals by determining oxidation state and structure for actinides in spent nuclear fuels, ceramic waste forms, cements, and soils, thereby providing a rational scientific basis for ongoing projects involving nuclear and environmental materials management. Future LLNL projects will use XAS to characterize actinides in environmental and materials research programs, while continuing to improve XAS capabilities to study systems at cryogenic temperatures and lower concentrations.

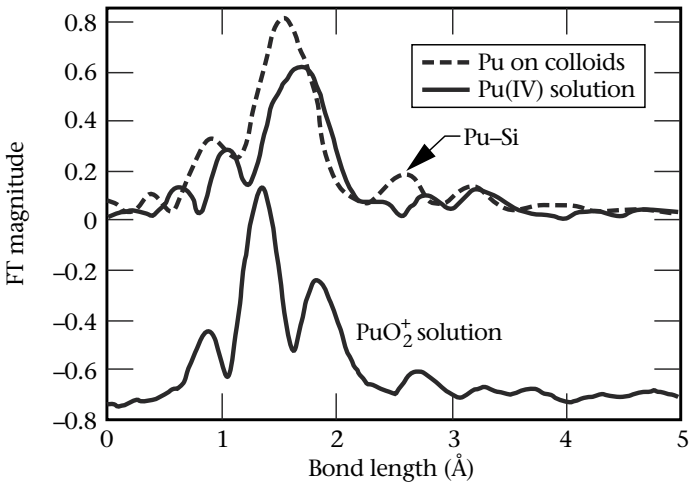

Plutonium x-ray absorption spectroscopy (XAS) Fourier transforms (FTs) of colloidal and solution samples show reduction to Pu(IV) and formation of mononuclear surface complexes at silicon sites.

Back to main TOC

Development of Accelerator Mass Spectrometry Capability for Plutonium and Other Actinides

T. F. Hamilton

98-ERD-100

The need for ultralow-level detection of plutonium (Pu) isotopes is not currently being met by existing technologies, especially in the areas of human bioassay and radiation protection of workers. Conventional alpha-particle spectrometric methods commonly employed around the DOE complex have detection limits for plutonium-239 (^{239}Pu) on the order of 100 to 200 µBq, well above the requirements to satisfy regulatory standards for internal dosimetry programs. Consequently, a long-standing technological shortfall has existed in assuring adequate radiation protection for workers potentially exposed to Pu. Alternative techniques have included fission track analysis (FTA), inductively coupled plasma mass spectrometry (ICP-MS) and thermal ionization mass spectrometry (TIMS). Many of these techniques suffer from one or more of the following problems: uncertainty in levels of recovery and/or removal of fissionable uranium, isobaric or other interferences from molecular species, high background count rates, high sample preparation and measurement costs, and limited throughput for routine bioassay measurements. Previous studies conducted at the Australian National University (Canberra, Australia) had demonstrated that accelerator mass spectrometry (AMS) has the potential to avoid many of these disadvantages and provide a low-level detection capability for ^{239}Pu in the attogram range.

The goals of this project were (1) to develop the necessary sample preparation and analysis techniques/data acquisition routines for low-level actinide AMS measurements while performing the essential upgrades to the CAMS spectrometer in order to (2) allow transport of the heavy isotopes (>100 amu) and (3) improve on isotope selectivity in both the high energy and injection spectrometers.

This project, completed in FY2000, successfully demonstrated the viability of the LLNL AMS for detection of ultralow levels of Pu isotopes for a number of different applications. The final spectrometer included a 45-deg cylindrical electrostatic analyzer (ESA) designed to improve on uranium (U) rejection. Total rejection of U is presently in the order of 1×10^7, yielding reproducible backgrounds on the order of 400 aBq for ^{239}Pu. The demonstrated minimum detection amount (MDA) for ^{239}Pu using ANSI 13.30 for urine bioassay was 4 µBq, but it is conceivable that the combination of longer count times and reducing the sample loading mass could reduce the level of detection down to less than 100 nBq. Instrumental precision was limited by time-dependence in the negative ion output. We developed a fast-switching data-acquisition mode to average out the signal over several passes, and improve on both precision and accuracy. Several hundred analyses have been performed on artificial and human urine, soil, sediment, water, and air filter samples. Measurements of Pu concentrations and isotopic ratios in International Atomic Energy Agency (IAEA) reference materials showed good agreement with reference values and with recent analyses performed by ICP-MS and alpha-spectrometry. AMS offers high efficiency, high rejection of interferences, and low susceptibility to matrix components; it also allows rapid measurement throughput (>50 unknowns per 24 h) and provides for a large dynamic range.

This work clearly demonstrates that the LLNL AMS spectrometer is well suited for detection of ultralow levels of Pu and other actinides, and provides for rapid, cost-effective and robust measurements over a wide range of applications.

Back to main TOC

Mechanisms of Entry for Inhaled Metals into the Central Nervous System: MicroPIXE Analysis of Field Tissue Samples

G. Bench, T. M. Carlsen, P. G. Grant, J. S. Wollett Jr., R. E. Martinelli, J. L. Lewis, K. K Divine

98-ERI-004

Department of Energy sites requiring environmental restoration are characterized by various mixtures of inorganic and radionuclide constituents. Levels of some constituents are sufficient to present human health risks. However, risk evaluation is hindered to the extent that environmental exposure conditions deviate from controlled laboratory studies. In addition, laboratory studies are often not validated through the analysis of tissues from subjects environmentally exposed to these contaminants. A method that can perform spatial, quantitative, multi-element analyses of biological matrices would improve risk evaluation. Field verification using such methods would allow better extrapolation of laboratory data and better prediction of ecological and human health impacts when contaminant exposures occur.

As a demonstration project, we assessed the capability of microbeam proton-induced x-ray emission (microPIXE) to provide such analyses, by investigating factors controlling the transport and toxicity of inhaled metals by the central nervous system (CNS). In FY1999, we trapped California ground squirrels (*Spermophilus beecheyi*) at LLNL's Site 300 facility as subjects, and began using microPIXE to determine the manganese (Mn) and cadmium (Cd) profiles in their olfactory bulbs. Atomic-absorption spectrophotometry was used to measure the Mn and Cd in soil taken from the trapping sites and in the livers and leg muscles of the ground squirrels.

During FY2000, we (1) completed our analysis of ground-squirrel samples, (2) determined (as a reference) the Mn profiles in olfactory bulbs from laboratory rats exposed via nose-only inhalation to 0.53 mg/m^3 Mn in the form of $MnCl_2$, and (3) analyzed our results.

The data from laboratory rats revealed that Mn uptake into the olfactory bulb occurs via inhalation exposure. Data from ground squirrels and our knowledge of the collection sites indicated that olfactory uptake by fossorial rodents affords a significant exposure route for Mn and Cd in soils, although several other routes of exposure may occur. Measured biotransfer factors (the ratio of the metal content in leg-muscle tissue to that in soil) for Cd in ground squirrels were 103 times greater than exposure-modeling estimates based on oral Cd-uptake data from livestock.

Our measurements for ground-squirrel tissues show that a researcher conducting ecological risk assessments for natural habitats should take considerable care in selecting transfer factors. Specifically, transfer factors derived from data pertaining to comparable exposure pathways and ecological settings should be used wherever possible. Although we realize the difficulties in interpreting data from multiple exposure pathways in these field studies, we can relate the olfactory Mn contents in groups of animals to the Mn contents of the soils in their respective habitats. Furthermore, the Mn contents of the olfactory bulbs are higher than the Mn contents of the livers, and the shape of the Mn profiles in olfactory bulbs suggests olfactory uptake. The fact that we can characterize differences in our field sites and potentially use that information to interpret any differences in results, both between sites and between field and laboratory data, should provide us with valuable tools to define future research.

This was the final year of LDRD funding for this project. Exploration of the potential neurotoxic effects of olfactory uptake of Mn compounds will continue under funding by the National Institutes of Health.

Colloidal Transport of Actinides in the Vadose Zone

A. B. Kersting, N. L. Hakim, M. Zavrin, P. G. Allen, L. Wang, P. Zhao, D. K. Smith, C. R. Carrigan

00-ERD-011

Understanding the mechanisms and pathways that control the potential transport of highly toxic, long-lived radionuclides in the subsurface is key to helping design effective storage, cleanup, and containment methods at many Department of Energy sites. Previous actinide-sorption laboratory experiments based on the solubility of the actinides in groundwater suggested limited mobility; yet, this is in direct contradiction to field observations. Our earlier work documented, for the first time, the transport of plutonium (Pu) downgradient from an underground nuclear test at the Nevada Test Site (NTS). There, Pu and other radionuclides [americium (Am), europium (Eu), and cesium (Cs)] were associated with the colloidal (<1-µm particulates) fraction of the groundwater. Colloids are naturally occurring minerals and organics; because of their small size, they are readily transported in groundwater. Currently, there are no adequate conceptual models for understanding actinide transport in the subsurface. Even less is known about the transport mechanisms in the partially-saturated subsurface, called the vadose zone.

In this project, we have undertaken an integrated field, laboratory, and modeling approach to pursuing the dominant geochemical controls on colloid-facilitated transport of actinides [e.g., Pu, neptunium (Np)]. We are investigating mechanisms for Pu sorption on mineral colloids collected at NTS, but in well-controlled laboratory experiments in which the field chemistry and colloidal content are constrained. This work integrates both field and laboratory studies into a reactive-transport model of subsurface transport. Our ultimate objective is to develop a framework for predicting when colloid-facilitated transport of actinides may occur in the vadose zone, quantitatively describe these results, and develop a flow and transport model based on our experimental results.

During FY2000, we successfully collected and analyzed vadose-zone waters affected by underground nuclear tests in Rainier Mesa, NTS. The purpose of our field study was to determine what radionuclides were transported in fractured volcanic tuff, their concentrations, if they were associated with the colloidal fraction of the groundwater, and if so, the identity of the mineral colloids. These results help focus our experimental evaluation of the sorption capacity of Pu on mineral colloids detected in the field. Plutonium, Am, strontium (Sr), Cs, and tritium were detected in the water, and more than 95% of the Pu and Am activity was associated with the colloidal fraction of the water. Colloids consisted of clays, zeolites, and calcite.

Sorption experiments using Pu(IV) and P(V) were carried out on the zeolite, clinoptilolite. Sorption for Pu(IV) on clinoptilolite is quite strong. Initial x-ray atomic fine structure (XAFS) analysis of the experimental-run products showed that the Pu(IV) remained as Pu(IV) oxidation state, but the Pu(V) was reduced and sorbed as Pu(IV) (see Fig.). This is the first time this reduction process has been documented; it has important implications for modeling the transport of Pu.

In FY2001, we will (1) continue our sorption experiments of Pu onto clays and calcite colloid minerals found in the vadose-zone water at NTS to determine which minerals preferentially sorb Pu, and (2) initiate Np-sorption experiments and model our results. We will also use high-resolution transmission electron microscopy (TEM) to image the actinides on the mineral surfaces of both the natural samples from NTS and the experimental-run products.

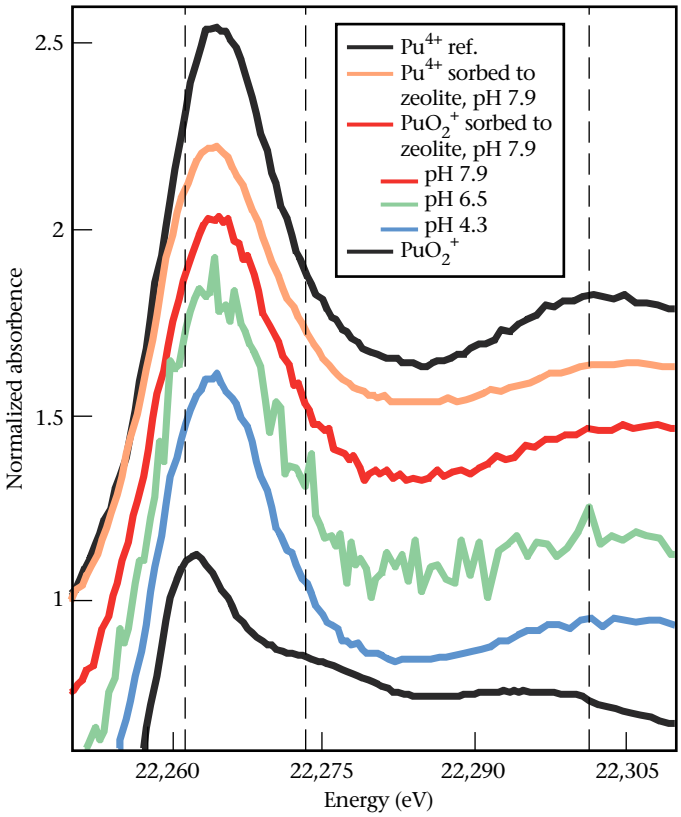

X-ray absorption near-edge structure (XANES) spectroscopy of Pu sorbed onto clinoptilolite compared with reference standards Pu(IV) and Pu(V). All experimental samples contained Pu(IV).

Research Concerning the Direct Conversion of Fossil Fuels into Electricity

N. J. Cherepy, R. Krueger, J. F. Cooper

00-ERD-059

Direct conversion of fossil fuels into electricity offers more efficient use of fossil fuels and reduced CO_2 production per unit of energy. Our research into the direct electrochemical conversion of reactive carbons into electricity shows experimental evidence of total efficiencies exceeding 80% of the heat of carbon combustion at reaction rates approaching those of hydrogen fuel cells (100 mA/cm^2). Fuel cell technologies involve synthesizing hydrogen, which itself is an energy-intensive process. Direct carbon conversion, an electrochemical process that obviates the need for synthesizing hydrogen, represents a potential breakthrough technology. Together with technologies for extracting reactive carbons from a wide range of fossil fuels, direct carbon conversion addresses the ultrahigh (>70%) efficiency objectives of the Department of Energy's 21st Century Fuel Cell program and the broader objectives of managing CO_2 emissions and using fossil fuel resources at increased efficiency.

Our research focuses on (1) developing electrochemical cells in which carbon is efficiently converted into electricity and (2) using these cells to explore the reactivity of carbons derived from diverse sources, including pyrolyzed hydrocarbons, petroleum cokes, purified coals and biochars. Our goal is to empirically identify highly reactive fuels and relate electrochemical reactivity to fundamental nano/microstructural characteristics of the carbon samples.

Our electrochemical cell uses a Li_2CO_3/K_2CO_3 (46.6/53.4 wt %, 38/62 mole %) carbonate electrolyte and oxygen (air) in the cathode compartment, and a slurry consisting of molten carbonate electrolyte and carbon fuel in the anode compartment. A porous ceramic separator transports dissolved CO_2 and carbonate ions between the two compartments, which allows the cathodic half reaction: $O_2 + 2CO_2 + 4e^- = 2CO_3^{2-}$ and the anodic half reaction: $C + 2CO_3^{2-} = 3CO_2 + 4e^-$ to occur. The net reaction is $C + O_2 = CO_2$. During FY2000, we demonstrated working rates as high as 100 mA/cm^2 at 0.8 V and 200 mA/cm^2 at 0.5 V with a particularly reactive fuel, Carbon 3. The Fig. shows dramatically different power density curves for three carbon samples, Carbons 1, 2 and 3. The more power per area in the same electrochemical cell, the more reactive the carbon.

Correlating structural characteristics of the carbon samples with their reactivities provides important insight into the basis for electrochemical reactivity. We use several techniques to characterize candidate fuels: (1) transmission electron microscopy (TEM) reveals primary particle size and aggregate size, (2) nitrogen-2 adsorption provides specific surface area measurements, (3) x-ray diffraction exposes the layer spacing (*d*-spacing) and relative lattice disorder (L_c), (4) thermal gravimetric analysis (TGA) shows chemical reactivity to air oxidation. Small L_c values, low decomposition temperatures, and high surface area are correlated with high reactivity.

During FY2001 we plan to continue testing a wide range of candidate carbon fuels, correlating their electrochemical reactivity with structural characteristics. We will focus on samples, provided by potential industrial partners, that possess characteristics we know to correlate with reactivity. A scaled-up direct carbon conversion cell, capable of producing from 0.1 to 1 kW per stackable cell, will also be built.

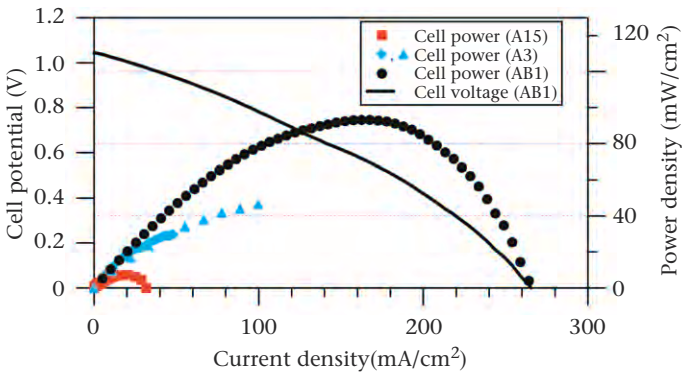

One carbon sample, Carbon 3, shows a peak power near 100 mW/cm^2.

Back to main TOC

Investigation of the Effect of Magnetic Configuration on Spheromak Performance

D. N. Hill

00-SI-008

The Sustained Spheromak Physics Experiment (SSPX) device was designed to study how well the spheromak can contain plasma energy while the confining magnetic fields are maintained by dynamo processes in the plasma itself. The SSPX design offers the potential of dramatic improvements in operation over previous spheromak experiments because it is compact, free of field coils linking the vacuum vessel, and can be operated in a steady state with voltage applied to external electrodes. Scientists have predicted that the ability of the SSPX to contain the plasma thermal energy will increase with increasing plasma electron temperature—the hotter it is, the better it will work. Our near-term goal is to determine which of several different magnetic field configurations works best to produce hot, well-confined spheromak plasmas. We also want to verify the predicted inverse relationship between plasma temperature and heat loss and use these results to design an even higher-temperature follow-on experiment that will push closer to fusion conditions.

Compared to previous spheromaks, the new features of the SSPX device include a large-radius coaxial plasma injector to improve efficiency, a conformal flux conserver to minimize open field lines around the plasma, a divertor to aid in cold-particle exhaust, and a set of programmable-bias magnetic-field coils to vary the magnetic geometry.

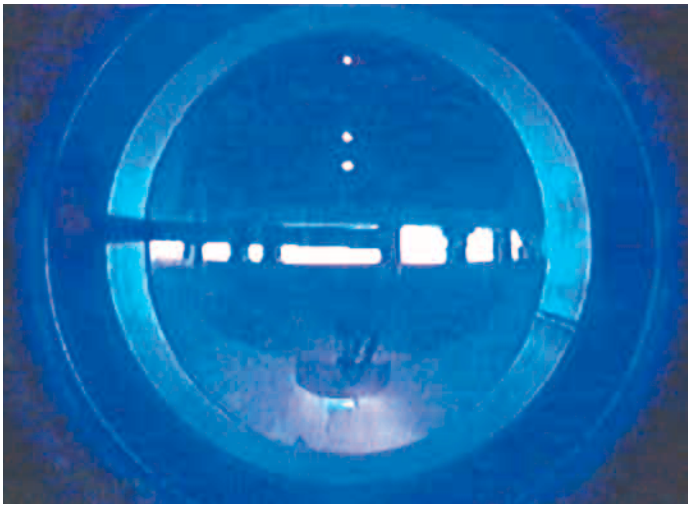

This photograph, taken from a viewport looking inside the Sustained Spheromak Physics Experiment (SSPX), shows a horizontal band of bluish-white light coming out of the observation slot from the two-million-degree plasma contained within.

A number of sophisticated instruments are required to diagnose our experiments, including vacuum ultraviolet spectrometers, high-speed TV cameras, and a Nd:YAG Thomson-scattering system, which measures the interior plasma density and temperature. In addition, we plan to measure the structure of the internal magnetic fields produced by the plasma dynamo using a transient internal probe, now being installed by a graduate student from the University of Washington. This device will measure the Faraday rotation of laser light inside a small glass bullet, which is fired through the plasma at 1.5 km/s by a gas gun. Taken together, these measurements will provide our team with unprecedented detail on how the spheromak works and how it heats the plasma contained in it.

During FY2000 we carried out experiments to determine how well the SSPX device is working in its initial magnetic field configuration, and we commissioned new hardware designed to reduce the impurity (carbon, oxygen, and nitrogen) contamination of the plasma. Impurity radiation losses were high at first, but application of glow discharge cleaning and titanium gettering reduced them to acceptable levels. Our measurements show that the SSPX device is now working as expected, and we are making detailed comparisons between numerical simulations (the CORSICA and NIMROD codes) and experimental data.

At the end of FY2000 we stopped operating SSPX to install a new set of six magnetic field coils that will allow us to form plasmas with four different magnetic configurations. These configurations should allow the spheromak to obtain higher internal magnetic fields and hotter plasmas through better utilization of the vacuum field and reduced plasma turbulence. Preliminary experiments using the initial SSPX coil set to simulate some aspects of operating with the new coils yielded encouraging results.

Plasma temperatures in SSPX so far match the best results from previous sustained spheromak experiments (see Fig.), and higher temperature plasmas are expected once we start operating with the new bias magnetic field coils. Initial Thomson-scattering measurements show the peak electron temperature of 120 eV during a period where magnetic field fluctuations are at low levels. We are now analyzing magnetic field measurements to see if this is a new mode of spheromak operation. During FY2001 we will further explore this operating regime and will evaluate three new magnetic-field configurations using the recently installed bias-field coils.

Lasers/ Electro-optics/ Beams

6

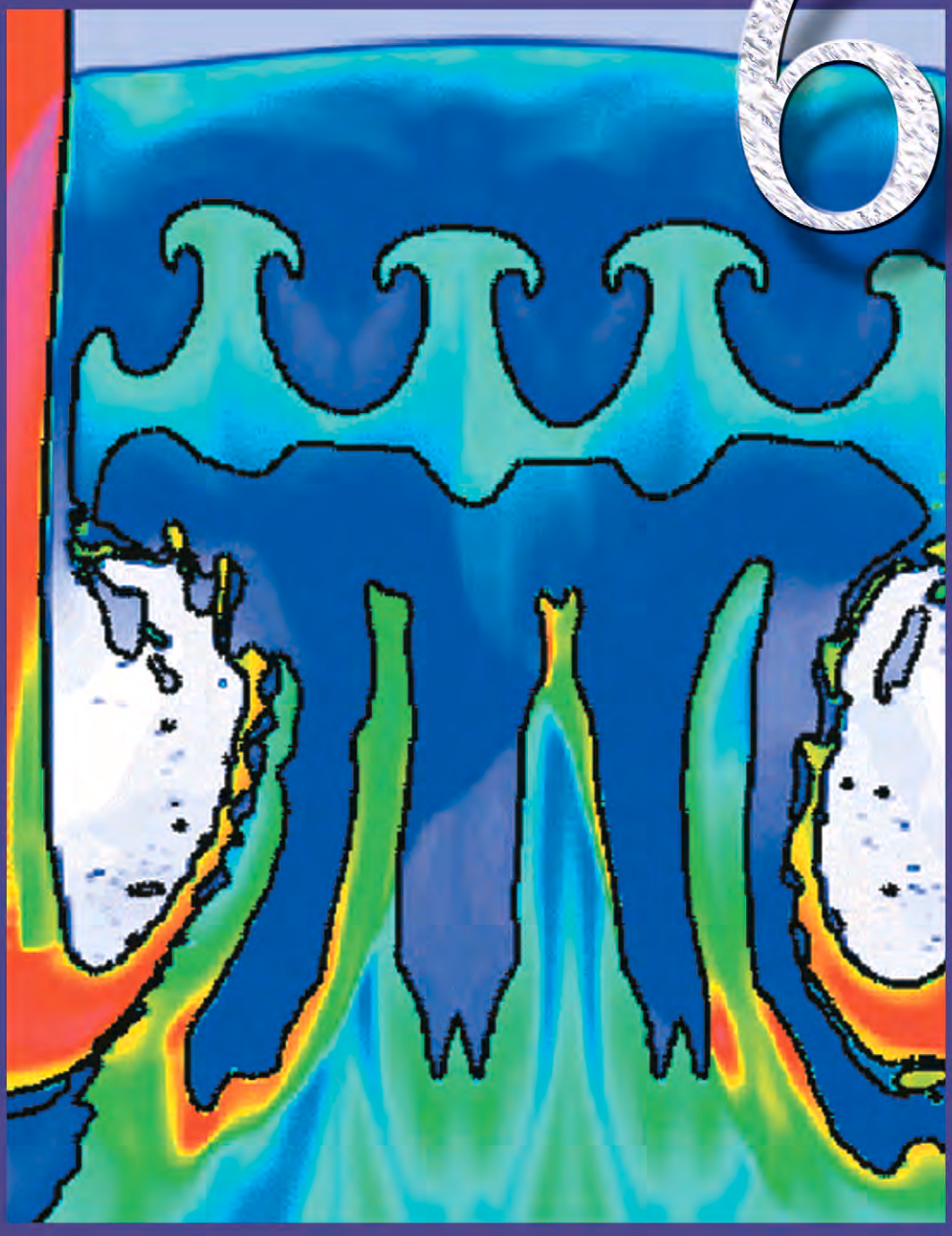

Section 6—Lasers, Electro-Optics, and Beams

Advanced Wavefront-Control Techniques

S. S. Olivier, C. A. Thompson, M. W. Kartz, J. M. Brase, C. J. Carrano, R. M. Sawvel, D. A. Silva

98-ERD-061

Programs at LLNL that involve advanced laser systems depend on the maintenance of laser-beam quality through precise control of the optical wavefront. This can be accomplished using adaptive optics (AO), which compensate for time-varying aberrations that are often caused by heating in high-power laser systems. Over the past two decades, LLNL has developed a broad capability in AO technology for both laser-beam control and high-resolution imaging. This AO capability has been based on thin, deformable glass mirrors with individual ceramic actuators bonded to the back. In the case of high-power lasers, AO systems have successfully improved beam quality. However, many high-power laser systems would benefit from additional correction of high-spatial-frequency aberrations that require control of hundreds or thousands of phase points.

The largest conventional deformable mirrors currently available have approximately 1,000 actuators and cost about $1M, or $1,000 per actuator, making deformable mirrors prohibitively expensive for many applications that require high-spatial-frequency wavefront control. A new approach with the potential to solve this problem, liquid-crystal (LC) spatial light modulator (SLM) technology, provides high-spatial-frequency wavefront control, with hundreds of thousands of degrees of freedom, more than two orders of magnitude greater than the largest deformable mirror. Furthermore, even with the increased spatial resolution, the cost of these devices is nearly two orders of magnitude less than the cost of the largest deformable mirror. Thus, LC SLM devices have the potential to create a paradigm shift of four orders of magnitude in the cost per phase-control point for advanced AO.

During FY2000, the third and final year of this project, we integrated a commercially available LC SLM device into the AO testbed that we had previously developed for this project. Our testbed employs a high-resolution wavefront sensor that measures the slope of the wavefront at 2000 points across the aperture. This slope information is then processed to yield the wavefront phase. To reduce the computation time for phase reconstruction, we developed new algorithms. Based on Fourier transform techniques, these algorithms require fewer computations than the traditional matrix–vector multiplication approach for systems with large numbers of phase-reconstruction points.

After integrating the LC SLM into the testbed, we performed a detailed characterization of the high-resolution wavefront-control performance of this device. Our tests successfully demonstrated near-diffraction-limited performance of the LC SLM at a wavelength of 594 nm [Figs. (a,b,c,d)].

To our knowledge, these are the first quantitative measurements to demonstrate near-diffraction-limited performance of a wavefront-control system that incorporates an LC SLM. The combination of the large number of phase-control points and the demonstrated wavefront quality makes this technology a viable choice for high-performance beam-control and image-compensation applications that require high-order correction beyond the capability of conventional deformable mirrors.

On the basis of our work, new projects have begun to apply this technology to systems for precision laser drilling and to studies of enhanced human vision. Many other laser and imaging systems could ultimately benefit from this technology.

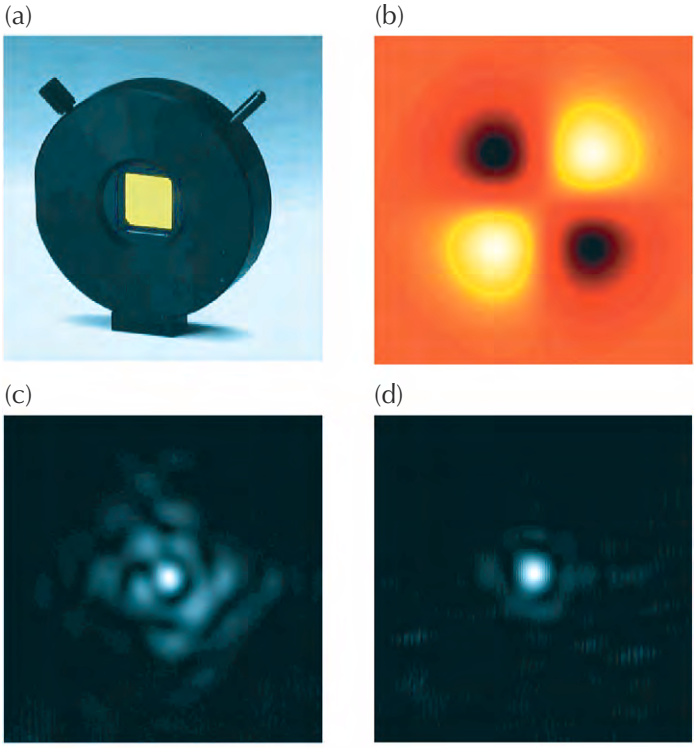

Using (a) a commercially available liquid-crystal (LC) spatial light modulator (SLM), we applied (b) a wavefront-aberration and obtained (c) the resulting aberrated far-field image. After closing the control loop, we obtained (d), a corrected far-field image of near diffraction-limited quality.

3ω Damage: Growth Mitigation

L. Hrubesh, M. Kozlowski, S. Demos, Z.-L. Wu, J. Wong, B. Penetrante

98-ERD-063

The design of high-power ultraviolet (UV) laser systems is limited by laser-induced damage of transmissive fused silica (SiO_2) optics. Laser-induced damage involves two key issues: initiation at some type of precursor and rapid growth due to subsequent laser pulses. The objectives of this 3ω damage effort were to apply state-of-the-art characterization tools to elucidate the nature of the initiated damage sites and to use mechanistic models to quantify and potentially reduce the risk of damage to fused silica surfaces. During the first two years of this effort, we focused on optical characterization and reduction of damage initiation. Although we achieved significant reductions in the density of damage sites on polished surfaces, statistically some amount of damage initiation should always be expected. In FY2000, we focused on the damage-growth issue. Our goal was to understand the cause(s) of the rapid growth of damage sites and develop and apply means to mitigate that growth.

The prevailing hypothesis for the growth mechanism involves a synergism of some means for absorption of 3ω light at the damage site and at local field enhancement due to cracks. In FY2000, we focused on identifying the absorbing species and developing growth-mitigation techniques for removing both the absorbing species and the cracks. One proposed mechanism for damage growth involves the transformation of nonabsorbing SiO_2 to form an absorbing layer of d-SiO_x. Here, d-SiO_x implies that SiO_2 is modified in terms of either the formation of other stoichiometries (e.g., SiO; Si; or more generally SiO_x with $0 < x < 2$) or significant concentrations of defects (broken bonds, vacancies, etc.). We applied a variety of analytical tools, including photoluminescence (PL) spectroscopy, optical and photothermal microscopies, high-resolution transmission electron microscopy (TEM) and electron spin resonance (ESR), x-ray photoelectron spectroscopy (XPS) and secondary-ion mass spectroscopy (SIMS), x-ray microtomography, and cathodoluminescence (CL). We mapped regions of high absorption within the damage sites and showed that within those sites there is a densified layer that contains E′ centers, nonbonding oxygen hole centers (NBOHC), and oxygen-deficient centers (ODC II). We correlated the PL spectral signatures (see Fig.) and the CL results with certain defects in silica such as the NBOHC and ODC II. No evidence for d-SiO_x was found.

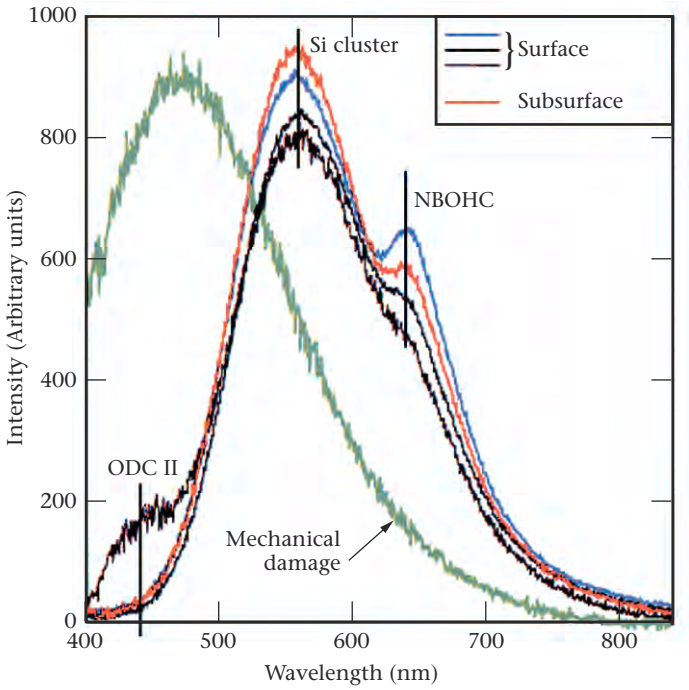

Luminescence emission from a typical laser-induced damage site on fused silica. Shown are peaks identified with certain defects at the molecular level: oxygen-deficient centers (ODC II) and nonbinding oxygen hole centers (NBOHC). Silicon (Si) clusters are most likely related to the central peak, but this assignment is still uncertain.

We concluded from analytical and experimental results that, for successful mitigation, a process could not be applied superficially; it must be able to affect the silica well below the damaged surface. We demonstrated that chemical etching of the silica surfaces to depths greater than 5 μm raised the damage threshold by 30% and effectively mitigated growth for 60% of the tested sites at laser fluences from 6.9 to 8.4 J/cm^2. We achieved partial mitigation of damage growth for fluences as high as 8 J/cm^2. The process was successful because it mended cracks and returned the defect-rich densified layer to the normal amorphous state, thus eliminating both conditions responsible for the damage growth.

In addition to a partially successful mitigation process, we achieved a basic and detailed understanding of the morphology, microstructure and defect chemistry of initiated damage sites, and the damage growth behavior.

Picosecond X-Ray Source Development via Laser–Plasma and Laser–Electron-Beam Interactions

K. B. Wharton, J. Crane, T. Ditmire

99-ERD-036

This project had the goal of creating a picosecond-duration, hard x-ray source using the 35-fs, 5-TW Falcon laser to produce K-alpha radiation from solid and foil targets. Titanium (Ti) was the primary target material for the ideal 4.5-keV characteristic x-ray energy.

Although other groups have had success in making a picosecond copper (Cu) K-alpha source from intense, short-pulse, laser–solid interactions, this project met with difficulty repeating the process with Ti foil targets. The x-ray yield was found to vary daily by more than an order of magnitude. Further investigation revealed that low-intensity prepulses were negatively affecting the primary laser–solid interaction. This new line of research yielded a paper (in press).

Based on our research, we presented theoretical and experimental evidence that nonionizing prepulses with intensities as low as 10^8 to 10^9 W/cm^2 could substantially alter high-intensity laser–solid interactions. Prepulse heating and vaporization of the target can lead to a preformed plasma once the vapor is ionized by the rising edge of the high-intensity pulse (see Fig.) Our FY2000 results indicated that peak prepulse intensity is not the only important parameter to consider in determining preformed plasma thresholds; a more comprehensive analysis of the prepulse duration and target material is required.

This work explained the anomalous results from our Ti targets and suggested how to best design future short-pulse x-ray sources using high-reflectivity, high-thermal diffusivity materials such as Cu for the front layer. In addition, the results also help explain the widely known but little-understood difference between transparent and opaque targets in high-intensity laser–solid interactions, as well as other anomalous high-intensity results.

The most important result of this project, completed in FY2000, was the demonstration that conventional wisdom concerning long-duration (nanosecond) laser prepulses is incorrect. While some sources claim that prepulses below 10^{11} W/cm^2 are irrelevant, this work conclusively shows that, for some situations, prepulses as low as 10^8 W/cm^2 can dramatically affect the subsequent high-intensity interaction. These results will have important consequences for many high-intensity laser–solid experiments.

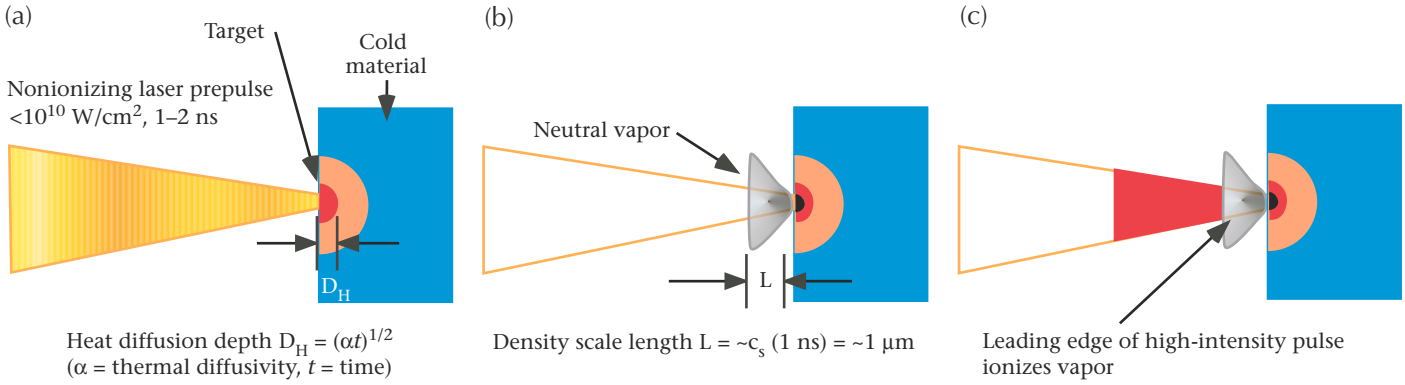

By a three-step process, a traditionally nonionizing pulse (10^8 to 10^9 W/cm^2) can lead to a preformed plasma on a solid target: (a) a nonionizing laser prepulse creates (b) a neutral-gas plume, which is then (c) ionized by the rising edge of the subsequent high-intensity laser pulse.

Fundamental Studies for High-Brightness, High-Average-Power Laser Design

L. Zapata, R. Beach and S. Payne

99-ERD-037

The interest and motivation to press forward with laser weapons for the 21st century fighter is emerging as a compelling national need. The average power for laser weapons is at least 20 kW, though 100 kW would be more desirable and well beyond industry standards. Higher output industrial lasers—100 kW or more—would enable applications that are mere speculation today. For example, welding, drilling and cutting of thick plates, such as those used in the shipping industry, would be technically and economically possible.

Our goal for this project is to prove the applicability of several innovations that will be used in building a diode-pumped, solid-state laser of scaleable, high-average power with beam quality. Our thin-disk laser designs can be adapted to yield extremely high-average power levels. Experiments conducted in FY2000 have given us the confidence in our scalability arguments to envision the development of laser devices that are capable of producing 100-kW and higher output power. Continuous laser power at such levels makes credible deployment of laser weapons with the ability to engage high-speed maneuverable targets (i.e., missiles) with speed-of-light reaction time. Furthermore, it will provide opportunities for an unexplored realm of industrial applications.

In our approach, a very thin Yb:YAG gain disk is soldered to one large face of a cooler and is diffusion bonded to a thicker, index-matched, optically passive "cap-disk" on the other large face. The resulting composite, laminated laser disk has the dual purpose of preventing parasitic lasing buildup while facilitating the pumping of the gain medium by diode-pump light introduced at the edges. Prismatic facets cut into the edges provide a method by which copious pump light is introduced and trapped within, thus passing repeatedly through the gain medium. Similarly, spontaneous emission within escapes the laser-active volume via these facets. A large face of the laser disk is opened and used for laser extraction—described as edge pumping with face cooling.

In FY2000, two designs of the Yb:YAG/YAG composite gain element were fabricated. The HiBriTE project team achieved laser action with the samples using the apparatus shown (see Fig.). Pump delivery into the ends of the undoped YAG-Yb:YAG composite gain element was achieved using two radiance-conditioned laser diode arrays and lens ducts. Laser power of 260 W at low duty factor ensued. The data were used to anchor the laser modeling codes. Strong excitation and cooling of the thin 0.2-mm laser gain medium within the much thicker laser disk was demonstrated and found to be consistent with predictions. Amplified spontaneous emission and parasitic lasing were absent and gain distributions were consistent with our models in these initial experiments. The efficacy of heat removal using our first-generation cooler was tested; calorimetric data under continuous pumping showed that we reached a maximum heat dissipation rate of 1.1 kW/cm^2, which was confirmed by our thermal code, and gave us confidence in our advanced cooler design.

In FY2001, we will continue to develop the high-performance, high-reflectivity coatings required in lasers to withstand the stressing thermal environment associated with our approach. We also will experiment with telescopic resonators. Advances in these two areas will enable continuous laser output with high beam quality.

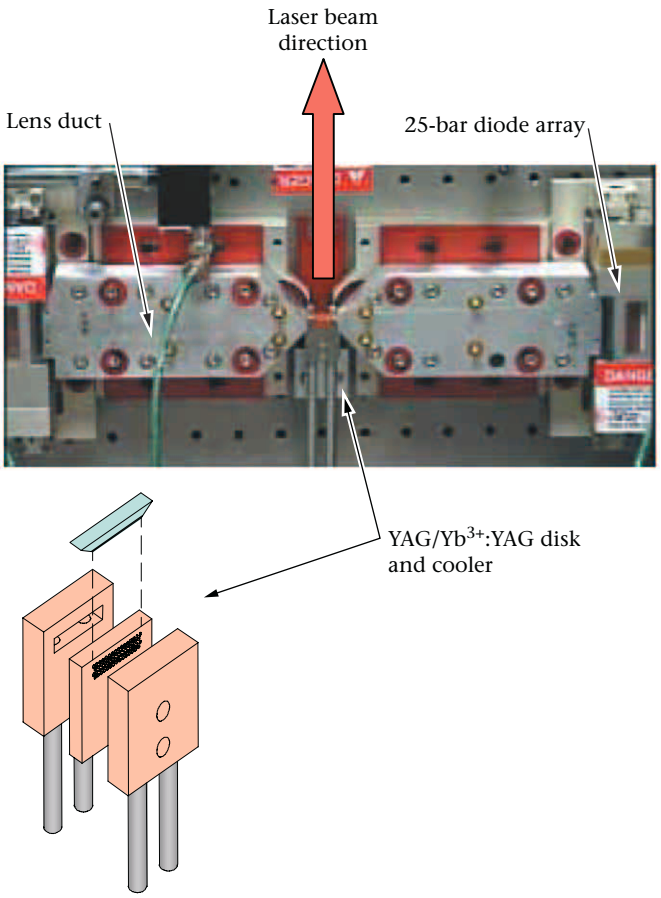

Two radiance-conditioned diode stacks concentrated by lens ducts that inject pump light into the composite laser disk soldered to the cooler in the center.

Critical Density Interaction Studies

P. E. Young, C. H. Hansen, H. A. Baldis

99-ERI-007

For many years, the interaction of high-intensity electromagnetic waves with the coronal plasma surrounding ignition targets has been of interest to many Laboratory projects, including the Fast Ignitor project, direct-drive studies for the National Ignition Facility (NIF), and investigations involving x-ray radiography research, high-energy x-ray backlighters, and laser cutting. Understanding laser propagation through under-dense plasmas is important because—in many laser–target experiments—the laser beam can filament or self-focus, changing the laser intensity at the target from that measured in a vacuum. A secondary effect of filamentation is that the levels of the stimulated Brillouin and Raman scattering (SBS and SRS, respectively) instabilities can change because filamentation changes the laser intensity, the density, and the density gradients upon which the growth of the SBS and SRS instabilities depend. These instabilities may be important because SBS can also modify the amount of light coupling into the target, and SRS can generate hot electrons that can heat the target.

In this project, we addressed three aspects of laser–target coupling: (1) absorption mechanisms in high-intensity, short-pulse, laser–target interactions; (2) control of laser-propagation properties in under-dense plasmas by changing the shape of the laser pulse; and (3) development of simulations to accurately model the propagation of high-intensity laser pulses through high-density plasmas.

In FY2000, we published the results of critical density interaction studies using 130-fs-long laser pulses at intensities up to 5×10^{16} W/cm^2. By observing the intensity scaling of the second-harmonic spectral shape for different incident-laser polarizations, we were able to show that the dominant absorption mechanism for near-normal incidence is the anomalous skin effect. The anomalous skin effect, a collisionless absorption mechanism, becomes important when the intensity of the incident laser is high enough that the mean free path of the electrons exceeds the skin depth. This effect is vital to understanding the coupling of high-intensity light to high-density plasmas.

We also analyzed data from the Janus laser in which a 1-ns-long laser pulse propagated through an under-dense plasma. Less spreading caused by the filamentation instability was observed with a Gaussian-shaped pulse than with a square pulse with a leading-edge risetime of 100 ps. Hydrodynamic simulations using adiabatically rising pulse shapes showed that, if the risetime of the pulse is less than the time for the plasma to move out of the beam, then filamentation can be avoided—if the density of the laser channel is lowered such that the pulse is always below the filamentation threshold.

During FY2000, our collaborators at the University of Alberta developed theoretical tools for modeling filamentation and SBS at high plasma densities. These instabilities involve plasma waves with a wave number such that the product of the wave number and the mean free path for electron–ion collisions is of order 1. They derived a theory of SBS and filamentation from a nonlocal hydrodynamic model that is valid in the entire range of the product of the wave number and the mean free path and that also includes thermal processes. Their results were published.

As a result of their work, we identified important absorption mechanisms at critical density. We also continued the development of new modeling capabilities for designing pulse shaping that allow propagation of focused laser beams through coronal plasmas.

Computational and Experimental Development of a Compton X-Ray Source

H. A. Baldis, F. V. Hartemann

99-ERI-008

Remarkable advances in ultrashort-pulse laser technology based on chirped-pulse amplification and the recent development of high-brightness, relativistic-electron sources allow the design of novel, compact, monochromatic, tunable, femtosecond x-ray sources using Compton scattering. Such new light sources are expected to have a major impact in a number of important fields of research, including the study of fast structural dynamics, advanced biomedical imaging, and x-ray protein crystallography. However, the quality of both the electron and laser beams is of paramount importance in achieving the peak and average x-ray spectral brightness required for such applications.

One of the primary purposes of our work has been to establish a theoretical formalism capable of fully describing the 3-D nature of the interaction between electrons and photons, and the influence of the electron and laser-beam phase-space topologies upon the spectral brightness of the x-rays. During FY2000, we completed both these tasks—ours was the first detailed analysis of its kind. The Fig. shows an example of the level of detail reached by our 3DCOMPTON code, where the "imprint" of the quadrupole focusing magnets clearly appears on the x-ray beam.

Technical breakthroughs in the fields of diode-pumped solid-state lasers (DPSSLs) and high-brightness electron sources have provided us with a unique opportunity to develop an entirely new class of advanced x-ray sources, with characteristics approaching those of third-generation light sources, in a much more compact and inexpensive package. This, in turn, offers the possibility of an important spinoff of ultrashort-pulse laser technology into the field of molecular biology, which is currently growing at an exponential rate. In addition, a new paradigm for rational drug design has now emerged, using both recombinant DNA technology and x-ray protein crystallography.

In protein crystallography, recombinant DNA technology is used to produce large quantities of a given protein by splicing the corresponding coding DNA sequence into the genetic material of a bacterium. The key characteristics of an x-ray source useful for protein crystal lography are its small size, low angular divergence, good transverse coherence, and high average spectral brightness. These requirements determine the necessary electron and laser beam quality.

Our goal for FY2001 is to apply our FY2000 results and LLNL's expertise in ultrashort-pulse laser technology toward completing the design of a compact, 1-Å Compton scattering x-ray source for use in x-ray protein crystallography. We plan to use a compact, high-quality, integrated electron linear accelerator (linac); a high-brightness photoinjector; and a tabletop, terawatt laser to produce high-brightness x-ray flashes at a repetition rate of 10 Hz. This system will demonstrate proof-of-principle Compton x-ray generation and will also allow the detailed benchmarking of our 3-D x-ray code. Scalability to higher repetition rates will also be an important component of this endeavor.

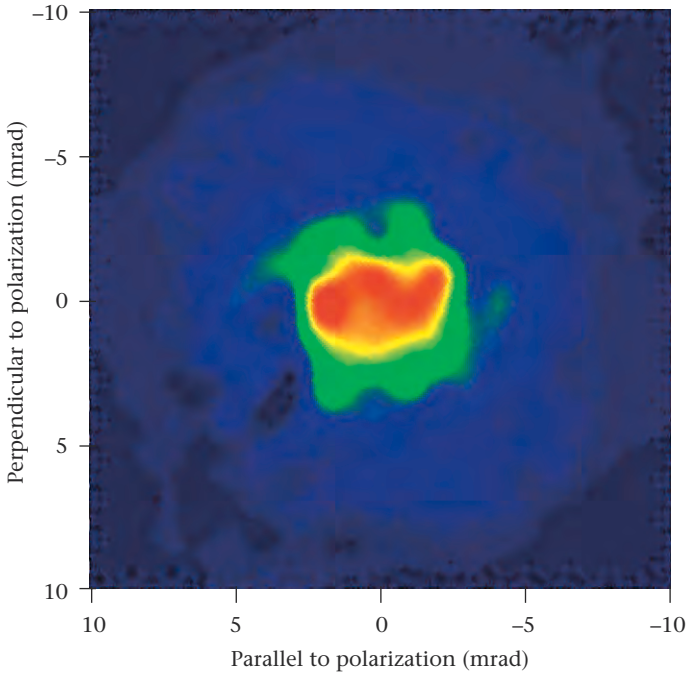

Simulation of a 1-Å x-ray output from our 3-D Compton scattering code 3DCOMPTON, showing the effect of quadrupole focusing.

Back to main TOC

An Inner-Shell Photoionized X-Ray Laser at 45 Angstroms

F. A. Weber, P. M. Celliers, S. J. Moon, L. B. Da Silva

99-LW-042

Long before lasers capable of generating x-rays were developed, researchers had already anticipated their applications and benefits in biology, biomedical imaging, materials science, and plasma physics. With the advent of a new generation of chirped-pulse amplification techniques, powerful and ultrashort-pulse-duration pump lasers now have the capability of shrinking source dimensions from occupying whole rooms to tabletop size. Most applications require x-ray laser wavelengths within or even below the water window (from 26 to 44 Å) which tabletop-sized schemes cannot produce, as has been demonstrated in recent years.

In this project, we have pursued the inner-shell photoionization (ISPI) approach to x-ray lasing. The laser transition is pumped by an incoherent x-ray source realized through the impact of a high-intensity, ultrashort laser pulse onto a high-atomic-number absorber coated on top of a light-element lasant material. Using carbon (C) as an example, the underlying concept is based on the fact that the photoionization cross section is much larger for the tightly bound inner-shell (1s) electrons than for the more loosely bound outer-shell (2s, 2p) electrons. Photons with energies above the carbon K-absorption edge (~286 eV) selectively knock out the inner-shell electrons, leaving a hole state $1s2s^22p^2$ in the singly charged carbon ion. This generates a population inversion to the radiatively connected state $1s^22s^22p$ in C^+, leading to a gain on the 1s-2p transition at 45 Å. The resonant character of the lasing transition in the single ionization state intrinsically allows much higher quantum efficiency compared to other schemes. Competing processes that deplete the population inversion and rapidly quench the gain include autoionization, Auger decay, and, in particular, collisional ionization of the outer-shell electrons by electrons generated during photoionization.

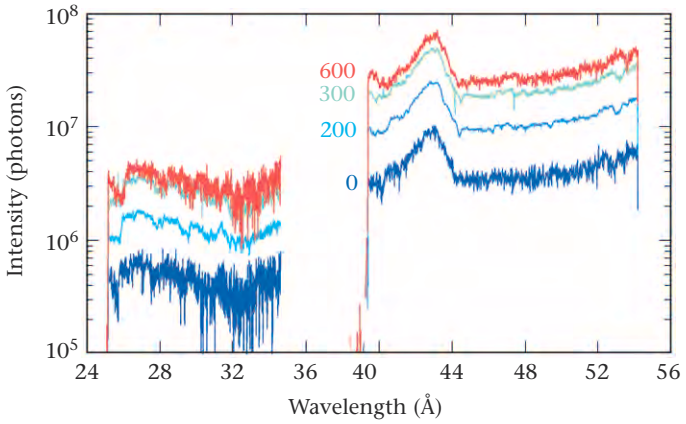

Time-integrated target (200 Å Au/1 kÅ Ti) backside emission for various focal distances: 0 μm, 200 μm, 300 μm, and 600 μm.

In FY2000, we completed the static spectroscopic investigation of x-ray emission from the target backside. The optimal target comprises a 200-Å gold absorber coated with 1 kÅ of titanium (Ti) for soft x-ray attenuation. The Fig. shows the measured spectral composition of the x-ray output around the carbon K-absorption edge (43.7 Å) for various focal distances. Data were taken using maximum energy through the four-pass amplifier and the air-pulse compressor at the Ti:sapphire-based Falcon ultrashort-pulse laser facility. We achieved 100 mJ of energy in a single 35-fs pulse at center wavelength of $\lambda = 820$ nm. The laser was focused on target by means of an off-axis parabola at *f*/2. The spot size at best focus measures 23 μm full width at half maximum (FWHM), which corresponds to a laser intensity on target of 6.9×10^{17} W/cm^2. The conversion efficiency at maximum backside emission is 1×10^{-4}. Double- and multiple-pulse experiments did not show an increase in the output x-ray intensity or the conversion efficiency independent of delay. The pump energy must be delivered over the length of the lasing medium, with a rise time of 50 fs, which can be accomplished by a traveling wave scheme.

We finalized the design of an all-reflective optical system relay imaging a diffraction grating onto the target surface to provide the required tilt in the group velocity. The design employs a holographic grating that compensates for primary aberrations and an arrangement of spherical optics.

In FY2001, we plan to complete dynamic target x-ray spectroscopy and assemble and install the holographic-grating-based, traveling wave-pumping system at the Falcon laser facility. This should enable us to measure gain and x-ray laser characteristics from a low-density (10^{20} at/cm^3) C lasant by the end of this fiscal year.

Intense Laser–Electron Interaction Research for Future Light Sources

G. P. Le Sage, J. K. Crane, T. E. Cowan, T. R. Ditmire

00-ERD-032

An important step in the development of next-generation x-ray light sources is production of picosecond and subpicosecond pulses of hard x rays for dynamic studies of a variety of physical, chemical, and biological processes. Present hard x-ray sources are either pulse-width or intensity limited, and allow picosecond-scale temporal resolution only for signal averaging of highly repetitive processes. A much faster and brighter hard x-ray source is being developed at LLNL, based on Thomson scattering of femtosecond laser pulses by a relativistic electron beam that will enable x-ray characterization of the transient structure of a sample in a single shot (see Fig.). Experimental and diagnostic techniques relevant to the development of next-generation sources, including the Linac Coherent Light Source, can be tested using the Thomson scattering hard x-ray source. This source combines a radio-frequency (rf) photoinjector with a 100-MeV S-band linac.

In principle, femtosecond-scale pump-probe experiments can be used to temporally resolve the structural dynamics of materials on the time scale of atomic motion. With the machine being developed at LLNL, we intend to improve the performance of a Thomson source, previously used at Lawrence Berkeley National Laboratory, in which 300-fs, 30-keV x-ray pulses were generated. Our ultimate goal is to increase the x-ray brightness by 4 to 5 orders of magnitude. The LLNL source will provide a means of performing pump-probe experiments on a subpicosecond time scale, with flux suitable for single-shot measurements. These measurements will enable experiments on samples undergoing irreversible damage (e.g., shocks, plasma ablation, or ultrafast melting).

The LLNL Thomson scattering x-ray source combines a 35-fs laser system that produces 0.6 J at a 1-Hz repetition rate, with an upgraded system that produces 4 J at a 0.1-Hz repetition rate; a photoinjector capable of producing 5-MeV electron pulses, with a charge of up to 1-nC and a pulse length of 0.2 to 10 ps; a normalized root-mean-square (rms) emittance of less than 10 mm-mrad; and an rf linac with output energy that is adjustable from 30 to 100 MeV.

The photoinjector cavity and diamond-turned cathode were constructed using high-isostatic-pressure-annealed oxygen-free, high- conductivity (OFHC) copper. With the experience of the groups involved in the construction of previous photoinjectors, development of the LLNL photoinjector progressed quickly: high-power rf was applied to the photoinjector in July 1999, and the first photoelectron beam was produced in January 2000.

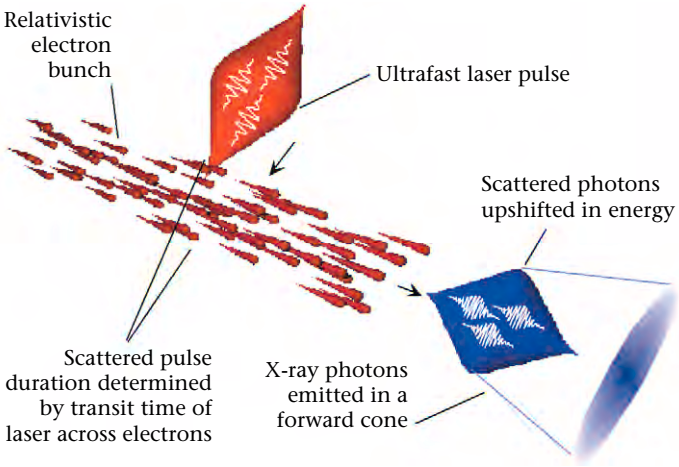

Thomson scattering occurs when photons produced by the high-power, short-pulse laser system are relativistically up-shifted in energy by the electron beam pulse.

The photoinjector produces a peak-accelerating gradient of 112 MV/m, with an rf drive power of 7.1 MW. The field emission current of the structure has been measured, and is very low in comparison to similar accelerators constructed with more conventional materials. The electron beam has been fully characterized, and has an energy of 5 MeV and a peak current of 28 A in a 7.1-ps pulse length. The measured emittance under these conditions is 5.8 mm-mrad.

Future plans for this project include integration of the completed photoinejctor and rf linac, characterization of the 100-MeV beam produced by the combined system, and the first characterization experiments for the high-brightness x-ray source. Current experiments include Thomson scattered x-ray production using the 5-MeV photoinjector beam and a 10-mJ infrared laser pulse.

Astrophysics on Intense Lasers

B. A. Remington

00-ERD-039

In February of 1987, a spectacular outburst of light from SN1987A, a core-collapse supernova (SN), was first observed in the Large Magellanic Cloud. Several forms of observations implicated extensive hydrodynamic mixing of the inner layers into the outer layers of the exploded star. X-ray emission from nitrogen and carbon, generated in the shock-induced explosive burning within the silicon layer, was observed at about 6 mo; 1-D, spherically symmetrical numerical simulations, however, predicted observation at about 1 yr. The peak velocities of the carbon were observed to be well in excess of 3000 km/s. Early 2-D numerical simulations, by comparison, produced peak velocities less than 2000 km/s. More recent 2-D simulations—beginning just after core bounce—found very large initial velocities (up to 4000 km/s) for the newly created iron-group elements. After impact with the reverse shock at the helium–hydrogen interface, however, the simulated velocities were significantly decelerated to a value below 2000 km/s. Thus, the discrepancy between observation and simulation persists.

Two possibilities exist for resolving this problem. The first possibility is that the assumptions underlying previous numerical simulations are incorrect or contain incomplete physics. An example is the recent work of Khokhlov et al. at the Naval Research Laboratory (NRL) that brings the additional effects of rotation and magnetic fields into the problem. In this model, the stellar-core collapse launches a highly asymmetric explosion with bipolar jets and the formation of bow shocks and Mach disks, thereby demonstrating that the assumption of spherical symmetry may be incorrect.

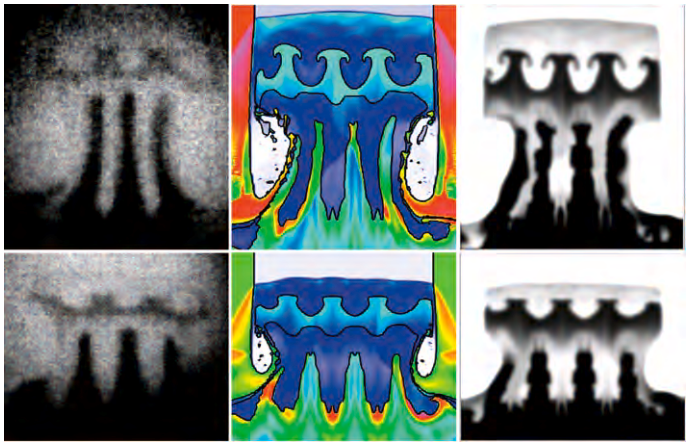

Three-layer experiment simulating the shock hydrodynamics of exploding stars, carried out on the Omega laser at the Universiy of Rochester, NY. The shock-induced mixing from the experiment (left) is in good agreement with the predictions using the LLNL radiation-hydrodynamics code CALE (middle) and the supernova computer code PROMETHEUS (right).

The second possibility is that existing computer models may be incorrectly calculating the hydrodynamic evolution of the system. All numerical methods necessarily include approximations in the underlying equations. Different schemes use different orders of accuracy, employ nonphysical artificial viscosities to ensure stability of the calculations, and in spherical geometry can suffer from vanishing metrics and grid-induced numerical instability. Numerical results often agree at the largest scales of motion, but can differ strongly at smaller scales.

In an effort to address this second possibility, we have been conducting laboratory experiments to provide a set of benchmark data with which to validate the performance of astrophysical codes.

The first goal of the project was to establish the range of astrophysical phenomena that can be addressed on a laser facility. To that end, we developed a series of scaled laboratory experiments on LLNL's Omega laser to isolate and explore four separate issues of relevance to the SN mixing problem. Our first experiment explored the effects of spherical divergence on the instability evolution. The second studied the possibility of coupling between two spatially separated interfaces (see Fig.). The third compared and quantified the difference between instability growth in two and three dimensions; and the fourth began to investigate the evolution of an interface of more complicated modal content.

The second goal of this project was to provide a first rough assessment of the validity of the numerical codes used for astrophysics. For each experiment, comparisons of astrophysical code simulations with the acquired data will be made, and the implications and relevance to the SN problem will be assessed. Meeting this goal would require, for each experiment, comparisons of astrophysical code simulations with the acquired data and an assessment of the implications and relevance to the SN problem. This will be pursued with astrophysical collaborators in subsequent years.

Two invited talks and three contributed presentations at the 42nd Annual Meeting of the American Physical Society Division of Plasma Physics held in October 2000, plus four publication submissions resulted directly from this project.

Chip-Level Optical Interconnects for High-Performance Computing

S.W. Bond, J. Brase, M. Larson

00-ERD-040

The Laboratory's core national security programs are highly dependent on continuing long-term growth in computation capabilities. Our approach to Stockpile Stewardship and to many intelligence and Department of Defense programs is centered on high-performance computing. The performance of electrical interconnect technologies and the resulting gap between computation and communication rates will present serious obstacles to this continued growth in the next five to ten years.

The objective of the project is to exploit emerging optical technologies to move chip-level interconnects to the terabit-per-second regime. Optical interconnect technology will allow chip-to-chip communication to scale at essentially the same rate as on-chip computational performance. Key to this technology is the development of optical transmitters that (1) work at the low voltages, (2) will be available in future integrated circuits, and (3) will be compatible with optical fiber components. Vertical-cavity, surface-emitting lasers (VCSELs) operating at 1.3- to 1.55-µm wavelengths can satisfy these requirements.

In FY2000, we reported, for the first, time room temperature continuous-wave (CW) operation of GaInNAs VCSEL diodes emitting at a wavelength of 1.2 µm and grown all-epitaxially in a single step on a GaAs substrate. Oxide-apertured devices demonstrated CW threshold currents as low as 1 mA, slope efficiency above 0.045 W/A, and thermal impedance of 1.24 K/mW. The Fig. shows the light output curve as a function of CW-drive current for a 5-µm × 5-µm device. Larger-sized devices exhibited pulsed threshold current density of 2 to 2.5 kA/cm^2 and slope efficiency above 0.09 W/A.

In addition, we have developed growth techniques to extend the emission wavelengths of GaInNAs quantum-well lasers beyond 1.3 µm by incorporating nitrogen in the GaAs barrier layers, forming GaNAs barriers. The nitride barriers held up to thermal annealing; edge-emitting lasers demonstrated operation wavelengths at 1296 nm. Furthermore, the temperature characteristics of the nitride (GaNAs) barrier lasers were studied to determine the classic measure of temperature dependence, the characteristic temperature, TO. The results of the GaNAs barrier lasers were substantially improved over the non-nitride barrier lasers, evident by the increase of TO from 105 K to 145 K, indicating that the threshold current of nitride barrier lasers remains low, compared to the non-nitride barriers, even at higher operating temperatures.

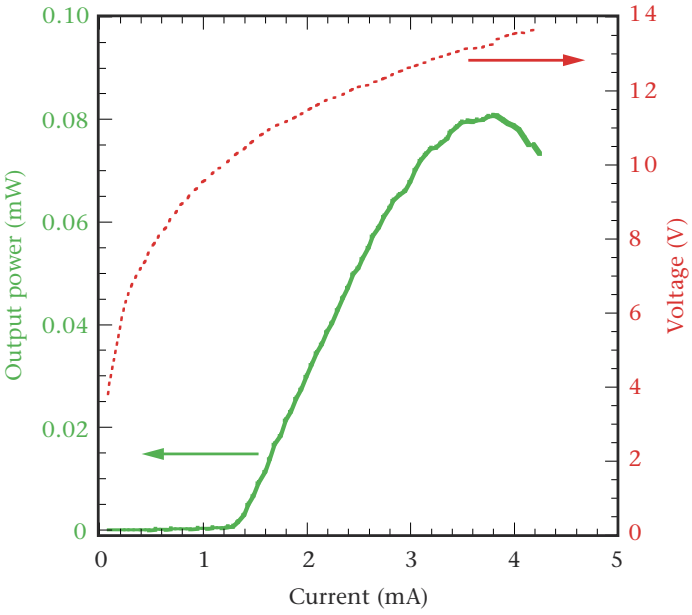

Light output power and voltage vs. injection current under room-temperature, continuous-wave operation.

Magnetically Collimated Energy Transport by Laser-Generated Relativistic Electrons

M. H. Key

00-ERD-045

Fast ignition (FI) offers higher gain than conventional spark ignition, which opens the way to fusion-energy production with laser drivers. The key to FI is the efficient transfer of energy from a short-pulse laser beam to the ignition spark through conversion into a beam of relativistic electrons, which heats the spark. Experiments with the PetaWatt laser at LLNL have shown up to 40% conversion of laser energy to relativistic electrons. Heating a solid target to 300 eV has been deduced from x-ray spectra, and temperatures exceeding 500 eV have been inferred from the neutron yield of D-D thermonuclear fusion. Collimated energy transport in a columnar annular pattern has been seen in images of thermal x-ray emission.

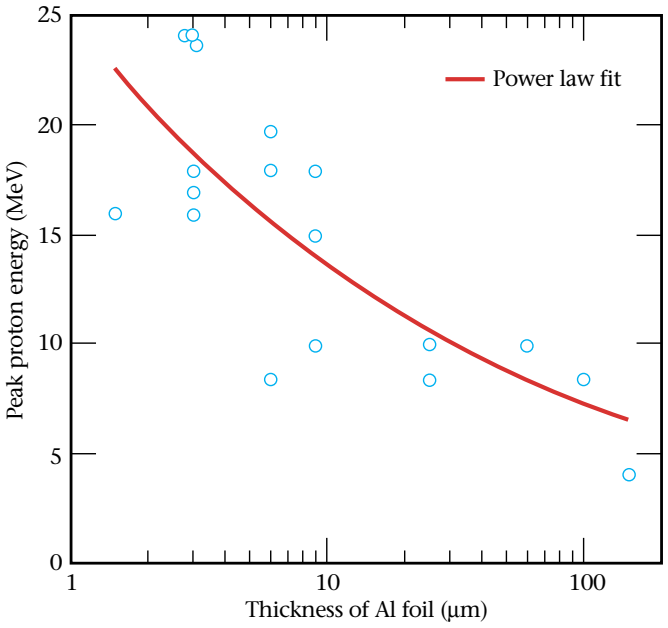

Variation of maximum proton energy with target thickness for aluminum (Al) targets heated by the Janus ultrashort-pulse (JanUSP) laser.

The principal goals of this project were to (1) negotiate and plan collaborative FI experiments, and (2) devise new ways to measure energy transport by relativistic electrons.

During FY2000, we established overseas collaborations with the Rutherford Appleton Laboratory in the United Kingdom, Laboratoire pour L'Utilisation des Lasers Intenses (LULI) in France, and the Institute for Laser Engineering (ILE) in Japan.

At LLNL, we began experiments using LLNL's 100-TW, 100-fs, 10^{20} W/cm^2, Janus ultrashort-pulse (JanUSP) laser. These experiments enabled further studies of the generation of high-energy proton beams from the rear surface of laser-irradiated thin-foil targets, which we had previously discovered in experiments with LLNL's Petawatt laser. We had postulated that relativistic electrons penetrating through thin-foil targets created a high electric field in a Debye sheath on the rear surface, which then accelerated ions into vacuum. A contrary explanation assumed that laser-light pressure at the front surface drove ions through the target. The reduction of proton energy with thickness L of the target was measured (see Fig.). The results can be understood through the reduction in number density Ne of hot electrons (scaling as L^{-1}) trapped electrostatically in thicker targets. There is a corresponding reduction (scaling as $Ne^{0.5}$), in the electric field of the Debye sheath and therefore also a reduction in the proton energies. The JanUSP data give further support to our Debye-sheath model of the process.

Identification and Elimination of Mechanisms Leading to UV Damage of DKDP

A. Burnham, M. Runkel, S. Demos, and L. Chase

00-ERD-064

The design of ultraviolet (UV) laser systems is often limited by the laser damage performance of the third harmonic generator, which is made from deuterated potassium dihydrogen phosphate (DKDP). The purpose of this project is to understand the mechanisms of both bulk and surface damage initiation in DKDP to be able to locate and eliminate the initiation sources, thereby enabling long-term high-fluence laser operation.

During FY2000, we significantly increased our understanding of laser exposure and crystal growth conditions leading to bulk damage of DKDP. First, laser-induced bulk damage resistance of DKDP is 1.5 to 2 times less when the light propagates along the a(x), b(y), or tripler crystal axes compared to the c(z) axis of the crystal. Damage does not depend on laser polarization, and occurs for both rapidly and conventionally grown crystals and for both laser-conditioned and -unconditioned crystals. Second, laser pulse-scaling measurements from 1 to 10 ns indicate that the normalized number of bulk damage pinpoints scales as $(t_{ref}/t)^{1/3}$, where t_{ref} is a reference pulse length. The size of the pinpoint increases with pulse length because of increased energy absorption, so the obscuration due to scattering from damage sites scales as $(t_{ref}/t)^{1/4}$ (see Fig.). Together, the orientational and pulse-length dependencies were used to establish an improved performance criterion for laser tripler crystals. In addition, tests of crystals grown at various rapid growth conditions found that the most important growth parameter affecting damage resistance is the growth temperature. Unfortunately, low-growth temperatures also increase the likelihood of surface crazing, which is caused by surface stress related to the exchange of deuterium by hydrogen in ambient humidity.

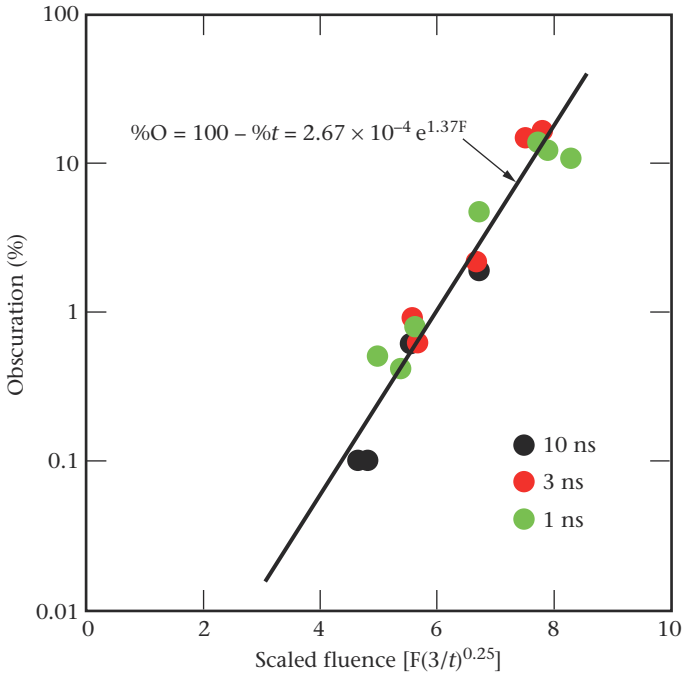

Obscuration by scattering from bulk damage scales as $(t_{ref}/t)^{1/4}$; 3 ns is used for t_{ref}.

Bulk damage is thought to occur from absorbing nanoparticles. The important role of growth temperature on damage resistance would require increased production or incorporation of nanoparticles at higher growth temperatures. Results from analyses performed in FY2000 neither proved nor disproved this hypothesis. Analysis of several bulk damage sites by secondary ion mass spectrometry (SIMS) showed no evidence for hypothesized particulate iron content. Examination of growth solutions by laser breakdown spectroscopy also showed no evidence of absorbing particulates at fluences (10 to 20 J/cm^2) that caused significant bulk damage in crystals. An oriented particle model was considered as an explanation for the propagation-direction dependence of damage resistance, but was eliminated due to a lack of observed polarization dependence.

Surface damage can occur from near-surface bulk damage or from surface fabrication defects. Earlier work found fluorescent defects on the surface of a finished crystal at a size and concentration not present in the bulk. During FY2000, we demonstrated that these fluorescent defects usually lead to surface damage. In contrast, defects detected by light scattering do not lead to surface damage, presumably because such defects are caused by external dust particles that are easily removed by laser cleaning. These correlations were based on several observations on a relatively poor-quality crystal having many defects and a few observations on a high-quality crystal having few defects.

In FY2001, we will analyze other samples to determine the chemical characteristics of the defects and a sounder correlation between the type of defect and damage initiation.

Surface Dynamics during Environmental Degradation of Crystal Surfaces

P. Whitman, J. De Yoreo, T. Land, E. Miller, T. Suratwala, C. Thorsness, E. Wheeler

00-ERD-065

The ever-increasing internal quality of crystal optics and the rising demand of ultraviolet (UV) applications, such as UV photolithography, have led to widespread use of crystal optics in systems where surface degradation is unacceptable. While such surfaces generally can be isolated in vacuum chambers or purged environments, it is not always possible to do so. This problem may be particularly pronounced when the surface has a porous antireflective or high-reflective coating that acts like a getter for volatile contaminants.

Successful deployment and operation of a high-power UV system depends on the ability of a number of optical surfaces to survive high-fluence UV environments. Recently, the formation of pits with distinct geometrical features was discovered on the surfaces of the sol-coated KH_2PO_4 (KDP) and KD_2PO_4 (DKDP) crystals that were used for optical switching and frequency conversion on Nova, Omega, and Beamlet, after these surfaces were coated with antireflective coatings. These pits scattered up to 10% of the incident light, resulting in both a loss of energy on target and the potential to produce collateral laser damage. We have identified these pits as the product of dissolution by water that is absorbed into the coating and have focused our efforts on elucidating the physics and surface chemistry resulting in their formation.

Using in situ optical microscopy, atomic force microscopy, and scattering measurements, we have followed the evolution of surface morphology during etching and measured surface etching rates as a function of humidity and undersaturation. Pit formation is characterized by a nucleation and growth process: the introduction of water creates a condition of undersaturation at the crystal surface. Equilibrium pit shapes, determined by the orientation of the optic surface with respect to the crystal axes, are established shortly after nucleation. The onset of pit formation during exposure to 55% relative humidity (RH) is detectable within a few hours. Most of the etching process is complete within 48 h but pits continue to grow for a week or longer. At 75% RH, pits are detectable within minutes. The total volume of the pits qualitatively scales with coating thickness and relative humidity, indicating that the adsorption of water into the porous coating determines the size of the available solvent reservoir. Equilibrium is reached when the reservoir is saturated.

Subtle modifications of the KDP surface or the sol-coating chemistry and structure can enhance or retard the growth of etch pits under otherwise similar conditions. Intentional modification of the surface of the porous sol by reaction with hexamethyldisilizane (HMDS) to increase hydrophobicity results in measurable reduction of adsorbed water and can eliminate etch-pit growth at 55% RH. Thermal annealing of the crystal before coating strongly inhibits pit formation; most surfaces show no evidence of dissolution after months at high humidity. The reduction in etch-pit formation is correlated to the formation of an insoluble dehydrated layer of linear polymeric phosphate on the surface of the KDP. This layer was identified through Fourier transform infrared (FT-IR) spectroscopy, electron spectroscopy for chemical analysis (ESCA), x-ray fluorescence (XRF), and x-ray diffraction.

The primary objective of this project was to develop a fundamental understanding of the physics and chemistry of the environmental degradation processes at crystal surfaces. We have established a firm scientific basis for robust mitigation strategies and attained a broader understanding of the physics of surface etching.

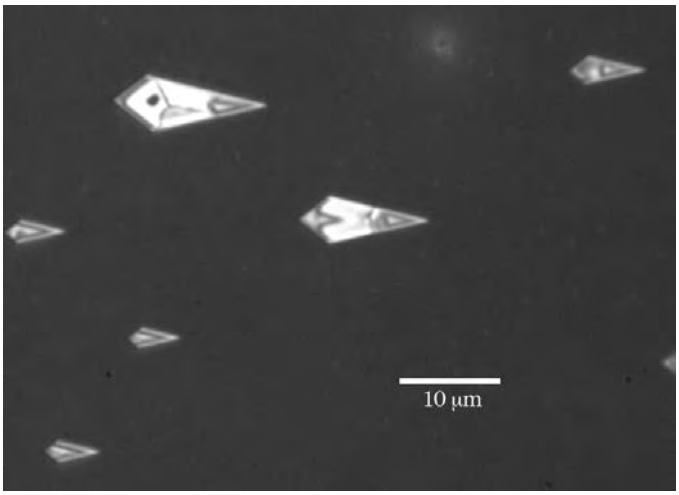

Etch pits grown on a sol-coated crystal and exposed to 75% relative humidity. Equilibrium step directions and low-index facets of KDP determined the characteristic orientation and shape.

Modeling of Laser-Induced Damage in High-Power-Laser UV Optics

M. D. Feit

00-ERD-066

Curtailing laser-induced damage to ultraviolet (UV) optics is important for high-power lasers. Recent experimental and theoretical progress has led to reductions in the number of surface initiators in fused silica that damage at low-energy fluences (6 J/cm^2) and to increased understanding of the evolution of damaged area growth upon multiple laser-pulse irradiation. Work is continuing to identify and allow near-elimination of surface damage initiators in the 8- to 14-J/cm^2 fluence range. Since it is unlikely that all initiators can be removed, especially under operational conditions, it is also important to understand how damaged areas grow upon repeated irradiation and to determine the factors that most influence growth.

During FY2000, we undertook a broad modeling effort both to investigate possible physical mechanisms underlying observed damage behavior and to aid design and interpretation of related experiments.

Initial laser damage in nominally transparent materials can be due to extrinsic factors such as absorbing contaminants. To identify initiators we investigated the energy absorption by such contaminants and the resultant damage craters. Because of the small sizes possible for potential absorbing particles, Mie theory was used to calculate absorption cross sections for a range of materials and particle sizes. Resultant heating of the absorber and surrounding material can be calculated easily for weak fields and gives insight into threshold behavior. Typical observed initiation craters range in size from a few micrometers to a few tens of micrometers in size. We semiquantitatively understand the dependence of crater size and depth on laser and material properties (see Fig.). Detailed numerical simulations with LLNL materials codes were begun, and are continuing to provide a quantitative description of the final state of the damaged material.

We demonstrated that the small-particle absorption model explains the observed dependence of the bulk potassium dihydrogen phosphate (KDP) damage threshold on laser pulse duration. Using this model and measured values of total beam obscuration, we predicted that the smallest damage sites are about 1 μm in size.

The role played by microcracks created by surface finishing is of particular interest for damage growth. Two ways such cracks can be important are through local electric field intensification (due to total internal reflection) and through light-absorbing contaminant trapping. Cracks can also exhibit absorbing electronic surface states. We carried out simulations of field intensification in the vicinity of typical crack networks and began evaluating its importance for both damage initiation and subsequent growth. Together with absorption and intensification simulations, detailed numerical simulations of crater formation and growth are helping us to develop a comprehensive model of laser damage.

Future simulations of damage-crater formation, shock-wave-induced spallation and the influence of crack networks will continue to develop the scientific basis for understanding laser-induced damage in important optical materials.

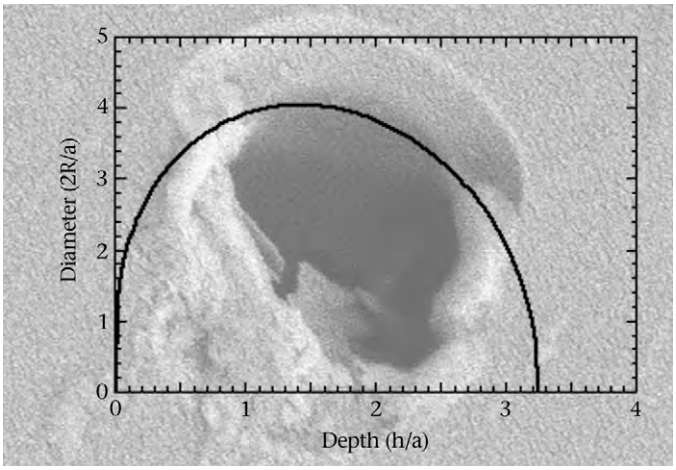

Theoretical relationship between crater diameter (2R) and depth of absorber beneath surface (h). Initiation crater in background. Diameter and depth are given in units of absorbing particle radius (a).

Back to main TOC

Laser Damage Inspection

J. T. Salmon, J. M. Brase, R. A. Sacks, C. Carrano, L. M. Kegelmeyer, C. D. Orth

00-ERD-067

In FY2000, we developed algorithms to detect and characterize laser optic damage. Initial work focused on (1) developing Web-based interfaces to the experimental system in the laboratory, (2) developing protocols for an image database, and (3) defining architectural approaches to detecting defects on laser optics.

We used bright-field and dark-field images of samples with mechanically ground defects and chrome-dot masks on the experimental scale-model beamline to analyze defects. First, we computed signal-to-noise ratios for single defects on a single optic, determined the limit of detection for these, and evaluated our ability to accurately estimate their size. Second, we demonstrated an algorithm that can detect a defect on one optic and determined the optic on which it resides when a single image is complicated by multiple passes and multiple conjugate planes in the imaging system. Finally, we used that algorithm to detect defects on two separate optics in the same system and successfully determined which defect was on which optic.

We assembled an experimental model of a high-power, multipass, re-imaging beamline based on dimensional analysis of passive propagation of a beam through the large optics of a laser capable of generating 20-kJ pulses with pulse widths less than 20 ns. We inserted flat optics with damaged sites into the model where the beam is collimated, and images—both bright-field and dark-field—were obtained and used as input for the algorithms being developed.

Work on a numerical modeling code included simulations of both a high-power, multipass amplifier system operating at a wavelength of 1.053 μm and the experimental model previously described. Algorithms representing beam obscurations (flaws) and spatial filters were generalized to facilitate these studies. Additional information was included in the beam-dump files, thus improving post-processing and expanding the use of restart capability. The code's graphical output was upgraded to improve readability and information content. Algorithms for treating image astigmatism and higher-order phase aberrations introduced by amplifier slabs at Brewster's angle were analyzed in detail. Phase masks representing optical figure errors, mounting and gravity stresses, and an estimate of heated air turbulence corresponding to temperature profiles one-to-two hours after a shot were added. Initial images suggest that flaws as small as 0.25% of the beam size can be detected. Thus, we are exploring design tradeoffs such as bright-field versus dark-field images, image variation with dark stop radius, two-pass versus four-pass operation, and selective use of cavity pinholes to simplify image interpretation.

A comparison of the simulation results to the experimental model showed good agreement, except for sharper edges in the numerical image of a given flaw. This discrepancy was traced to severe spherical aberration (>2.5 waves) in the final lens in the diagnostic system that was not in the numerical model.

The algorithms developed (1) can rapidly and reliably process images from the damage inspection system and ensure operator safety; (2) should help operators remove damaged optics for refurbishment before the damage becomes too severe; and (3) should be applicable to a wide variety of large, high-powered laser systems.

CASFLU: Composition Analysis by Scanned Femtosecond Laser Ultraprobing

M. Y. Ishikawa, J. P. Armstrong, B. C. Stuart, L. L. Wood, A. E. Wynne

00-ERD-068

Composition analysis by scanned femtosecond laser ultraprobing (CASFLU) exploits a new physical principle to perform fully automated, high-speed analysis of complex 3-D objects of any nature with microscopic (and potentially submicrometer) resolution.This new technology can be applied to analysis of semiconductor device failure, mechanism wear/failure, object construction, and biological tissue. CASFLU may be favorably compared to other 3-D composition determinative technologies such as x-ray tomography, magnetic resonance imaging, and microtome-to-slide-to-optical-microscope imaging. Like them, CASFLU is an enabling technology that allows many of the most important aspects of the composition of all types of inhomogeneous solid objects to be automatically and quickly analyzed into chemical–elemental and isotopic constituents and molecular states on microscopic resolution scales.

CASFLU leverages the ability of laser pulses of less-than- or equal-to-femtosecond time scales and sufficiently high fluence levels (≥1 J/cm^2) to ablate submicrometer thickness layers of surfaces without significantly heating or shocking the underlying material. The resultant tiny plumes of laser-ablated material may be input directly into a mass spectrometer for real-time analysis of their isotopic or molecular composition. Raster scanning of the focused, repetitively pulsed laser beam over the entire surface of an object generates a 2-D composition map of the surface and is extendable into three dimensions by iterating the 2-D mapping process. This optical milling of layer after layer of the object being examined, analyzing each plume of material in rapid succession, allows a detailed 3-D composition map to be built up during the process.

Three-dimensional dissective capabilities may also be used to extract micro-objects embedded within solids. The laser may be directed to shut off when a "forbidden" or unknown material is encountered. In this way, composition-selective removal of material from complex 3-D objects can be performed in microscale, without accompanying significant heat- or stress-induced damage.

A first demonstration of the CASFLU capability took place in FY1999 and formed the basis for our patent applications. In FY2000, the CASFLU unit was first tested on an industrial-standard, 200-grid, copper test mesh pattern on silicon. CASFLU successfully revealed microscopic warping in the test pattern on several micrometer scales (see Fig.).

A final real-world CASFLU proof-of-principle demonstration (also in FY2000) featured the successful dissection, analysis, and composition mapping reconstruction of a commercially available silicon Darlington transistor. Real-time composition data taken during active scanning of the transistor by a femtosecond laser was successfully reconstructed into a 3-D composition map of the object. The composition map clearly revealed aluminum, silicon, and separate aluminum/silicon mixing on different levels in the transistor, as well as extant 3-D features such as channels, leads, and grooves embedded within and on the object. We are pursuing licensing opportunities.

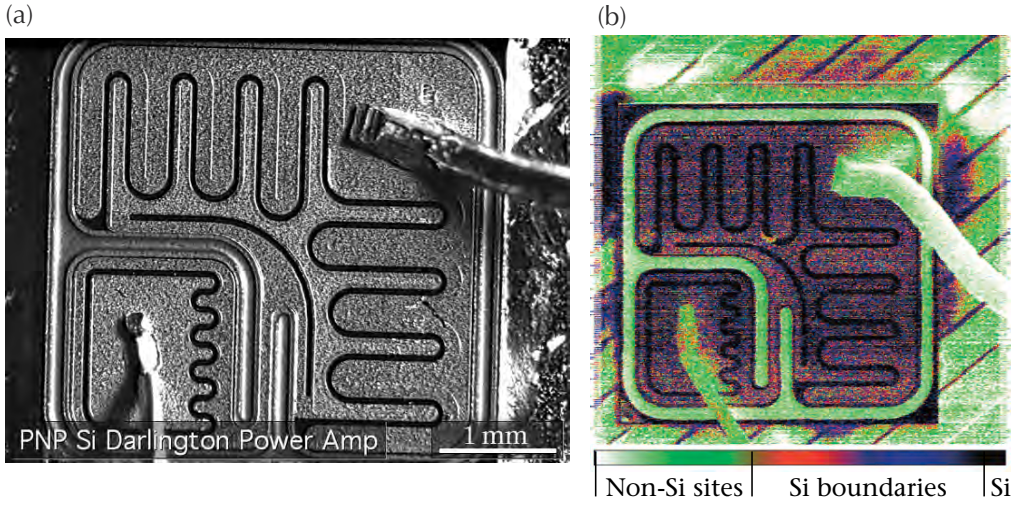

A side-by-side comparison of (a) a high-resolution microscope photograph of a semiconductor and (b) the top data layer from a CASFLU 3D composition map of the same object. The contrast between the silicon (Si) boundaries and non-Si sites are clearly visible in the analog image.

Back to main TOC

Flight Dynamics and Impact Characteristics of Thin Flyer Plates Driven by Laser- and Electrically Produced Plasmas

R. Lee, J. Colvin, A. Frank, L. Fried, J. Reaugh, B. Remington

00-ERD-069

The purpose of this project is to provide the scientific underpinnings for advanced development work on the new detonators that will be needed within the next ten years for use in the Laboratory's national security mission. To do this, we are conducting experimental and computer modeling studies of the launching, flight characteristics, and impacts of thin flyer plates driven by laser ablation under drive conditions where the plate remains a solid and retains its strength. Specifically, we are investigating the coupling of laser energy into the flyer plate during the launch phase, melting and instability growth in the flyer during launch, and—at the explosive-grain scale—the shock-to-detonation transition when a flyer plate hits an explosive target.

The knowledge and modeling capability developed in this project will enable us to tailor the launching and acceleration conditions of thin flyer plates to produce an optimal impact for initiating high explosives. Experimental and computational studies of the shock-to-detonation transition will allow us to develop the most efficient initiating explosives for use in future detonators.

We began work on this project in mid-FY2000. The primary experimental activity was preparation for moving the Pleiades laser into the Micro-Detonics Facility (μDF) at LLNL. For this purpose, we (1) prepared an integrated work sheet, operational plans, and safety-system software and hardware; (2) installed a large-aperture polarizer on the laser to provide a uniform energy distribution in the beam; and (3) prepared a 70%-reflectivity Fabry-Perot laser velocimeter with a 300-ps fill time to allow subnanosecond, velocity-time measurements.

A principal accomplishment during this period was our completion of a detailed calculational model for flyer-plate dynamics using the 2-D radiation-hydrodynamics code LASNEX. The much different range of densities, temperatures, and physical processes for laser-light absorption in the flyer-plate-modeling problem required numerous additions to the code. We added prescriptions for calculating (1) the correct ionization state and electron densities for metals and insulators as a function of temperature, and (2) the low-fluence absorption of the laser beam on the solid/liquid metal surface of the flyer. We also added a photoionization absorption model to describe the absorption of the low-fluence laser beam and a constitutive model for the material strength of the flyer.

We then applied our new calculational model to an experiment that had been performed at LLNL in 1994. In this experiment, 25 J/cm^2 of 1.06-mm laser light, in a 15-ns full-width, half-maximum (FWHM) Gaussian pulse, was incident through a fused-silica fiber onto a foil consisting of a thin aluminum (Al) ablator layer separated from a 3-mm-thick Al flyer by a thin alumina insulating layer. The velocity calculated using our new model agrees with the measured velocity of about 4 km/s. We found little sensitivity in the calculations to the band-gap energy of the insulator and some sensitivity to metal reflectivity at low temperature, but not at high temperatures. Thermal conduction from metal vapor into the substrate boils away some of the glass substrate, adding to the pressure driving the flyer and enhancing flyer velocity by about 25%. Without the thermal insulation layer, the flyer fully melts after only 60 mm of flight instead of after about 200 mm.

In FY2001, we intend to (1) measure instability growth, impact-wave profiles, and ablation depth for various-thickness flyers, (2) measure velocity thresholds for hexanitrostilbene (HNS) and pentaerythritol tetranitrate (PETN), (3) construct a grain-scale initiation model for PETN and compare it against experimental data, and (4) benchmark our working calculational model against new experiments and make necessary changes to its parameters.

Back to main TOC

New Front-End Technology for Chirped-Pulse Amplified Laser Systems

D. M. Pennington, I. Jovanovic, B. Comaskey

00-ERD-070

We are developing a new front-end technology for chirped-pulse amplified laser systems. In chirped-pulse amplification (CPA), a broad-bandwidth laser pulse is temporally stretched, reducing the power to safe levels for further amplification in traditional optical materials. Following amplification to a high energy, the pulse is temporally recompressed to provide a high-peak power laser pulse. Optical parametric chirped-pulse amplification (OPCPA) combines the CPA technique with optical parametric amplification (OPA) and enables the generation of high-energy broadband pulses. It also provides a high-contrast pulse shape by eliminating the fluorescence pedestal and leakage pulses characteristic of regenerative amplifiers. High-contrast pulses are particularly desirable for applications ranging from laser materials processing to fast ignition for laser-driven inertial confinement fusion. OPCPA also has the potential to generate 15-PW pulses using current pulse-compression technology and to enable a new regime of basic scientific experiments.

Another exciting class of applications emerges by scaling short-pulse lasers to high-average power (>100 W). Currently, existing laser materials cannot be scaled to high-average power while supporting pulses that are less than 100 fs in duration. Using OPA, a completely elastic process, it should be possible to achieve high-average power because material absorption is the only heat load. Hence, the thermal issues are effectively separated from the amplification process and are limited to the long-pulse pump lasers.

In FY 2000, we focused on theoretical modeling/design and technology development. We developed a 3-D finite-element code for OPA with nanosecond pulses and investigated the performance of nonlinear crystals for OPA. We also modeled the effect of beam quality on conversion efficiency in OPA because it is important to calculate the expected efficiency reduction in OPAs pumped by real beams with various distributions of angular dephasing. Our model rigorously derives expected maximum conversion efficiencies for several state-of-the-art nonlinear materials. This work has provided invaluable information about the requirements of pump lasers for next-generation, OPCPA-based, materials-processing lasers.

Furthermore, we completed designs for both high-energy and high-average-power OPCPA systems. We designed and built a Nd:YAG laser for injection seeding a pump laser, which delivers 0.5-mJ, 3.5-ns pulses at 2 kHz. Amplification of these seed pulses to the 40-mJ level is in progress for use as a high-average-power OPA pump beam. The high-average-power OPCPA system should produce 1 to 2-mJ pulses at a 2-kHz repetition rate and less than 200-fs pulse width.

In FY 2001, we will construct the pump laser for use with the high-energy OPCPA design we completed in FY2000. Using this design, we expect to produce 50-mJ pulses at a 10-Hz repetition rate and less than 200-fs pulse width. Focused intensities from this system should be $>10^{17}$ W/cm^2, providing a useful, high-contrast source for experiments. In addition, the sources center wavelength of 1054 nm makes it ideal for further amplification using large Nd:glass amplifiers to boost the energy while retaining the low prepulse level.

We will also (1) complete both pump lasers and experimentally demonstrate the expected level of performance from OPCPA in both the high-repetition rate and the high-pulse energy regimes, and (2) study the application of OPCPA to the next generation of high–average-power, short-pulse materials-processing lasers.

Back to main TOC

The Chirped-Pulse Inverse Free-Electron Laser: A Tabletop, High-Gradient Vacuum Laser Accelerator

H. A. Baldis, F. V. Hartemann, A. L. Troha

00-ERI-003

The inverse free-electron laser (IFEL) concept has been experimentally demonstrated as a viable process at several laboratories. The concept is attractive because the interaction occurs in a vacuum, away from boundaries, thus allowing a large interaction region. Because a plasma is not employed as the accelerating medium, a number of problems are resolved, including plasma instabilities, nonlinear laser propagation, shot-to-shot reproducibility, and the extremely small accelerating potential well ("bucket") that characterizes laser–plasma acceleration schemes. In addition, the IFEL wiggler can provide good focusing and electron-beam optics and transport, thus potentially producing the high-quality electron beams required for advanced light sources, biomedical applications, and the Next Linear Collider (NLC). However, the IFEL acceleration scheme has several limitations.

In this project, we are working to overcome the limitations of the IFEL by (1) examining the IFEL interaction both theoretically and computationally, and (2) investigating a new accelerating concept—the chirped-pulse inverse free-electron laser (CPIFEL).

One of the limitations of the IFEL acceleration scheme is the dephasing of the trapped electron with respect to the drive-laser wave. As the electron energy increases, the free-electron laser (FEL) resonance condition is not maintained, and the electron reaches a maximum energy given by the FEL interaction bandwidth. In FY2000, we resolved this by chirping the drive-laser pulse, which maintains the FEL resonance condition beyond the usual dephasing limit, thus further improving the electron energy gain (see Fig.). Up to now, IFEL gradients have been comparable to those possible with high-frequency microwave systems (~100 MeV/m).

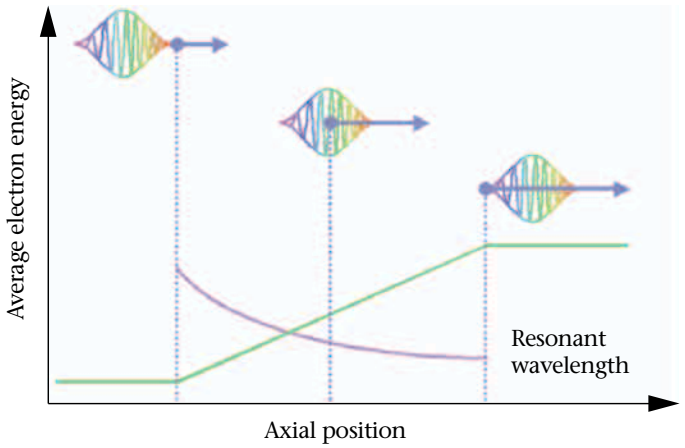

Chirped-pulse inverse free-electron laser (CPIFEL) acceleration, showing how the resonance condition changes as the average energy increases.

Another limitation of IFEL is the diffraction of the drive-laser pulse. This limitation is alleviated by using the ultrawide bandwidth of the chirped laser pulse. Negative dispersion-focusing optics produce a chromatic line focus, where long wavelengths are focused first, while the shorter wavelengths that maintain the FEL resonance condition at higher energies are focused further along the interaction region. In FY2000, we performed a ray-tracing analysis of this chromatic line focus. We showed numerically that the accelerating IFEL bucket is very wide compared to the plasma-based schemes.

We also considered the IFEL interaction in which femtosecond, terawatt-class, drive-laser pulses generated by tabletop systems using chirped-pulse amplification (CPA) are used. For femtosecond pulses, the IFEL interaction bandwidth is considerably wider than it is for lower-intensity drive pulses with durations greater than a nanosecond. The FEL resonance condition indicates that when the electron slips over one laser optical cycle, it also propagates over one wiggler period. Thus, for femtosecond pulses, the wiggler interaction region is extremely short, and the IFEL resonance bandwidth is wide. Because the electron energy now increases significantly before the IFEL interaction detunes, the CPIFEL yields a high accelerating gradient (>1 GeV/m).

In sum, during FY2000, we showed that by using a femtosecond-duration, ultrahigh-intensity drive-laser pulse, the IFEL interaction bandwidth and accelerating gradient are increased, thus yielding large energy gains. Using a chirped pulse and negative dispersion focusing optics we can take advantage of the laser bandwidth and produce a chromatic line focus, maximizing the gradient. Combining these ideas results in a compact vacuum laser accelerator—a CPIFEL—capable of accelerating picosecond electron bunches with a high gradient (GeV/m) and very low energy spread.

Ultrafast Dynamics of Plasma Formation and Optical-Material Modifications under High-Fluence Laser Irradiation

S. G. Demos

00-ERI-004

Although the problem of laser-induced damage has existed since the invention of the laser, the mechanisms of damage initiation and its evolution still require fundamental understanding. The goals of this project are to examine (1) the photophysical processes associated with the damage initiated because of the presence of excessive localized light absorption by an optical material, and (2) subsequent absorption at damage sites leading to damage growth. A major portion of this effort is devoted to potassium dehydrogen phosphate (KDP) crystals, its deuterated analog (DKDP), and fused silica.

Our approach is threefold. First, during FY2000, we began using steady-state and time-resolved spectroscopy and fluorescence microscopy to examine the characteristics of the plasma formed during the damage processes. Time-resolved spectroscopy provides information regarding the starting time of plasma formation and its evolution under 355-nm, 3-ns, high-power laser irradiation. Microscopic imaging using the plasma emission provided a direct correlation of the damage processes with plasma formation and preexisting defect features.

Second, we began investigating the dependence on wavelength of the damage threshold in the optical materials for advanced laser systems. The damage-correlated absorption spectra of the material provides important information on the electronic processes leading to laser-induced damage. For example, if damage is initiated by a nanoparticle, the peak temperature grows as the square of particle size in wavelength units, implying a similar behavior of the damage threshold. On the other hand, the measurements of the wavelength dependence of plasma (damage) initiation can reveal the absorption spectrum of the responsible contaminants. Laser interaction with optically active defect formation prior to and following irradiation by a high-power laser and/or plasma formation can be responsible for damage initiation or damage growth.

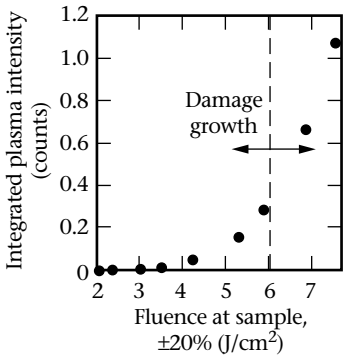

Measurements of the integrated plasma emission intensity (data points) with increasing laser fluence in a sample of deuterium potassium dehydrogen phosphate (DKDP) show that the onset of laser-induced damage growth (represented by the vertical dashed line) coincides with rapid increase of plasma intensity. The two-headed arrow represents the variation in the onset of damage growth at different damage sites.

For this reason, the detection and characterization of crystalline band-zone electronic-defect structures is the third emphasis in our project. In FY2000, we began—for the case of KDP crystals—both an experimental investigation using optical and electron paramagnetic resonance (EPR) spectroscopy and a theoretical investigation in which we are modeling electronic states and defect formations.

Although modeling and EPR spectroscopy are being performed through university collaborations (West Virginia University and California State University, Northridge, respectively), during FY2000 we developed a number of experimental capabilities at LLNL. To test the correlation between preexisting defect formations and damage initiation, we built an in situ, damage-testing microspectroscopy imaging system that obtains light-scattering, fluorescence, and plasma images of the same site. Using this system, we found that plasma formation correlated with (1) damage, and (2) preexisting material defects such as cracks and impurity or defect formations. We also demonstrated that significant, damage-induced material modifications on both KDP and SiO_2 are responsible for additional damage growth. We observed plasma re-ignition at localized areas of the modified material at laser fluences as low as 2J/cm^2 (355 nm, 3 ns). Damage growth appears only when the laser fluence is sufficient to cause a large plasma "explosion" (see Fig.). We also obtained time-resolved spectra of plasma emission during laser-induced damage and, on the basis of these preliminary results, developed instrumentation that will yield accurate estimates of plasma temperature and density. At the close of FY2000, we had nearly completed the experimental setup for investigating wavelength-dependent damage thresholds.

In FY2001, we plan to (1) investigate the damage threshold using a laser system tunable from 290 to 1200 nm, (2) investigate plasma formation in the bulk and on the surface of KDP and DKDP crystals and on the surface of fused silica, (3) perform theoretical modeling of defects in KDP, and (4) conduct an experimental investigation of material modifications and their interaction with 355-nm laser pulses.

Back to main TOC

Fusion Neutron Production from Exploding Deuterium Clusters

K. B. Wharton, J. K. Crane, T. Ditmire

00-LW-021

Fast neutrons are used in a wide array of applications, including radiography and materials science. However, the possibility of ultrafast studies using neutrons, either to pump or to probe, is usually not considered because no high-flux sources of these short neutron pulses exist. Such a source would need to have a short initial pulse width, small size, and a monochromatic spectrum so that the ultrafast temporal structure is maintained over a reasonable distance from the source. Although high fluxes of energetic neutrons can be produced with a number of devices, including accelerators and plasma pinches, these devices yield neutron pulses with durations typically longer than a few nanoseconds. Neutron sources based on nuclear fusion in a hot plasma (like those produced in plasma pinches) produce nearly monochromatic neutrons, with energy near 2.45 MeV for neutrons produced from the fusion of deuterium. For short-lived fusion plasmas, it is possible to produce a short burst of fast neutrons. Such a short-pulse neutron source could have multiple applications, including testing first-wall designs for laser-fusion reactors, simulating neutron damage for high-power-laser target chamber materials, and probing dynamic shocks in high-*Z* materials for stockpile stewardship. We reported the detection of fusion neutrons in a deuterium cluster source in an article in *Nature* in 1999.

We produce fusion neutrons by focusing an intense laser pulse at the output of a high-pressure, pulsed gas nozzle inside a large spherical vacuum chamber. By cooling the nozzle, the high-density deuterium molecules condense into large clusters containing several hundred atoms. At the focus of the laser, we can produce irradiances of 10^{18} W/cm^2. At this intensity, the electric field of the laser can rapidly strip all the electrons from the deuterium atoms, causing the clusters to explode. The ions ejected from this type of Coulomb explosion can reach energies of 1 MeV. At these ion energies, the probability for two deuterium ions colliding and undergoing a D–D fusion reaction is significant.

In FY2000, we concentrated on characterizing and optimizing the production of neutrons from this new type of source. We assembled a Rayleigh scattering diagnostic and laser interferometer to measure the cluster size and density as a function of nozzle-backing pressure and temperature. At 55 atm backing pressure and 85 K, we measured an average cluster diameter of 100 Å. At 70 atm backing pressure and 100 K, nearly 90% of the laser energy is absorbed, corresponding to ~5 keV/ion. Plotting neutron yield versus cluster diameter, we observe a rapid increase in neutron production with increasing cluster size as expected from the correlation of laser absorption to cluster size. However, the neutron yield reaches a maximum for cluster diameters of 50 Å and decreases slightly for further cluster-size increase, which we attribute to an increase in absorption and scattering from the larger clusters. We characterized the energy spectrum and pulse width of the neutrons using an array of fast scintillator detectors placed at various distances from the neutron source. By plotting neutron pulse width versus distance from the source, we can extrapolate the neutron pulse width and production rate or fusion burn time at the neutron source. We measured a fusion burn time of 500 ps.

Large-Aperture, Lightweight Space Optics

R. A. Hyde, S. N. Dixit, M. C. Rushford

00-SI-003

This project is aimed at fabricating a thin, 5-m aperture, diffractive lens for earth observation and astronomy. The primary purpose of this effort is to demonstrate that large, optical-quality, diffractive lenses can be successfully fabricated. Our finished 5-m aperture (Palomar-class) lens will incorporate the materials, weight, and foldability characteristics needed for advanced space-based optics.

The basic approach we have chosen for building the lens is to assemble it by seaming together multiple, thin glass panels, rather than adopting either a monolithic design or using a polymer membrane. The material selection takes advantage of LLNL's experience in optical processing of glass, and avoids polymer space-stability uncertainties. The multipanel approach is attractive because it splits the lens fabrication into two separate and feasible tasks: optical engineering, to create meter-scale lens panels, and mechanical engineering, to align and join panels across the full 5-m aperture. The use of multiple panels also provides a practical way to fold our large glass lens, since all folding can occur at the joints between flat panels.

In order to fabricate lens panels, we need meter-sized sheets of thin glass, each smoothed to a uniform, identical thickness, and patterned with the proper diffractive surface profile. We have chosen to make our lens panels from glass microsheets, as these are commercially available in the proper sizes and thicknesses. As purchased, these glass sheets contain several micron-deep thickness ripples; but to be useful for our lens, the panel must be smoothed to a ~0.1-μm accuracy. We have developed a new approach to achieve such broad-area smoothing and have successfully demonstrated it at intermediate sizes. After the panels are uniformly smoothed, we use lithographic surface patterning (state of the art here at LLNL) to make each of them act as a segment of the overall diffractive lens.

Once all the individual lens panels are produced, they are assembled into a complete lens by accurately placing each panel at its proper site and then attaching them together with precise, foldable joints. We have developed a local-metrology alignment method in which global positioning accuracy is achieved by aligning fiducials along the borders between panels. We have prototyped two different joint technologies, one using flexible metal foils and the other using glass hinges.

Our FY2000 process development effort culminated in the fabrication and successful testing of a 75-cm, six-segment, foldable lens. We achieved our goal of demonstrating that thin, segmented, diffractive lenses could be built with sufficient alignment and seaming accuracy. The Fig. shows the completed lens and its measured focal spot; this segmented lens achieves the same focal performance as would a monolithic lens.

Our emphasis during FY2001 will be to prepare for production of an 81-segment, 5-m lens in FY2002. We will continue the lens-panel development, scaling panel sizes up to the 60 × 80-cm size needed for the full lens. Our other focus will be on designing and constructing a semiautomated assembly machine that will be used to place, accurately align, and seam together the lens panels to form our overall 5-m lens.

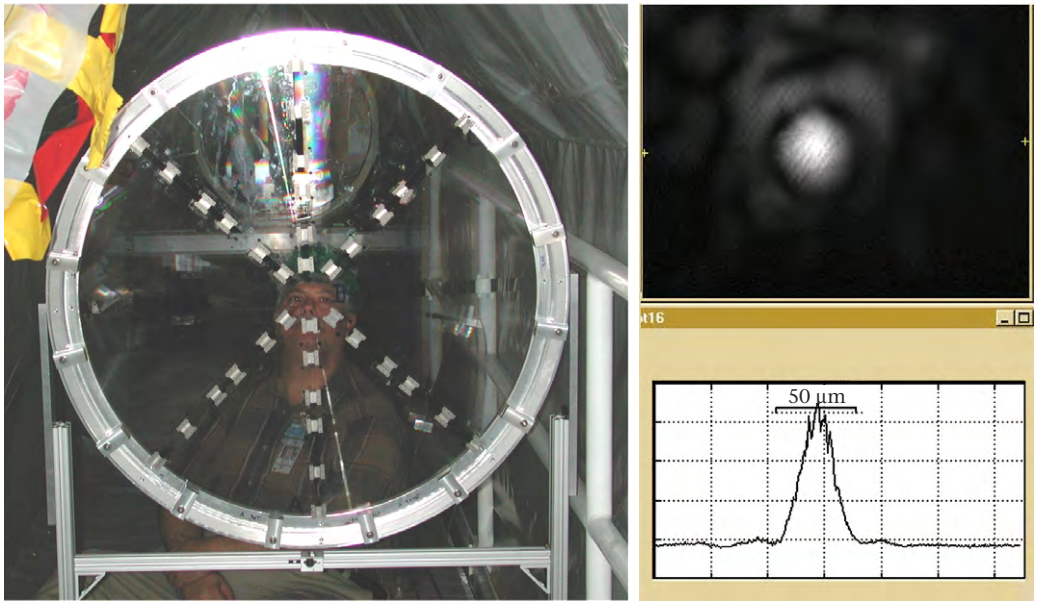

Multipanel diffractive lens (left) delivers a diffraction-limited focal spot (right).

Development of a High-Power Inertial Fusion Energy Driver Component

C. Bibeau, A. J. Bayramian, S. A. Payne, K. I. Schaffers, J. B. Tassano

00-SI-009

In FY2000 we began building the Mercury laser system as the first in a series of new-generation, diode-pumped, solid-state lasers (DPSSL). Mercury will integrate three key technologies—diodes, crystals, and gas cooling—within a unique laser architecture that is scalable to kilojoule and megajoule energy levels for fusion energy applications and high-energy-density plasma physics.

The primary near-term performance goals of Mercury include 10% electrical efficiencies at 10 Hz and 100 J with a 2- to10-ns pulse length at 1047-nm wavelength. The design requires the use of 4 × 6 × 0.75-cm crystalline slabs of Yb:S-FAP [Yb^3+:$Sr_5(PO_4)_3F$]. These slabs offer 1-ms storage lifetime and can be pumped with 900-nm laser diodes, which offer both high efficiency and reliability (10^8 shots). Laser amplification is accomplished through four passes of the beam through two gas-cooled amplifier head assemblies, each of which houses seven crystalline slabs.

The project concentrates on the critical development and production of sufficient-size, high-optical-quality Yb:S-FAP crystals. Growing full-aperture crystals has been a challenge because of the number of defects that can be present in the crystals, including cloudiness in as-grown boules, an anomalous absorption, grain boundaries, bubble core, cracking, and small inclusions around the outside of the boules. After solving or adequately reducing these defects, reproducibility and scaling up of the crystal size (>3 cm in diameter) will be required before production growth can begin.

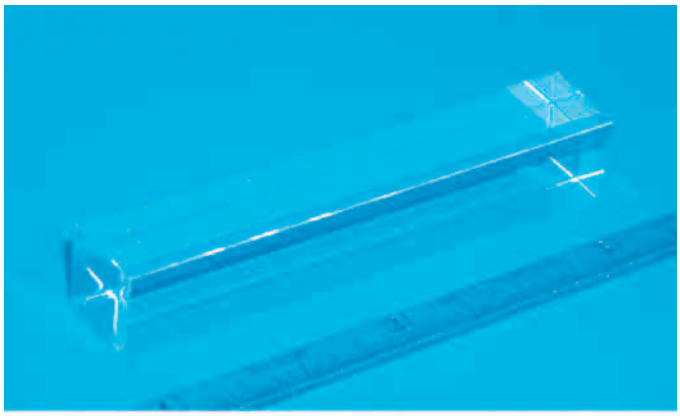

A polished section of a high-quality, small-diameter Yb:S-FAP crystal.

Significant progress has been made in understanding the growth characteristics and defect chemistry of Yb:S-FAP crystals. To fully understand and eliminate the defects and find a feasible growth technique for producing high-optical-quality crystals, a collaborative effort has been formed within LLNL and among experts in the high-temperature crystal-growth community. Under contract, a team of growth experts from the Litton-Airtron/Synoptics Group has been working to solve the defects in the crystals and provide a commercial source for high-optical-quality Yb:S-FAP. A reproducible process has been developed to nearly eliminate each of the defects in the crystals. Excess SrF_2 in the initial melt and a c-axis orientation for growth have proven successful in preventing cloudiness and the anomalous absorption, respectively. Furthermore, growth geometry, thermal gradients in the furnace, and small-diameter crystals have proven effective in controlling the formation of grain boundaries and bubble core. With significant reduction in the defects and lower thermal stresses in the crystal during cooling, cracking is no longer an issue.

In FY2001, the collaborative team will develop a modified furnace design and use compositional tuning to control scattering inclusions in the crystals. Boules grown using these modifications yield subsize crystals (<3cm) with high optical quality (see Fig.). Additionally, small-diameter crystals will be grown from which subscale slabs (2 × 6 cm) can be harvested. Diffusion-bonding technology will then be used to bond together two subscale slabs to form a full-size (4 × 6 cm) slab. Interferometric analysis of Yb:S-FAP test samples shows no evidence of the bond.

Materials Synthesis and Characterization

7

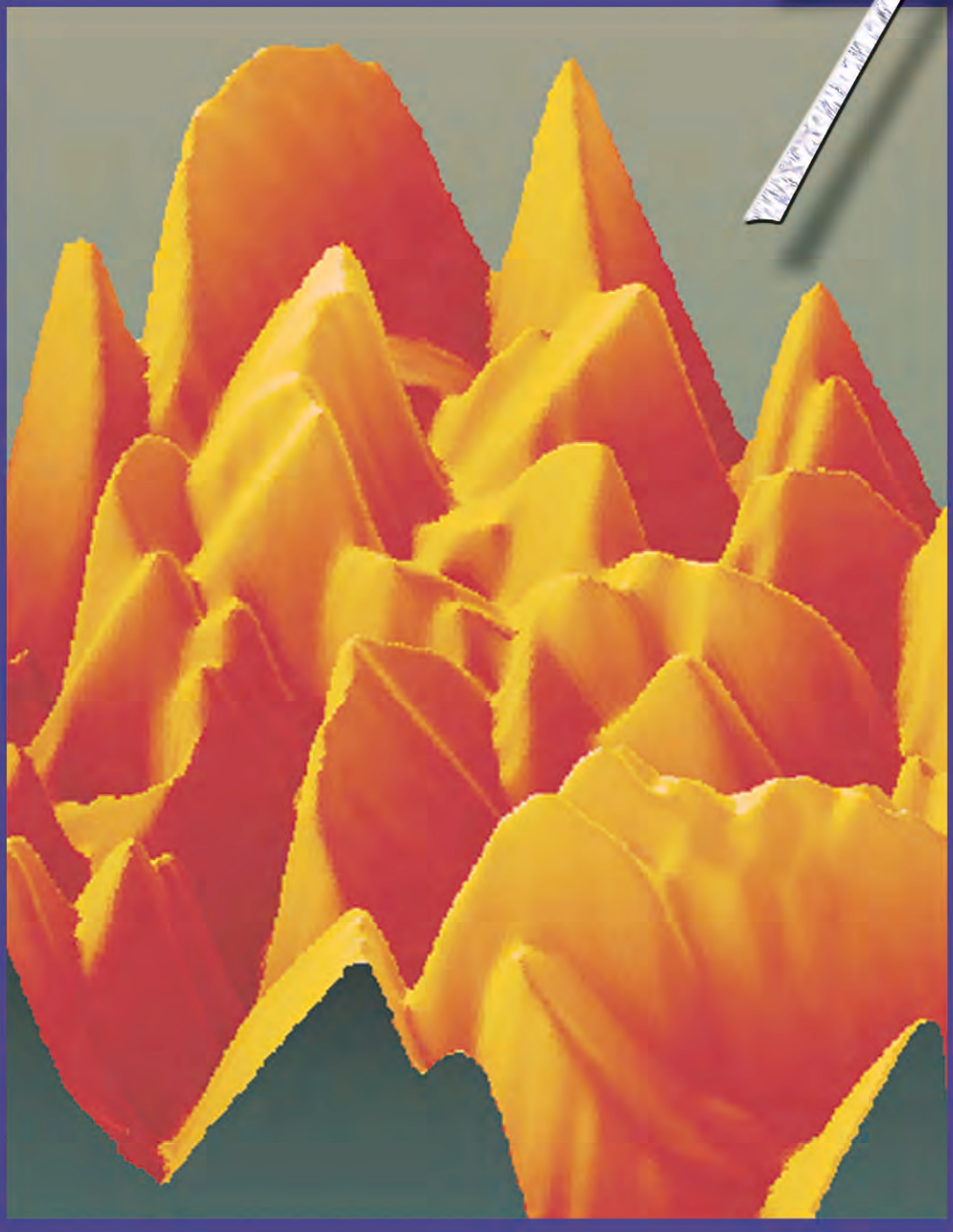

Section 7—Materials Synthesis and Characterization

Back to main TOC

Fundamental Aspects of Radiation-Induced Microstructural Evolution in Plutonium–Gallium

M. J. Fluss, B. Wirth, M. Wall, T. Diaz de la Rubia, T. Felter

98-ERD-028

Predicting the aging of plutonium (Pu) metals from radiation damage is important to our national security. However, the defect physics of Pu metals has only cursorily been investigated. For in-depth investigation, one must understand the fundamentals of the initial damage event—the emission of a 5-MeV alpha particle and the 85-keV uranium recoil (U-recoil)—along with the mass transport of vacancies, interstitials, and their aggregates.

Our goals in this project were to (1) measure important kinetic parameters for point and extended defects in Pu–gallium (Ga) alloys; (2) from annealing curves, deduce the parameters needed to accurately model the microstructural evolution driven by self-irradiation in Pu; (3) obtain insight into the fundamental aspects of the radiation-damage cascade; and (4) provide critical materials data to both molecular-dynamics and kinetic Monte Carlo (KMC) models.

Earlier in this project, we performed experiments in which we used either 3.4-MeV accelerator protons or self-decay (U-recoils) to accumulate damage in 10-µm-thick, 1-cm^2 Pu (3 at.% Ga), face-centered-cubed (fcc) metal foils at 10 to 20 K—where defects are immobile. The protons produced isolated, vacancy-interstitial pairs, whereas U-recoils resulted in clusters of vacancies and interstitials. Ultrahigh-precision resistometry and an isochronal annealing temperature algorithm were then employed to track damage annealing.

Our objectives for FY2000 were to (1) compare how proton and self-irradiated defect populations annealed as we systematically raised the temperature using an isochronal protocol, and (2) determine the actual and effective activation energies for vacancy and interstitial transport following proton and self-irradiation damage, respectively.

An unexpected result of our experiments was the discovery of a large Kondo-like (i.e., exponential, negative temperature dependence), inverse resistivity temperature effect for defects and defect clusters in Pu–Ga. Our discovery reveals the complexity of defect physics in f-electron metals, where localization and hybridization conspire to develop unusual properties.

We know that for high-purity fcc metals, the annealing curves exhibit five distinct stages. Stage I, observed at very low temperature, is due to interstitial motion; Stage II is due to interstitial clustering; Stage III is due to vacancy motion; Stage IV is due to vacancy aggregation. Finally, in Stage V, vacancy clusters dissolve and annihilate at sinks such as interstitials or grain boundaries. Alloying and defect–impurity interactions tend to make these stages less well defined.

For self-irradiation—where large defect clusters are produced in the initial radiation-cascade event—annealing curves show well-defined stages that are suggestive of a pure metal. For proton irradiations, however, the annealing curve is "washed-out" (but measurable) because of defect–impurity interactions. Although these data were confusing at first, they are now well understood. Our modeling, using molecular-dynamics and KMC methods, showed that the difference in annealing curves resulted from the dramatic differences in the damage-source terms. With this successful comparison, we now have an important validation for our models of the annealing properties of this important but complex alloy system.

By performing the isochronal annealing for different soak times (100 and 300 s), we were able to observe a measurable shift to lower temperature with increased soak time; thus, we could deduce some activation energies. Unfortunately, the full set of activation energies requires additional experimentation because the statistics of the higher-temperature stages is very limited. However, the deduction of any activation energies for a Pu alloy is a first-time achievement.

During FY2000, we also performed experiments in which we tracked the temperature dependence of the specific resistivity of the defect populations that resulted from low-temperature damage accumulation and annealing at a higher temperature. The specific resistivities of the defect populations from proton and self-irradiation were followed from 30 to 10 K, 150 to 10 K, and 250 to 10 K. For all, we observed large, Kondo-like effects in the defect populations. From 250 to 10 K, the specific resistance increased by 10 times. This effect is extraordinary. It should yield insight into (1) the role of the interplay of atomic structure and electron configuration in thermodynamically unstable materials, and (2) the possible role of heretofore unobserved spin effects—as evidenced by what appears to be anomalous impurity scattering of the conduction electrons by the sharpening Fermi surface in the vicinity of the radiation accumulation.

Grain-Boundary Engineering for Improved and Predictable Materials Properties

A. J. Schwartz, M. Kumar, W. E. King

98-ERD-080

Grain-boundary engineering is an emerging field within the materials-science community that enables significant property improvements through modifications to the grain-boundary network. Investigations have shown that grain boundaries with "special" misorientations can exhibit enhanced properties when compared to more random boundaries and that materials with high fractions of special boundaries exhibit superior properties. A tenfold improvement in certain properties is not unusual for grain-boundary-engineered materials. The enhanced properties, such as intergranular corrosion, creep, and ductility, are directly correlated to a change in the grain-boundary character distribution (GBCD) through an increase in the fraction of special boundaries.

Engineering of the grain-boundary microstructure involves deformation followed by annealing. During the annealing step, the boundary network is modified by the replacement of random boundaries with special boundaries through recrystallization, annealing, twinning, or strain-induced boundary migration. In this project, we focused on elucidating the underlying mechanisms of property improvements that were achieved by modifications to the boundary network. Our investigation coupled to LLNL's programmatic interests in (1) understanding nucleation, growth, and coalescence of voids during dynamic failure; (2) determining the influence of grain boundaries on deformation when multiscale materials are being modeled; (3) improving performance of shaped-charge liners; and (4) enhancing corrosion resistance for long-term storage of wastes.

During FY2000, our experimental and modeling effort led to a Record of Invention and provided insight into the mechanisms of how grain-boundary networks evolve. We demonstrated that the deformation path and annealing temperature each play a strong role in determining the connectivity of the random-boundary network and GBCD. Sequential strain–recrystallization was shown to be much more effective than either one-step compression or rolling deformation in disrupting the random-boundary network. Relatively low-temperature annealing proved more effective than high-temperature annealing. We concluded that the basis for property improvements is most likely the breakup of the connectivity of random-boundary networks rather than solely an increase in the GBCD.

To identify the susceptibility of specific grain boundaries to corrosive attack, we coupled electron backscatter diffraction with atomic force microscopy (AFM) and corrosion measurements. Figure (a) reveals that random grain boundaries and triple junctions exhibit a substantial increase in corrosion as compared to special boundaries. This work was instrumental in demonstrating that special boundaries disrupt the percolative paths of the random grain boundaries.

The principal challenge of our theoretical work was to develop a microstructural evolution model based on an understanding of the cooperative energetic processes that drive the evolution of boundary networks. Theoretical considerations suggest that the probability of occurrence of each boundary is dependent, to first approximation, on a ratio that is a function of the surface energy and extrinsic energetic considerations imposed on the system (e.g., strain and thermal energies). This is modified deterministically in accordance with geometric and crystallographic constraints of the triple junctions to ensure that a self-consistent microstructure is produced from the simulations. As shown in Fig. (b), our preliminary results are in remarkable agreement with the experimental data on the grain-boundary character and triple-junction distributions. When completed, this statistical approach, constructed with full knowledge of the constraints that grain boundaries encounter at triple junctions, will enable an extension of grain-boundary design and control concepts to other materials.

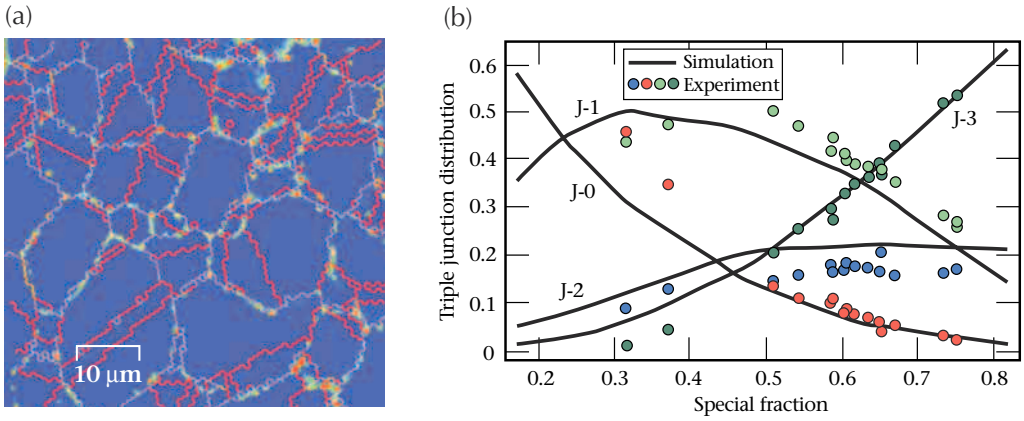

Results of grain-boundary engineering, showing (a) positive influence of "special" grain boundaries, as revealed by overlay of a grain-boundary map on an atomic force microscopy (AFM) topological false-color image; and (b) excellent agreement between experimental and theoretical grain-boundary character and triple-junction distributions.

Beryllium Materials for Inertial Confinement Fusion Targets

R. L. McEachern

99-ERD-002

Future high-powered lasers will require spherical ignition capsules approximately 2 mm in diameter with a 120- to 150-μm-thick ablator. Beryllium-(Be-) based alloys are promising candidates for ablator material due to their combination of low opacity and relatively high density (compared to polymer coatings). For optimum performance, the Be-coated capsules require a smooth surface finish, uniform thickness, microscopic homogeneity, and—preferably—high strength. The coatings must contain on the order of 1 at.% of a high-*Z* dopant [such as copper (Cu)] and permit the capsule to be filled with fuel, which will be a mixture of hydrogen isotopes. These demanding requirements can be met through a synthesis method with a focus on microstructure control. We believe that the sputter deposition process can be manipulated to decrease grain size, thereby reducing roughness and improving homogeneity.

The material properties of sputter-deposited coatings are sensitive to their microstructure and growth morphology. To meet the requirements for Be-coated capsules, the goal of this project is to optimize microstructure and growth morphology through the control of deposition process parameters.

Prior experimental studies of evaporation and sputter deposition revealed that the grain size of 99.8 at.% pure Be can be reduced by adding insoluble metal impurities such as iron (Fe) or titanium (Ti). These higher-atomic-weight elements can replace the requirement of adding 1 at.% Cu to the Be. Grain size can also be reduced by using metallic-glass-forming additives such as boron. Finally, the microstructure can be modified by changing the energy or angular distribution of the depositing flux.

In FY2000, we focused on manipulating the deposition process to improve the morphology of the deposited coatings. Application of a negative substrate bias draws positive ions from the ambient sputter gas, inducing bombardment of the growing film. The ion-assisted deposition process results in dense columnar growth and reduced grain size. The effect on mechanical strength is also favorable: introduction of ion bombardment increases the fracture stress of Cu-doped Be capsules from less than 40 to greater than 200 MPa. The roughness of 10-μm-thick coatings has been reduced from ~150- to ~30-nm root-mean-square (rms). Results from a similar experiment with thicker coatings are shown in the Fig. Atomic force microscope (AFM) images from capsules deposited with and without ion bombardment are compared, demonstrating the reduction in grain size and roughness produced by bombardment during coating.

In support of these experiments, we developed a technique for producing a variable-intensity glow discharge above the substrate. This provides a means for adjusting the bombardment current at a fixed energy. We have routinely obtained films on planar substrates with roughly 10-nm-rms surfaces. The other process modification we studied was to restrict the angular distribution of the depositing atoms. When atoms land on a growing film from all directions (isotropic deposition), surface roughness tends to be amplified by the process of self-shadowing. By using an aperture to restrict the flux to near-normal incidence, coatings were produced with a grain size of roughly 60 nm and a roughness of 5-nm rms.

Although not all process parameters were optimized for sputter-deposited Be capsules at the end of the project, this LDRD produced a good roadmap to guide future development of this technology.

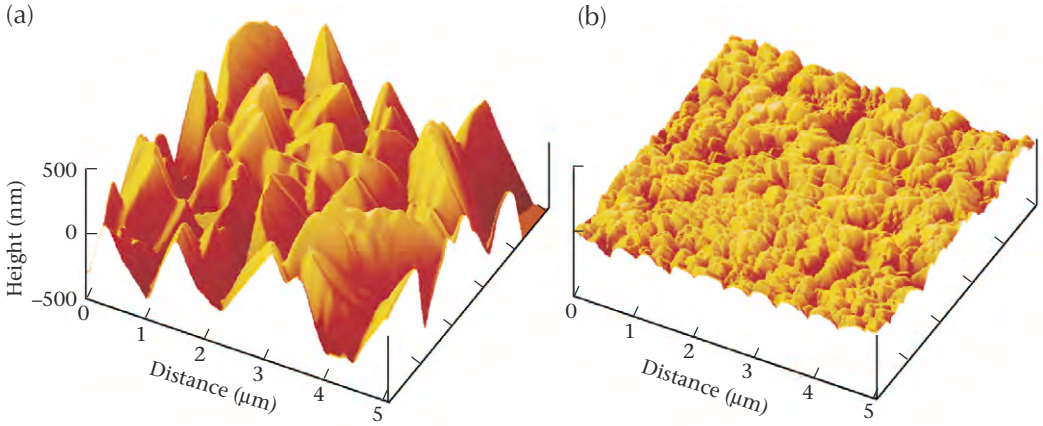

Atomic force microscopy (AFM) images of Be/1 at.% Cu sputter-coated capsules. The starting mandrels were 1-mm-diam plasma polymer capsules with a 20-μm coating thickness. (a) Coating deposited with no bias applied, Rq (rms roughness) = 263 nm; (b) Coating deposited using 80-V bias, Rq = 33 nm.

Chemistry and Processing of Nanostructured Materials

G. A. Fox, T. F. Baumann, A. L. Vance

99-ERD-004

This research combines dendrimer chemistry with LLNL's expertise in organic aerogels for the design of novel nanostructured materials. Organic aerogels are typically prepared by means of sol-gel polymerization, a process that transforms reactive monomers into nanometer-sized clusters that then cross link to form the 3-D network or gel state. While sol-gel chemistry provides the opportunity to synthesize new material compositions, it cannot separate the process of cluster formation from gelation. This limitation results in structural deficiencies in the gel that impact the physical properties of the dried xerogel, aerogel, or nanocomposite. To control the properties of the resulting gel, one should be able to regulate the formation of the clusters and their subsequent cross-linking.

We are using dendrimer methodology to separate the cluster formation from the gelation so that new nanostructured materials with controlled composition and topologies can be produced. Dendrimers are three-dimensional, highly branched macromolecules that are prepared in such a way that their size, shape and surface functionality are readily controlled. Consequently, incorporation of dendrimer chemistry into sol-gel synthesis should allow for greater control over both the composition and topology of the resultant nanostructured materials.

In FY2000, we focused our efforts on building functionality into new sol-gel precursors for the preparation of novel aerogels. Because resorcinol is one of the main starting materials for organic aerogels, we focused efforts on the preparation of new sol-gel precursors containing two or more resorcinol units attached to a functional core molecule. These core molecules can be metal complexes, binding sites, fluorophores or templated moieties. From these core molecules, dendrimer chemistry is employed to attach multiple resorcinol units to the core. These molecules can be polymerized using the sol-gel process to generate functionalized organic aerogels.

With this strategy, we have prepared two main types of dendritic molecules in FY2000: (1) sol-gel precursors containing templates and (2) sol-gel precursors based on metal binding sites. Using templates in sol-gel synthesis allows the preparation of aerogels that contain specific molecular recognition sites within the gel matrix. We prepared first-generation sol-gel precursors through esterification of simple templates such as ethylene glycol or glycerol, with 3,5-dihydroxybenzoic acid. These gel precursors were then reacted with formaldehyde under sol-gel polymerization conditions to generate new sol-gel materials. Current efforts are directed toward the removal of the template from these products to yield imprinted gels that can specifically recognize and bind the template molecules. Once the conditions for the template removal have been established, sol-gel precursors based on more significant templates will be prepared. We also synthesized sol-gel precursors in which the central core contains a metal binding site. Functionalization of a metal-chelating unit with 3,5-dimethoxybenzyl chloride, followed by removal of the methyl protecting groups, yields a sol-gel precursor capable of coordinating metal ions. These precursors can either be polymerized directly to generate gels with metal binding sites [Fig. (a)] or the precursors can be reacted with the metal ion of choice prior to gelation as a method to introduce metal ions into the gel framework [Fig. (b)]. As a first step, we have prepared gel precursors in which the central cores are sulfur-based ligands. These compounds have been polymerized under sol-gel conditions and their properties are currently under investigation.

In FY2001, we plan to (1) investigate the utility of new protecting groups in the synthesis of larger generation dendrimers; (2) prepare generation two and three dendrimers with a variety of cores; and (3) polymerize new dendrimers using the sol-gel process to produce new xerogel and aerogel materials.

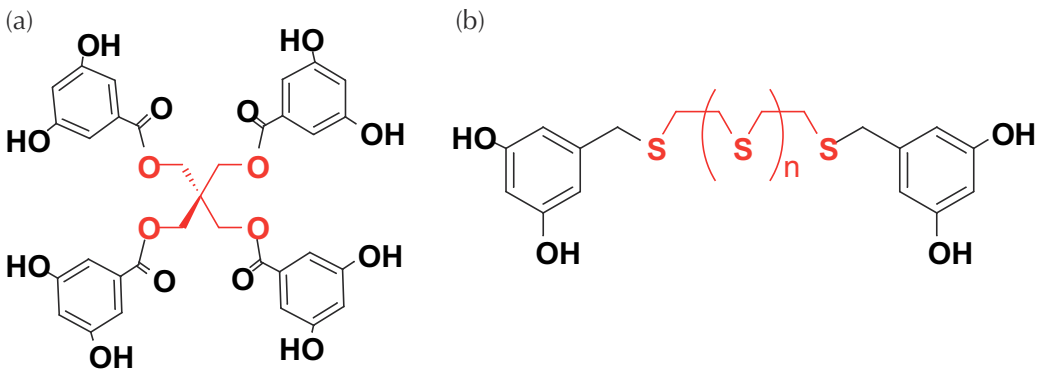

Examples of sol-gel precursors containing templates (a) and metal binding site (b).

Studying the Kinetics and Surface Dynamics of Solid–Solid Phase Transitions at High Pressures and Temperatures

J. M. Zaug, C. S. Saw, D. L. Farber

99-ERD-007

To understand geological phenomena, high-pressure chemical synthesis, planetary physics, and combustion and detonation processes, we must have time-resolved measurements of phase-transition and chemical-reaction rates at high pressures and temperatures. These measurements are insufficient in the published literature. Our goal in this project is to build up a quantitative, experimental database that begins to systematically illustrate how the kinetics of solid–solid phase transitions in energetic materials (EMs) depend on grain size, impurity content, temperature, pressure, initial compaction density, polymer content, and strain rate. The capabilities spun off from this project are relevant to LLNL programmatic requirements.

During FY1999, we had established a new experimental capability at LLNL—second harmonic generation (SHG)—in the Lab's high-temperature diamond anvil cell (DAC). During FY2000, we improved the SHG experiment; built and used an in-house, high-pressure, x-ray diffraction capability; and made new experimental observations of the solid–solid phase transition of the high explosives HMX, LX-04, and TATB using (independently) SHG at LLNL and high-flux x-ray radiation at both the Stanford University and Brookhaven National Laboratory synchrotron laboratories.

Our FY2000 experimental procedures involved subjecting DAC-enclosed samples to a temperature jump (450°C/min) to reach a target temperature at 1 bar. We used either SHG or x-ray powder diffraction (XRD) [Figs. (a,b), respectively] to monitor the structural phase change over time. Pressure was used to drive samples back to lower-volume phases. These experiments can also be initiated at high-pressure; hence, they permit determination of activation energies and volumes for each transition encountered.

The following observations signify the successful completion of our experimental design, construction, and tests of project feasibility. The phase-transition rates of pressed powders of EMs, such as those used in the weapons complex, are slower than unpressed powders. Pressed HMX materials undergo a repeatable and complex phase-transition process. The complex nature of this process [e.g., peaks and dips seen on the initial $\beta \rightarrow \delta$ growth curve in Fig. (a) and the variation in amorphous background seen in Fig. (b)] become systematically washed out as the temperature of the experimental target is pushed further above the equilibrium phase-transition temperature of about 158°C for our pure-HMX samples. We postulate that this effect is related to the variation of mean surface energy at grain boundaries. Single-crystal HMX samples ($150 \times 50 \times 50$ mm) transition much faster to the δ-phase than do unpressed powders, which in turn transition faster than pressed samples. The induction period for the phase transition increases as the average grain size decreases, and it decreases with increasing temperature. Adding binder to EMs increases the time the material takes to transition from a low-volume to a larger-volume crystal lattice. We postulate that the expanding polymer matrix and ensuing pressure increase favor the β-phase and thereby increase the overall transition time. At room pressure and temperature, δ-phase HMX samples do not rapidly convert back to the β-phase; the conversion may take months or years to complete. After the HMX has been pressed and as heating (<150°C) occurs, a clear and viscous residue builds up on the diamond culets. We have found no mention of such a residue forming under our experimental conditions in the open literature, and we plan to analyze this product. At the close of FY2000, we were quantifying our observations.

During FY2001, we plan to conduct simultaneous SHG/XRD experiments on several polymer blends of EMs.

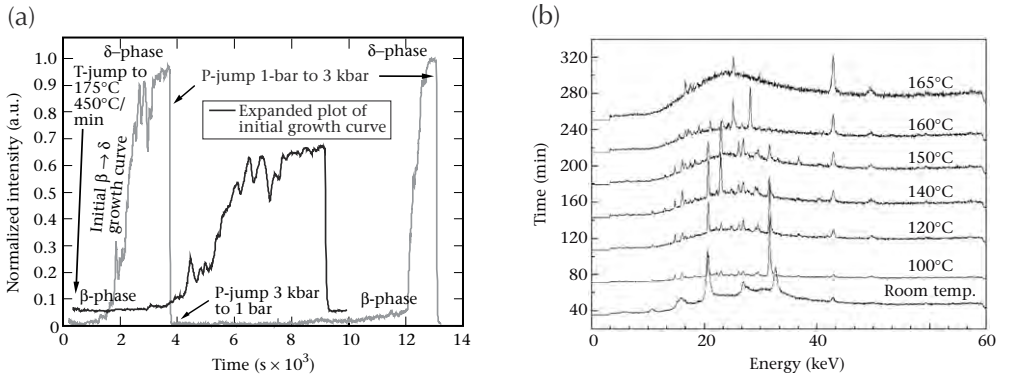

Structural phase change over time, showing (a) the second harmonic generation (SHG) time-profile of the high-temperature and pressure $\beta \rightarrow \delta \rightarrow \beta$ transition of pressed HMX high explosive, and (b) an energy dispersive x-ray diffraction (EDXRD) profile of the high-temperature pressed HMX $\beta \rightarrow \delta$ transition.

Back to main TOC

Determining the Structure of Biomaterials Interfaces Using Synchrotron-Based X-Ray Diffraction

M. T. McBride, J. J. De Yoreo

99-ERI-011

Many organisms exhibit control over biomineralization processes, the result being exquisitely tailored crystalline architectures. Control may involve the introduction of acidic macromolecules that interact with growing crystals, or carefully timed introduction of ions, the removal of trace elements, the introduction of specific enzymes, and so on. These processes occur at crystal surfaces; specifically, they are processes mediated by atoms at the solid–solution interface. Understanding such processes requires tools for probing surfaces and near-surface atomic structure in fluids.

Surface x-ray diffraction (SXRD) techniques have recently been used to determine the atomic ordering of crystal surfaces in liquids and the near-surface ordering of the liquid phase. Because it can be applied in situ, SXRD provides a dynamic picture of the system under study, giving crystal structure, surface molecular structure, the stereochemistry of adsorbates, and the stereospecifity of binding sites. This method provides a crucial link between experimental surface techniques such as scanned-probe microscopy and theoretical tools such as kinetic Monte Carlo and molecular dynamics. All these techniques are playing increasing roles in detection, identification, and characterization of biological molecules and materials.

The purpose of this project is to explore the feasibility of using SXRD to determine the surface structure of biominerals in electrolyte solutions and of the adsorbed layer of acidic amino acids that are believed to play a central role in the control of biomineral formation and function. Our work is a critical component in the development of an integrated picture of the physical and chemical bases for deposition and dissolution at solid–liquid interfaces in biological systems; it brings a new and very powerful surface-sensitive capability to LLNL. We chose as our model systems calcium carbonate and calcium phosphate in aspartic and glutamic acid-bearing solutions. The calcium compounds are ubiquitous among biomineral structures, while the two acidic amino acids are the dominant constituents of protein mixtures that are implicated in the control of biomineralization.

Using a variety of experimental techniques, during FY2000 we determined that (1) aspartic acid strongly modifies calcite surfaces; (2) the stereospecific binding interaction involves two sites on {hk0} faces, whereas interactions on {104} faces are insignificant; and (3) surface free-energy modifications are a thermodynamically driven process, not a kinetic one. In our SXRD studies of calcite, we looked for changes in the surface structure of calcite upon the addition of aspartic acid. Measurements were made for both pure calcite and calcite in aspartic-acid-bearing solution. Our results showed clear evidence for the presence of an organic thin film on the {104} face; however, because of beam-induced damage of the film we were unable to draw conclusions about the ordering of the film.

Towards the close of FY2000, we employed sophisticated energy calculations to model the interactions of both D- and L-aspartic acid with {hk0} faces of calcium carbonate; our results show that the differences in binding geometries are quite subtle.

We also began work that we will continue during FY2001. First, to understand the nature of mineral-adsorbate interactions that occur in the body, we began SXRD experiments that probe the nature of surface modifications of fluorapatite in the presence of a carefully selected suite of adsorbates, including carboxylates and diphosphonates. Second, as a preview to our planned FY2001 investigation of calcium phosphates—the primary mineral constituent of bones and teeth—we used SXRD for measurements of brushite ($CaHPO_4 \cdot 2H_2O$) and fluorapatite ($Ca_{10}(PO_4)6F_2$).

Smart Membranes

T. van Buuren, T. F. Baumann, A. Vance

00-ERD-009

Smart membranes combine several structural and functional properties, including mechanical and chemical stability, high permeability, and species selectivity. Designing smart membranes with these characteristics is a challenging task, requiring novel synthetic techniques that tailor membrane materials for specific applications such as gas separation, reverse osmosis, microfiltration, and biomedical separation.

The goal of this project is to design a smart and selective membrane through the manipulation and control of the surface chemical groups and the pore-size morphology. This will be accomplished by (1) exploiting the phenomenon of molecular self-assembly to change the chemical nature of the surface and (2) using lithographic methods to modify the pore morphology of the substrate. Formation of self-assembled monolayers (SAMs) on porous silicon (Si) provides the opportunity to design a versatile class of new materials. With control over both the pore morphology and the nature of the monolayer, we can fabricate and tailor the chemical interaction and filtering capability of the smart membrane to selectively recognize and bind to the substrate molecules, such as DNA fragments, proteins, enzymes and other biologically relevant macromolecules. Silicon wafers with pore sizes ranging from a few nanometers to many micrometers can be prepared through the electrochemical dissolution of Si. SAMs typically derive their chemical selectivity from the terminal functional group of the adsorbed species. As a result, a variety of surfaces with specific interactions can be produced with fine chemical control. This fundamental research will enhance the Laboratory's chemistry and material science core capability in nanotechnology, and the bioscience that directly supports the chemical weapon and biological weapons detection programs at LLNL.

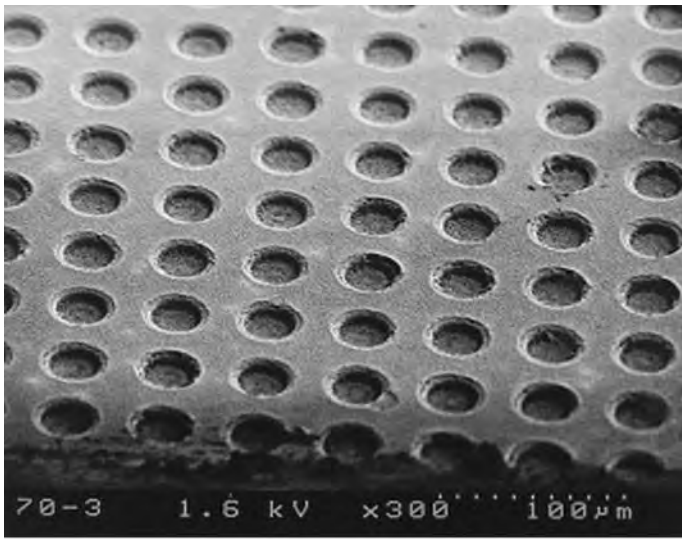

Regular array porous silicon (Si) with 20-µm pore diameter.

During FY2000, we focused on the preparation of simple monolayers on gold (Au)-coated Si to establish a protocol for the assembly of SAMs within the pores. Characterization and understanding of these systems will lead to the design of more complex and functional membranes. The mechanism of how the thiols bond to Au substrates and form SAMs is not completely understood. To address this we have attached simple alkanethiols onto Au-coated Si substrates and then characterized them by x-ray absorption spectroscopy, photoemission spectroscopy and atomic force microscopy (AFM). We have found that longer-chain alkanethiols (carbon chain longer than five) give better coverage and order better than short-chain thiols. Also we find that the reaction time of the thiols on the Au has to be greater than 20 h to give quality SAMs shorter time given nonuniform films.

To fabricate the silicon (Si) scaffolding we have constructed a special electrochemical cell for the synthesis of the regular array porous Si, which can be synthesized by anodization of Si in an HF/ethanol electrolyte that etches straight channel pores. To drive the anodization reaction the n-type Si wafer needs to be illuminated to photogenerate electron hole pairs needed in the electrochemical reaction. We have demonstrated that the diameter of the pore can be adjusted between 100 nm to 2 µm depending on the intensity of back illumination. The Fig. shows a regular array of 20-µm pores etched into n-type silicon .

In FY2001 we will attach the first generation SAMs onto the Au-coated porous Si and characterize structure and properties using AFM, and photoemission. Also we will synthesize SAMs with more complex terminal groups and different types of tethers. Self-assembly of monolayers on porous Si will represent an exciting new class of materials. With control of the pore-size morphology and the terminal groups at the SAM interface, we can design smart and selective membranes.

Slow Crack-Growth Behavior in Fused Silica

T. I. Suratwala, R. A. Steele, J. H. Campbell

00-ERD-012

Fused silica glass is largely inert, is resistant to high temperatures, has a very low thermal-expansion coefficient, and has excellent optical qualities. Hence, fused-silica materials are utilized in a variety of technologies, including optics, ultraviolet (UV) lithography, and windows for vacuum chambers, Space Shuttles, submarines, and aircraft. These materials often operate under stressed conditions in which flaws (cracks) can grow at stresses below that required for catastrophic failure. This type of crack growth is often called slow crack growth (SCG), or subcritical crack growth.

In addition to its high technological importance, fused silica is an ideal glass to study scientifically. It has a single-component glass structure consisting of connected $(SiO_4)^{-4}$ tetrahedra. This relatively simple structure makes it an ideal glass for modeling fractures using quantum-mechanical molecular-dynamic simulations and for investigating fundamental mechanisms of fracture.

Slow crack growth behavior has been extensively studied in a variety of materials (e.g., polymers, metal, and glasses). Also, properties of fused silica have been very well characterized in the literature. However, the understanding of SCG behavior in fused silica is surprisingly limited. In fact, only limited experimental measurements of SCG in fused silica have been made. Such measurements are critical to comparing and supporting fundamental modeling of environmentally assisted fracture processes.

In this project, we are measuring slow-crack velocities using the double-cleavage-drilled-compression (DCDC) technique in various environments (i.e., different stresses, temperatures, humidities, and atmospheres) and modeling them based on the stress-corrosion mechanism. Successful completion of our work would (1) provide a greater fundamental understanding of SCG behavior in fused silica, and (2) allow quantitative prediction of crack velocities in fused silica exposed to different environments.

During FY2000, we designed, built, and calibrated the experimental setup shown in Fig. (a) to measure SCG in fused silica, and we began collecting crack-velocity measurements as a function of temperature and humidity. We mounted rectangular glass samples with a hole drilled through their centers in the mechanical testing setup within an environmentally controlled chamber and applied a compressive stress. By monitoring the position of the crack as a function of time using a charge-coupled device (CCD) camera, we determined the velocity of a crack originating from the hole in the sample.

Crack velocities expressed in plots of log of velocity vs. stress intensity (K_i) commonly show three distinct regions of behavior (regions I, II, and III)—as Fig. (b) shows. Region I refers to the range of conditions for which crack growth is reaction-rate limited; it is characterized by a linear increase in the plots of the log of the velocity vs. K_i. In other words, enough H_2O is present at the crack tip so that crack growth is limited by the rate of reaction between H_2O and the Si–O–Si bonds in the glass structure. Region II refers to the conditions where the crack velocity becomes constant with increasing K_i, that is, where crack velocity is mass-transport-limited by the rate of H_2O diffusion to the crack tip. Finally, region III refers to the condition where crack velocity becomes independent of the H_2O environment and is limited by the atmospherically induced stress corrosion.

During FY2001, we will (1) continue to measure crack velocities in various environments (temperatures and humidities), (2) complete the data analysis, and (3) examine the effect of residual impurities (e.g., OH, Cl, and F) on SCG.

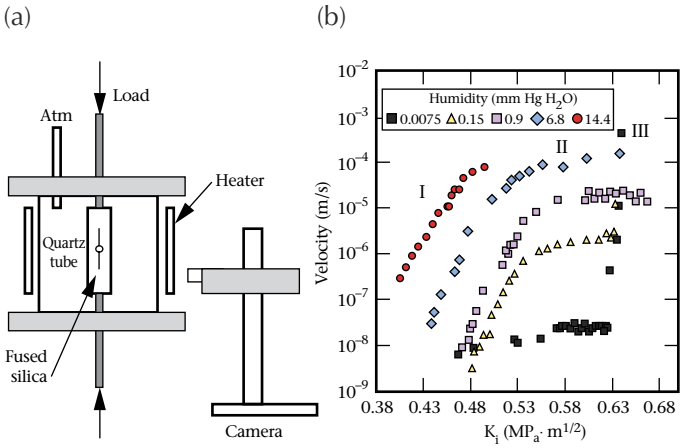

Investigation of slow crack growth (SCG), showing (a) the experimental setup, and (b) measured SCG velocities in fused-silica glass as a function of stress intensity (K_I) and humidity at 20 to 25°C.

Back to main TOC

Subpicosecond Laser Deposition of Thin Films

F. Y. Génin, B. C. Stuart, W. McLean, L. L. Chase

00-ERD-013

The femtosecond time scale in science and engineering is growing in importance and maturity—as evidenced by the 1999 Nobel Prize in Chemistry awarded for the application of femtosecond spectroscopy to chemical reactions. At LLNL, understanding the interaction between materials and high-energy-density light in pulse-length regimes ranging from tens of femtoseconds to nanoseconds during the manufacture and processing of materials has become a key issue in both programmatic and fundamental research.

The purpose of this project is to compare the fundamental behavior and materials properties of thin films deposited using pulsed lasers operated in the femtosecond regime with those resulting from other, conventional deposition techniques. In particular, we want to identify the advantages and disadvantages of femtosecond pulsed-laser deposition (PLD) over nanosecond PLD—especially those aspects related to producing thin films by ablating material with intense, ultrashort laser pulses.

During FY2000, we focused on using high-purity graphite as the initial ablation material. Our objectives were to (1) compare the microstructure and materials properties of the films deposited using lasers operated in the femtosecond and nanosecond pulse-length regime, (2) perform a mechanical characterization of the deposits, and (3) increase the deposition rate.

We deposited diamond-like carbon (DLC) in vacuum, measured ablation rates, and characterized the physical and chemical properties of the films. Our mechanical characterization of the deposits showed improved film–substrate adhesion properties that allowed us to build 200-µm-thick layers using 150-fs pulses. We found that (1) DLC films produced with nanosecond pulses delaminated as soon as the thickness reached only a couple of micrometers, (2) the stresses in the films were greatly influenced by the fluence and the duration of the laser pulses, and (3) the microstructure and surface morphology of the films did not vary significantly with the processing parameters that we evaluated (pulse length and fluence). Finally, we demonstrated that it is possible to significantly increase the deposition rate with shorter pulses at a given fluence. In particular, with this technology, DLC could be deposited at 25 µm/h.

Our primary goal for FY2001 is to influence and optimize the deposition process by analyzing and modeling the relationship between the characteristics of an ablation plume (energy, charge, and mass) and the growth behavior of the film. We also plan to determine if the laser parameters influence the stoichiometry of the deposits when compounds or alloys are used as ablation targets. We will investigate materials such as TiC, SiC, AlN, and polymers.

Back to main TOC

Photothermal Microscopy: Next-Generation Nanoscale Imaging

D. J. Chinn, C. J. Stolz, P. K. Kuo

00-ERD-019

As structures move to the nanoscale, higher-resolution nondestructive characterization techniques such as photothermal microscopy (PTM) are needed. We were motivated to undertake this project because of the many technical problems, including laser-damage to optical coatings, to which PTM can be applied.

Photothermal microscopy was originally developed to detect optical absorption and micrometer-sized thermal inhomogeneities in optical coatings. Offering a higher spatial-resolution alternative to infrared imaging, this powerful tool is used for thermal nondestructive characterization of surface and subsurface features with micrometer spatial resolution. It is of great importance in the study of (1) energy deposition in optical structures, e.g., high-power laser diodes and laser optics; (2) defect detection in coatings, e.g., silicon multilayers; and (3) materials science and manufacturing research.

Photothermal microscopy uses raster-scanning pump and probe lasers with a photodetector to measure thermal absorption of materials. The pump laser heats the test object while the probe laser and photodetector measure the diffraction of light resulting from surface deformation as the heat is absorbed. The spatial resolution of PTM is limited by the pump-laser beam size, which can be focused down to the diffraction limit (~1 mm), as described by classical optics.

In FY2000, we worked on increasing the spatial resolution of PTM to 100 nm. We investigated implementation of near-field optical techniques to PTM and installed and evaluated a near-field scanning optical microscope (NSOM) for use in nanoscale photothermal experiments. An NSOM produces subwavelength-resolution optical images by scanning an optical fiber over materials. At nanoscale resolution, PTM requires use of the NSOM fiber probe as the PTM pump laser. An NSOM probe will be used in the PTM pump-probe configuration in an attempt to achieve nanometer PTM.

The NSOM we purchased consists of a unique scanning stage and is supported at three points by piezoelectric tubes. The three-point support configuration allows a PTM probe laser beneath-the-sample access. We captured and assessed optical images with the NSOM to determine the potential for nanoscale PTM.

The NSOM scanning stage has a tuning fork oscillator that is attached to the fiber tip and serves as a proximity indicator for sensing the distance between the fiber tip and the sample surface. When the tuning fork is driven at its resonant frequency by a lock-in amplifier, the presence of the sample surface within nanometers of the fiber tip increases damping. A feedback loop from the lock-in amplifier controls the vibration of the tuning fork and keeps the fiber tip at a constant distance from the sample. An evaluation of the NSOM found that the feedback control system can be further optimized by varying the phase of the lock-in amplifier. This improvement to the feedback control system will give more precise fiber–part offset distances.

In FY2001, we plan to complete needed modifications to the NSOM so that we can test PTM for nanometer resolution. We will also develop a camera-based imaging system to increase the speed of micrometer resolution for PTM.

Back to main TOC

Predicting and Effecting Precise Deformation of Nonrigid Objects

K. L. Blaedel, D. W. Swift, E. P. Kasper, S. R. Patterson

00-ERD-020

In traditional dimensional inspection, objects are assumed to be essentially rigid. Measurements are taken under constraints that have minimal effect on the overall uncertainty of the measurement. The results are compared to a design specification, and a statement of uncertainty is made. However, when the object to be measured is not rigid, the contribution of the boundary conditions to the uncertainty in the measurement result becomes significant. Additionally, the dimensional characteristics of the fixtures and supports become confounded with the characteristics of the object being inspected; thus, the true shape of the object cannot be determined. Finally, if the nonrigid object is used under boundary conditions that differ from those present during inspection, the in-use shape is unknown.

Joining thin, hemispherical shells to make a sphere; mounting thin potassium dehydrogen phosphate (KDP) crystals in advanced laser systems; holding thin photomasks for use in extreme-ultraviolet (EUV) lithography; and assembling automobile sheet-metal parts are all examples in which nonrigid components are used under boundary conditions that differ from those present during inspection. To extend the precision to which these objects can be specified, inspected, and assembled, a new technique for dimensional inspection must be developed and employed.

Our first goal in this project is to understand methods for restraining or actuating nonrigid objects so that their resulting deformation is repeatable and predictable. While this may appear to be a straightforward analysis problem, it is subject to many sources of error, which must be reduced before such analysis can be applied with high precision. Our second goal is to develop a methodology for designing restraints or actuators that produce a predictable deformation on the surface of a nonrigid object and that can be modeled analytically with minimum uncertainty. This technique will be applied to a nonrigid cylinder first and then extended to include other shapes.

The most noteworthy results from our FY2000 work were that three dominant finite-element analysis (FEA) uncertainties were identified and quantified. The first was the use of an idealized geometry vs. the exact geometry for the analysis. We found that using the idealized geometry introduced an error in the result of about 0.2%. The second dominant uncertainty centered on the material properties. We found that uncertainties in the material properties (e.g. elastic modulus, Poisson's ratio, orthotropy) were directly proportional to uncertainties in the analytical result. This uncertainty amounted to an error of about 0.4% in the analytical result. Finally, we determined that contact at the restraints was difficult to model and characterize and thus contributed to an error in the results of about 14%. However, because the development of contact algorithms is beyond the scope of this project, we are confining our measurements and analytical comparisons to the regions of the cylinder that are outside the area affected by localized contact.

Our goals for FY2001 are to complete the measurements on the thin cylinder and compare them to the analytical results under various displacement and force boundary conditions. From there, we will extend our technique to a thin, hemispherical shell. Additionally, we will formalize the methodology for designing restraints and actuators as a set of design guidelines. These guidelines will serve as the foundation for designing fixtures, mounts, and other constraining devices for nonrigid objects. Finally, to aid in the specification and acceptance of nonrigid objects we will develop a set of metrics that is based on function rather than on geometry.

Structures of High-Density Molecular Fluids

B. Baer, H. Cynn, V. Iota, C. S. Yoo

00-ERD-024

By merging the techniques of coherent anti-Stokes Raman spectroscopy (CARS) and diamond-anvil-cell laser heating, we are developing a new, pulse-heated, molecular-probing technology for observing high-energy states of dense matter by characterizing in situ, high-pressure, and high-temperature fluid material. This state-of-the-art technology will be capable of characterizing chemical bonding, molecular structures, and intermolecular interactions at the conditions of pressure, temperature, and time scales comparable to shock-wave and other dynamic compressions. Thus, it will provide a critical tool for the Stockpile Stewardship Program. Our results will also have important implications for high-explosive (HE) detonation, planetary models, and syntheses of novel materials.

Our main goal is to obtain spectroscopic information at temperatures and pressures that have been previously inaccessible. Our investigation has three parts: we will examine (1) diamond melting and the theoretically suggested, first-order, liquid–liquid carbon phase transition; (2) hydrogen metallization; and (3) the molecular potentials of various HE products.

During FY2000, we constructed a system that is capable of obtaining vibrational spectra of high-density fluids at high pressures and temperatures by applying CARS to continuous-wave- (CW) and ns-pulse-heated samples in diamond-anvil cells. Our preliminary tests on methane and nitrogen had shown them to be excellent candidates for this type of investigation, given their significantly large CARS signal.

Coherent anti-Stokes Raman spectroscopy is a third-order, nonlinear process that requires two, high-peak-power (megawatt) laser pulses of different colors to overlap in a sample, both spatially and temporally [see Fig. (a)]. A third color is produced by the sum-frequency addition of two photons of the bluer (w1) color and the subtraction of one of the redder (w2) colors [see Fig. (b)]. The intensity of the CARS signal is related to the third-order susceptibility of the resonant and nonresonant Raman transitions.

To achieve the necessary experimental conditions, we use laser heating to raise the sample's temperature to thousands of Kelvin while it is under high pressure in a diamond-anvil cell. However, direct laser heating is often difficult because many materials lack a strong electronic or vibrational transition that is coupled to the incoming laser light. Therefore, a major goal of our project is to fabricate a target that (1) can absorb sufficient laser light, so that high temperatures can be achieved; (2) is partially or wholly transparent, so that the CARS experiment can be conducted simultaneously with the laser heating; (3) is not only small enough to fit inside the miniscule sample volume, but also allows enough space for the sample to surround it; and (4) has an extremely high melting point, so that it retains its shape and does not undergo chemical change.

During FY2000, we investigated two different targets. First, we used sapphire disks (~20-μm thick, ~80-μm diam) as the target heated by CO_2 laser irradiation. Sapphire is relatively inert, has a high melting point, and is optically transparent. Second, we fabricated metal toroids of similar thickness and diameter with a 40-μm center hole for heating by an Nd:YAG laser. The latter method of using toroids has the advantage of allowing the laser beams used with CARS to focus inside the target (the hole) rather than near the target surface to analyze the sample.

In FY2001, we intend to obtain CARS spectra of nitrogen that considerably exceed 10 GPa and 2000 K. We expect that the same can be done with hydrogen and possibly with methane.

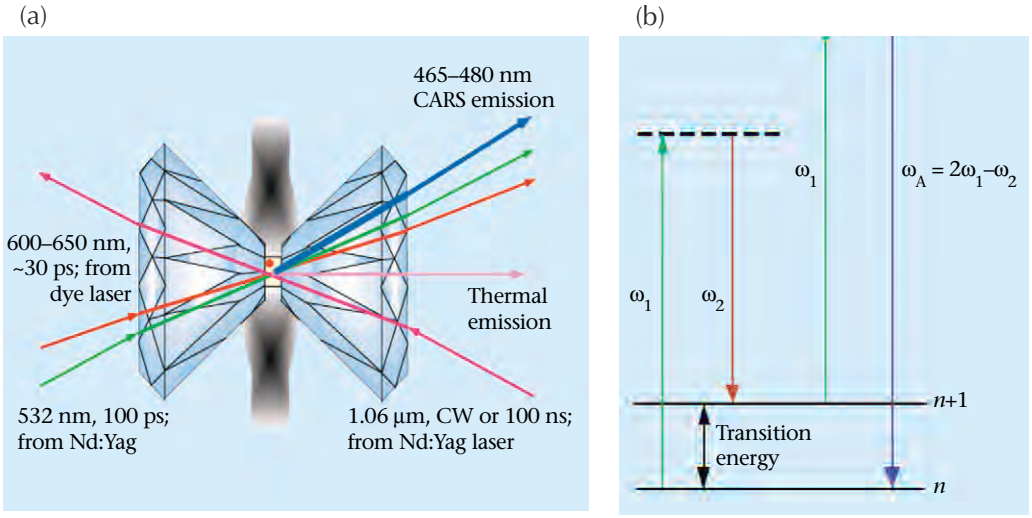

***Simultaneous laser heating with coherent anti-Stokes Raman spectroscopy (CARS), showing (a) the beam configurations, and (b) the CARS process for obtaining a third color, ω_A, using ω_1 and ω_2 to probe the transition energy from vibrational state* n *to state* n+1.**

Surface Nanostructures Formed by Intense Electron Excitation

A. V. Hamza, M. W. Newman, H. W. H. Lee, T. Schenkel, J. W. McDonald, D. H. Schneider

00-ERD-029

Intense, ultrafast electronic excitation of a surface produces a severe energy imbalance between the electronic and atomic degrees of freedom. The far-from-equilibrium situation can drive the formation of novel structures. If the volume of the excitation is small (~100 nm^3), it is possible to "freeze in" these novel but metastable structures.

Because of the indirect nature of its band gap, externally excited bulk silicon (Si) is typically a poor photon emitter. However, as the crystal size approaches nanometer scales, the band gap widens due to quantum confinement and may become direct, thereby allowing for more efficient photon emission.

Our goal in this project was to produce, characterize, and apply localized (nanometer sized) phase transitions on semiconductors using intense, ultrafast electronic excitation.

During FY2000, we produced nanometer-sized structures in Si using phase transformations induced by intense, ultrafast electronic excitation from slow, highly charged ions. We used beams of highly charged ions of various charge states (from 20^+ to 69^+) and various kinetic energies (from 5 to 14 keV times charge) to induce this phase transformation in clean Si surfaces (see Fig.). The new phase is characterized by ex situ photoluminescence (PL) from the irradiated area after excitation with laser wavelengths from 379 to 514 nm. Photoluminescence spectra from the exposed areas show emission centered at about 540 nm, which is consistent with emission observed from 1- to 2-nm-diam silicon nanocrystals. The series of sharp lines at 565, 555, and 548 nm that is present in the PL spectrum from areas exposed to Xe^{44+} is characteristic of an excitonic series in nanometer-sized material. To our knowledge, this is the first observation of excitonic structure in nanometer-sized silicon structures.

In FY2000, we further characterized these Si nanostructures via photophysical interrogation. The temperature dependence of the PL from the Xe^{44+} irradiated surface (fluence = 1×10^{12}; kinetic energy = 616 keV) was particularly enlightening. The PL signal decreased with decreasing temperature from 190 to 20 K. The PL signal decrease with increasing temperature only above 190 K. The observed temperature dependence is explained by considering the electron-hole exchange interaction for the exciton. Spectroscopically, radiative recombination from the triplet state is spin forbidden. Radiative transitions are allowed transitions from the singlet state of the exciton. Population of the singlet state from the triplet ground state requires the electron hole to exchange energy, which can be supplied by the annihilation of a phonon. Raising the temperature of the sample from 20 to 175 K increases the population of the singlet state and hence the observed higher PL efficiency of the exciton at 175 K. An Arrhenius plot of the PL signal vs. inverse temperature yields 20 MeV for the electron-hole exchange energy splitting. This exchange energy is in remarkable agreement with measurements reported in the literature for porous Si and Si nanoparticles embedded in silica.

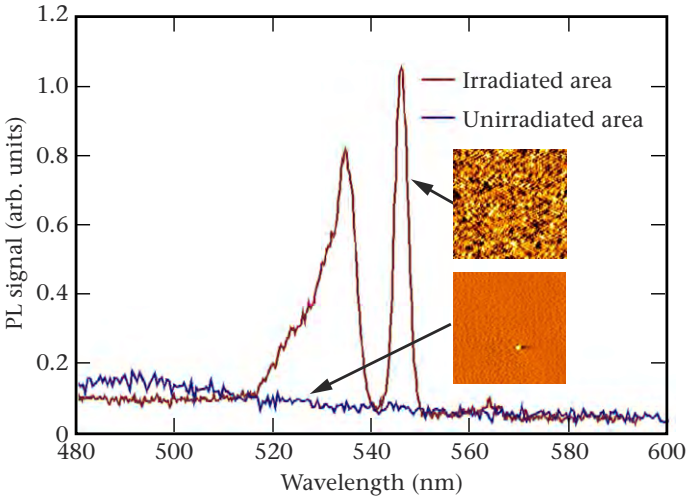

Photoluminescence (PL) from nanometer-sized silicon (Si) features caused by bombardment with Xe^{44+} ions onto the Si substrake. The inset shows atomic-force microscopy (AFM) images corresponding to the irradiated (1×10^{12} cm^{-2}) and the unirradiated areas (both measure 500 by 500 nm). Note the surface structures on the irradiated sample.

In FY 2000, we also measured the dispersion (energy–momentum) relationship of the exciton localized in the Si nanostructure. If we change the laser excitation energy, the emission energy of the exciton shifts. From the value of the shifts, we mapped the dispersion of the exciton. Then, from the map we determined that the effective mass and the binding energy of the exciton are 0.11 m_e (where m_e is the rest mass of an electron) and 76 meV, respectively.

The localized, intense, ultrafast electronic excitation of semiconductor surfaces provides a novel method to produce metastable materials with extraordinary properties. These properties have application in photonics and sensor technology.

Interfacial Deformation Mechanisms in TiAl–Ti_3Al Microlaminates

L. Hsiung

00-ERD-072

Enhancing the performance of the next generation of engines for automobiles and gas-turbine engines for high-speed aviation vehicles is driving a continued search for new propulsion materials with increased strength, lower density, higher temperature capability, and adequate toughness and ductility. Their good oxidation and environmental resistance, low density, high melting point, and good strength retention at elevated temperatures have led to interest in the use of intermetallic aluminides such as Ti_3Al (α_2), and TiAl (γ) for engine components.

A potentially important venue for improving the performance of titanium aluminides is through the synthesis of in situ TiAl–Ti_3Al microlaminate composites. An appealing characteristic of this approach is that changing the thicknesses of the alternating lamellae can alter the deformation response of the composite material. Despite the technology advances for fabricating the material, the multitude of mechanisms contributing to the overall deformation response in these materials is not well understood. Before their structural applications can be realized, it is important to verify the interrelationships between the structures and properties of the material.

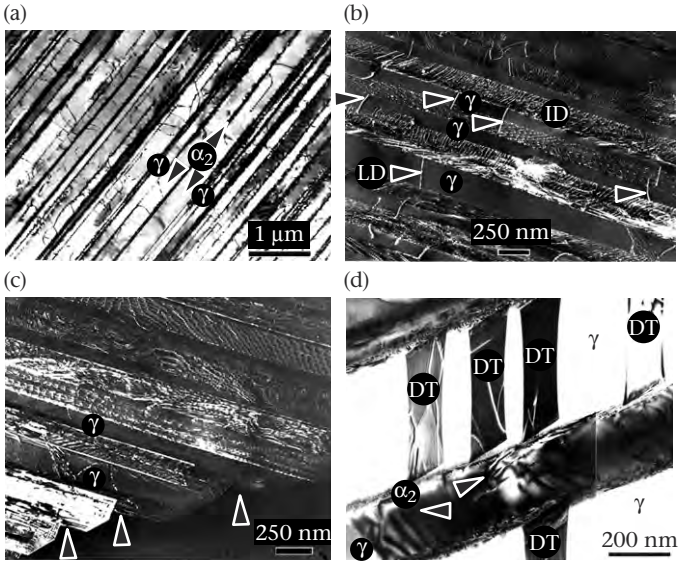

Deformation mechanisms of TiAl–Ti_3Al microlaminate composites observed using transmission electron microscopy (TEM) and showing (a,b) microstructures of an as-fabricated microlaminate and also the deformation structures in material that was creep-tested at (c) 138 MPa and (d) 518 MPa. In the images, ID, LD, and DT stand for interfacial dislocation, lattice dislocation, and deformation twinning, respectively; γ and α_2 identify layers of TiAl and Ti_3Al, respectively.

In this project, we are exploring the fundamental deformation mechanisms of in situ TiAl–Ti_3Al microlaminate fabricated by a powder-metallurgy technique that involves the hot extrusion of gas-atomized powder at temperatures near 1400°C.

During FY2000, we used transmission electron microscopy (TEM) to observe typical, edge-on, lamellar microstructure of as-fabricated microlaminates [Fig. (a,b)]. The thicknesses were measured to be in the range of 100 to 300 nm and 10 to 50 nm for TiAl and Ti_3Al lamellae, respectively. Both lattice dislocations (LD) within gamma lamellae and a high density of interfacial (Shockley partial) dislocations (ID) on inclined lamellar interfaces can be seen clearly in Fig. (b). The density of ID is much greater than that of LD, and the LD are primarily threading dislocations that terminate their two ends at lamellar interfaces.

Transmission electron microscopy results that we obtained from creep-tested specimens [Fig. (c,d)] reveal that (1) the creep deformations of a TiAl–Ti_3Al microlaminate are mainly controlled by ID (i.e., by interface sliding) at a low-stress regime (<400 MPa), (2) grain-boundary ledges (marked by arrows) formed as a result of the interface sliding caused by the motion of ID arrays on lamellar interfaces, and (3) interface-controlled deformation twinning (DT) occurred at a high-stress regime (>400 MPa).

To further understand and elucidate the interfacial deformation mechanisms in the microlaminate, we plan to conduct both static and in situ TEM experiments. Our goal is to investigate (1) dislocation dynamics (dislocation multiplication, motion, and reactions) of ID and LD, and (2) nucleation mechanisms for DT. We expect that the in situ TEM experiments at both room and elevated temperatures will provide insight regarding the underlying mechanisms and their interplay in different deformation conditions. We should then be able to identify the optimal defect microstructures (lamellar interfaces and interfacial dislocations) as targets during future development of the microlaminate composites. The physical insights generated by our research will have wide implications for understanding the interrelationships between the interface and bulk mechanisms of crystal plasticity.

Fundamental Studies of Next-Generation Quantum-Dot Nanostructures

B. R. Taylor, P. A. Thielen

00-LW-010

New quantum phenomena often give rise to revolutionary technologies. Many believe that the unique and interesting properties of semiconductor quantum dots (QDs), which are extremely small particles of semiconductor that have properties different from bulk, will define the next generation of nanotechnology involving microelectronics and photonics. The ultimate commercialization of these concepts—the use of single-electron processes and QDs—is an enormously difficult scientific and technological problem. Our research addresses some of the initial work required to begin this essential research and development effort. An important goal of this project is the synthesis of new nanostructures such as (1) QDs that are surface-terminated with organic groups, and (2) interconnected QDs. Previously, we succeeded in chemically attaching alkyl groups to the surface of germanium (Ge) QDs; researchers at the University of California, Davis collaborating with us attached alkyl groups to Si QDs. We pioneered this reaction scheme for chemically (covalently) attaching organic groups (or molecular tethers) to QD surfaces.

During FY2000, we attached other, more active molecular tethers to the QD surface. These coupled QDs can then interact via the tethers in a controllable manner and can thus generate more interesting quantum phenomena. As an important first step in generalizing our synthesis scheme to new QD nanostructures, we succeeded in chemically attaching vinyl and allyl groups, two of the simplest organic systems that contain delocalized electrons, to the surface of Ge QDs.

Another important goal during FY2000 was to interconnect two or more QDs. Fourier transform infrared (FTIR) spectra showed that the surface allyl groups have polymerized, providing evidence that the QDs are interconnected. This massive interconnection of QDs represents an important achievement.

We showed for the first time that light emission from nanostructured Si can be stable at room temperature and continuously tunable from the red to the ultraviolet (UV) through a single mechanism, that is, through quantum confinement. Our results offer new and realistic opportunities to fulfill the promise of red-to-UV light emitters for Si-based optoelectronics.

Using our new QD nanostructures, during FY2000 we also successfully demonstrated single-electron devices operating at room temperature using Si QDs. An example is shown in the Fig. Here, a single QD functions as a microelectronic unit such as a transistor or tunneling diode. The peaks in the conductance curve are evidence of Coulomb blockade behavior, where each peak corresponds to the transport of a single electron through a QD. The room-temperature operation is significant and directly results from the size and stability of our QDs.

The work planned for FY2001 involves (1) designing and synthesizing new quantum nanostructures (e.g., interacting quantum systems), (2) investigating the fundamental properties of these new nanostructures (e.g., collective phenomena from interacting quantum systems), and (3) designing and developing new applications enabled by the new quantum properties of these new nanostructures.

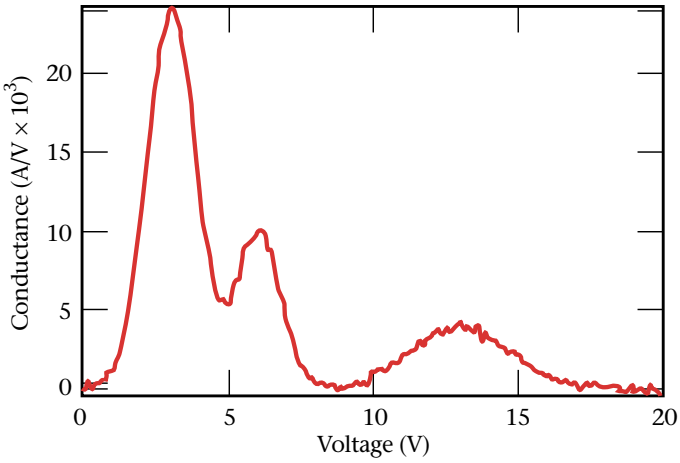

Conductance vs. bias voltage for a single electron device.

Metal–Insulator Transition in Lithium and LiH

M. Bastea

00-LW-037

The observation of a pressure-generated insulating phase in a good metal such as Li would be a first in the history of physics. Neaton and Ashcroft at Cornell University predicted that the Li atoms would pair at about 100 GPa and that their valence electrons would become localized in the interstitial regions—and would therefore be nonconducting. Investigating LiH provides the unique opportunity to understand the effects of coupling two elements with opposite tendencies at extreme conditions and to study fundamental principles such as metallization and pairing.

The main purposes of this project are to (1) search for a nonmetallic high-pressure phase of Li, and (2) find the metallization conditions for LiH.

During FY2000, our main challenges were technical and computational. Because both Li and LiH are very reactive materials and electrical transport measurements are extremely sensitive to sample quality, it was necessary to build a laboratory in which we could not only handle target assembly and sample preparation in a controlled Ar atmosphere but also fulfill requirements for outstanding cleanliness. In addition, we developed a sample-preparation technique that is appropriate for solids, while observing the significant constraints placed on procedures because of the reactivity of Li and LiH. Problems that we solved included minimizing (1) contact resistance caused by imperfect mechanical contact and interfacial oxidation, and (2) void formation and noise generated at impact because of Ar trapped during target assembly. To measure the transport properties of Li, which is a highly conducting metal at ambient conditions, we developed a new measurement technique that increases the accuracy and significantly widens the range in which we can perform measurements, thereby allowing us to tackle new problems such as diagnosing melting.

Our experiments were designed and modeled using hydrodynamic simulations (the 1-D code ONEDEE), for which we developed equations of state (EOS) for Li and LiH. We modeled (1) the effects of both the sample's initial conditions (temperature, density) and the anvil materials on the final shock-state parameters; and (2) experiments using ramp-wave generators (fused quartz), single-crystal sapphire, LiF, and polyethylene—to assess the most appropriate experimental geometry. Aside from the metal–insulator transition and pairing at extreme conditions, it is also possible to identify the melting line of Li at high pressures. Calculations indicate that if the sample is precooled at pressures below 100 GPa, the final state of the system in a shock-reverberation experiment is solid. This would be a very interesting problem to study in a future project.

During FY2000, our experimental work primarily emphasized the study of Li. We successfully measured the conductivity of Li at 120 GPa with very good accuracy. The Fig. shows a sample of our experimental data. Our results indicate that at these pressures Li is a poor metal with a conductivity of about $3.6 \times 10^3/\Omega\cdot$cm, which is about two orders of magnitude lower than at ambient conditions. At year's end, we had not seen evidence of the nonmetallic state. We also measured the electrical conductivity of LiH at 80 GPa. LiH appears to remain a good insulator at this high pressure.

For FY2001, we plan a full series of experiments with Li in which we will span the pressure range between 50 and 200 GPa. We also plan a complete investigation of LiH.

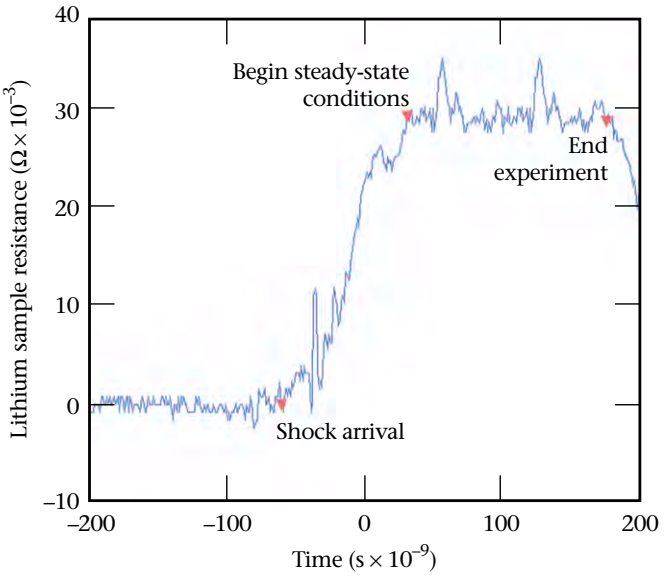

Resistance as a function of time of an Li sample up to 120 GPa.

Back to main TOC

Surface-Enhanced Raman Spectroscopy for Detection and Identification of Single Molecules and Nanomaterials

T. Huser, C. Orme, M. Yan, W. Siekhaus

00-LW-058

The identification of individual molecules and the determination of how they are influenced by their local environments are critical steps towards a better understanding of complex organic systems, and are essential for materials research at LLNL. In the past, optical detection techniques have played a central role in the nondestructive and noninvasive analysis of complex materials. Recently developed, highly sensitive detection techniques based on optical fluorescence can now be used to probe biomolecular processes even at the single-molecule level. However, the detection of fluorescence from single molecules depends on site-specific information from marker molecules and does not provide detailed molecular information on the chemical environment of these molecules. In addition, techniques based on the detection of optical fluorescence have two drawbacks: a relatively broad spectral emission and photodecomposition of the molecules involved. In contrast, Raman spectroscopy is one of the few optical techniques that can not only identify molecular species but also determine their chemical bonds by observing their distinct vibrational fingerprints.

In this project, we are developing a new method for probing Raman fingerprint spectra of single molecules with high spatial resolution. Our approach combines confocal Raman microscopy with surface-enhanced Raman spectroscopy (SERS) that is generated by placing nanometer-scale gold particles at the end of the tip of a scanning-probe microscope. The scanning SERS probe generates an image of the physical structure of a sample together with detailed chemical information. Thus, our initial goal is to identify materials at the molecular scale by simultaneously measuring topography and Raman spectra. Our ultimate goal is to be able to identify the spatial position of molecular processes at bases of macromolecules such as DNA.

During FY2000, we first rigorously optimized the detection sensitivity of our existing confocal optical microscope. This optimization enabled us to simultaneously perform spectroscopy on single fluorescent molecules with very short integration time per spectrum and to obtain intensity transients with millisecond time resolution. This capability has enabled us to study energy-transfer mechanisms in aggregated molecules of conjugated polymers with unprecedented temporal and spectral resolution. This newly achieved sensitivity was successfully applied to a number of fluorescing quantum systems, among which were single fluorophores, single semiconductor nanocrystals, and isolated conjugated polymer molecules.

As s a prerequisite for Raman imaging with SERS probes, we built our instrument into an ultrasensitive micro-Raman spectrometer and microscope system, which allows us to obtain Raman images of biological and chemical samples, such as single biological cells.

As a final step during FY2000, we demonstrated the SERS-based detection of amino-acid molecules adsorbed to single, isolated, gold nanoparticles. Because we were able to detect slight differences in the side-chain sequence of the amino acids, we were able to distinguish and identify them.

In FY2001, we plan to (1) use our FY2000 results to monitor the folding and unfolding of biopolymers such as proteins, (2) gain more information on the basic physics of SERS by using near-field scanning optical microscopy to investigate the local field-enhancement mechanism of single gold particles, and (3) prepare the first SERS probe tips by attaching gold nanoparticles to force-microscope tips.

Nuclear/ Atomic Science and Technology

8

Section 8—Nuclear and Atomic Science and Technology

Mapping of Enhanced Nuclear Stability in the Heaviest Elements

K. J. Moody, J. F. Wild, N. J. Stoyer, M. A. Stoyer, R. W. Lougheed, C. A. Laue

98-ERD-050

Predicting the properties of nuclides near the extreme limits of nuclear stability provides a measure of how well we understand the fundamental properties of matter. Predictions of an "island of stability" of long-lived superheavy nuclei beyond the limits of the known elements date back more than 30 years; during this time, many scientists have searched unsuccessfully for these nuclei. Recently, however, there have been major efforts to systematically characterize the properties of the intervening unstable nuclei. In an on-going collaboration with scientists at the Joint Institute for Nuclear Research (JINR) in Dubna, Russia, we have observed the decays of previously unknown isotopes of elements 104, 106, 108, and 110. The properties of these elements are determined by subtleties in the nuclear structure caused by the shell effects that are predicted to result in the island of stability in the heavier elements. Theorists in Europe have successfully modeled our experimental data, and their refined predictions of the decay modes and production rates of the superheavy elements have enabled us to design experiments to produce and study these elusive nuclides.

In this project, continuing our collaboration with the scientists at JINR, we performed experiments to discover and characterize the superheavy isotopes around the "magic" nucleon numbers Z = 114 and N = 184, produced in the bombardment of actinide targets with calcium-48 (^{48}Ca) ions. Products of the complete fusion of the two nuclei recoil from the target into the Dubna gas-filled separator, which isolates any superheavy-element products from beam particles and the unwanted products of side reactions and delivers them to a position-sensitive detector array. The impact of the recoil atom and any subsequent alpha- and spontaneous-fission (SF) decays are tagged with times and positions that allow the decay sequence to be reconstructed.

During the first two years of this project, we performed long irradiations of a plutonium-244 (^{244}Pu) target and were able to observe the decays of two atoms of element 114. The detection of these surprisingly long-lived nuclides —about 30 s—constituted the discovery of the element in FY1999 and, more importantly, verified the existence of the island of stability. This work was published in *Scientific American*.

In FY2000, we continued irradiating ^{244}Pu and isolated the signature of yet another element-114 atom. We then switched to targets of curium-248 (^{248}Cm) in an attempt to produce an isotope of element 116. After several months of effort, we were successful—producing a single atom of the mass-292 isotope, which alpha decayed in 47 ms to the mass-288 isotope of element 114 [Fig. (a)]. The new element-116 isotope has 176 neutrons in its nucleus, giving it the highest neutron number of any known isotope and approaching the magic number N = 184. Figure (b) shows our previously measured decay chains of the element-114 daughter.

Because of our work, along with recent discoveries at the Lawrence Berkeley National Laboratory and by another group in Dubna, four isotopes of element 114, two isotopes of element 116, and a single isotope of element 118 are now known.

We feel that we have made an excellent start at mapping the extent and strength of the nuclear-shell effect that results in the island of stability. Our colleagues at JINR are continuing the experiments.

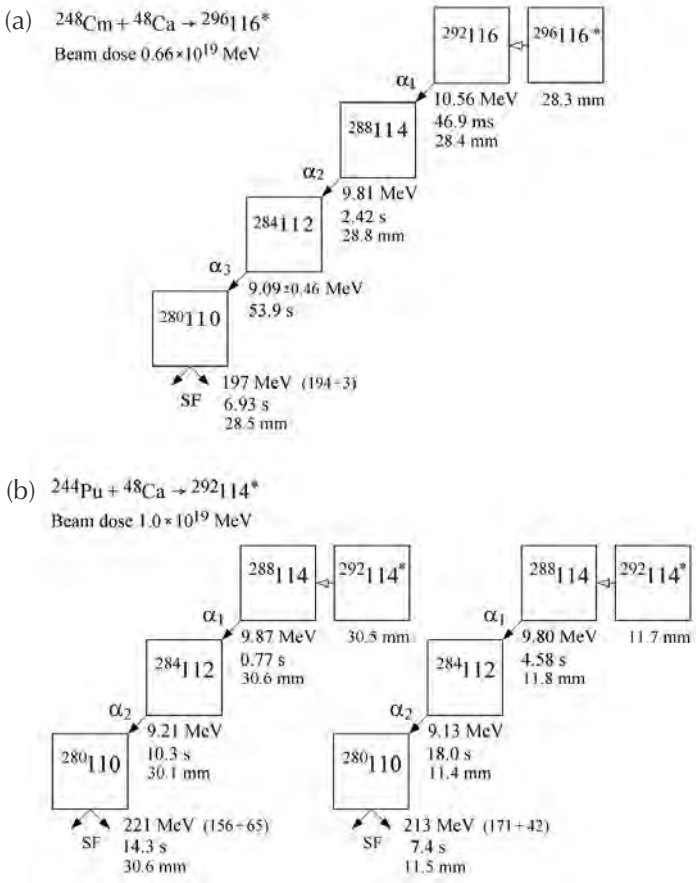

The observed decay sequence for the new element-116 isotope (a); and (b) for comparison, independently measured decay chains of the element-114 daughter.

Back to main TOC

New Physics at the B Factory: Search for Charge/Parity Violation

D. M. Wright

98-ERD-058

Charge/parity (CP) violation, an asymmetry between the physics of matter and antimatter, is a crucial problem for particle physics and cosmology. Charge/parity violation is a necessary ingredient in cosmological models that explain the predominance of matter over antimatter in the universe. Only one CP-violating physics process has ever been discovered; however, it falls short of providing the mechanism required for cosmology, and the origin of the effect remains a mystery. This project has played an important role in one of the leading efforts to explore this fundamental physics question.

Although the theory of particle physics has been extremely successful, the mechanism that explains CP violation has never been stringently tested. By studying the decay of B mesons (a heavy form of matter that can be produced in accelerators), a definitive set of experiments can be conducted to test the theory. Every major accelerator laboratory in the world has a high-priority experimental program to search for CP violation in B mesons.

LLNL physicists, engineers, and technicians played a major role in constructing the B Factory accelerator at the Stanford Linear Accelerator Center (SLAC). The B Factory is an accelerator that produces large quantities of B and anti-B mesons. An international collaboration, including LLNL, assembled the BaBar detector, the only detector at the B Factory. By September 1999, the B Factory had achieved high-luminosity running; it continues to set world-record levels of event production.

The most sensitive tests of CP violation using BaBar can be made from the K^0_S decay channel of the B meson. This mode is easy to detect and has very little background from other physics processes. Equally sensitive, but more challenging to detect, is the K^0_L decay channel. To make a convincing discovery, BaBar should observe a signal in both channels. In this project, the focus of the LLNL effort has been on the important K^0_L channel and K^0_L detection system.

In FY2000, a member of our project team was selected as the operations manager for the entire K^0_L detector system for the critical first physics run. He led the data-collection and calibration effort, developed the operating procedures, and led the commissioning of the automated data-collection systems.

In addition to our hardware involvement, we created software tools for K^0_L identification and made the first measurement of K^0_L production in the data. We (1) implemented algorithms to identify K^0_L particles in the electromagnetic calorimeter and K^0_L detector system, (2) developed techniques to reject energetic photons that can fake a K^0_L signal, and (3) developed algorithms to reject background from other physics processes, (4) used our software tools to measure the yield of K^0_L from B-meson decay in the first BaBar data sample. Our results were presented with the first physics results of the BaBar collaboration at conferences during the summer of 2000. We have also begun to develop the software tools to fit the K^0_L data so that we can measure the CP-violating asymmetry in this mode.

In parallel, we conducted an analysis of non-B-meson events to validate the performance of our K^0_L software. We wrote event filters that allowed these events to pass the BaBar event-selection trigger, skimmed the entire data set to collect these events, and created an analysis that predicted the location of the K^0_L particle without using any detector signal for the K^0_L itself. Using this data set, we were able to compare and correct the predictions of the K^0_L signal from Monte Carlo simulations of BaBar events, and continued to exploit the parallel processing capabilities at LLNL to produce millions of Monte Carlo simulations of BaBar physics events. These simulations were written directly into the BaBar data store at SLAC and are used by the entire collaboration.

LLNL has been a major contributor to the detector and software systems for the BaBar detector. In the next few years, the BaBar experiment will collect large and statistically significant data sets from which we expect to discover or rule out CP violation in B-meson decay. LLNL is well positioned to play a crucial role in this exciting new area for particle physics.

Back to main TOC

Exploratory Research for a Proton-Radiography Demonstration Experiment

E. P. Hartouni, E. Ables, M. Aufderheide, P. D. Barnes, Jr., H. Park, A. Schach von Wittenau, R. Soltz, D. Wright

98-ERD-088

Radiography is expected to play a central role in the certification of the safety and reliability of the U.S. nuclear weapons stockpile. Proton radiography is a relatively new technology that promises a capability that matches the certification requirements. In previous years, this project supported a study of low-cost proton accelerator facilities. This year we studied techniques and detector technologies for dynamic proton radiography, and began to explore aspects of high-energy proton radiography utilizing facilities at the Brookhaven National Laboratory's (BNL's) Alternating Gradient Synchrotron (AGS) proton accelerator.

One of the uses of proton radiography is to extend our knowledge of the transient phenomena associated with shocked metal plates. Of particular interest is understanding what particles are ejected from the plate (size, density, timing, etc.) at early times in the shock. At later times the plate breaks apart (spalls) as the shock wave dissipates within the metal plate. In FY2000, an initial set of experiments, "Hopyard," was performed using tin plates of varying thicknesses, shocked by a high-explosive (HE) charges. For each experiment, the profile of the HE and plate was illuminated with a series of proton pulses from the Los Alamos Neutron Science Center (LANSCE) in the Line-C beam line. The protons that transmitted through the shot were viewed by a series of diagnostics, designed and built at LLNL, that allowed a high-resolution 2-D image to be made at a single time during the shot and several 1-D images be made at multiple times during the shot. These data were used both to demonstrate the capability of proton radiography and provide input to hydrodynamic models of these physical systems. The Fig. shows one such comparison. This set of experiments has led to the submission of a proposal to LANSCE for additional experiments: a follow-on to the Hopyard series, a study of collisions of plates and stationary objects, and a study of rip failures in metal plates.

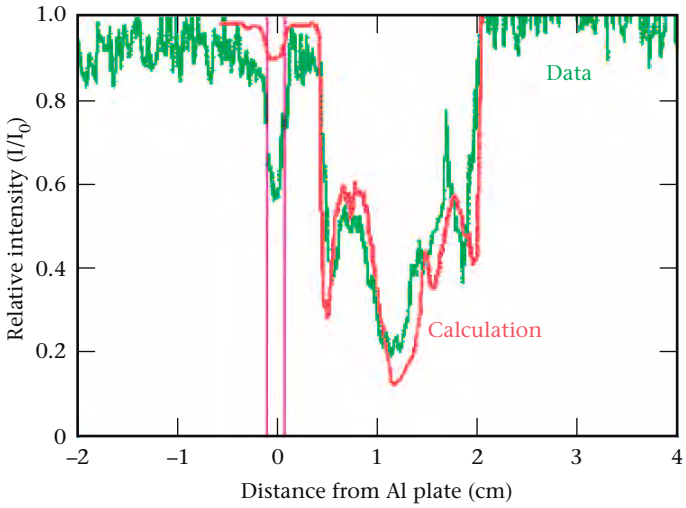

A comparison of the experimental result using CALE (C-language-based arbitrary Lagrangian-Eulerian), a 2-D hydrodynamic simulation code. The ratio of the transmitted protons (I) to the initial proton beam (I_O) as a function of the distance from the starting position is shown for data and calculation.

The second series of experiments we conducted in FY2000 took place at BNL to study proton radiography at high energy. The major goal of these experiments was to demonstrate the sensitivity of the proton radiographic technique to object-density distributions, feature resolutions, and material composition. Another important aspect of these experiments was to quantify the backgrounds present in a radiographic beamline. (Backgrounds were estimated to be less then 5% of the integrated intensity of the image under some beamline configurations.) These static radiography experiments have led to a more elaborately designed experiment, which we designed and conducted at BNL in January 2001.

100-Gigabar Shock Heating with the 100-Terawatt JanUSP

P. T. Springer, P. A. Patel, D. F. Price, S. C. Wilks

99-ERD-049

We are conducting experiments to test the predicted ability of LLNL's high-focal-intensity laser, the Janus ultrashort-pulse (JanUSP) laser, to produce ion shock heating of targets to energy densities rivaling those produced in stars and nuclear weapons. A successful demonstration would provide important new capabilities for stockpile stewardship—using direct measurements to test radiative- and particle-transport models of weapons plasma.

The 100-TW JanUSP laser is the world's brightest laser. In earlier work prior to the start of the project, we demonstrated the highest focal intensities ever achieved in a laser system, in excess of 10^{21} W/cm^2, a key requirement for this project. Although extreme intensity is needed to achieve adequate ion flux and energy, extreme control of the laser prepulse is simultaneously required for interaction with the solid. The latter is necessary both for the creation of 100-Gbar ion shocks and for achieving thermal equilibrium in high-temperature targets.

Our goals in this project are to provide (1) critical tests of the physics of laser–matter interaction in these new regimes, (2) new capabilities and physics data for weapons science, and also (3) significant advances in science and technology of interest to other Laboratory programs.

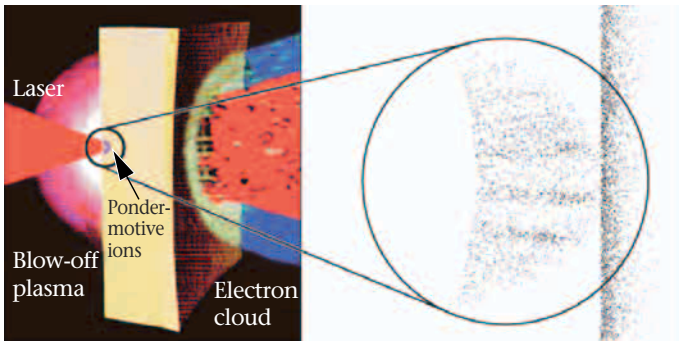

Our target-interaction concept, showing the production of intense beams of electrons and ions produced in the interaction of a high-intensity, short-pulse laser with a high-density target.

In FY2000, we achieved the planned millionfold improvement in laser prepulse control to the 10^{-10} level, sufficient for our ion-shock-heating experiments. For additional control, we also produced a large, aperture-doubling crystal. Target diagnostics were fully implemented and used to test predictions for laser ion-acceleration and target-heating experiments. We explored recent discoveries of electron- and ion-acceleration mechanisms, testing models in new regimes. The Fig. illustrates our use of photonuclear activation and electron and ion spectrometers to detect energetic electrons (in excess of 20 MeV) and related protons accelerated from the rear surface of the target.

Our demonstration of intense ion fluxes in excess of 1 MJ/cm^2 was a key milestone for ion-heating experiments. If these efficiencies can be retained for heavier ions, we expect to achieve the desired ion-energy depositions approaching 1 GJ/g in micrometer-scale, solid-density plasmas.

We also (1) measured the proton-beam emittance, thereby resolving issues raised in the PetaWatt laser experiments before it was decommissioned; and (2) explored electron acceleration in gas-jet targets by testing 3-D particle-in-cell (PIC) simulations, which predicted that GeV electron energy—and associated pions—could be achieved.

In FY2001, we will use an optimized prepulse to measure the gradient scale length and the production of energetic electrons and ions. To isolate ions that undergo pondermotive acceleration through the foil, we will use targets constructed of two layers of aluminum and gold. The intensity, spectra, and divergence of these ion beams will be measured and compared with the 2-D PIC predictions. We plan to measure Doppler shifts of line radiation from the emitted plasma and to use ion time-of-flight (TOF) spectroscopy to characterize ion heating and stopping power in plasma. Our experiments will then focus on studies of thermalization in high-*Z* targets. Measurements of emission spectra from buried targets will determine electron and ion ranges, and the degree of ionization in high-*Z* targets will corroborate achieved energy densities and approach to equilibrium. We will also measure ion-stopping in characterized plasma and test departures from idealized models.

X-Ray Optics and Applications for Fourth-Generation Light Sources

A. Wootton, A. Toor, R. Bionta, R. London, D. Ryutov, V. Shlyaptsev, I. Barbee, Jr.

00-ERD-025

A collaboration of national laboratories and universities is conducting research developing a fourth-generation light source based on a linac-driven x-ray free electron laser (XFEL). The team has proposed to construct a linac coherent light source (LCLS) to produce an XFEL with unprecedented brilliance. LLNL is responsible for the x-ray optics and diagnostics in this national program. The wavelength will be variable between 1.5 and 15 Å. The LCLS will generate x-ray pulses with ~2 mJ per pulse, a beam diameter of ~100 µm, a pulse length of ~250 fs, and a rep-rate of 120 Hz. At longer wavelengths, a single pulse from the LCLS will transform most solids placed in the beam into plasma. This environment presents many new challenges for x-ray optics. Our goal is to develop methods to characterize and manipulate the intense XFEL beam.

In FY2000, we (1) examined the radiation interaction with matter and developed conceptual designs for novel optical components to meet the LCLS challenge (see Fig.), and (2) developed codes to characterize the XFEL radiation parameters vs. electron kinetic energy and to calculate the x-ray dose delivered to any material placed at arbitrary distances from the source. These codes allow us to calculate the real and imaginary parts of the electric field at arbitrary locations and to evaluate the performance of optical components placed in that field.

Our novel diagnostics included an asymmetric Michelson interferometer to measure the FEL's temporal coherence and an attenuation cell to characterize the spontaneous radiation and determine the electron-beam emittance. We designed and numerically evaluated two types of focusing optics: a LiH capillary plasma lens to be used in high-fluence XFEL applications, and multilayer coated ellipsoidal mirrors that will be used at lower fluence. Because several proposed LCLS experiments require a pulse duration of less than 40 fs, we developed four concepts to slice and/or compress the 250-fs pulse down to ~10 fs. These concepts require a ~2% chirp on the electron beam energy. One of the slicing concepts uses the bandpass of a multilayer to reflect a small temporal fraction of the XFEL. A second concept uses an off-axis zone plate to change the energy chirp into a spatial chirp, which is passed through a slit. The slit width determines the pulse's temporal duration. Compression concepts use matched gratings as dispersive elements to cause the first photons in the pulse to travel a greater distance than the last photons. By introducing a 250-fs difference in path length, one could compress the pulse to 1 fs, in principle. In these studies, we identified a new, important short-pulse effect that temporally dilates the beam due to the photon phase velocity being greater than its group velocity.

In FY2001, development of the optics code for calculating electric field strength will continue. Our initial experiments at LLNL's Janus/ ultrashort pulse (JanUSP) facility will characterize the thresholds for damage and consider measurements of the kinetics in grazing incidence mirrors at extreme heat loads. We plan to study the short-pulse effects for optical components being developed for the LCLS; and we will build, test, and evaluate key x-ray optics prototypes, including high-resolving-power and low-Z multilayers. In addition to developing LLNL's capabilities to replicate small optics, we will work with our collaborators to elucidate specific optical and diagnostics requirements, and then determine the technology requirements to meet these needs.

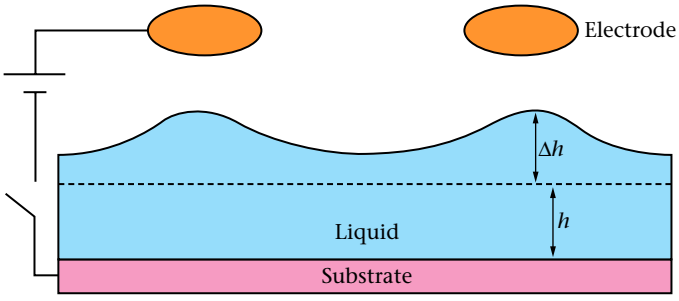

Parabolic mirrors can be created in thin liquid layers controlled by electrostatic forces. The example shows electrodes 0.5-cm above the 50-µm deep Hg surface, with a 50-cm focal length, and voltage of 1.5 kV.

Exploring Quantum Chromodynamics at the Relativistic Heavy Ion Collider with Two-Particle Correlations

R. A. Soltz, E. P. Hartouni, S. C. Johnson, M. Heffner

00-ERD-026

The quantum chromodynamics (QCD) theory of the strong interaction predicts that, at sufficiently high energy and baryon density, nuclear matter will exist as a plasma of quarks and gluons. Detecting and studying this new phase of matter is the purpose of the Relativistic Heavy Ion Collider (RHIC), which was commissioned during FY2000 at Brookhaven National Laboratory. The RHIC program is at the forefront of research in nuclear physics, and it is being used to explore a fundamentally new regime. Our goal, as participants in the Pioneering High Energy Nuclear Ion eXperiment (PHENIX) at RHIC, is to use the Hanbury Brown–Twiss technique of two-particle correlations to measure an important parameter in this exploration—the size of the collision source. We are also providing essential computing cycles for Monte Carlo event simulations.

The RHIC met all expectations for FY2000, achieving 10% of its design luminosity for collisions of gold–gold (Au–Au) ions at a center-of-mass energy of 130 GeV/c. The PHENIX experiment also performed very well, collecting over 5 million events for subsequent analysis. Using these data, during FY2000 we completed a preliminary analysis of the two-particle correlation function, using unidentified tracks in the PHENIX central tracking detectors. We also made initial estimates of the possibility of performing a similar analysis with neutral pions measured in the PHENIX calorimeter. If successful, this analysis would be the first measurement of its kind in particle physics. Through these efforts, LLNL has established itself as the lead institution in the physics analysis of two-particle correlations within PHENIX.

PISA, the PHENIX Monte Carlo simulation code, was first ported to the LCC alpha cluster in the spring of FY2000. Large-scale running of simulated events is beginning as we improve the software. At the close of FY2000, we completed an initial run of single-track events, which will be made available to the general PHENIX collaboration. In addition to working on PISA, a member of our team is now serving as the software-release manager for the PHENIX analysis pass, in which detector hits are converted into particle tracks.

Once the official analysis pass (the process by which detector hits are converted to particle tracks) has been completed, we will refine our preliminary measurement using identified particles. During FY2001, we will concentrate on three species of particles: pions, kaons, and protons. Each will give independent information on the dimensions of the collision source. With the pions, which are most abundant, we will study the variation in the source size with the momenta of the particles and with collision geometry. The former provides information on the expansion velocity of the source; the latter may indicate the onset of a phase transition.

Our simulation efforts during FY2001 will include running full-scale simulated events (needed to understand multiplicity effects) and comparing results from our model with our experimental data. We will present these results at the Quark Matter 2001 Conference, the pre-eminent international conference in the field.

Ab Initio Nuclear Structure from Helium to Oxygen

W. E. Ormand

00-ERD-028

The study of how nuclei are put together is of fundamental interest to physics and to the application of nuclear physics to national security. An important goal in physics is formulating a complete description of complex nuclei from first principles. This difficult enterprise has been accomplished only for the lightest nuclei. Our goal is to use new developments in many-body theory and the computational power of the Accelerated Strategic Computing Initiative (ASCI) system to extend these ab initio calculations to heavier nuclei.

Our starting point is effective interaction theory within the framework of the shell model. The foundation of the shell model is the inclusion of relevant degrees of freedom through a set of many-body configurations. However, because of the nature of the strong interaction, an infinite set of these configurations is required. This requirement can be circumvented by using effective interactions. The most important aspect of effective-interaction theory is the presence of "induced" higher-body components, which arise even if the effective interaction is derived from a fundamental (bare) interaction that is only two-body in character. Our goal is to achieve a nearly exact treatment of nuclear structure by including, for the first time, these higher-body components of the effective interaction.

An important tool for this project would be a shell-model program that can (1) carry out large-scale calculations for nuclei between helium (He) and oxygen (O) with up to four-body interactions, and (2) be ported to ASCI. In FY2000 we wrote a new computer program (REDSTICK) to meet these requirements. Although the first version included only two-body interactions, it is designed to be flexible: it is an immediately useful tool for the nuclear physics community, it has a structure that facilitates its extension to three- and higher-body components of the effective interaction, and it can be executed on the ASCI system. In FY2000, REDSTICK successfully passed a series of tests for large-scale calculations using two-body interactions.

During FY2000, we completed calculations for the four-particle He system using a new nucleon–nucleon interaction based on quantum chromodynamics (QCD). In the Fig., the binding energy of He as a function of increasing number of many-body configurations (measured by N) is displayed for the "bare" interaction and for only the two-body component of the "effective" interaction. The Fig. shows that the effective interaction achieves convergence with the exact result with many fewer configurations than are required for the bare interaction. For this particular form of the fundamental interaction, converged three- and four-body components of the effective interaction can be developed that would yield exact results for N < 6. This is extremely encouraging, because realistic calculations for heavier nuclei can be carried out only with these converged higher-body components.

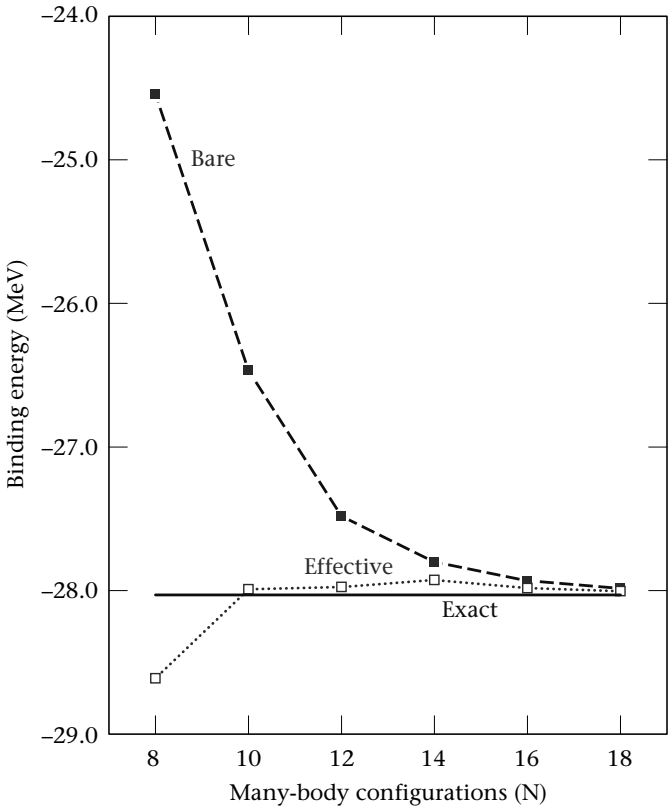

A new nucleon–nucleon interaction based on quantum chromodynamics (QCD), showing the binding energy of helium with increasing many-body configurations for the bare interaction and a two-body effective interaction compared with the exact result.

Finally, during FY2000 we established collaborations with physicists at the University of Washington and University of Arizona.

For FY2001, our primary software goals are to (1) modify REDSTICK to include three-body interactions, and (2) write a computer program to transform the three- and four-body interactions from Jacobi coordinates to standard shell-model input. Goal (2) is required to apply the full effective interaction to nuclei with more than four constituents. Other goals include improving the method for determining the effective interaction, and carrying out the first calculations that use three-body effective interactions.

New Realms of Nuclear Physics Using Radioactive Ion Beams

L. Bernstein, J. A. Becker, P. E. Garrett, W. Younes

00-ERD-035

The proposed rare-isotope accelerator (RIA) and the existing radioactive ion beam (RIB) facilities offer an unprecedented opportunity to address many of the outstanding questions in nuclear structure, reactions, and astrophysics. The joint Department of Energy and National Science Foundation (DOE/NSF) Nuclear Science Advisory Committee has named development of a major new RIB facility (the RIA) in the U.S. as the highest priority for nuclear physics, upon completion of the Relativistic Heavy-Ion Collider (RHIC) at Brookhaven National Laboratory. RIA will greatly expand our understanding of nuclear-reaction dynamics by allowing the observation of nuclear reactions with radioactive targets and/or beams.

This project will develop the tools needed to exploit RIA to gain a detailed understanding of nuclear-reaction dynamics on radioactive nuclei and isomeric nuclear states important for both astrophysics and stockpile stewardship.

Our main focus during FY2000 was on establishing LLNL as a lead laboratory in level-density studies using radioactive beams. To this end, LLNL hosted an international workshop on nuclear-level densities in October 1999, which attracted 44 people from 12 different U.S. and international institutions.

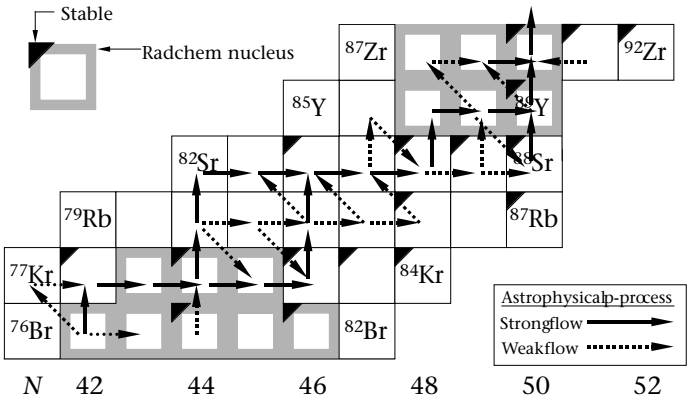

A portion of the chart of the nuclides, showing several of the nuclei that are important to both stockpile stewardship (radiochemistry) and astrophysics (stellar nucleosynthesis). Nuclei in this region are the focus of our work in this project.

Level densities are critically important for stellar nucleosynthesis and stockpile stewardship reaction-network cross-section calculations. The Fig. shows a portion of the chart of nuclides where the astrophysical and stockpile stewardship interests overlap. In addition, level densities in these nuclei are ideal probes of nuclear-shell structure as a function of temperature. However, no experimental technique exists that is capable of measuring them at energies greater than 2 to 3 MeV.

During FY2000, we worked on developing a technique to fill this need that can be implemented at a radioactive beam facility. We analyzed and interpreted data from a two-part experiment at the 88-in. cyclotron at Lawrence Berkeley National Laboratory (LBNL). The first part was a proof-of-principle experiment that measured the level density in a nucleus where it is already known, aluminum-26 (^{26}Al). The second part probed level densities in nuclei near yttrium-89 (^{89}Y) and zirconium-90 (^{90}Zr) that are important for stockpile stewardship, astrophysics, and nuclear-structure studies (see Fig.).

A secondary goal of our project during FY2000 was to aid in the development of neutron-rich radioactive beams that are important for stockpile stewardship and for explosive stellar nucleosynthesis experiments from fission on a uranium target. We measured prompt neutron-induced fission-product yields for a uranium-235 (^{235}U) target for incident neutron energies from 0 to 200 MeV using the germanium array for neutron-induced excitations (GEANIE) spectrometer at the Los Alamos Neutron Science Center (LANSCE) Weapons Neutron Research (WNR) facility.

In FY2001, we plan to continue our level-density measurements with three experiments slated to run at the University of Oslo, Norway. In addition, we will begin developing techniques to measure charged-particle and neutron-induced cross sections using radioactive beams. A partial list of the facilities we will consider using includes the 88-in. cyclotron at LBNL, the University of California, Berkeley (UCB) Rotating Target Neutron Source (RTNS), and the radioactive beam facility at Canada's National Laboratory for Nuclear and Particle Physics (TRIUMF).

Soft X-Ray Emission from Comets

P. Beiersdorfer

00-ERD-037

Recent observations of several comets in the solar system obtained from different x-ray satellites have firmly established comets as x-ray sources. The mere fact that comets emit x rays has far-reaching implications for understanding their interaction with the solar system and has opened up a new wavelength band for studying both dynamical interactions between comets and the Sun and cometary atmospheres and dust comae. Charge transfer of heavy ions in the solar wind has been proposed as the main mechanism for producing x-rays. However, charge-transfer-induced x-ray production is only poorly understood, and best-guess estimates must be made in the x-ray-production models. Improving our understanding of these x-ray production mechanisms greatly benefits LLNL's core missions in high-temperature plasma and atomic physics and broadens our expertise in modeling short-wavelength radiation phenomena.

The goals of this project are to (1) simulate—in a controlled laboratory setting—the conditions that cause comets to emit x-rays, (2) assemble the necessary experimental database for describing charge-transfer-induced x-ray emission in low-energy collisions between highly charged ions and atoms or molecules, and (3) incorporate our results into models that accurately describe the emission of x-rays by comets.

During FY2000, we experimentally validated charge exchange as a viable mechanism for producing cometary x-rays. Using medium-resolution x-ray detectors, we examined the K-shell spectra of bare and hydrogen-like ions that were undergoing charge-transfer reactions. The Fig. shows a typical charge-exchange spectrum. Using the x-ray data from K-shell ions, we were able to develop a preliminary model for cometary x-ray emission that matches satellite observations, but that differs substantially from models used in the literature.

In our measurements, we discovered that low-energy collisions that simulate the conditions of the cometary bow shock produce spectra that are very different from those produced at higher energies outside the bow shock. The change in the spectra can be observed even with low-resolution instrumentation. This discovery opens the door to an entirely new class of x-ray diagnostics that can be used to study the plasma kinetics of the solar wind as it picks up mass in the coma and slows down.

We collaborated with researchers from the National Aeronautics and Space Administration (NASA) Goddard Space Flight Center to improve the resolution of our x-ray detectors by implementing a magnetically cooled x-ray calorimeter on our ion source. This calorimeter is a one-of-a-kind detector built at the Goddard Space Flight Center in the course of the Astro-E satellite mission. It has a 12.5-mm^2 detection area and monitors the 400- to 10,000-eV energy region with 9-eV resolution—20 times better than our previous detector. First measurements show that the instrument provides excellent data that will enable us to study charge-exchange-induced x-ray transitions in utmost detail.

In FY2001, we intend to use the Goddard calorimeter to carry out high-resolution measurements of the K- and L-shell emission of the carbon, oxygen, neon, magnesium, silicon, and iron ions found in the solar wind. We will use the new high-resolution data to update our cometary x-ray model and to include L-shell emission. In addition, we will investigate the subtle effects on the spectral emission caused by different neutral gases and further develop the diagnostic utility of x-ray spectra for studying comets in the solar system.

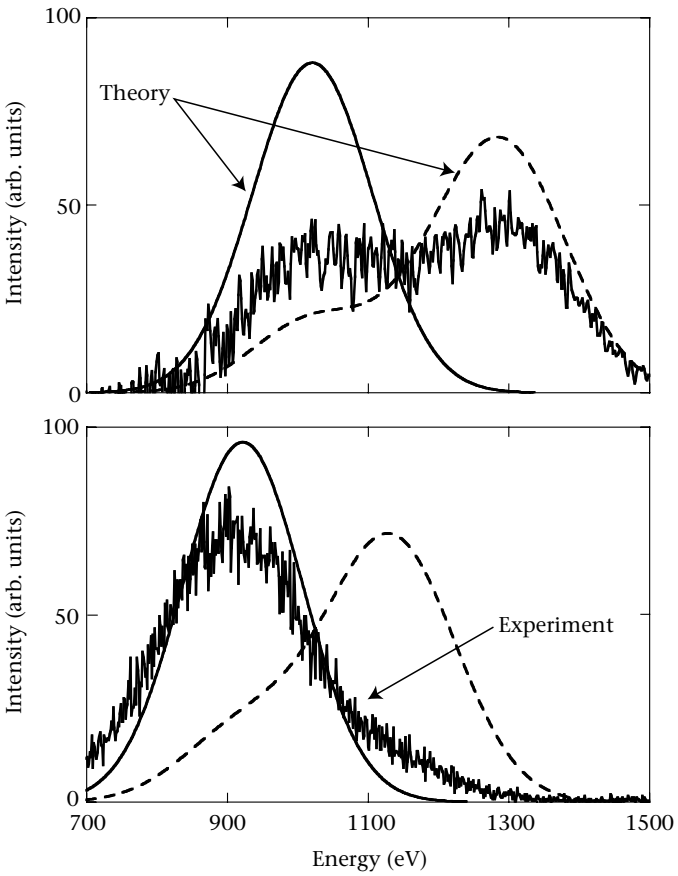

X-ray emissions from (a) Ne^{8+} and (b) Ne^{9+} ions observed in our experiments demonstrate the inadequacy of present cometary emission models (shown by solid and dashed curves).

Back to main TOC

Feasibility of Measuring the Strength of Gravity at a Range of 100 Micrometers

R. M. Bionta

00-FS-001

Current theoretical trends in particle physics and cosmology suggest that the strength of the force of gravity between two objects may not obey classical gravitational force law when the distance between the two objects is small. In some theories, the departure from Newtonian gravity is observable at distances as large as 100 µm to 1 mm. Such predictions have led to numerous proposals to experimentally measure these effects, and at least two groups are actively building and running apparatus to do so. The majority of these experiments are clever modifications of the basic Cavendish experiment involving test masses suspended from torsion fibers. Another approach utilizes a mechanically resonant sensor to measure the force produced by a nearby vibrating mass. In this project, we studied the feasibility of directly measuring the force of gravity between a 100-µm gold sphere and a tiny rotor suspended by a magnetic field at separation distances of less than 100 µm.

Our work in FY2000 centered on the construction of a six-degree-of-freedom computer simulation of the rotor and its surroundings. The C++ simulation assembles the rotor and surrounding objects out of an assortment of primitive masses consisting of spheres, rods, beams, and disks. The positions, sizes, materials, and types of primitive masses comprising each object are specified in separate files, allowing different configurations of rotor and test mass to be run. After assembling the rotor, the simulation constructs the principal-axis coordinate system, centered on the rotor, in which the dynamical calculations are done. The simulation proceeds by time steps. At each time step, it advances the rotor to a new position based on a calculation of the instantaneous forces and torques on the rotor. The gravitational forces are handled by further subdividing the primitive masses into small submasses and summing the vector force between all pairs of submasses. In FY2000, the numerical simulations done with this code are in agreement with the approximate analytical calculations that formed the basis of this proposal, thus verifying the basic feasibility of the proposed experiment. Further studies of backgrounds and optimization of the rotor shape remain to be done with the code.

The next step will be to use the code to create a detailed design of the rotor that minimizes the effects of backgrounds. When the rotor is built, its dynamics will be compared with the computer simulation. Once the simulations agree with the observed rotor motion, the apparatus will be ready to measure the force of gravity at small distances.

Nanotube Applications for Weapons-of-Mass-Destruction Detectors

B. Andresen, A. Alcaraz, F. Kelly, T. Tillotson

00-FS-002

Since their accidental discovery nine years ago, carbon nanotubes have displayed a considerable number of unique properties. Researchers have found them stronger and tougher than steel, capable of carrying higher current densities than either copper or superconductors, and capable of forming transistors only a few nanometers wide. Unlike diamond and graphite, which are both insulators, a remarkable property of nanotubes is their ability to act either as a metal or as a semiconductor. Future applications range from ultrasmall electronic circuits, to ultrathin cathode-ray tubes (CRTs), to bulletproof armor. Derived from spheroidal fullerenes ("Buckyballs"), a nanotube is a long and hollow array of hexagonal-pattern carbon atoms. Similar to a single layer of graphite rolled into a tube, they are typically 2 nm in diameter and several hundred micrometers long.

Previously, little work has focused on the chemistry of nanotubes as collectors and concentrators of target compounds in air, for example, as detectors of airborne weapons of mass destruction (WMD). In this project, we focused on the feasibility of (1) designing an apparatus to prepare nanotubes, and (2) developing analytical protocols to test this new material for its collection affinities for compounds related to chemical warfare (CW).

A search of the literature revealed that nanotubes could be prepared by applying a direct-current arc discharge (18 to 35 V and 100 to 200 Ω), typically from an arc welder, between two graphic electrodes in an inert atmosphere. Accordingly, we constructed an *xy*-robotic apparatus to apply an electrical arc to a stationary carbon surface. The graphite cathode was allowed to move over a carbon surface so that fresh, cool carbon was always available to the electrical discharge. Pure nanotubes were then collected and isolated using solvent filtration and centrifugation.

We followed standardized methods to determine the collection efficiencies of new nanotube materials. At first, we airbrushed uniform, 1-cm metal disks with a solution of the nanotubes. However, problems developed in the preparation of uniform coatings. Subsequently, we obtained a uniform coating by suspending the nanotubes uniformly in a solvent containing polydimethylsilane as a binder and then applying ultrasonic impulses to the spray apparatus.

For comparison, we coated a single, standardized 1-cm disk with an identical weight of Carboxen—a commercial air-filtration medium with very high collection efficiencies that is the optimized carbonized polymer for collecting CW-related vapors.

We then exposed the coated disks to a controlled atmosphere containing three CW surrogates. To quantitatively measure airborne-collection efficiencies, we used solid-phase microextraction (SPME) and gas-chromatography mass spectrometry (GC-MS) to obtain weight-per-weight comparisons. As shown in the Fig., the nanotube-coated disks possessed high collection efficiencies. In fact, we found that the nanotubes were four times more efficient than Carboxen in extracting, concentrating, and retaining one of the surrogates— dimethylmethyl-phosphonate (DMMP). This was a significant finding.

We now have shown that nanotubes provide another very useful new substrate for the collection of target compounds associated with WMD at dilute concentrations in air samples. When incorporated in new collection tools, nanotubes will be potentially very useful in nonproliferation applications.

A patent disclosure has been submitted for this discovery.

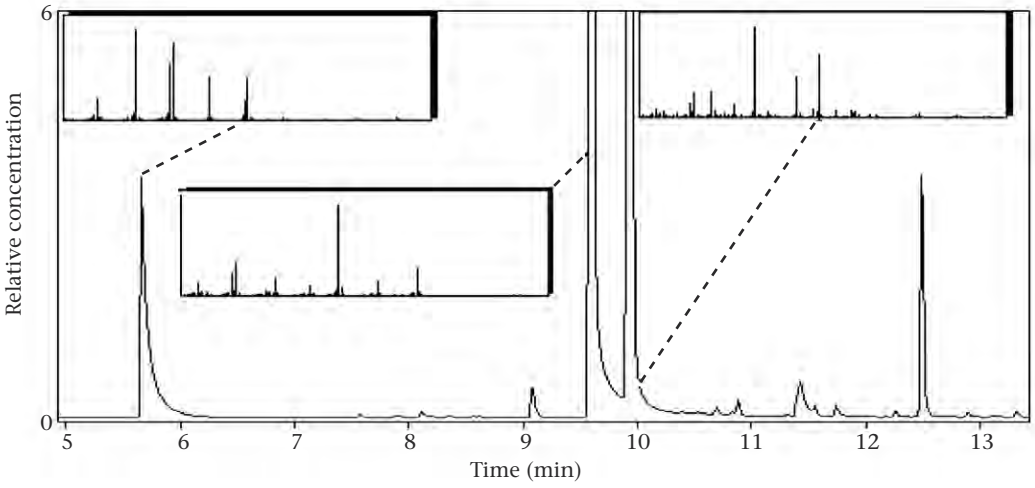

Gas-chromatography mass spectrometry (GC-MS) retention times and identification of three target compounds [dimethylmethylphosphonate (at 5.7 min), diisopropylaminoethanol (at 9.5 min), and diisopropylmethylphosphonate (at 9.9 min)] that were collected as fugitive air emissions using nanotube technology. The concentrations of the collected target compounds far exceeded commercial polymeric materials. Bar-graph inserts show the confirming mass-spectral data for each compound.

Measurement of Nuclear Magnetization Distribution in Heavy Atoms

K. L. Wong, P. Beiersdorfer, S. B. Utter, J. A. Britten

00-LW-090

A complete understanding of the physical properties of the atomic nucleus is crucial to our knowledge of the elements that comprise the universe. Although we know much about the nucleus—such as the number of protons and neutrons, their energy levels, and their decay schemes—the actual distribution and interaction of these particles is not completely understood. Scattering experiments in which high-energy charged particles are deflected off the nucleus have provided a great deal of information on the arrangement and electric-charge distribution of the protons in the nucleus. However, since magnetic monopoles do not exist, similar experiments to probe the magnetic nature of the nucleus have not been done. As a result, knowledge of the nuclear currents and magnetic distributions inside the nucleus is limited.

Current models account for the nuclear magnetic fields by describing the fields as caused by either (1) a sum of contributions from some or all the nucleons; or (2) the spin from a single unpaired nucleon, where the spins of each of the paired nucleons cancel. In the limiting case far away from the nucleus, all models predict the correct magnetic field, and they differ only in their descriptions of fields within the nucleus. Exact knowledge of the fields within the nucleus has far-reaching consequences beyond understanding the nucleus itself. These consequences range from improved tests of the standard model in atom-based parity nonconservation experiments to the search for nuclear and electron dipole moments.

In this project, we have focused on developing a probe to measure the distribution of magnetic fields in the thallium (Tl) nucleus that is used in parity-violation experiments. As opposed to scattering experiments that accelerate free particles, our approach uses a single, bound electron. An electron in the innermost orbit has a finite quantum mechanical probability of being found inside the nucleus; thus, it probes the fields there. This finite probability of the electron's being found in the nucleus causes shifts in the electron's energy levels. By measuring a particular transition—called the hyperfine transition—between energy levels, we can determine the effect of the distribution of magnetic fields in the nucleus. This effect accounts for approximately 2% of the transition energy. An accurate measurement of the hyperfine splitting to within 0.01% would provide a stringent test of the models.

In FY2000, we implemented our technique by employing two very high-resolution transmission-grating spectrometers that are sensitive to light near 3800 Å, which corresponds to the hyperfine transition of the single electron bound to a thallium nucleus, Tl^{80+}. Each new spectrometer consists of a large-diameter transmission grating and various focusing optics coupled to an ultrasensitive, low-noise, charge-coupled device (CCD) camera. The gratings were manufactured at LLNL, using our unique expertise in manufacturing high-throughput optics. The two spectrometers complement each other by doubling the signal rate and providing two independent measurements.

The spectrometers were first aligned and calibrated in situ on LLNL's Super Electron Beam Ion Trap (SuperEBIT). The SuperEBIT facility is the only device capable of producing Tl^{80+} in sufficient quantities to carry out the measurements. The measurements ran for three months because the transition is very weak, and we took background and calibration spectra along with the data. Identifying the lines was a real challenge. In the end, we observed a candidate line for isotopes ^{203}Tl and ^{205}Tl. The lines are 20 Å from their location, as predicted by the best theory. This discrepancy can be attributed to the nuclear model used in the calculation.

Our colleagues at Göteborg University in Sweden have set up the theoretical framework for extracting the nuclear magnetic distribution from our experimental data. Combining our measurements with their calculations produced a new value for the radius of nuclear magnetization that is (1) about 10% larger than the best model predictions to date, and (2) gives the first hint of a nuclear electric-dipole moment in the thallium nucleus. Our approach of using optical spectroscopy of highly charged ions has generated a new tool for probing some of the most hidden aspects of the nucleus and establishes LLNL as a leader in the fields of both experimental atomic and nuclear physics.

High-Energy Physics at the Next Linear Collider

K. van Bibber, J. Gronberg, E. Cook, S. Jensen, W. Stein

00-SI-005

The next generation of high-energy accelerators in the teraelectronvolt energy range will certainly yield new discoveries beyond the prevailing Standard Model of particle physics. The origin of the masses of particles is very likely bound up with the existence of the Higgs boson; similarly, the unification of forces at energies associated with the Big Bang strongly argues for the observation of supersymmetric particles at energies accessible to these new machines. Although the first discoveries are likely to be made at proton colliders, a high-luminosity electron–positron linear collider will also be needed to produce very large data samples for precision studies of the new physics.

This project has as a twofold aim to (1) develop technologies enabling the construction of a TeV-scale linear collider, and (2) prepare for the Laboratory's physics role in such a project. In linear-collider technologies, we have focused on the main linear-accelerator (linac) system, which would constitute most of the 25-km length of such a facility. The linac system encompasses the generation and delivery of radio-frequency (rf) microwave power and the accelerating structures, within which the electron bunches gain energy.

Our principal achievement during FY2000 was the development of an inductive solid-state modulator. In a linac, the modulators convert line power into fast, high-voltage pulses, which drive the rf-generating klystrons. Our application of modern technology from the Laboratory's induction linac program—high-density energy-storage capacitors; fast, high-current transistor switches; and low-loss ferrite cores—has resulted in a fundamental change in modulator design. Our new design is projected to be less expensive, more efficient, and more reliable than the old hydrogen, thyratron-triggered, pulse-forming network—a relic from the post-World War II beginnings of electron linacs. We have built a first 10-stage modulator, which is already in long-term testing with an S-band klystron in the main Stanford Linear Accelerator Center (SLAC) linac gallery (see Fig.). Our goal for FY2001 is to design and begin to build a prototype modulator capable of driving eight X-band linear-collider klystrons with a total peak power of 1 GW.

The main linac technologies also require the development of precision-fabricated accelerator structures. These structures would couple power to the electrons over many kilometers without increasing the size of the electron bunches, which are required to have dimensions of only a few nanometers at the collision point.

During FY2000, we also began designing a photon collider—a separate interaction region for a linear collider—that produces collisions of gamma rays at energies of many hundred gigaelectronvolts. In our scheme, the high-energy photons are generated by Compton-backscattering; short-pulse laser light from the electron bunches just before the interaction point. Our photon collider, which leverages unique Laboratory capability in high-average-power, short-pulse-laser technology, would open up entirely new and complementary physics to electron–positron collisions. For example, measuring Higgs production by two gamma rays could indirectly reveal the existence of new generations of particles of masses far exceeding the energy reach of any accelerator ever built. In FY2001, we will (1) carry out detailed design of both the laser and the optics that bring the laser beams into collision with the electron beams deep inside the detector, and (2) continue the Monte Carlo simulations of the physics and backgrounds in the photon collider.

A prototype inductive solid-state modulator (left) driving a S-band klystron (right) at the Stanford Linear Accelerator Center (SLAC).

Space Science and Technology 9

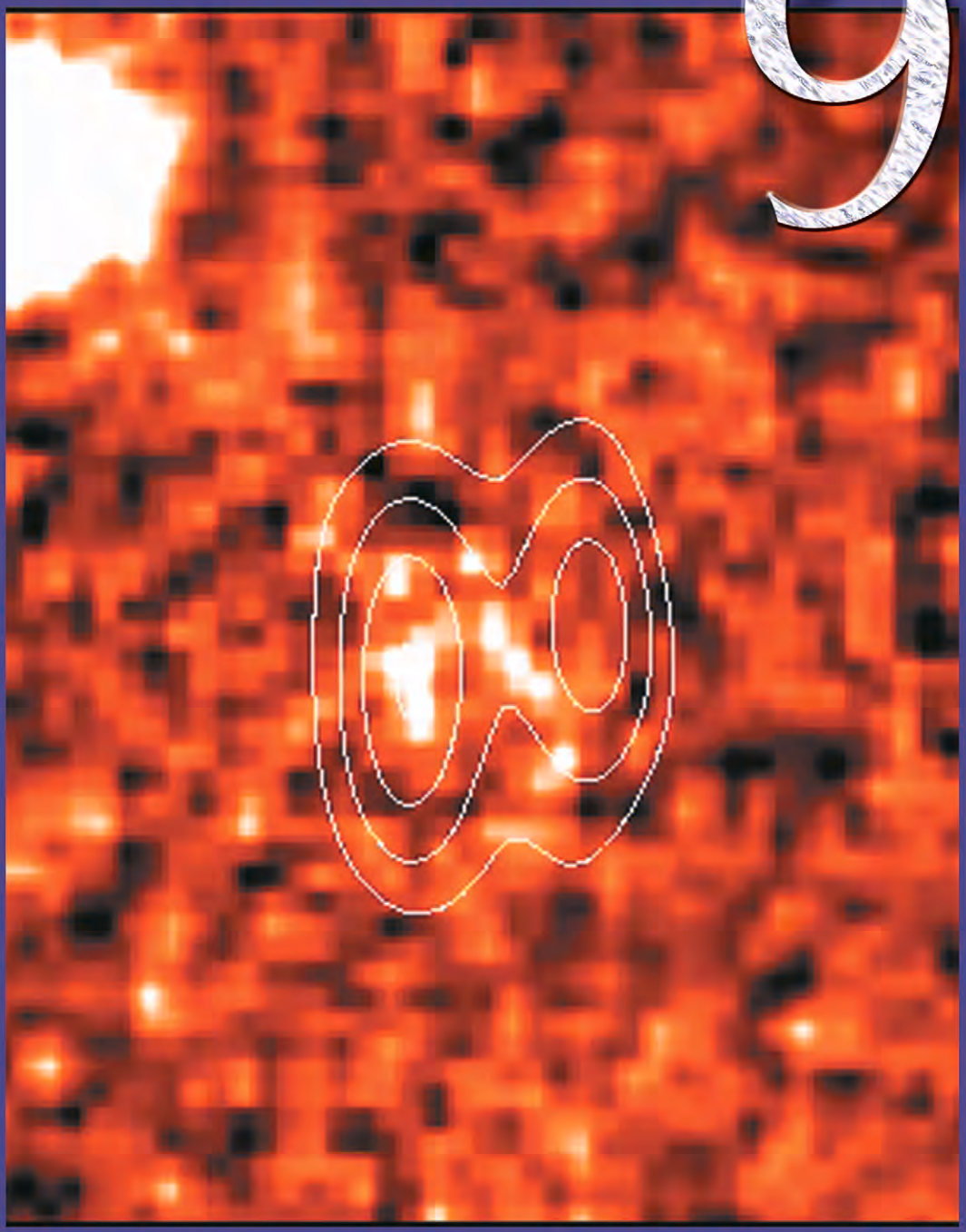

Section 9—Space Science and Technology

Ultrahigh-Contrast Imaging

C. E. Max, S. Olivier, B. A. Macintosh, C. Carrano, J. Brase

98-ERD-036

Adaptive optics (AO) is a technique for enhancing the resolution of ground-based telescopes and for improving other optical systems such as high-powered lasers. By using high-speed sensors and computers to measure atmospheric turbulence or other distortions, and shape-changing deformable mirrors to correct these distortions, AO allows a large, ground-based telescope like the 10-m-diam Keck Telescope to produce images that are even sharper than those obtained by the Hubble Space Telescope.

A timely application for this technology is the direct detection of light from extrasolar planets. Over 40 planets orbiting other stars have been recently discovered by indirect methods, that is, by observing their periodic gravitational pull on their parent star. But only by *direct* detection can one separate the light from a planet from that of its parent star to measure the planet's color and orbital properties. Seeing such a planet directly is extremely challenging: a Jupiter-mass planet in a young solar system would be 100,000 to 1,000,000 times fainter than its parent star, and Jupiter itself is over a billion times fainter than our Sun. Adaptive optics opens the possibility of observing light from such planets by suppressing the glow from the star and concentrating the light from the planet into a sharp point.

In this project, we explored ultrahigh-contrast imaging, using AO to detect very faint objects close to bright ones. We enhanced AO technologies to achieve this goal, exploiting AO expertise developed at LLNL and using AO systems at the Lick and Keck Observatories.

In important ways, the technical issues in high-contrast imaging of extra-solar planets resemble the problems relating to precision beam control and high-fidelity optical measurement that are found in the Department of Energy's and LLNL's advanced laser projects. In these situations, one must precisely characterize and (where possible) suppress all sources of scattered light or aberrations.

Over the first two years of this project, we developed precision AO imaging techniques. During FY2000, we used the Lick Observatory's AO system to perform a survey of nearby stars already known from their spectra to have planetary systems. We detected and imaged low-mass companions around five of these nearby stars using the Lick Observatory's Infra-Red Cal (IRCAL) camera. Figure (a) shows our results for a star named HD 114762, whose very faint companion has an 84-day orbital period. Figure (b) shows the IR spectrum of this companion that we obtained using the Keck Observatory's near-infrared spectrograph (NIRSPEC). The spectrum shows lines characteristic of a very low-mass star (a late M subdwarf). At Lick Observatory, we are now able to image companions that are 100,000 times fainter than their parent star.

During FY2000, we also worked to understand the properties and performance of the new AO system on the Keck Telescope. Using this system, it is possible to detect a companion that is one- to ten-million times fainter than its parent star. This is the range needed to image Jupiter-mass planets around young, nearby stars. Candidate systems that we detected during this project are in the process of being confirmed and identified.

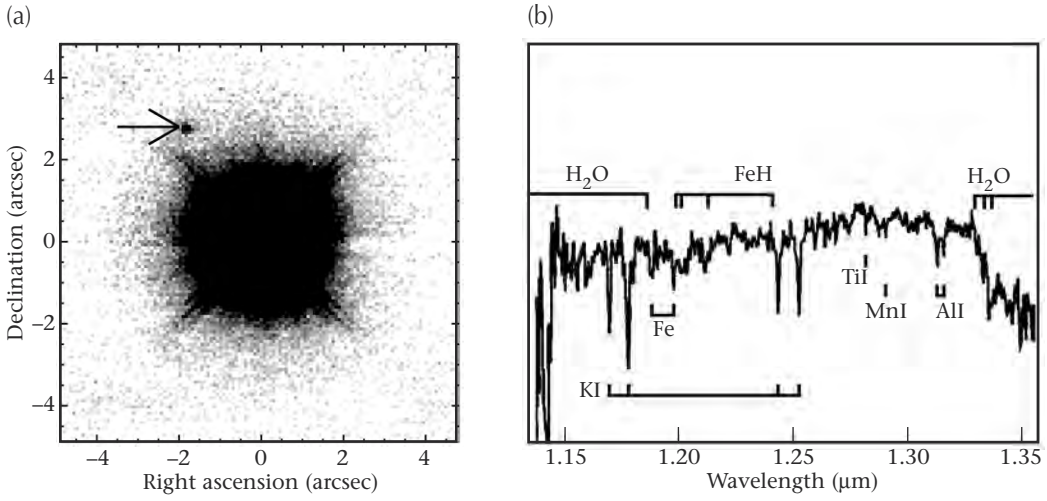

Use of adaptive optics (AO) for ultrahigh-contrast imaging: (a) infrared (IR) image of star HD 114762 with its 1000-times-fainter companion (arrow), and (b) spectrum of the companion, revealing it as low-mass star (late M subdwarf).

Back to main TOC

Stellar Velocimetry with a Novel, High-Efficiency Interferometer

D. J. Erskine, J. Ge

98-ERD-054

The search for extra-solar planets continues to be one of the most exciting fields in astronomy and one that attracts great interest from the public. The most popular method of detecting planets is by using the Doppler effect to measure the gravitational tug of the planet on the parent star. Planets the size of Jupiter and Saturn create 12- and 3-m/s signatures, respectively.

Although many institutions endeavor to join the search, they are hampered by the lack of affordable instruments that have sufficient velocity resolution. Conventional high-spectral-resolution grating spectrometers, or velocimeters, have two drawbacks. First, they are massive (5 m) and extremely expensive. Second, because of their extreme sensitivity to the path of the input beam, the most accurate velocimeters must use the iodine vapor cell (which does not deviate the beam because of its absorptive nature) as a spectral reference. This limits their operation to green light. Because of this second limitation, most of the photons from a star are wasted, particularly those from red stars. Thus, despite constituting more than 60% of near-Earth stars, red stars are currently under represented on planet-search surveys because of their relative weakness in the green part of the spectrum.

In this project, we developed a new method for measuring Doppler shifts of starlight that has many practical benefits. First, the method is based on combining an interferometer with a small, low-resolution diffraction grating, the result being a dispersive interferometer. Therefore, because the Doppler effect is measured by fringe shifts, and not directly by the grating, the required spectral resolution of the grating can be reduced by a factor of 3 to 10. Second, the system tolerance to imperfections in the grating is much higher. These properties allow the overall instrument to be dramatically smaller (TV-sized vs. kitchen-sized), inexpensive, and portable. Airborne and spaceborne platforms are now possible for the first time. Furthermore, the interferometer is 1000 times less sensitive to errors in the beam path, which enables the use of an emission lamp as a spectral reference. The emission lamp allows the interferometer to use all the colors emitted by the star while maintaining high velocity precision, thus increasing the measured flux from red stars by an order of magnitude.

During FY2000, we conducted proof-of-principle tests of our prototype instrument on sunlight and bright starlight. Figure (a) shows that we can detect the 12-m/s amplitude signature of the Moon as it tugs the Earth—the same amplitude as Jupiter exerts on the Sun—which demonstrates that our velocity resolution and stability are already competitive with those of conventional instruments, despite the lack of refinements of a mature instrument. Figure (b) demonstrates velocimetry on bright starlight at the 1-m telescope at Lick Observatory. This installation at Lick Observatory also demonstrates both the portability of our instrument and its relative insensitivity to hostile wind and temperature swings in the observatory dome. To achieve the same velocity resolution, conventional instruments need stringent environmental control.

Our technique offers many benefits in other areas that require advanced spectroscopy and metrology, such as stockpile stewardship and nonproliferation efforts.

This was the final year of LDRD funding. One of the investigators (Erskine) has been invited to continue developing the instrument at the University of California, Berkeley, Space Sciences Laboratory; the other (Ge) plans to build a similar instrument for the Hobbly-Eberly Telescope at Pennsylvania State University.

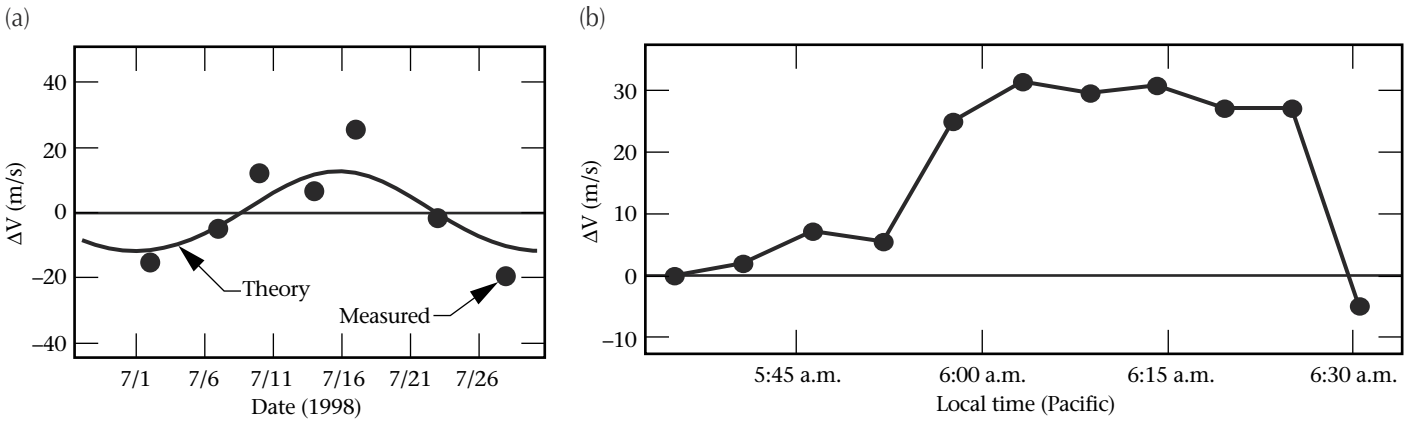

In proof-of-principle experiments, our prototype dispersive interferometer successfully (a) used sunlight to detect the Moon's 12-m/s tug on Earth; and (b) when installed on the Lick Observatory's 1-m telescope, used starlight to measure the real-time velocity of Arcturus. For (a), geocentric, annual orbital motions were subtracted.

Primordial Quasars and Starbursts in Protogalaxies

W. van Breugel

98-ERI-005

Within standard cosmological models, the formation of galaxies is a hierarchical process. Large galaxies are thought to grow through the merging of smaller systems, and the most massive objects form in over-dense regions that will eventually evolve into the large clusters of galaxies seen today. Some models also suggest that the first massive black holes may either have grown in similar hierarchical fashion, together with their parent galaxies, or that they may have preceded galaxy formation and be primordial. It is therefore of great interest to find the progenitors of the most massive galaxies and their central, active black holes (quasars) at the highest possible redshifts or z (an astronomical measure of distance and time) and to study their properties and cosmological evolution.

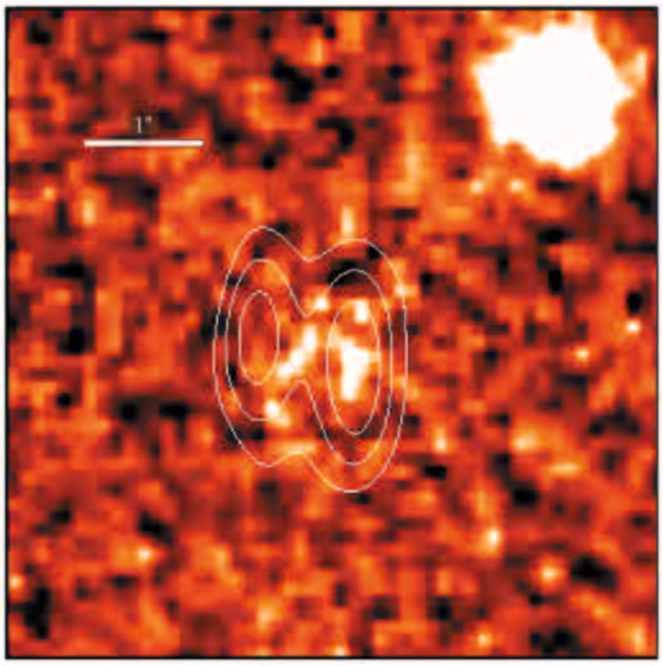

An infrared false-color image of the most distant known radio galaxy, at a redshift of 5.19, with the source structure outlined as contours. The galaxy, TN J0924-2201, is very young and still forming through merging of smaller galaxy components.

In this project, we focused on the key questions: how do we actually find these objects, and what do they look like?

Previously, we had shown that powerful, ultrasteep-spectrum radio sources can locate massive forming galaxies very efficiently through near-infrared (-IR) identification. The success of this method was illustrated by our discovery of the most distant radio galaxy known, TN J0924-2201 at $z = 5.19$ (see Fig.). During FY2000, we completed the final selection of a large sample of 669 high-redshift radio-galaxy candidates. After extensive near-IR and optical observations at the Keck and other telescopes, we discovered nearly a dozen radio galaxies with redshifts larger than 3. These galaxies can now be used to study the formation of massive galaxies and their central black holes, and they can serve as beacons for searches of large-scale structure around them.

In FY2000, we also combined these new data with information from the literature to investigate the spectroscopic properties of a sample of 165 radio galaxies as a function of redshift, or cosmological time. One of the striking results is that cold, neutral hydrogen gas appears to be most commonly found among the smallest radio sources. This suggests that these sources may be relatively young (a few million years old) and that they are still embedded in a dense, protogalactic medium. Furthermore, our analysis of emission-line ratios, in particular of singly and doubly ionized carbon, showed that the ionization in these small sources may be shock-dominated, presumably because of the strong interactions of jet outflows with the surrounding dense gas.

FY2000, the final year of this project, also produced new redshift records for quasars: we discovered a quaser at $z = 5.50$ and another at $z = 5.82$. We also showed that the most distant galaxy claimed previously, STIS 123627+621755 at $z = 6.68$, is actually at a much lower redshift of $z = 1.51$ and is most likely a low-luminosity dwarf galaxy like the Small Magellanic Cloud. Thus, the quasar we discovered at $z = 5.82$ is currently the most distant known object, whether galaxy or quasar.

The Size, Shape, and Composition of the Milky Way

K. H. Cook

99-ERD-041

The objective of this project is to exploit our large dataset comprising the photometric histories of tens of millions of stars to determine the size, shape, and composition of the Milky Way. Astronomers still do not know the size, the mass, or the composition of the Milky Way. One thing is clear: most of the mass is in some form of dark matter that astronomers cannot directly detect. At LLNL, we have used the gravitational microlensing effect to draw conclusions about the abundance of massive objects, luminous or dark, along different lines of sight through our galaxy. The Milky Way's dark matter is thought to be distributed in a large, spherical halo, but its constitution is unknown because it emits no detectable radiation.

Using the microlensing effect, we have searched for dark matter in the form of planets, brown dwarfs, and black holes or any other massive compact halo objects (MACHOs) having a mass range of $10^{-7}\ M_{Sun} < M < 30\ M_{Sun}$.

The microlensing of stellar light is produced when a massive object (e.g., a star) passes very close to the line of sight between the source star and the observer. The classical signature of the simplest microlensing is a characteristic achromatic light curve that is time-symmetric with respect to the epoch with the highest flux. The probability of a detectable microlensing event is very low. Therefore, we have monitored millions of stars in the Large and Small Magellanic Clouds (LMC; SMC) as well as the Galactic Center for several years.

In FY2000, the MACHO Project released a milestone analysis summarizing the search for microlensing towards the LMC. Analysis of 5.7 yr of photometry on 11.9 million stars in the LMC reveals 13 to 17 microlensing events, depending upon the selection criteria (see Fig.). A detailed treatment of the detection efficiency shows that this is significantly more than the approximately two to four events expected from lensing by known stellar populations. The spatial distribution of events is consistent with an extended lens distribution such as that expected from a Milky Way or LMC halo. Interpreted in the context of a Galactic dark-matter halo, consisting partially of compact objects, a maximum-likelihood analysis gives a MACHO halo fraction of 20% for a typical halo model, with a 95% confidence interval of 8% to 50%. A 100% MACHO halo is ruled out at the 95% confidence level for all except the most extreme halo model. Interpreted as a Galactic halo population, the most likely MACHO mass is between 0.15 and 0.9 M_{Sun}, depending on the halo model, and the total mass in MACHOs out to 50 kpc is found to be 9 [the uncertainty is not symmetric and is +4/–3] $\times 10^{10}\ M_{Sun}$, independent of the halo model.

Besides a larger data set, this work also includes an improved efficiency determination, improved likelihood analysis, and more thorough testing of systematic errors. We stress that the supernovae in galaxies behind the LMC are important sources of background. In addition to the dark matter implications of this work, we continue to mine the database for interesting time-variable astronomy.

In FY2001, we plan to complete our analysis of Galactic-bulge microlensing. We hope to determine the parameters of important components of the Milky Way such as its disk and central bar, thus shedding more light on the controversial subject of the structure of the Milky Way. We will also analyze the time-scale distribution of microlensing events and, for the first time, draw robust conclusions about typical masses of distant lenses.

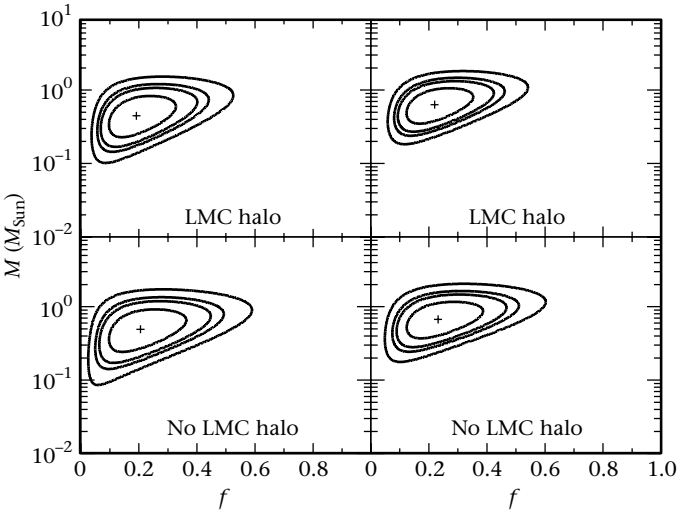

Likelihood contours for massive compact halo object (MACHO) mass M and halo fraction f for the standard Galactic halo. Two sets of criteria for selection of microlensing events were used in our analysis, which yielded sets of 13 (left panels) and 17 (right panels) microlensing events. For each set, the likelihood analysis was done assuming no Large Magellanic Cloud (LMC) dark halo (top) or an LMC dark halo with the same MACHO fraction as the Milky Way's halo.

Back to main TOC

Laboratory Simulations of Accretion-Powered X-Ray Sources

M. E. Foord

99-ERD-044

Accretion—the dominant energy-conversion process in the universe—involves the flow of material down a deep gravitational well of a massive compact object, such as a neutron star or black hole. As the mass piles up or "accretes" onto the surface, it strongly radiates and photoionizes the gas and other material that surround the star, creating a class of objects known as accretion-powered x-ray sources. With the recent launch of two x-ray satellite observatories—Chandra X-Ray Observatory and X-Ray Multi-Mirror Mission—the astrophysics community is beginning to collect the high-resolution spectral data that are needed to unravel the mysteries of accretion-powered x-ray sources. This multibillion-dollar, internationally funded space effort promises to open a new era in x-ray astronomy.

To infer conditions in accreting x-ray sources, the satellite data must be interpreted using astrophysical analysis codes. The main goal of this project is to generate a similar radiative environment in the laboratory and to perform well-diagnosed experiments that can be used to directly test the analysis codes that are being used by the astrophysical community.

During FY2000, we performed experiments at Sandia National Laboratory's Z-facility. To study the astrophysically abundant element iron (Fe), the pinch was designed to produce a sufficient flux of high-energy x rays ($E > 1$ keV) to ionize a low-density Fe sample into the L-shell. That is, more than 16 electrons were ionized from each ion. The sample densities were also chosen so that the radiation pulse (10 ns) was sufficient to bring the samples into equilibrium.

The radiation source was generated by inductively coupling a 20-MA, 100-ns-risetime current pulse into a 2-cm-diam tungsten-wire array. The electromagnetic forces drove the wires radially inward onto the central axis, creating a 10-ns, 120-TW, 180-eV blackbody radiation pulse.

The pinch emission was measured using an absolutely calibrated transmission-grating spectrometer. Besides photoionizing the samples, the pinch also provided a relatively continuous source for backlighting the samples in the wavelength range 9 to 17 Å. The backlit absorption spectrum was then used to unfold the distribution of charge states in the plasma.

Low-density samples were positioned a few centimeters from the pinch at various orientations to obtain both the absorption and emission spectra. A three-crystal Johann x-ray spectrometer was developed specifically for this application. Sodium (Si) and fluorine (Fl) were comixed into the Fe to provide additional information about the samples' temperature and velocity distribution.

From our analysis of the absorption spectra, we found that the low-density iron samples ionized into the L-shell. The density was independently determined from pinhole images of the plasma. We also observed numerous Fe, Si, and Fl emission lines, which will allow detailed comparisons with astrophysical line-emission codes. The continuum emission from the helium-like Si ion yielded electron temperatures near 30 eV (350,000°C). We believe these results provide the first set of well-characterized data that can be used to benchmark photoionization and spectral-synthesis codes for a strongly photoionized plasma.

During FY2001, in our next series of experiments, we will vary the ionization regimes and investigate other materials of astrophysical interest.

An Imaging Fourier Transform Spectrometer for Astronomy

K. H. Cook, J. R. Graham, C. L. Bennett, S. Blais-Ouellette, E. H. Wishnow, R. Wurtz

99-ERD-065

The astrophysical community is becoming accustomed to "data mining" vast data sets. Unfortunately, the data sets available for mining have been a patchwork of imaging and spectroscopy. Experience has shown that the most efficient use of the photons striking a telescope's aperture would be to produce a hyperspectral datacube that could later be investigated in detail. Although there is no shortage of new ideas for acquiring these datacubes, most techniques are still in their infancy.

LLNL has a proven record of reformulating astronomical observation by introducing novel instruments and techniques [e.g., work with compact massive halo objects (MACHOs), laser guidestar, etc.]. Our pioneering, recently developed hyperspectral infrared imaging spectrometer (HIRIS) now offers the greatest promise for obtaining astronomical hyperspectral imaging in the immediate future. HIRIS obtains datacubes by means of an imaging Fourier transform spectroscope (IFTS).

In this project, we are extending the HIRIS technique to image faint objects that are emitting visible light. Our IFTS will produce a spectrum for every spatial pixel, thereby achieving what is called 3-D imaging in astronomy. Our instrument has generated significant interest in the astronomical community and is attracting collaborators.

By the beginning of FY2000, we had developed a collaboration with scientists at the University of Washington and at the 3.5-m telescope at the Apache Point Observatory (APO) in New Mexico. We are also working with a commercial company that specializes in custom interferometers [e.g., an interferometer for the Canadian Space Agency and a small-scale infrared IFTS for a National Aeronautics and Space Administration (NASA) probe].

In early FY2000, we designed and built optics that are matched to the APO's optical prescription and supported by a novel, lightweight, low-deflection optical breadboard. We integrated this system with two high-quantum-efficiency, low-noise, high-speed-readout, imaging charge-coupled device (CCD) cameras. We also designed and built (1) a compensated beamsplitter for the IFTS that will allow us to obtain lower-resolution datacubes with shorter integration times, and (2) signal-to-noise simulators for our instrument for use in planning data-accumulation observations at APO.

In April 2000, the purchased interferometer was integrated with the rest of the apparatus (see Fig.), and the whole was shipped to APO. After our IFTS had been installed on the telescope, we demonstrated that (1) the system did not degrade images either by blurring or because its support structure flexed, and (2) the integrated control system has minimal deadtime and can be operated remotely.

Although the interferometer had been built to demonstrate long-term metrologic stability—holding a fixed position to optical tolerance—problems occurred with the interferometer's metrology system when it was on the moving telescope. We have been working to solve these problems through simulation, analysis, and redesign. Another objective is improving the entire IFTS so that it can be operated without interruptions for fine adjustment—an important consideration for astronomical observing.

Our goal for FY2001 is to complete the redesign and implement the changes to the motion portion of the interferometer. Then, we plan to return to APO with our IFTS as a regular visiting instrument for obtaining science-grade data.

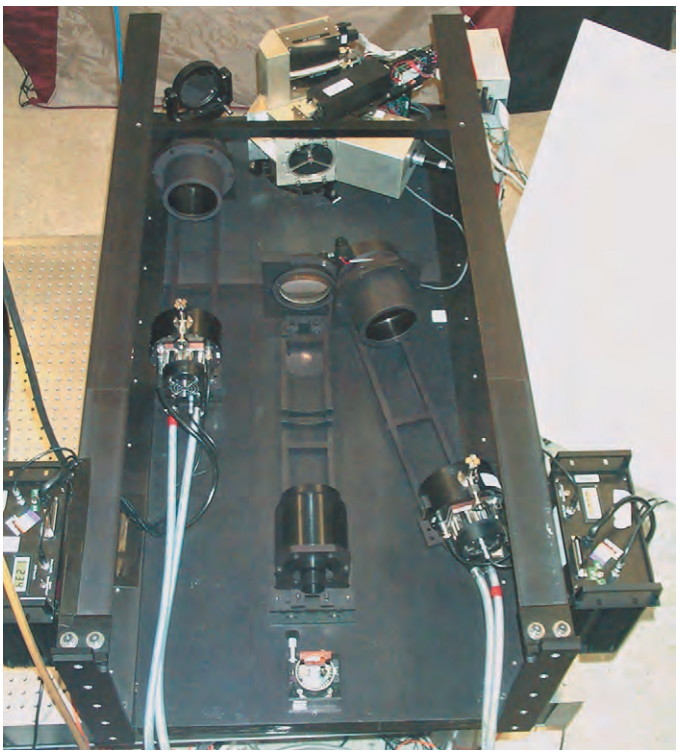

Our second-generation, astronomical imaging Fourier transform spectroscope (IFTS) was designed for installation on the 3.5-m telescope at the Apache Point Observatory (APO) in New Mexico. The interferometer unit is at the far end. Internal baffles have been removed to show the optical elements more clearly. Light from a telescope enters at the near end, is collimated, and passes through the interferometer. Light from the interferometer's two output ports is re-imaged by the optical elements on either side of the collimator into two thermoelectrically cooled, charge-coupled device (CCD) cameras.

Primitive Planetary Systems via the Keck Telescope

B. Macintosh, S. Gibbard, J. Patience, C. Max

99-ERI-003

One of the most fundamental questions in modern astronomy is the possibility of the existence of other solar systems like our own—those with potentially habitable planets. Although many other planetary systems have now been detected through indirect methods, all are quite different from our solar system, with massive Jupiter-like planets occupying the inner part of the system where Earth-like planets would be expected. It is unclear which of the two systems is the most common. Current theories of star and planet formation have not yet found a compelling explanation for these systems.

In this project, we are using the adaptive optics (AO) system on the 10-m W. M. Keck Telescope—the most significant advance in astronomical capabilities since the launch of the Hubble Space Telescope—to study the formation and evolution of planetary systems like our own. Adaptive optics correct for distortions caused by the Earth's atmosphere and allow ground-based telescopes to reach their theoretical maximum resolution. The resolution of the Keck AO system allows us to study processes taking place in young stellar systems on scales comparable to that of our own solar system. We are studying young stellar systems in the process of formation, especially in the Trapezium region in Orion, the closest large-scale star-formation region to our sun.

Using the Keck AO system, in FY2000 we surveyed nearly 100 very young stars in the Trapezium, including several of the protoplanetary disks known as proplyds. Figures (a) and (b) show the improved resolution obtainable with the Keck AO system.

In addition to studying planetary systems that are still forming, the Keck AO system is now sensitive enough to detect the young planets themselves. Jupiter-sized planets that are 10 million years old or younger will still retain their heat of formation and give off significant near-infrared (-IR) light. With the combined sensitivity and resolution of the Keck AO system, we can see massive planets as close as 20 AU from their parent stars.

In FY2000, we began a search for such planets, initially following up on targets detected by our collaborators at the University of California, Los Angeles (Ben Zuckerman and Eric Becklin), using the now-defunct near-IR camera and multi-object spectrometer (NICMOS) on the Hubble Space Telescope. At the end of the year, we were in the process of using these follow-up observations to study a brown dwarf—approximately 20 times the mass of Jupiter— that orbits a binary star. Keck AO observations detect all three components of the system and will allow us to study the orbits and hence masses of the stars, thereby providing a testbed for theoretical models of stellar evolution.

We are also following up a candidate, young, Jupiter-sized planet associated with another young star. Careful Keck observations in FY2001 will determine if this is in fact a true planet or merely a background star. If confirmed, this will be the first direct image of a planet orbiting a star other than our own.

(a)

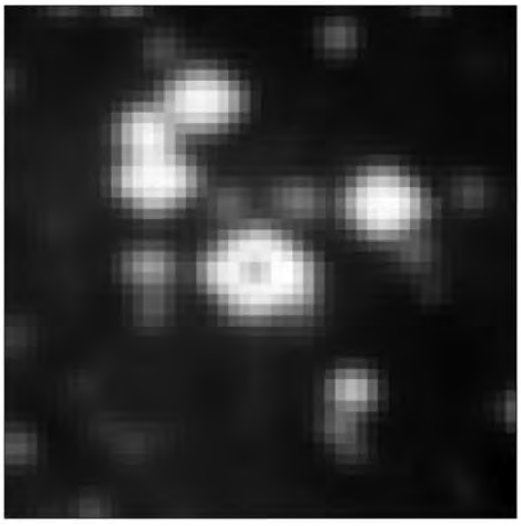

(b)

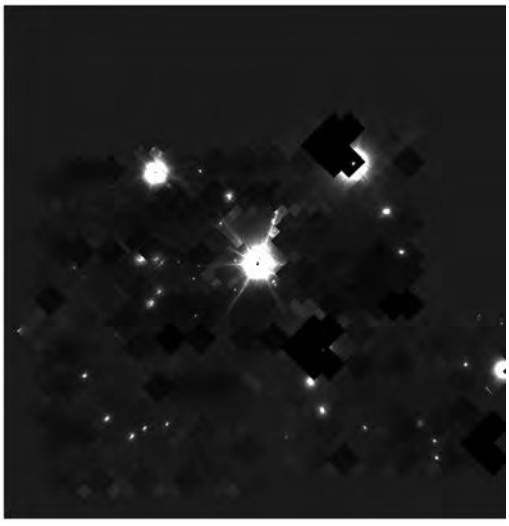

(a) Conventional telescope and (b) Keck adaptive optics (AO) mosaic of the Trapezium region in Orion.

Planetary Interiors in the Laboratory

R. Chau, M. Bastea, W. J. Nellis

00-ERD-033

The recent discovery of extra-solar planets whose masses are comparable to the giant planets in our own solar system has focused attention on the nature of giant planets. Giant planets such as Jupiter and Uranus are primarily made up of hot, dense fluids. To understand how these planets formed as well as their properties, we must determine the composition and nature of the fluids within their interiors. For example, the very complex magnetic fields of Uranus and Neptune are generated by the convective dynamo motion of electrically conducting fluid in their deep interiors. Unfortunately, the extreme pressures and temperatures within the giant planets coupled with their large distances from Earth make direct probes of the planetary interiors impossible. Ground-based observation and space probes such as Voyager 2 provide only limited information. What remains is laboratory simulation of states comparable to deep, planetary interiors.

This project builds on experimental capabilities developed for LLNL's Stockpile Stewardship Management Program (SSMP) and will enhance the Lab's competency in shock physics. The materials important in planetary interiors such as hydrogen, methane, and water are also important to LLNL's work in inertial confinement fusion (ICF) and energetic materials. Hydrogen is the basic fuel for ICF; water, methane, and ammonia are the basic reaction products of energetic materials. The project builds upon over two decades of work and development on the shock physics of low-*Z* materials at LLNL.

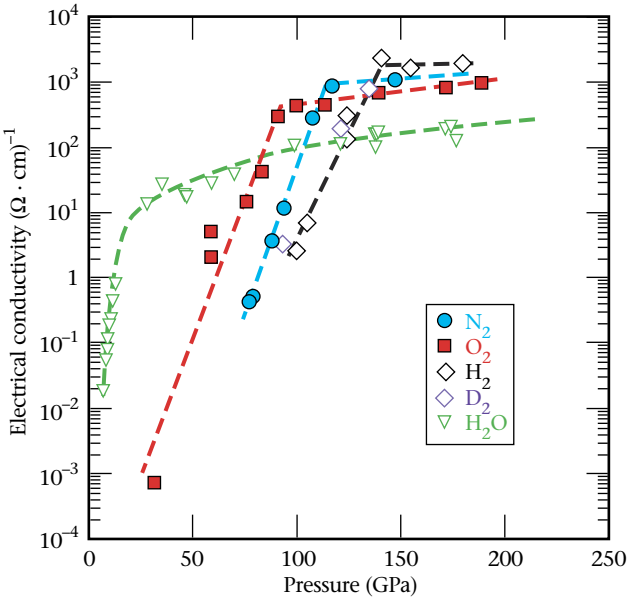

Electrical conductivity of oxygen (O) and nitrogen (N) as a function of shock pressure (closed symbols). Shown for comparison are the conductivities of hydrogen (H) and water (open symbols) previously measured here at LLNL and elsewhere. Dashed lines are guides to the eye.

In this project, we are using gas-gun drivers to simulate conditions within the interiors of giant planets. Dynamic compression using gas-gun drivers can achieve both high temperatures and high pressures simultaneously. Thus, we can attain in the laboratory, albeit for a short time, the same conditions that exist deep within giant planets—upwards of 7000 K and 200 GPa. We are coupling dynamic high pressures with real-time measurements of the electrical conductivity. Electrical conductivities provide information about the concentrations of electrons and ions, which in turn indicate chemical composition and thus the equations of state (EOS) of planetary matter. Measured electrical conductivities are an essential input in modeling planetary magnetic fields.

During FY2000, we extended our understanding of the interiors of planets by measuring the electrical conductivity of oxygen (O) and nitrogen (N) at pressures up to 190 GPa. The electrical conductivity of O is necessary to interpret the electrical conductivity of H_2O—the primary component of the fluid within Uranus and Neptune—which was previously measured here at LLNL and elsewhere. The conductivity of O is similar to that of hydrogen (H). Below 100 GPa, O is semiconducting and has a thermally activated mobility gap. Above 100 GPa, O becomes metallic and reaches the minimum metallic conductivity. The nonmetal–metal transition in O occurs at a lower pressure than for H. We found that the behavior of N—with a transition pressure of 120 Gpa— was similar to that of H and O.

The Fig. shows the electrical conductivities of O_2, and N_2 as a function of pressure in comparison to previously measured conductivities of H_2 and H_2O. The transition pressures for H_2, O_2, and N_2 scale with the size of the molecule and suggest a common mechanism for the nonmetal–metal transitions.

The Fig. also shows that the conductivity of water up to 200 GPa is purely ionic, whereas O and H are electronic. In other words, water does not behave simply as a mixture of H and O, although there are strong indications of molecular dissociation. Molecular-dynamics simulations performed at LLNL and elsewhere show that the state of the fluid is dynamic in nature. The interactions between atomic species indicate that chemistry is important at these extreme conditions.

In FY2001, we will focus on measuring the electrical conductivity of methane and ammonia up to the highest temperatures and pressures obtainable with a gas-gun driver. We will also further examine the role of chemistry at extreme conditions. We believe that molecular dissociation and chemical interactions between the many different atomic species suggest that a more complex composition within Uranus and Neptune than those previously used by planetary modelers.

Recreating Planetary Cores in the Laboratory

G. W. Collins, P. Celliers, L. B. DaSilva, R. Cauble

00-ERD-044

An accurate equation of state (EOS) for planetary constituents at extreme conditions is the key to any credible model of planets or low-mass stars. The cores of gas-giant planets are thought to reach pressures near 10 Mbar and temperatures near 10,000 K. However, very few materials have had their high-pressure (more than a few Mbar) EOS experimentally validated, and even then, only on the principal Hugoniot.

The goal of this project is to provide rigid constraints for planetary models at their most extreme pressures, densities, and temperatures. Our path is to (1) develop a database for planetary fluids on the principal Hugoniot, (2) develop techniques and measure the EOS close to predicted planetary isentropes, and finally (3) use the data to correct for planetary models. Our techniques would allow access to a new regime of high-densities at moderate temperatures, information that is crucial to a deep understanding of both planets and weapons physics.

During FY2000, we measured the shock-wave EOS of water, a primary constituent of Neptune and Uranus, at pressures from 100 to 500 GPa (5 Mbar). Over this pressure range (see Fig.), no data were available, and water was predicted to transition from an ionic to an electronic conductor. The highest pressure reached in conventional single-shock gas-gun experiments of water is 80 GPa (there is one data point at about 1400 GPa that was published by Russian researchers). The Hugoniot compression curve for water is shown in the Fig. Both an LLNL chemical model (not shown) and the SESAME database match the data very well.

Of particular interest is identifying on the phase diagram of water the shock pressure at which water becomes an electronic conductor. We determined this by measuring optical reflectance. The shock-front reflectance in water drops to low levels for shock pressures below 140 Gpa. However, the reflectance is not zero; even at pressures as low as 100 Gpa, the reflectance is 10%. Thus, the transition to an electronically conducting state occurs gradually, beginning at pressures less than 100 GPa and leveling off at about 400 GPa pressure. (In allied work at LLNL, both the Hugoniot and reflectivity data are being used to benchmark the codes used for Neptune and Uranus.)

Gravitational force compresses planetary and stellar interiors so that material states follow a line of isentropic compression (ignoring phase separation). These states exist at temperatures lower than principal Hugoniot states at similar pressures, but at higher temperatures and pressures than can be achieved with diamond anvils. In FY2001, our goal is to develop techniques that will enable us to reach these high-density states for the first time in the laboratory. To achieve this, we will develop precompressed targets and double-shock techniques for laser-shock experiments.

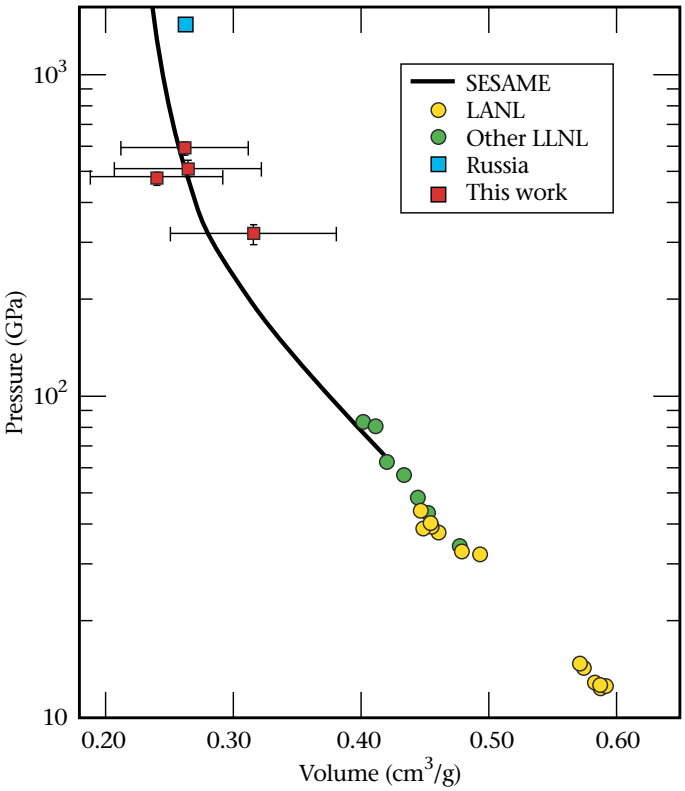

Pressure vs. volume along the water shock-compression curve (principal Hugoniot). Our new experimental measurements confirm predictions from equation-of-state (EOS) calculations made using the SESAME database.

Nearby Active Galactic Nuclei

C. E. Max, D. Gavel, B. Bauman, D. Pennington, J. Patience

00-ERD-049

Some galaxies exhibit high-energy phenomena in their cores that cannot be attributed to stars alone. At the center of these galaxies, a small central region (well less than a cubic parsec)—known as the Active Galactic Nucleus (AGN)— emits up to 10,000 times the normal luminosity of a galaxy. The high-luminosity, small volume, and nonthermal spectrum characteristic of these AGNs led to the hypothesis that accretion onto supermassive black holes provides the energy source in the nucleus.

For 30 years, Department of Energy (DOE) laboratories have been doing pioneering work on the high-energy processes involved in black-hole formation and emission (DOE computer simulations were the first to describe black-hole formation). However, only in the past few years has direct evidence for black holes begun to emerge—in the form of high-spatial-resolution observations that probe regions (AGNs) close to the central black hole.

In this project, we are using adaptive optics (AO) and laser guide stars on ground-based telescopes at both Lick and Keck Observatories to observe directly the processes of accretion and emission in the most massive black holes known today. With the improvement in spatial resolution made possible by AO, during FY2000 we obtained near-infrared (-IR) images and spectra of the regions in AGNs that are within 100 to 1000 parsecs of central black holes. This permits exploration of the disk structure, scattering, and hot-dust emission around the central black hole. We also found double nuclei symptomatic of galaxy-merger events, which can be the triggers for black-hole formation.

Figure (a) shows a visible-light image of the active galaxy NGC 6240 that we obtained during FY2000 with the charge-coupled device (CCD) camera at the Lick Observatory's 40-in. telescope. NGC 6240 appears to be two galaxies in the midst of a merger process; the "tails" are stars and gases in the galaxies' disks that have been tidally distorted by the merger process. Figure (b) shows our Keck Telescope AO image of the small central nuclear region of NGC 6240. The nucleus is double, with the two components separated by 1.6 arcsec (750 parsecs). Using the newly commissioned near-IR spectrograph (NIRSPEC) built at the University of California, Los Angeles, and installed at Keck Observatory, we also obtained separate spectra of the two nuclei. The spectra show that molecular hydrogen gas close to the (joint) nuclear region is in an excited state that is probably caused by shock waves that form when the interstellar media of the two galaxies encounter each other at high velocities.

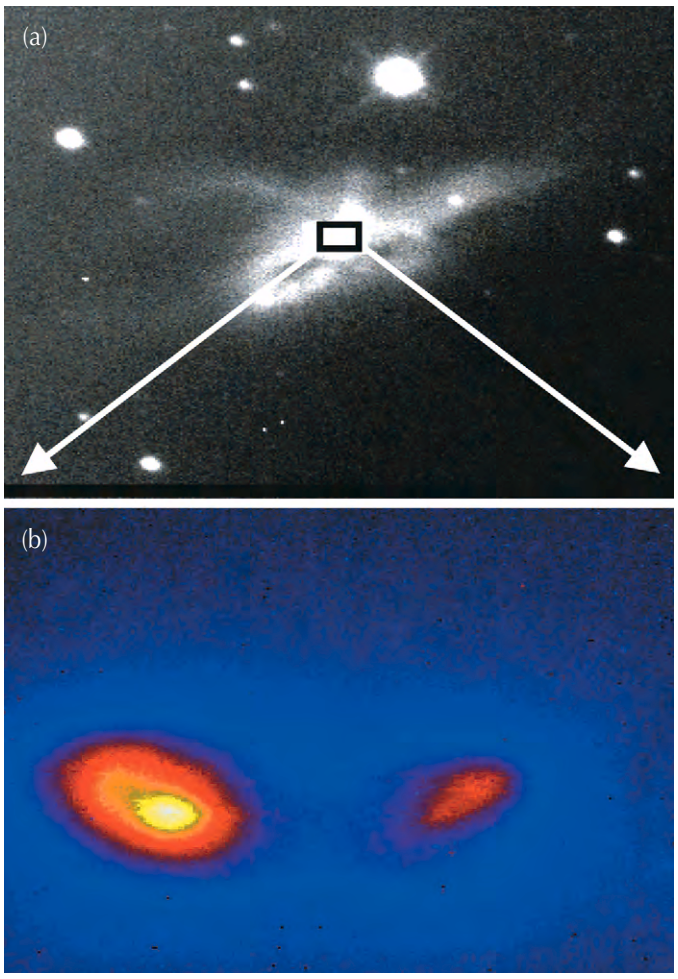

Active galaxy NGC 6240, apparently two galaxies in the process of merging: (a) a conventional visible-light image, and (b) Keck adaptive optics (AO) image of the nuclear region, showing dual nuclei.

In addition to NGC 6240, in FY2000 we obtained AO images of four other AGNs. These observations were made possible by major improvements in our AO and laser-guide-star technologies at Lick Observatory: we (1) greatly improved the throughput of the AO system; (2) successfully commissioned the Infra-Red Cal (IRCAL) camera; (3) upgraded the laser guide star for high stability and ease of use; and (4) designed and installed an optical metrology system for the AO bench.

In FY2001, we will expand our sample of active galaxies by using the laser guide star at Lick Observatory and by further AO observations at the Keck Telescope.

Back to main TOC

Autonomous On-Orbit Proximity Operations and Docking Capability

A. Ledebuhr, L. Ng, M. Jones, B. Wilson, J. Whitehead

00-ERD-071

The capability for autonomous proximity operations, such as close-in inspections, docking, and formation flying of a microsatellite around another target satellite in low-Earth orbit would open up a host of potential new missions that could revolutionize robotic operations in space. However, these capabilities must first be developed and demonstrated on the ground. The goal of this project was to demonstrate, in the laboratory, the critical capabilities and technologies necessary for these autonomous operations.

During the course of FY2000, we completed the development of a prototype engineering test vehicle, the ETV-250, which was designed to carry out repeated docking experiments on a simulated zero-gravity, five degrees-of-freedom (DOF) dynamic air table. This vehicle was conceived as a forerunner of future microsatellites with the ability to perform complex proximity operations and docking maneuvers in space. We prototyped a 3-D, vision-based, object-tracking system that uses stereo-ranging and laser-ranging systems to support a series of autonomous docking functions. A major development consisted of an integrated, proximity-operation sensor (IPOS) system along with its avionics package and the software necessary to control and operate it. In addition, we began characterizing a miniaturized, hot-gas-driven, pumped propulsion system that uses hydrogen peroxide (H_2O_2) as a safe, nontoxic propellant. Once fully developed, this system will enable the precision on-orbit maneuvers required for these missions. A cold-gas propulsion system was used in the docking target (ETV-150) and ETV-250 vehicles for ground testing.

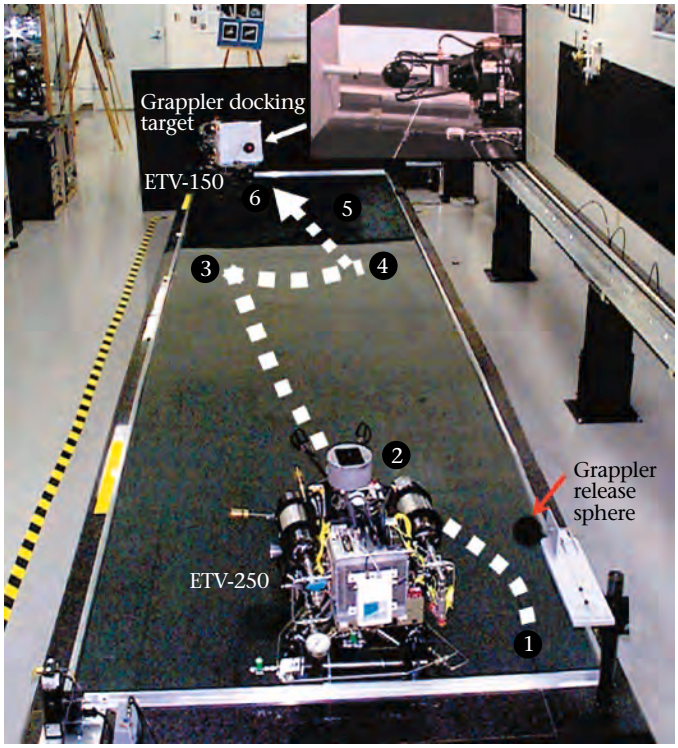

Numbers (see text for explanation) indicate the autonomous docking sequence of our prototype engineering test vehicle (ETV). The inset shows the final successful docking, with the robotic arm grappling the sphere mounted on a target vehicle.

To demonstrate proximity operations and docking capability, the ETV-250 was equipped with a smart sensor head and several intelligent software modules. The sensor head included an on-axis, high-resolution camera for object recognition; a robotic grappling arm with four fingers for docking; a pair of stereo cameras to provide stereo vision and range; an inertial measurement unit (IMU) for vehicle stability and control; and a laser ranger for millimeter-level precision translation control. The smart sensor head included a Star Tracker camera to provide updates to correct the slow drift in the vehicle's IMU. This function was not used in the indoor tests.

The Fig. shows a typical docking experiment. The vehicle floats on a spherical air bearing, which is mounted on a tripod that in turn floats on a cushion of compressed air beneath the tripod's footpad disks. This configuration allows near-frictionless translational motion to any position on the table and over a large range of vehicle angular orientations (in roll, pitch, and yaw). The experiment was set up on a 3- by 8-m table with a docking target (ETV-150) at the far end and the docking vehicle (ETV-250) at the near end, where it was initially secured to a mooring station. For the autonomous docking task, the test vehicle executed a series of maneuvers as marked on the Fig.: (1) autonomously release from a mooring station (note grappler release sphere), (2) slew to acquire the target with the high-resolution camera, (3) estimate target range and bearing from the stereo pair, (4) advance to about 2 m from the docking surface, (5) perform correction maneuvers to align itself with the surface normal of the ETV-150 target for the final approach and advance to the target using precision laser-range information, and (6) activate the grappler to secure the docking sphere.

In actual space operations, the docking vehicle could either (1) first circle the target to reconstruct a 3-D object surface map from the stereo imagery so as to identify the location of the object to be grappled, or (2) operate in a telerobotic mode with a link to a ground-control station. The next step in the development of this vehicle would be to further enhance its dynamic capability by using a H_2O_2-pumped propulsion system to increase the capabilities and range of vehicle maneuvers.

A patent application for the concept has been submitted.

Back to main TOC

Surveying the Outer Solar System with Robotic Telescopes

S. Marshall, K. Cook, R. Porrata

00-ERI-007

The outer region of the solar system is perhaps the least understood of the known regions. Since as early as 1943, the region beyond the orbit of Neptune has been suspected of containing planetary material. Further work by Kuiper and others led to the suggestion of the existence of a disk-like population of remnant trans-Neptunium objects (TNOs). This region has been dubbed the "Kuiper Belt," with its constituents called KBOs (Kuiper Belt Objects). Some consider the "planet" Pluto to be the largest known KBO. There is substantial scientific interest in the history and properties of this population.

Searches for objects beyond Neptune are difficult because KBOs are small and the brightness of reflected sunlight declines rapidly. Photographic surveys covering large areas of sky near the ecliptic have been performed, but with only one detection: Pluto, and later its moon, Charon were the only KBOs known at the beginning of the 1990s. Since then, surveys using more sensitive charge-coupled devices (CCDs) have enabled detections of much fainter objects, but only in restricted areas. The result is that the distribution of known KBOs includes objects that are both bright and sufficiently numerous.

In this project, we are carrying out two novel surveys for KBOs. These surveys provide data at both the bright (large) and faint (small) ends of the range of objects, where data are sparse. Our work extends LLNL's competency in advanced sensors, system integration, and the processing of large data sets.

We are exploiting two robotic-telescope systems: (1) the Taiwanese American Occultation Survey (TAOS) system, which will probe for objects as small as 2 km using the occultation technique that we have pioneered; and (2) the wide-field Massive Compact Halo Objects (MACHO) Telescope System, which will probe for larger objects. The MACHO Telescope is available for this purpose during calendar years 2000 to 2002. With it, we can search much larger areas than is possible with existing CCD-based surveys. Both systems take advantage of LLNL's resources to obtain data that other groups are not currently capable of accessing. The occultation discoveries or limits will be at much fainter magnitudes than any other survey; the bright-object search has the potential of discovering a "planet X."

The large-object KBO survey on the MACHO Telescope started taking data in January 2000, as work began to automate the telescope. During FY2000, we installed closed-cycle CCD cooling and weather and cloud sensors (for automatic dome control). We also implemented software that automatically focuses the telescope. The telescope has operated automatically since late May 2000.

The TAOS project is preparing for installation of four telescopes at Lulin Mountain in Taiwan. Substantial improvements to the infrastructure needed to support the project have been completed at the site. The first TAOS telescope arrived at LLNL in February 2000, was shipped to Taiwan, and installed at Lulin. The second TAOS telescope is at LLNL; delivery of the third is expected in early FY2001. We plan to use telescopes two and three for testing and further software development during early FY2001.

Appendix

Appendix

Publications

These documents reporting LDRD research in FY2000 were published under the auspices of the Department of Energy and denote LLNL publication numbers in compliance with contract W-7405-Eng-48.

Alcock, C. et al., "Binary Microlensing Events from the MACHO Project," *Ap J*, **541**, 270A, UCRL-JC-143118, 99-ERD-041.

Alcock, C. et al., "The MACHO project 9 million star color-magnitude diagram of the Large Magellanic Cloud," *AJ,* **119,** 2194A, UCRL-JC-137591, 99-ERD-041.

Alcock, C. et al., Searching for periodicities in the MACHO light curve of LMC X-2," *MNRAS*, **316**, 729A, UCRL-JC-143117, 99-ERD-041.

Alcock, C. et al., The MACHO project sample of galactic bulge high-amplitude and delta; Scuti stars: pulsation behavior and stellar properties," *Ap J*, **536**, 798A, UCRL-JC-136490, 99-ERD-041.

Aufderheide III, M. B., D. Slone, A. Schach von Wittenau, "HADES, a radiographic simulation code," *Review of Progress in Quantitative Nondestructive Evaluation,* D. O. Thompson and D. E. Chimenti, Eds. (Plenum Press, New York, NY, 2001), UCRL-JC-138605, 00-ERD-015.

Barsky, D. et al., "New insights into the structure of abasic DNA from molecular dynamics simulations," *Nucleic Acids Res.*, **28**, 2613, UCRL-JC-136464, 98-SI-009.

Barsky, D., and M. E. Colvin, "Guanine-cytosine base pairs in parallel-stranded DNA: an ab initio study of the keto-amino wobble pair versus the enol-imino minor tautomer pair," *J. Phys. Chem. A*, **104**, 8570, UCRL-JC-134817, 98-SI-008.

Bastea, M. A., A. Mitchell, W. Nellis, " Metallic and non-metallic states of matter under high dynamic compression: oxygen and lithium," UCRL-JC-139248 Abs, 00-LW-037.

Becker, R., "The gravitation lens candidate FBQ 1633 + 3134," *Astrophys. J.*, in press, UCRL-JC-140144, 98-ERI-005.

Bedrossian, P., A. Schwartz, M. Kumar, W. King, "Observation of localized corrosion of Ni-based alloys using coupled orientation imaging microscopy and AFM," *MRS Proc.*, **586**, 81, UCRL-JC-135219, 98-ERD-080.

Beiersdorfer, P. et al., "Current research with highly charged ions in EBIT and SuperEBIT," *Phys. Scripta*, in press, UCRL-JC-139075, 00-ERD-037.

Beiersdorfer, P. et al., "Hyperfine structure of hydrogen-like thallium isotopes," submitted to *Phys. Rev. A*, UCRL-JC-142136, 00-LW-090.

Beiersdorfer, P. et al., "X-ray emission following low-energy charge exchange collision of highly charged ions," *Phys. Rev. Lett.*, in press, UCRL-JC-140506, 00-ERD-037.

Bell, J., P. Duffy, C. Covey, L. Sloan, "Analysis of temperature variability in sixteen climate model simulations," *Geophys. Res. Lett.,* **27**, 261, UCRL-JC-134206, 99-SI-001.

Benedict, L., "Dielectric function for a model of laser-excited GaAs," *Phys. Rev. B*, **63**, 075202, UCRL-JC-140607, 98-ERD-052.

Bernstein, L. A. et al., "Studying the role of nuclear structure effects in neutron-induced reactions using GEANIE at LANSCE," *Proc. Nuclear Structure 2000 Conf.*, UCRL-JC-140578, 00-ERD-035.

Berryman, J., L. Barcka, and G. Papanicolauou, "Time reversal acoustics for multiple targets," submitted to *JASA*, UCRL-JC-140465, 99-LW-045.

Bertram, M., M. A. Duchaineau, B. Hamann, K. I. Joy, "Bicubic subdivision-surface wavelets for large-scale isosurface representation and visualization," *IEEE Vis 2000*, UCRL-JC-136993, 99-ERI-009.

Bertram, M., M. A. Duchaineau, B. Hamann, K. I. Joy, "Wavelets on planar tesselations," *Imaging Science System and Technology*, Las Vegas, NV, 2000, UCRL-JC-137755, 99-ERI-009.

Bonnel, K. et al., "Constructing material interfaces from data sets with volume-fraction information," *IEEE Vis 2000,* UCRL-JC-138292, 99-ERI-009.

Bowers, M. W., J. Cooke, J. Benterou, "Speckle reduction for lidar using optical phase conjugation," *Proc. Conf. on Lasers and Electro-optics*, San Francisco, May 2000, p. 222, UCRL-JC-136326, 99-ERD-024.

Brezina, M. et al., "Algebraic multigrid based on element interpolation (AMGe)," *SIAM J. of Sci. Comp.*, in press, UCRL-JC-131752, 00-ERD-018.

Brown, P. N. and C. S. Woodward, "Preconditioning strategies for fully implicit radiation diffusion with material-energy transfer," *SIAM J. of Sci. Comp.*, in press, UCRL-JC-139087, 98-ERD-022.

Brown, P. N., B. Chang, U. Hanebutte, "Spherical harmonic solutions of the Boltzmann transport equation via discrete ordinates," *Prog. in Nucl. Eng.*, in press, UCRL-JC-132006, 98-ERD-022.

Brown, P. N., B. Chang, U. Hanebutte, C. Woodward, "The quest for a high-performance Boltzmann transport solver," *Proc. 6th Intl. Conf. on App. of High-Performance Comp. in Eng.*, UCRL-JC-135151, 98-ERD-022.

Bulatov, V. V. et al., "Parameter-free modeling of dislocation motion: the case of silicon," *Phil. Mag. A*, in press, UCRL-JC-140494, 00-SI-011.

Bulatov, V. V., "Connecting the micro to the mesoscale: review and specific examples," *Multiscale Phenomena in Plasticity*, J. Lepinoix et al., Eds., UCRL-JC-135534, 00-SI-011.

Burnham, K. et al., "Effect of vacuum on the occurrence of UV-induced surface photoluminescences, transmission loss, and catastrophic surface damage," *SPIE*, **4134**, 243–252, UCRL-JC-137123, 00-ERI-004.

Campbell, E. M., et al., "Automated, high-speed, high-resolution specimen recovery from matrix with femtosecond laser pulse trains," *Proc. Soc. Vertebrate Paleontology*, UCRL-JC-133900, 00-ERD-68.

Candy, J., D. Chambers, "The role of the time reversal processor in acoustic signal processing," *JASA*, **108**, 5, p. 2483, UCRL-VG-141160, 99-LW-045.

Candy, J., D. Chambers, R. Huber, G. Thomas, "Ultrasonic matched-filed imaging for nondestructive evaluation," *Proc. Ocean Imaging Conf.*, May 2000, UCRL-JC-136369, 99-LW-045.

Cantu-Paz, E. and C. Kamath, "Using evolutionary algorithms to induce oblique decision trees," *Proc. Genetic and Evolutionary Computation Conf. 2000*, Las Vegas, NV, UCRL-JC-137202, 99-ERI-010.

Cantu-Paz, E., "Genetic algorithms," *Encyclopedia of computers and computer history,* R. Rojas, Ed., in press, UCRL-JC-137552, 99-ERI-010.

Cantu-Paz, E., "On the effects of migration on the fitness distribution of parallel processing," *Proc. Genetic and Evolutionary Computation Conf. 2000*, Las Vegas, NV, UCRL-JC-138729, 99-ERI-010.

Cantu-Paz, E., "Selection intensity in genetic algorithms with general gaps," *Proc. Genetic and Evolutionary Computation Conf. 2000*, Las Vegas, NV, UCRL-JC-137169, 99-ERI-010.

Cantu-Paz, E., *Comparing selection methods of evolutionary algorithms using the distribution of fitness*, UCRL-JC-138582, 99-ERI-010.

Catellani, A., and G. Galli, "Defects at the carbon terminated SiC(001) surface," *Diamond and Related Materials*, in press, UCRL-JC-140788, 98-SI-008.

Catellani, A., G. Galli, P. Rigolli, "Carbon lines on SiC(001) surfaces," *Phys. Rev. B,* in press, UCRL-JC-138359, 98-SI-008.

Caturla, M. J. et al., "Comparative study of radiation damage accumulation in Cu and Fe," *J. Nucl. Mat.*, **276**, 13, UCRL-JC-135256, 98-ERD-090.

Caturla, M. J. et al., "Heavy ion radiation and annealing of lead: atomistic simulations and experimental validation," *J. Nucl. Mat.*, **276**, 186, UCRL-JC-134201, 98-ERD-028.

Cauble, R, R. et al., "Equation of state and material property measurements of hydrogen isotopes at the high pressure, high temperature insulator-metal transition," *Astrophys. J.*, **127**, 281, UCRL-JC-132210, 00-ERD-44.

Cauble, R. R. et al., "Shock-compressing diamond into the metallic phase," UCRL-JC-131400 Abs, 00-ERD-044.

Celliers, P. M. et al., "Optical measurements of strongly shocked water," UCRL-JC-138777, 00-ERD-044.

Celliers, P. M. et al., "Shock transformation of deuterium from molecular to liquid metal, *PRL*, **84**, 5564, UCRL-JC-130339 Rev 1, 00-ERD-044.

Celliers, P. M. et al., "VISAR for measuring EOS and shock propagation in liquid deuterium and other dielectrics," UCRL-JC-138446 Abs, 00-ERD-044.

Chambers, D., and J. Gautesen, "Time reversal for a single spherical scatter," submitted to *JASA*, UCRL-JC-141165-Rev-1, 99-LW-045

Chau, R., A. C. Mitchell, R. W. Minich, W. J. Nellis, "Electrical conductivity of water compressed dynamically to pressures of 70–180 GPa (0.7-18. Mbar)," *J. Chem. Phys.*, UCRL-JC-135379, 00-ERD-033.

Cherepy, N., R. Krueger, J. F. Cooper, "Direct electrochemical conversion of carbon anode fuels in molten salt media," *Electrochemical Soc. 198th Meeting Abs.: Power Sources for the New Millennium*, UCRL-JC-139288, 00-ERD-059.

Chin, H.-N. et al., "A study on the retrieval of continental low-level stratiform clouds: impact of sub-adiabatic character on the macroscopic microphysical properties and radiation budgets," *Monthly Weather Rev.*, **128**, 2511–2527, UCRL-JC-133190, 00-ERD-055.

Chuang, C. C. and K. E. Grant, *Parameterizations of the optical properties of dust and sea salt particles for use in global climate models*, UCRL-JC-137183, 00-ERD-055.

Chuang, C. C. et al., "Effects of anthropogenic aerosols on cloud susceptibility: a sensitivity study of radiative forcing to aerosol characteristics and global concentration," *Geophys. Res.*, in press, UCRL-JC-139097, 00-ERD-055.

Chuang, C. C. et al., *Toward a new era of research in aerosol/cloud/climate interactions at LLNL*, UCRL-ID-140570, 00-ERD-055.

Chuang, C. C., J. E. Penner, Y. Zhang, *Simulations of aerosol indirect effect for IPCC emissions scenarios*, UCRL-JC-135993, 00-ERD-055.

Chuang, C., J. E. Penner, K. E. Grant, "Global modeling of tropospheric aerosols and their contribution to climate variation," UCRL-JC-135616 Abs, 00-ERD-055.

Chung, B., A. Q. Pham, J. Haslam, R. S. Glass, "The influence of electrode configuration on the performance of electrode-supported fuel cells," *Proc. of the 198th Electrochemical Soc. Meetings*, 2000, UCRL-JC-138491 Rev 1, 98-ERD-031.

Cleary, A. et al., "Robustness and scalability of algebraic multigrid," *SIAM J. of Sci. Comp.*, **21**, 1886–1908, UCRL-JC-130718, 00-ERD-018.

Collins, G. W. et al., "Laser-shock-driven laboratory measurements of the equation of state of hydrogen isotopes in the megabar regime," *High Pressure Res.*, **16**, 281, UCRL-JC-135406, 00-ERD-044.

Cooper, J. F. et al., "Direct carbon conversion: application to the efficient conversion of fossil fuels to electricity," *Electrochemical Soc. 198th Meeting Abs.: Electrochemistry and Global Climate Change*, UCRL-JC-140629, 00-ERD-059.

Cooper, J. F., N. Cherepy, *A high capacity CO_2 battery of low thermal signature adapted from current technologies*, UCRL-ID-140040, 00-ERD-059.

Cooper, J. F., N. Cherepy, M. Steinberg, A. Pasternak, "Direct electrochemical conversion of carbon: systems for efficient conversion of fossil fuels to electricity," *Proc. Fuel Cell 2000 Conf.*, UCRL-JC-138900, 00-ERD-059.

Criss, R. E., M. L. Davisson, J. Kopp, "Geographic separation of nonpoint sources in the Lower Missouri River, 1995–1999," *J. Am. Water Works Assoc.*, **92**, UCRL-JC-140490, 98-ERD-046.

Cunningham, C. T., R. S. Roberts, "An adaptive path planning algorithm for cooperating unmanned air vehicles," *Proc. IEEE Intl. Conf. on Robotics and Automation*, May 2001, Seoul, Korea, UCRL-JC-140415, 00-ERD-023.

Davisson, M. L., G. Woodside, "Organic matter in urban southern California: relevance to potable reuse of storm runoff and treated waste water," *American Geophysical Union Spring Meeting*, UCRL-JC-138382, 98-ERD-046.

De Breuck, C. et al., "A sample of 669 ultra steep spectrum radio sources to find high redshift radio galaxies," *Astron. Astrophys.*, **143**, 303, UCRL-JC-137943, 98-ERI-005.

De Breuck, C., W. van Breugel, H. Rottgering, G. Miley, "VLT spectroscopy of the z = 4.11 radio galaxy TN J1338-1942," *Astrophys. J.*, **352**, L51, UCRL-JC-136302.98-ERI-005

Demos, S. G. and M. R. Koszlowski, "Spectroscopic investigation of SiO_2 surfaces of optical materials for high-power lasers," *SPIE*, **3933**, 316–320, UCRL-JC-136889, 00-ERI-004.

Demos, S. G. et al., "Surface defect generation in optical materials under high-fluence laser irradiation in vacuum," *Elec. Lett.*, **36**, 566, UCRL-JC-136671, 00-ERI-004.

deVries, W. H. et al., "HST/NICMOS observations of the host galaxies of powerful radio sources: does size matter?," *Astrophys. J.*, in press, UCRL-JC-139328, 98-ERI-005.

Diaz de la Rubia, T. et al., "Plastic flow localization in irradiated materials: a multiscale modeling approach," *Nature*, **406**, 871, UCRL-JC-137520 Rev 1, 98-ERD-090.

Dignon, J. C. et al., "Three-dimensional model for combined tropospheric and stratospheric sulfur cycle studies," UCRL-JC-134867 Abs, 00-ERD-055.

Dinh, L. et al., "GaAs nanostructures and films deposited by a Cu-vapor laser," *Appl. Phys. Lett.*, **75**, 2208, UCRL-JC-134528, 00-LW-040.

Ditmire, T. et al., "Nuclear fusion in gases of deuterium clusters heated with a femtosecond laser," *Phys. Plasmas*, **7**, 1993, UCRL-JC-136978, 00-LW-021.

Dorr, M. and X. Garaizar, "Simulation of laser plasma filamentation with adaptive mesh refinement," UCRL-JC-138329 Abs, 00-ERD-016.

Dorr, M. and X. Garaizar, "Simulation of laser plasma filamentation using adaptive mesh refinement," UCRL-JC-138330 Abs, 00-ERD-016.

Dorr, M., and X. Garaizer, "Adaptive laser plasma simulation (ALPS)," UCRL-TB-137290, 00-ERD-016.

Dorr, M., and X. Garaizer, "Laser–plasma AMR simulations," UCRL-JC-137547 Abs, 00-ERD-016.

Dowla, F., J. Brase, S. Olivier, C. Thompson, "Performance of a high-resolution wavefront control system using a liquid crystal spatial light modulator," *Proc. SPIE*, **4124**, UCRL-JC-139830, 98-ERD-061.

Duffy, P., J. Bell, C. Covey, L. Sloan, "Effect of flux adjustments on temperature variability in coupled models," *Geophys. Res. Lett.*, **27**, 763, UCRL-JC-134153, 99-SI-001.

Duffy, P., M. Eby, A. Weaver, "Climate model simulations of effects of increased atmospheric CO_2 and loss of sea ice on ocean salinity and tracer uptake," *J. of Climate*, in press, UCRL-JC-134083, 99-SI-001.

Ekwurzel, B. et al., "Nonpoint source MTBE movement through the environment: ultra low level (ppt) measurements in California," *Exploring the Environmental Issues of Mobile, Recalcitrant Compounds in Gasoline*, UCRL-JC-139723, 98-ERD-046.

Elmer, J., J. Klingmann, K. van Bibber, "Diffusion bonding and brazing of high-purity copper for linear collider accelerator structures," *Phys. Rev. Special Topic—Accelerators and Beams*, UCRL-JC-135547, 00-SI-005.

Fattebert, J.-L. and F. Gygi, "Continuous solvation model for ab initio molecular dynamics simulations," UCRL-JC-140605 Abs, 00-ERD-007.

Feit, M. D., "Modeling laser-induced damage in NIF UV optics," UCRL-TB-136126-00-09, 00ERD-066.

Feit, M. D., A. M. Rubenchik, M. Runkel, *Analysis of bulk DKDP damage distribution, obscuration, and pulse-length dependence*, UCRL-JC-139649, 00-ERD-066.

Fodor, I., "The search for bent-double galaxies: latest results," *Second Workshop on Mining Scientific Datasets*, Minneapolis, MN, 2000, UCRL-JC-139515, 99-ERI-010.

Fodor, I., E. Cantu-Paz, C. Kamath, N. Tang, "Finding bent-double radio galaxies: a case study in data mining," *Interface: Comp. Sci. and Stat.*, **33**, UCRL-JC-138073, 99-ERI-010.

Fowler, T. K. et al., "Pulsed spheromak fusion reactors," *Comm. Mod. Phys.*, **1(3)c**, 83, UCRL-JC-132109, 00-SI-008.

Fox, G. A., T. F. Baumann, A. L Vance, "Dendritic methodology applied to the prediction, design, and synthesis of sol gel materials," *ACM Symposium*, in press, UCRL-JC-133875, 99-ERD-004.

Galli, G. et al., "Physical properties of SiC(001) surfaces," *Appl. Surf. Sci.*, in press, UCRL-JC-136186, 98-SI-008.

Galli, G., "Large-scale electronic structure calculations using linear scaling methods," *Phys. Stat. Sol.*, **277**, UCRL-JC-136268, 98-SI-008.

Galli, G., R. Q. Hood, A. U. Hazi, F. Gygi, "Ab-initio simulations of compressed liquid deuterium," *Phys. Rev. B*, **61**, 909, UCRL-JC-135359, 98-SI-008 and 00-ERD-031.

Garrett, P. E. et al., " ^{92}Mo(n,xnypza) reactions for neutron energies up to 250 MeV," *Phys. Rev. C*, **62**, 054608, UCRL-JC-134769, 00-ERD-035.

Garrett, P. E. et al., "States in ^{92}Mo observed with the (n,n'γ) reaction with spallation neutrons, *Phys. Rev. C*, **62**, 014307, UCRL-JC-136986, 00-ERD-035.

Genin, F. et al., "Rear-surface laser damage on 355-nm silica optics due to Fresnel diffraction at front surface," *Appl. Opt.*, **39**, 3654, UCRL-JC-133839, 00-ERD-066.

Glassley, W. E., "Elemental composition of concentrated brines in subduction zones and deep continental crust," *Precambrian Research*, in press, UCRL-JC-136331, 98-SI-004.

Grant, P. G., G. Bench, J. Lewis, K. Divine, "Uptake of soluble manganese chloride via nose-only inhalation through the olfactory bulb," *Toxicologist*, **54**, 404, UCRL-MI-139154, 98-ERD-004.

Gregg, M. D. et al., "A close-separation double quasar lensed by a gas-rich galaxy," *Astron. J.*, **115**, 2535, UCRL-JC-138093, 98-ERI-005.

Gregg, M. D. et al., "A FIRST classic FR-II broad absorption line quasar," *Astrophys. J.*, in press, UCRL-JC-138357, 98-ERI-005.

Guilderson, T. et al., "Southwest subtropical Pacific surface water radiocarbon in a high-resolution coral record," *Radiocarbon*, **42**, 249–256, UCRL-JC-136185, 98-ERI-002.

Guilderson, T., K. Caldeira, P. Duffy, "Radiocarbon as a diagnostic tracer in ocean and carbon cycle modeling," *Global Biogeochemical Cycles*, **14**, 887–902, UCRL-JC-134783, 98-ERI-002.

Haerle, R., G. Galli, A. Baldereschi, "Structural models of amorphous carbon surfaces," *Appl. Phys. Lett.*, **75**, 1718, UCRL-JC-132667, 98-SI-008.

Haerle, R., G. Galli, A. Baldereschi, "Structural models of amorphous carbon and its surface by tight-binding molecular dynamics, *J. Non-Crystalline Solids,* **740**, 266–269, UCRL-JC-136231, 98-SI-008.

Hakem, N., P. G. Allen, E. R. Sylwester, *Effect of EDTA on plutonium migration*, UCRL-JC-139652, 98-ERD-094.

Hakem, N., P. G. Allen, E. R. Sylwester, *Sorption and diffusion studies of Pu (IV) and Pu (IV)-EDTA onto and through Hanford soil,* UCRL-JC-135799, 98-ERD-094.

Harrison, T.M. et al., "A record of superposed tertiary convergence in southeastern Tibet," *J. Geophys. Res.*, **105**, 19211–19230, UCRL-JC-139079, 00-ERI-009.

Hartemann, F. V. et al., "High-intensity scattering processes of relativistic electrons in vacuum and their relevance to high-energy astrophysics," *Astrophys. J. Suppl.*, **127**, 347, UCRL-JC-133349, 99-ERI-008.

Haslam, J., et al., " Processings and properties of the anode in anode-supported SOFCs," *Am. Chem. Soc. Annual Meeting 2000*, UCRL-JC-136380 Abs, 98-ERD-031.

Hatch, F. T., F. C. Lightstone, M. E. Colvin, "Quantitative structure-activity relationship of flavonoids for inhibition of heterocyclic amine mutagenicity," *Envir. & Mol. Mutagenesis*, **35**, 279, UCRL-JC-134708, 98-SI-008.

Hatchet, S., et al., "Electron, photon, and ion beams from the relativistic interaction of PetaWatt laser pulses with solid targets," *Phys. Plasmas*, **7**, 2076, UCRL-JC-135029, 99-ERD-063.

Hayes, S. et al., "Development of optically-polarized NMR with applications in materials science and biology," *Experimental NMR Conf. Abs.*, UCRL-JC-137321 Abs, 00-LW-040.

Heeter, R. et al., X-ray photoionized plasmas in the laboratory," *Atomic Data Needs for X-Ray Astronomy*, NASA209968, p. 135, UCRL-JC-137493, 99-ERD-044.

Heeter, R. et al., X-ray spectroscopy of the astrophysically relevant photoionized iron plasmas at *Z*," *Proc. 12th APS Topical Conf. on Atomic Processes in Plasmas*, **547**, 94, UCRL-JC-137660, 99-ERD-044.

Henshaw, W., *Mappings for overture, a description of the mapping class and documentation for many useful mappings*, UCRL-MA-132239, 00-ERD-017.

Henshaw, W., *Ogen, an overlapping grid generator for Overture*, UCRL-MA-132237, 00-ERD-017.

Henshaw, W., *The Overture Hyperbolic Grid Generator: User Guide, Version 1.0*, UCRL-MA-134240, 00-ERD-017.

Henson, V. and P. Vassilevski, "Element-free AMGe: general algorithms for computing, *SIAM J. of Sci. Comp.*, in press, UCRL-JC-139098, 00-ERD-018.

Hill, D. N., "Overview of recent SSPX experiments," UCRL-JC-139567 Abs, 00-SI-008.

Hill, D. N., "Overview of spheromak formation experiments on SSPX," *Innovative Confinement Concepts Conf. 2000*, UCRL-JC-137256 Abs, 00-SI-008.

Holcomb, C. T. et al., "Internal field measurements and magnetic reconstruction in SSPX," *Innovative Confinement Concepts Conf. 2000*, UCRL-JC-137258 Abs, 00-SI-008.

Holcomb, C. T., et al., "Non-perturbing field profile measurements of a sustained spheromak," *Rev. Sci. Instr.*, **72**, in press, UCRL-JC-139284, 00-SI-008.

Hooper, E. B., R. H. Cohen, D. D. Ryutov, "Theory of edge plasma in a spheromak," *J. Nucl. Mat.*, **278**, 104, UCRL-JC-130767, 00-SI-008.

Hrubesh, L. W. et al., *Chemical etch effects on laser-induced surface damage growth in fused silica*, UCRL-JC-139666, 98-ERD-063.

Hsiung, L. M. and D. H. Lassila, " Initial dislocation structure and dynamic dislocation multiplication in Mo single crystals," *Advances in Computational Engineering & Sciences*, S. N. Alturi, Ed., UCRL-JC-138788, 00-SI-011.

Hsiung, L. M. and T. G. Nieh, "Creep deformation of lamellar TiAl alloys controlled by the viscous glide of interfacial dislocations," *Intermetallics*, **7**, 821, UCRL-JC-130516, 00-ERD-072.

Hsiung, L. M. and T. G Nieh, "Effect of extrusion temperatures on the microstructural development of powder metallurgy TiAl alloys," *Proc. 9th Intl. Symp. Processing and Fabrication of Advanced Materials*, in press, UCRL-JC-137615, 00-ERD-072.

Hsiung, L. M., B. W. Choi, T. G. Nieh, " Interfacial dislocations and deformation twinning in full lamellar TiAl," *Mat. Sci. & Eng.* special issue for *Proc. 5th Intl. Conf. Structural and Functional Intermetallics*, in press, UCRL-JC-137647, 00-ERD-072.

Huser, T., M. Yan, L. J. Rothberg, "Single chain spectroscopy of conformational dependence of conjugated polymer photophysics," *Proc. Natl. Acad. Sci.*, **97**, 11187, UCRL-JC-138711, 00-LW-058.

Hyde, E., *The validity of paraxial approximation in the simulation of laser plasmas interactions,* UCRL-JC-139805, 00-ERD-016.

Ishikawa, M. Y., et al., "CASFLU, composition analysis by scanned femtosecond laser ultraprobing," (video), UCRL-MI-137705, 00-ERD-068.

Jones, J. and P. Vassilevski, "AMGe based on element agglomeration," *SIAM J. of Sci. Comp.*, in press, UCRL-JC-135441, 00-ERD-018.

Joy, K. I. and M. Duchaineau, "Boundary determination for trivariate solids," P*acific Graphics Conference*, Seoul, Korea, 1999, UCRL-JC-134275, 99-ERI-009.

Kamath, C. and E. Cantu-Paz , "On the design of a parallel object-oriented data mining toolkit," *KDD-2000 Workshop on Distributed and Parallel Knowledge Discovery,* Boston, MA, 2000, UCRL-JC-138973, 99-ERI-010.

Kamath, C., "On oblique decision trees and evolutionary algorithms," *Second Workshop on Mining Scientific Datasets*, Minneapolis, MN, 2000, UCRL-JC-139515, 99-ERI-010.

Kamath, C., "Sapphire: An Object-oriented Framework for Mining Science Data, "*First Workshop on Mining Scientific Datasets*, Minneapolis, MN, 1999, UCRL-JC-135563, 99-ERI-010.

Kamath, C., "SAPPHIRE: Large-Scale Data Mining and Pattern Recognition," UCRL-TB-132076, 99-ERI-010.

Kamath, C. and R. Musick, "Scalable data mining through fine-grained parallelism: the present and the future," *Advances in Distributed and Parallel Knowledge Discovery*, H. Kargupta and P. Chan, Eds., (AAAI Press, Menlo Park, CA) pp. 29–77, UCRL-JC-133694, 99-ERI-010.

Kamath, C., C. Baldwin, I. Fodor, I. N. Tang, "On the design and implementation of a parallel, object-oriented, image-processing tool," *SPIE Annual Meeting*, San Diego, CA, 2000, UCRL-JC-138953, 99-ERI-010.

Kamath, C., E. Cantu-Paz, N. Tang, "Sapphire: a high-performance object-oriented framework for mining scientific datasets," *Third Inl. Symp. for Computing in Object-Oriented Parallel Environments*, San Francisco, CA, 1999, UCRL-JC-135586, 99-ERI-010.

Kargupta, H., C. Kamath, P. Chan, "Distributed and parallel data mining: emergence, growth, and future directions," *Advances in Distributed and Parallel Knowledge Discovery*, H. Kargupta and P. Chan, Eds., (AAAI Press, Menlo Park, CA), pp. 409–417, UCRL-138954, 99-ERI-010.

Kent, A. J. R. et al., "The temperature of formation of carbonate in martian meteorite ALH84001: constraints from cation diffusion," *Geochimica et Cosmochimica Acta*, **64**, in press, UCRL-JC-133070 Rev 1, 98-ERD-042.

Kim, B.-M. et al., "Collagen structure and nonlinear susceptibility: effects of heat, glycation, and enzymatic cleavage on second harmonic signal intensity," *Lasers in Surgery & Medicine*, **27**, 329–335, UCRL-JC-136350, 00-LW-063.

Kim, B.-M. et al., "Confocal imaging of biological tissues using second harmonic generation," *SPIE Proceedings*, **3914**, 435–440, UCRL-JC-138060, 00-LW-063.

Kim, B.-M., J. Eichler, L. B. DaSilva, "Frequency doubling of ultrashort laser pulses in biological tissues," *Appl. Optics*, **38**, 7145–7150, UCRL-JC-133643, 00-LW-063.

Kim, B.-M., M. D. Feit, A. M. Rubenchik, L. B. DaSilva, "Medical applications of ultrashort pulse lasers," *CLEO/PR 2000*, 43–44, UCRL-JC-133470, 00-LW-063.

King, W., J. Stölken, M. Kumar, A. Schwartz, "Strategies for analyzing EBSD datasets," *Electron Backscatter Diffraction in Materials Science*, A.J. Schwartz, M. Kumar, and B. L. Adams, Eds., (Kluwer Academic/Plenum, New York, NY, 2000). p. 153, UCRL-JC-139150, 98-ERD-080.

Kishimoto, M. et al., "UV spectropolarimetry of narrow-line radio galaxies," *Astrophys. J.*, in press, UCRL-JC-138907, 98-ERI-005.

Koslowski, M. R., S. G. Demos, J. Wong, Z. Wu, "Properties of modified silica detected within laser-induced damage sites," *SPIE*, **4102**, 106–111, UCRL-JC-136922, 00-ERI-004.

Krishnan, V. V. and M. Cosman, "A novel relaxation compensated method to measure amide proton exchange rates in biomolecules based on decorrelation of heteronuclear two-spin order," *Magnetic Resonance*, **38**, 789–794, UCRL-JC-13575, 99-LW-031.

Krishnan, V. V., K. H. Thornton, M. Cosman, "An improved experimental scheme to measure self-diffusion coefficients of biomolecules with an advantageous use of radiation damping, *Chem. Phys. Lett.*, **302**, 317–323, UCRL-JC-132333, 99-LW-031.

Kumar, M., A. Schwartz, W. King, "Correlating observations of deformation microstructures by TEM and automated EBSD techniques," *Mat. Sci. Eng. A*, UCRL-JC-137073, 98-ERD-080.

Kumar, M., A. Schwartz, W. King, "Modifications to the microstructural topology in fcc materials through thermomechanical processing," *Acta Mat.*, **48**, 2081, UCRL-JC-135761, 98-ERD-080.

Larson, M. C. et al., "Multiwavelength VCSEL transmitter for WDM parallel optical fiber interconnects," *IEEE LEOS 12th Annual Meeting*, **2**, 764–5, UCRL-JC-134719 Abs, 98-ERD-057.

Larson, M. C. et al., *Low-threshold oxide-confined GaInNAs long-wavelength vertical cavity lasers*, UCRL-JC-139014, 00-ERD-040.

Ledebuhr, A. and L. Ng, *Micro-satellite ground test vehicles for proximity and docking operations development*, UCRL-JC-141110, 00-ERD-071.

Lee, H. W. H. et al., "The origin and nature of stable red to ultraviolet light emission from silicon nanocrystals," *Crit. Rev. Opt. Sci. & Tech.*, **77**, 147, UCRL-JC-136328, 00-LW-010.

Liebisch, P. et al., "L-shell X-ray signatures of charge transfer reactions involving cold highly charged ions," *Phys. Rev. A*, in press, UCRL-JC-138938, 00-ERD-037.

Lightstone, F. C. et al., "Identification of novel small molecule ligands that bind to tetanus toxin," *Chem Res. in Toxicology*, **13**, 356, UCRL-JC-137541, 98-SI-008.

Lloyd, J. et al., "An adaptive optics survey for companions to stars with extra-solar planets," *Planetary Systems in the Universe*, A. J. Penny, P. Artymowicz, A.-M. Lagrange, and S. S. Russel, Eds., (Astronomical Soc. of the Pacific Conf Ser. A, in press), UCRL-JC-141491, 98-ERD-036.

Mackinnon, A. J. et al., "Effect of plasma scalelength on MeV proton production in short-pulse, high-intensity laser–plasma interactions," UCRL-JC-139604 Abs, 99-ERD-049.

Mackinnon, A. J. et al., "Effect of plasma scalelength on multi MeV proton production by intense laser pulses," *Phys. Rev. Lett.*, UCRL-JC-135008 Abs, 99-ERD-049.

Martz, H. E. Jr., et al., "HADES-CCG, a new tomographic reconstruction tool," *QNDE*, UCRL-JC-138604, 99-ERD-015.

Martz, Jr., H. E., M.B. Aufderheide III, D. Slone, A. Schach von Wittenau, "HADES, a new tomographic reconstruction tool," *Review of Progress in Quantitative Nondestructive Evaluation,* D. O. Thompson and D. E. Chimenti, Eds. (Plenum Press, New York, NY, 2001), UCRL-JC-138604, 00-ERD-015.

Max, N., P. Williams, C. Silva, "Volume rendering for curvilinear and unstructured grids by hardware-assisted polyhedron projection," *Intl. J. Image Sys. & Tech.*, in press, UCRL-JC-134175, 99-ERI-009.

Max, N., Weights for computing vertex normals from facet normals," *J. of Graphics Tools*, in press, UCRL-JC-134069, 99-ERI-009.

McAninch, J. E. et al., "Plutonium measurements by accelerator mass spectrometry at LLNL," UCRL-JC-134179 Abs, 98-ERD-100.

McAninch, J.E. and T. Hamilton, "Accelerator mass spectrometry measurements and actinide concentrations and isotope ratio," *AIP Meeting*, UCRL-JC-137476 Abs, 98-ERD-100.

McLean, H. S., et al., Particle control experiments in SSPX," *Innovative Confinement Concepts Conference 2000*, UCRL-JC-137280 Abs, 00-SI-008.

McLean, H. S., et. al., "Plasma diagnostics for the Sustained Spheromak Physics Experiment," *Rev. Sci. Instr.*, **72**, in press, UCRL-JC-129686, 00-SI-008.

Miller, E., T. A. Land, P. Whitman, *Effects of thermal annealing on the chemical composition of potassium dihydrogen phosphate (KDP) surfaces*, UCRL-ID-142259, 00-ERD-065.

Mirin, A. A. et al., "Very high resolution simulation of compressible turbulence on the IBM-SP system," *Supercomputing 99*, Portland, OR, 1999, UCRL-JC-134237, 99-ERI-009.

Morse, J. D. and A. F. Jankowski, "A novel thin-film solid oxide fuel cell for microscale energy conversion," *ASME Proc.*, UCRL-JC-133146, 98-ERD-091.

Morse, J. D. and A. F. Jankowski, "Novel proton exchange membrane thin-film fuel cell for microscale energy conversion," *JVST-A*, **18**, 1, UCRL-JC-134243, 98-ERD-091

Muscheler, R., J. Beer, G. Wagner, R. Finkel, "Changes in deep-water formation during the Younger Dryas cold period inferred from a comparison of ^{10}Be and ^{14}C records," *Nature*, **408**, 567–570, UCRL-JC-141241, 98-ERI-013.

Nelson, A. J. et al., "X-ray absoption analysis of KDP optics," submitted to *J. Electron Spectrosc. Related Phenomena*, UCRL-JC-138950, 00-ERD-065.

Nelson, C. and P. P. Eggleton, *A complete survey of case binary evolution with comparison to observed Algol-type systems*, UCRL-JC-140453, 00-SI-004.

Nguyen, L. H., D. Barsky, J. P. Erzberger, D. M. Wilson III, "Mapping the protein-DNA interface and the metal binding site of the major human apurinic/apyriminic endonuclease," *J. Mol. Bio.*, **298**, 447, UCRL-JC-137236, 98-SI-008.

Norton, M. A. et al., "Growth of laser-initiated damage in fused silica at 351 nm," UCRL-JC-139624, 00-ERD-066.

Ognessian, Y. T. et al., "Decay properties of ^{257}No, ^{261}Rf, and ^{262}Rf," *Phys. Rev. C*, **62**, 0643XX, UCRL-JC-139311, 98-ERD-050.

Ognessian, Y. T. et al., "Making new elements," *Scientific American*, **282**, 45, UCRL-JC-134651, 98-ERD-050.

Ognessian, Y. T. et al., "Observation of the decay of 292/116," *Phys. Rev. C*, **63**, 0113XX, UCRL-JC-140223, 98-ERD-050.

Ognessian, Y. T. et al., "The synthesis of superheavy nuclei in the ^{48}Ca + ^{244}Pu reaction: 288/114," *Phys. Rev. C*, **62**, 041604, UCRL-JC-137189, 98-ERD-050.

Ognibene, T. J. et al., "Low Charge State AMS for High Throughput ^{14}C Quantification," *Proc. Symp. on Synthesis & Use of Isotopically Labeled Compounds*, in press, UCRL-JC-139326, 98-ERI-012.

Ognibene, T. J. et al., *LLNL AMS System for Biochemical ^{14}C Measurements*, UCRL-JC-139562, 98-ERI-012.

Ognibene, T.J., et al., "Ion-optics calculations of the LLNL compact AMS system for biochemical ^{14}C measurements" *Nucl. Inst. & Meth. B,* in press, UCRL-JC-134095, 98-ERI-012.

Park, H.-S., et al., "Super-LOTIS early time optical counterpart measurements," *AIP Conf. Proc.*, **526**, 736, UCRL-JC-141127, 00-ERD-027.

Patel, R. R. et al., "Multi-mode fiber coarse WDM grating router using broadband add/drop filters for wavelength re-use," *IEEE LEOS 12th Annual Meeting*, **2**, 826–7, UCRL-JC-134637, 98-ERd-0057.

Patience, J. et al., "Stellar companions to stars with planets," submitted to *Astrophys. J.*, UCRL-JC-142747, 98-ERD-036.

Perkins, L. J. et al., "The investigation of high-intensity-laser-driven micro neutron sources for fusion materials research at high fluence," *Nucl. Fusion*, **40**, 11, UCRL-JC-132334, 99-ERD-049.

Petersson, W., *A note on volume grids, hole-cutting and viscous interpolation for overlapping grids*, UCRL-JC-13912, 00-ERD-017.

Pocha, M. D. et al., "Glass, plastic & semiconductors: packaging techniques for miniature optoelectronic components," *Proc. of SPIE,* **3912**, 130–140, UCRL-JC-134864, 98-ERD-057.

Porter, F. S. et al., "Laboratory astrophysics using a spare XRS microcalorimeter," *Proc. Intl. Symp. Opt. Sci. & Tech.*, 2000, in press, UCRL-JC-138656, 00-ERD-037.

Puso, M. A., "An energy and momentum conserving algorithm for rigid body dynamics," *Int. J. for Numerical Methods*, in press, UCRL-JC-142642, 99-ERD-018.

Remington, B. A. et al., "A review of astrophysics experiments on intense lasers," *Phys. Plasmas*, **7**, 1641, UCRL-JC-134961, 00-ERD-039.

Roberts, M. L et al., "A compact tritium AMS system," *Nuc. Instr. & Methods B*, **172**, 262–67, UCRL-JC-135902, 00-ERI-001.

Robey, H. et al., "An experimental testbed for the study of hydrodynamic issues in supernovae," *Phys. Plasmas*, in press, UCRL-JC-139454, 00-ERD-039.

Rubenchik, A. M., M. D. Feit, L. W. Hrubesh, J. Wong, *Scaling relations for laser damage-initiation craters,* UCRL-JC-139647, 00-ERD-066.

Runkel, M. A. et al., "Results of pulse-scaling experiments on rapid-growth DKDP triplers using the Optical Sciences Laser," UCRL-JC-139623, 00-ERD-066.

Ryerson, F. J., et al., "Active slip-rates on the Altyn Tagh Fault-Karakax Valley segment: constraints from surface exposure dating," *Trans. Am. Geophys. Un.*, **80**, F1008, UCRL-JC-138087 Abs, 00-ERI-009.

Sankaran, V., D. J. Maitland, J. T. Walsh, Jr., "Polarized light propagation in turbid media," *Proc. SPIE*, **3598**, 158, UCRL-JC-131122, 99-LW-001.

Sankaran, V., J. T. Walsh, Jr., D. J. Maitland, "Polarized light propagation through tissue phantoms containing densely packed scatterers," *Optics Lett.*, **25**, 239–241, UCRL-JC-135338, 99-LW-001.

Sankaran, V., J. T. Walsh, Jr., D. J. Maitland, "Polarized light propagation through tissue and tissue phantoms," *OSA Annual Meeting*, UCRL-JC-135239 Abs, 99-LW-001.

Sankaran, V., K. Schoenberger, D. J. Maitland, "Polarization discrimination of coherently propagating photons in turbid media," *Appl. Optics*, **38**, 4252, UCRL-JC-132681, 99-LW-001.

Sankaran, V., M. J. Everett, D. J. Maitland, J. T. Walsh, Jr., "Propagation in biologic tissue and phantoms," *Opt. Lett.*, **24**, 1044, UCRL-JC-133624, 99-LW-001.

Santer, B. D. et al., "Interpreting differential temperature trends at the surface and in the lower troposphere," *Science*, **287**, 1227–1232, UCRL-JC-135694, 99-ERD-056.

Santer, B. D. et al., "Statistical significance of trends and trend differences in layer-average atmospheric temperature time series," *J. Geophys. Res.* , **105**, 7337–7356, UCRL-JC-133622, 99-ERD-056.

Schenkel, T. et al., "Influence of hydrogen on the stability of positively charged silicon dioxide clusters," *J. Chem. Phys.*, **113**, 2419, UCRL-JC-138014, 00-ERD-029.

Schwartz, A., M. Kumar, P. Bedrossian, W. King, "Coupling automated electron backscatter diffraction with transmission electron and atomic force microscopies," *Microsc. Microanal.*, **6(2)**, 940, UCRL-JC-137364, 98-ERD-080.

Schwartz, A., M. Kumar, W. King, "Influence of processing method on the grain boundary character distribution and network connectivity," *MRS Proc.*, **586**, 3, UCRL-JC-134727, 98-ERD-080.

Schwegler, E., G. Galli, F. Gygi, "Water under pressure," *Phys. Rev. Lett.*, **84**, 2429, UCRL-JC-134297, 98-SI-008 and 00-ERD-031.

Seward, K. P., D. S. Nath, P. B. Ramsey, P. Krulevitch, "Thermomechanical characterization of nickel-titanium-copper shape memory alloys," *ASTM Symp. on Mechanical Properties of Structural Films*, UCRL-JC-136906 Abs, 98-ERD-062.

Shields, S. J., R. L. Balhorn, "Characterization of tetanus toxin protein-ligand non-covalent complexes using mass spectrometry," *American Chemical Soc. Meeting Abs.*, UCRL-MI-138760, 00-ERD-006.

Smith, C. A. and H. W. H. Lee, "Ultraviolet-blue emission and electron-hole states in ZnSe quantum dots," *Appl Phys. Lett.*, **75**, 1688, UCRL-JC-135317, 00-LW-010.

Snavely, R. et al., "Intense high energy proton beams from Petawatt laser irradiation of solids," *Phys. Rev. Lett.*, **85**, 2945, UCRL-JC-137050, 99-ERD-063.

Stallard, B. W., et. al., "Modeling of spheromak plasma buildup in SSPX by power balance and helicity injection," *Innovative Confinement Concepts Conf. 2000*, UCRL-JC-137257 Abs, 00-SI-008.

Stanford, S. A., D. Stern, W. van Breugel, C. De Breuck, " The FIRST sample of ultraluminous infrared galaxies at high redshift I. Sample and near-IR morphologies," *Astrophys. J. Suppl.*, in press, UCRL-JC-139101, 98-ERI-005.

Stern, D. et al., 'Discovery of a color-selected quasar at $z = 5.50$," *Astrophys. J. Lett.*, **533**, L75, UCRL-JC-138092, 98-ERI-005

Sylwester, E. R., E. A. Hudson, P. G. Allen, "The structure of uranium (VI) sorption complexes on silica, alumina, and montmorillonite," *Geochimica et Cosmochimica Acta*, **64**, 2431, UCRL-JC-134461, 98-ERD-094.

Sylwester, E. R., P. G. Allen, P. Zhao, B. E. Viani, "Interactions of uranium and neptunium with cementitious materials studied by EXAFS," *Proc. Mat. Res. Soc.*, **608**, 11, UCRL-JC-135790, 98-ERD-094.

Tang, M., M. Fivel, L. P. Kubin, "From forest hardening to strain hardening in body centered cubic single crystals at low temperatures: simulation and modeling," *Mat. Sci. & Eng. A*, in press, UCRL-JC-139714, 00-SI-011.

Thompson, C. et al., "Fast Fourier and wavefront transforms for wavefront reconstruction in adaptive optics," *Proc. SPIE*, **4124**, UCRL-JC-139877, 98-ERD-061.

Thulasira, V., S. McCutchen-Maloney, V. L. Motin, E. Garcia, "Detection, purification and identification of virulence factors in *Yersinia pestis* using SELDI protein chip arrays," *Biotechniques*, in press, UCRL-JC-138922, 99-ERD-083.

Tom, H. W. K. and M. D. Feit, *Time-resolved imaging study of material modification and crack formation during laser damage*, UCRP-LS00-006, 00-ERD-066.

Tsap, L. V., "Multiple input feature sets from real-time color and range data for reliable tracking," *Workshop on Digital and Computation Video*, Tampa, FL, 1999, UCRL-JC-136053, 99-ERI-009.

Tsap, L. V., "Real-time local range on demand for tracking gestures and dynamic regional range images," *IEEE Workshop on Human Modeling Analysis and Synthesis*, Hilton Head, SC, 2000, UCRL-JC-137651 Rev 1, 99-ERI-009.

van Breugel, W. et al., "No longer the most distant known galaxy," *Nature*, in press, UCRL-JC-140561, 98-ERI-005.

van der Woerd, J. et al., "Uniform slip-rate along the Kunlun Fault: implications for seismic behavior and large-scale tectonics," *Geophysical Res. Lett.*, **27**, 2353–2356, UCRL-JC-136818, 00-ERI-009.

Vogel, J. S., "AMS for human biochemistry: the practice and the potential," *Nucl. Inst. & Meth.*, in press, UCRL-JC-135391, 98-ERI-012.

Vogel, J. S., "Low background isotope tracing in biochemistry," *Nuclear Physics News,* **10**, 8–18, UCRL-JC-136766, 98-ERI-012.

Weaver, A., P. Duffy, M. Eby, E. Wiebe, "On the evaluation of ocean and climate models using present-day forcing," *Atmosphere-Ocean*, **38**, 271, UCRL-JC-133962, 99-SI-001.

Wharton, K. B. et al., "Effects of non-ionizing prepulses in high-intensity laser-solid interactions," *Phys. Rev. E, Rapid Comm.*, in press, UCRL-JC-141612, 99-ERD-036.

Wheeler, E. K. et al., "Scatter loss from environmental degradation of KDP crystals," submitted to *Appl. Phys. A.*, UCRL-JC-134819, 00-ERD-035.

White, J., E. Schwegler, G. Galli, F. Gygi, "The solvation of Na+ in water: first principles simulations," *J. Chem. Phys.*, **113**, 4668, UCRL-JC-136942, 98-SI-008.

Wickett, M., P. Duffy, G. Rodrigue, "A reduced grid for a parallel global ocean general circulation model," *Ocean Modeling*, in press, UCRL-JC-139249, 99-SI-001.

Wilks, S. C. et al., "Energetic proton generation in ultra-intense laser solid interactions," *Phys. of Plasmas*, UCRL-ID-137814, 99-ERD-049.

Wilks, S. C. et al., "Ion acceleration in ultra-intense, laser-plasma interactions," UCRL-JC-135008 Abs, 99-ERD-049.

Wilks, S. et al., "Energetic proton generation in ultra-intense laser-solid interactions," *Phys. Plasmas*, **8**, 542, UCRL-ID-137814, 99-ERD-063.

Williams, G., and H.-S. Park, "LOTIS Upper Limits and the Prompt OT from GRB 990123," *AIP Conf. Proc.*, **526**, 250, UCRL-JC-141126, 00-ERD-027.

Williams, R. V. et al., "Exceptionally pyramidalized olefins: a theoretical study of the cyclopropenyl fused tricycles tricyclo[3.2.1.0(2,4)]oct-2(4)-ene, tricyclo[3.2.1.0(2,4)]octa-2(4),6-diene," *J. Org. Chem.*, **65**, 562, UCRL-JC-135854, 98-SI-008.

Wirth, B. D., V. Bulatov, T. Diaz de la Rubia, "Atomistic simulation of stacking fault tetrahedra formation in Cu," *J. Nucl. Mat.*, **283**, 773, UCRL-JC-136398, 98-ERD-090.

Wong, J. et al., *Morphology, microstructure and defects in fused silica induced by high-power 3W (355 nm) laser pulses,* UCRL-JC-142167, 98-ERD-063.

Wood, R. D., et al., "Particle control in the sustained spheromak physics experiment," *J. Nucl. Mat.*, in press, UCRL-JC-139018, 00-SI-008.

Woodruff, S. et al., "Sustainment of a 1-ma spheromak by dc helicity injection," *27th European Physical Society Conference on Controlled Fusion and Plasma Physics*, UCRL-JC-137354 Abs, 00-SI-008.

Yin, A. et al., "Tertiary deformation history of southeastern and southwestern Tibet during the Indo-Asian collision," *Geol. Soc. Amer. Bull.*, **111**, 1644–1664, UCRL-JC-126601, 00-ERI-009.

Yoo, C. S. et al., "Crystal structure of carbon dioxide at high pressure," *Phys. Rev. Lett.*, **83**, 5527, UCRL-JC-134573 Rev 1, 00-ERD-031.

Zhib, H. M., T. Diaz de la Rubia, M. Rhee, J. P. Hirth, "3D dislocation dynamics: stress-strain behavior and hardening mechanisms in fcc and bcc metal," *J. Nucl. Mat.*, **276**, 154, UCRL-ID-134061, 98-ERD-090.

Zweiback, R. A. et al., "Characterization of fusion burn time in exploding deuterium cluster plasmas," *Phys. Rev. Lett.*, **85**, 3640, UCRL-JC-13700, 00-LW-021.

Zweiback, R. A.. et al., "Nuclear fusion driven by Coulomb explosions of large deuterium clusters," *Phys. Rev. Lett.*, **84**, 2634, UCRL-JC-136863, 00-LW-021.

Principal Investigator Index

Project Title Index

Tracking Code Index


DEPARTMENT OF ENERGY
UNITED STATES OF AMERICA


NNSA
National Nuclear Security Administration